Cometary dust and origin of matter in the protoplanetary disk

Baptiste Guérin

université PARIS-SACLAY

Cometary dust and origin of matter in the protoplanetary disk

Poussières cométaires et origine de la matière dans le disque protoplanétaire

Thèse de doctorat de l'université Paris-Saclay

École doctorale n° 127, Astronomie et Astrophysique d'Ile de France (AAIF)

Spécialité de doctorat : Astronomie et Astrophysique

Unité de recherche : Université Paris-Saclay, CNRS, IJCLab, 91405, Orsay, France

Référent : Faculté des Sciences d'Orsay

Thèse présentée et soutenue à Paris-Saclay,

le 13/12/2021, par

Baptiste GUERIN

Composition du Jury :

Alain ABERGEL Professeur, Université Paris-Saclay	Président
Mathieu ROSKOSZ Professeur, Sorbonne Université	Rapporteur & Examinateur
Anne-Magali SEYDOUX Directrice de recherche, Université Jean Monnet, St-Etienne	Rapporteur & Examinatrice
Christelle BRIOIS Maîtresse de conférences, Université D'Orléans	Examinatrice
Hervé COTTIN Professeur, Université Paris-Est - Créteil	Examinateur

Direction de la thèse

Cécile ENGRAND Directrice de recherche, Université Paris-Saclay	Directrice de thèse
Emmanuel DARTOIS Directeur de recherche, Université Paris-Saclay	Co-Encadrant de thèse

Thèse de doctorat

NNT : 2021UPASP138

université PARIS-SACLAY

ÉCOLE DOCTORALE
Astronomie
et Astrophysique
d'Île-de-France (AAIF)

Titre : Poussières cométaires et origine de la matière dans le disque protoplanétaire

Mots clés : matière organique ; disque protoplanétaire ; micrométéorites ; Poussières cométaires

Résumé : L'objectif de cette thèse est l'analyse de poussières extraterrestres collectées en Antarctique : les micrométéorites antarctiques chondritiques (AMMs) et les micrométéorites ultracarbonées (UCAMMs). Les modèles prédisent que 80% de la poussière qui tombe sur Terre est d'origine cométaire. Les AMMs partagent de nombreuses caractéristiques avec les poussières cométaires rapportées par la mission spatiale Stardust, et les caractéristiques des UCAMMs suggèrent une formation à très basse température, loin du soleil primitif. Les micrométéorites offrent donc une opportunité de comprendre les mécanismes de formation des poussières cométaires. Les UCAMMs sont majoritairement constituées d'une matrice organique contenant de petits assemblages minéralogiques. La grande quantité de matière organique (MO) présente dans les UCAMMs permet son analyse sans faire usage des méthodes d'extraction classiques utilisées pour extraire la matière organique insoluble (IOM) des météorites. L'analyse des AMMs par microspectroscopie Raman et infrarouge indique une MO polyaromatique présentant un fort degré de désordre, avec des caractéristiques proches de celles des grains cométaires rapportés par la mission Stardust. La variabilité des paramètres spectraux de la MO est cependant plus importante pour les AMMs chondritiques hydratées que dans celles ne contenant pas de phyllosilicates. Les spectres dans l'infrarouge moyen et lointain montrent que les AMMs non hydratées contiennent des silicates de type pyroxènes et olivines et que les phases aqueuses des AMMs hydratées sont principalement des phyllosilicates. Les analyses infrarouge et Raman sur les UCAMMs montrent une quantité relativement importante d'azote dans la matière organique, et la présence ponctuelle de groupements nitriles. Des analyses de la MO résolue spatialement par microscopie X en transmission (STXM-XANES) montrent la présence de 3 phases organiques de compositions distinctes au sein de la MO des UCAMMs. L'azote présent dans les UCAMMs n'est porté que par une de ces trois phases, qui présente des rapports atomiques N/C allant jusqu'à 0,2. Les phases inorganiques contenues dans les UCAMMs ont été analysées par microscopie électronique en transmission. Elles existent comme phases isolées, ou sous forme de petits assemblages minéraux dans la matrice organique, ou comme d'agrégats de différents minéraux, souvent cimenté par une matrice riche en silicium. Un minéral présentant une texture similaire à celle d'un phyllosilicate a été observé dans une des UCAMM analysées. La similarité entre la matière organique des UCAMMs et celle des particules cométaires suggère une formation de ces objets dans les régions externes du disque protoplanétaire. La présence conjointe de minéraux se formant à haute température et de minéraux hydratés au sein de cette matière organique implique un mécanisme de transport des régions internes vers les régions externes du disque protoplanétaire. L'observation d'un phyllosilicate potentiel dans les UCAMMs soulève aussi la question de la possibilité d'altération aqueuse directement sur les surfaces cométaires. Cependant, la présence de phase hydratées au sein de matériel cométaire pourrait également résulter de l'accrétion de grains déjà altérés sur un précédent corps parent. Les micrométéorites en général offrent donc un outil unique pour l'étude du continuum astéroïde-comète mis en évidence depuis le retour des échantillons de la mission Stardust, et pour mieux comprendre les relations entre les différents objets du système solaire jeune ainsi que les mécanismes d'altération qu'ils ont subis.

université PARIS-SACLAY

ÉCOLE DOCTORALE
Astronomie
et Astrophysique
d'Île-de-France (AAIF)

Title : Cometary dust and origin of matter in the protoplanetary disk

Keywords : micrometeorites ; organic matter ; protoplanetary disk ; cometary dust

Abstract:The objective of this thesis is the analysis of extraterrestrial dust collected in Antarctica: chondritic Antarctic micrometeorites (AMMs) and ultracarbonaceous micrometeorites (UCAMMs). Models predict that 80% of the dust that falls to Earth is of cometary origin. AMMs share many characteristics with the cometary dust reported by the Stardust space mission, and the characteristics of UCAMMs suggest formation at very low temperatures, far from the early sun. Micrometeorites therefore offer an opportunity to understand the mechanisms of cometary dust formation. UCAMMs are mostly composed of an organic matrix containing small mineralogical assemblages. The large amount of organic matter (OM) present in UCAMMs allows its analysis without using the classical extraction methods used to extract insoluble organic matter (IOM) from meteorites. Analyses of the AMMs by Raman and infrared microspectroscopy indicate a polyaromatic OM with a high degree of disorder, with characteristics close to those of the cometary grains reported by the Stardust mission. The variability of the OM spectral parameters is however more important for hydrated chondritic AMMs than for those without phyllosilicates. The mid- and far-infrared spectra show that the non-hydrated AMMs contain pyroxene and olivine silicates and that the aqueous phases of the hydrated AMMs are mainly phyllosilicates. Infrared and Raman analyses of the UCAMMs show a relatively large amount of nitrogen in the organic matter, and the occasional presence of nitrile groups. Spatially resolved X-ray transmission microscopy (STXM-XANES) analyses of the OM show the presence of 3 organic phases of distinct compositions within the UCAMM OM. The nitrogen present in the UCAMMs is carried by only one of these three phases, which has N/C atomic ratios up to 0.2. The inorganic phases contained in the UCAMMs were analysed by transmission electron microscopy. They exist as isolated phases, or as small mineral assemblages in the organic matrix, or as aggregates of different minerals, often cemented by a silicon-rich matrix. A mineral with a texture similar to that of a phyllosilicate was observed in one of the UCAMMs analysed. The similarity between the organic matter of UCAMMs and that of cometary particles suggests that these objects were formed in the outer regions of the protoplanetary disk. The joint presence of high-temperature-forming minerals and hydrated minerals within this organic matter implies a transport mechanism from the inner to the outer regions of the protoplanetary disk. The observation of a potential phyllosilicate in UCAMMs also raises the question of the possibility of aqueous alteration directly on cometary surfaces. However, the presence of hydrated phases within cometary material could also result from the accretion of already altered grains on a previous parent body. Micrometeorites in general thus offer a unique tool for the study of the asteroid-comet continuum highlighted since the return of the Stardust mission samples, and for a better understanding of the relationships between the different objects of the young solar system and the space weathering mechanisms they have undergone.

Remerciements :

Suite à ces 3 ans de thèse durant cette période un peu particulière de Covid vient le temps des remerciements.

Je souhaite dans un premier temps remercier Cécile et Emmanuel, mes encadrants de thèse, de m'avoir fait confiance pour travailler sur ce sujet complexe et passionnant. Je les remercie pour leur aide, leurs conseils et leur compréhension tout au long de ces 3 années marquées par la pandémie de Covid, qui m'ont permis de continuer à travailler dans les meilleures conditions possibles malgré les difficultés que j'ai pu rencontrer. Je remercie également Mattieu Gounelle et Thomas Pino d'avoir accepté de suivre mon travail de thèse durant ces 3 années.

Je remercie Anne-Magali Seydoux et Mathieu Roskosz d'avoir accepté d'être rapporteurs pour cette thèse et pour leurs retours sur le contenu du manuscrit. Merci également à Hervé Cottin et Christelle Briois d'avoir accepté de faire partie de mon Jury. Enfin, merci à Alain Abergel pour avoir accepté de présider ce Jury ainsi que pour son suivi et son soutien durant ces 3 années de thèse.

Je souhaite également remercier Corentin Le Guillou et Hugues Leroux pour leur aide, leurs conseils et les discussions fructueuses concernant les analyses de microscopie électronique en transmission. Merci tout particulièrement à Corentin pour son aide, sa patience, mais aussi pour avoir pris le temps de m'apprendre l'art du traitement de données avec Python malgré mes difficultés initiales avec le code.

Je souhaite aussi remercier l'école doctorale 127, et plus particulièrement Thierry Fouchet et Alain Abergel pour leurs conseils et leur suivi de mon travail de thèse en cette période difficile de pandémie.

Merci également à Julien, avec qui j'ai partagé un (deux) bureau(x) pendant ces 3 ans. Merci pour ces discussions à propos de nos sujets de thèse, pour son aide et sa patience avec mes dizaines de questions sur python, et pour toutes les autres conversations à propos de tout et de rien, qui m'auront aidé à surmonter les difficultés que j'ai pu rencontrer. Merci aussi à Lucie, pour ses conseils, son aide et son soutien pendant ces 3 années. Merci également à Marie de m'avoir initié à l'enseignement et pour tous ses conseils concernant mon monitorat, qui m'ont permis d'apprécier au maximum cette expérience.

Je remercie Réjane et Kim pour leur accompagnement dans les différentes démarches administratives au sein du laboratoire.

Enfin, je voudrais remercier ma famille et mes amis pour m'avoir toujours soutenu durant mes études, et durant ces 3 ans de thèse dans un contexte épidémique un peu particulier.

Table of contents

Chapter 1

1. Astrophysical context

This chapter outlines the general scientific context in which this work will take place, with a general overview of the solar system formation, from the pre-solar cloud to the recent solar system configuration. As this work focuses on the analysis of the cometary grains component in micrometeorite collections, this chapter will also focus on the formation and the presentation of different types of small bodies populating the solar system, such as asteroids and comets, as well as dust formation and dynamics within the solar system. Finally, the recovery method of Antarctic Micrometeorites (AMMs) at the Concordia station in Dome C will be described.

1.1. Solar System formation

The solar system formed about 4.6 billion years ago from the gravitational collapse of a molecular cloud referred to as the proto-solar nebula. Molecular clouds present a large range of densities, with low density regions of a few hundreds to thousands of hydrogen per cubic centimeter, and their core can reach molecular hydrogen density values larger than $10^5 cm^{-3}$ (Reipurth, 2005). They also present high turbulence behavior, probably caused by Supernova explosions and constantly supplied in energy by young star's energetic winds. These high turbulences ultimately lead to shock and collision within these giant structures and can generate coagulation processes within the dust and gas cloud which will start to condensate and form dense-enough structures to be gravitationally bound (Mac Low and Klessen, 2004; Reipurth, 2005). If the newly formed dense structure survive long enough in the cloud, their gravitational pull can lead to the formation of a proto-star. From there, the material surrounding the core will form a so-called 'circumstellar envelope' which will evolve with the star. The exact birth of a star can be defined at two different timings: when the static core has formed or when the stellar embryo reaches half of its final mass. However, the growth evolution of stars occurring on a relatively short timescale compared to the global evolution of a stellar system, the difference is tenuous for the present work.

Once a proto-stellar core is set, the newly born star will start to evolve through different stages to eventually form a stellar system. The different steps for the formation of a low mass star are summarized in Figure 1-1, from the proto-stellar core formation to solar-like configuration with a central star surrounded by debris and planets. The different stages of evolution of the star is based on the emission continuum of its circumstellar material. Class 0 objects are only detected at sub-millimeter wavelength due to the large amount of circumstellar material veiling the proto-star emission. The next proto-stellar phase corresponds to Class I object. In that case, the proto-star is still embedded in large amount of circumstellar material but the star has higher bolometric temperature and can be observed at infrared wavelengths. Class II objects correspond to the optically visible stage, known as classical T Tauri stars. The star is still surrounded by material under the form of a circumstellar disk called the protoplanetary disk, with temperature lower than 10K at large distances from the star. This circumstellar matter keeps falling toward the central star and is not replenished. Debris disk also leads to shock and collision and ultimately coagulation of small grains from circumstellar material into larger body, forming the building blocks of planets. Eventually, this will lead to the formation of Class III objects or weak-line T Tauri stars where the disk is slowly depleted in material by feeding the central star and processing it to form planetary building blocks. At this stage, nearly no infrared signature of the circumstellar material

is visible, because of the disk's mass being mostly incorporated in larger-sized body that do not emit at infrared wavelengths.

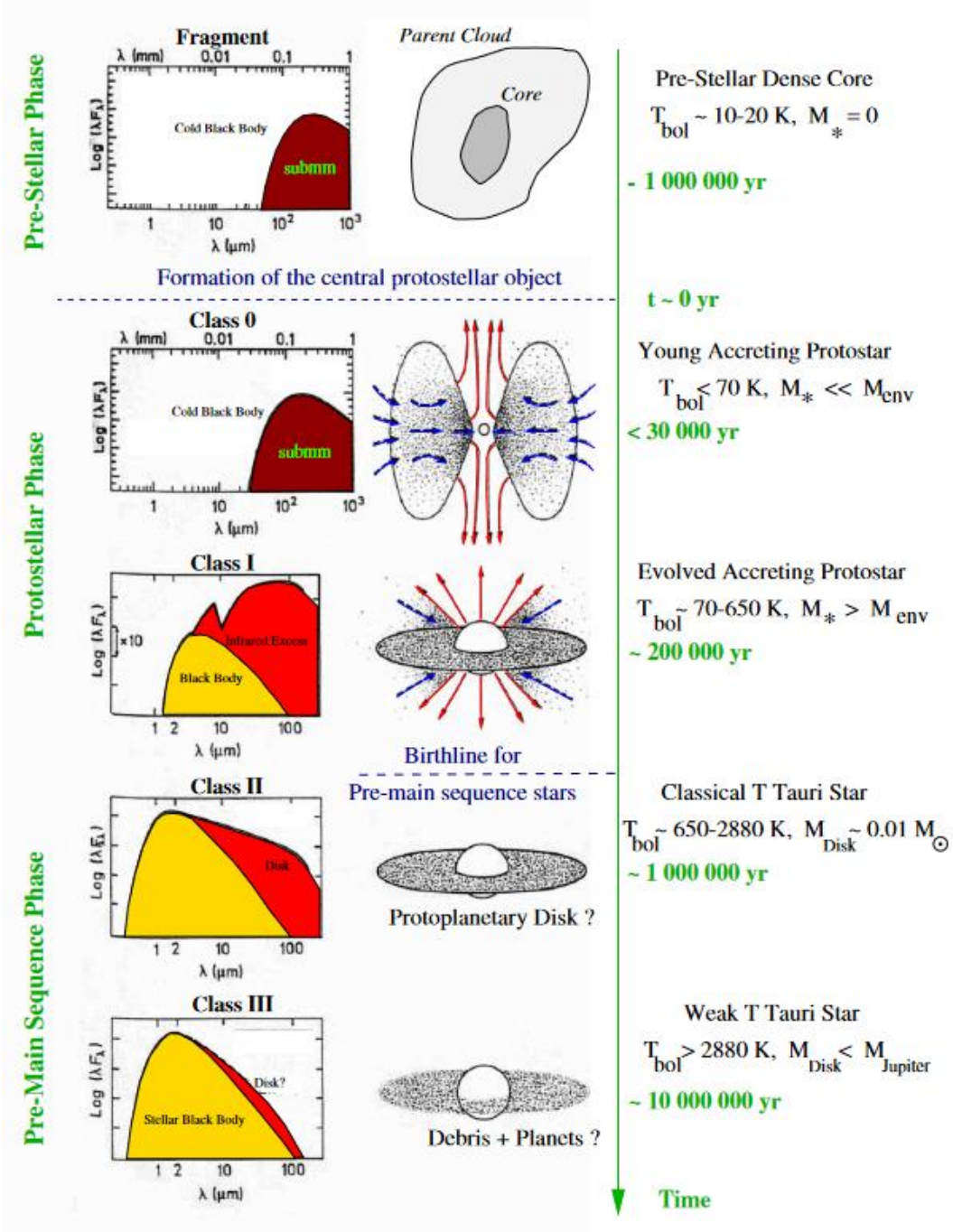

Figure 1-1: Evolution of star formation with five stages indicated. The different stages are characterized by different bolometric temperatures (right) and varying continuum spectra (left); figure from (Reipurth, 2005)

During the protoplanetary disk phase, after the sun has started its pre-main sequence, gas and dust start to aggregate and form larger sized bodies. These aggregation mechanisms are still unclear, but small micrometer-sized dust can coagulate up to kilometric bodies called planetesimals. Some will keep growing until reaching the sizes of planets by accreting all the material on their orbit. Some smaller bodies will stop their growth and have sizes up to several kilometers such as asteroids and comets. The progressive transformation of the disk into debris

and planets occurred on a relatively short timescale compared to the complete process of star formation, meaning that planetary formation occurs on a timescale of the order of 10^6-10^7 years.

From there, solar system bodies will evolve differently depending on their size, their components and their distance to the Sun. If they are large enough, solar system bodies experiment differentiation with the separation of their different constituents in layers arranged by density. The denser materials, like iron, will 'sink' to the center of the planet while lighter material rise up toward the surface. An essential constituent of the differentiation process is the heating source. The extent of planetary differentiation will also depend on the available heat during the process. The first-formed planetismals are thought to have accreted a certain amount of short-lived radionucleides which, by radioactive decay, provided heating to catalyze differentiation. ^{26}Al decay to ^{26}Mg is thought to be the main source of heat in early formed planetesimals. Radioactive decay of ^{60}Fe could have also played a role. Ultimately, differentiation will lead to the formation of planetary bodies with a 'layered configuration'. This process strongly alters the primitive composition of the planetary nucleus i.e.; it will not keep the information of the early material that formed it. In order to better understand the chemistry and physical processes of the early solar system, it is therefore necessary to investigate extraterrestrial samples that experienced the least planetary differentiation as well as subsequent hydrothermal effects.

1.2. Asteroids and comets

Asteroids and comets are both solar system bodies which formed late enough or which were small enough to escape to a high degree of differentiation and thus potentially retain the most pristine information on the initial chemistry constitutive of the building blocks of the solar system bodies.

1.2.1. Asteroids

Asteroids are rocky object, generally distributed at specific locations in the solar system. They are irregularly shaped bodies with sizes typically ranging from tens of meters to hundreds of kilometers. The larger ones could have experimented partial/incomplete differentiation, leading to different types of asteroids. Most of the asteroids population is located in the Main Belt (from 2 to 5 au), between the orbits of Mars and Jupiter, the so-called the asteroid belt. Smaller populations of asteroids are also present between Mars and the Earth (Near-Earth Asteroids), near Jupiter orbit (Trojans asteroids) and between Jupiter and Saturn (Centaurs). Although most small asteroids escaped planetary differentiation, secondary alteration processes may have occurred at their surface since their formation billions of years ago, among which the most important are the thermal metamorphism (e.g. generated by impact), hydrothermal alteration and space weathering.

Asteroids present different surface compositions that have been classified in different types based on spectral and photometric measurements. Using wavelengths from the ultraviolet (UV) to the mid infrared, the surface properties such as mineralogy, space weathering extent but also grain size can be determined remotely by observing them with space probes and telescopes. Study of numerous asteroids from the main belt led to the elaboration of a taxonomy based on their reflectance spectra (DeMeo et al., 2015). The different asteroid spectral classes are summarized in Figure 1-2. S-complex asteroids, for 'stony', are silicate and oxide-rich objects containing low amounts of carbon. They are thought to have experienced thermal metamorphism.

C-complex asteroids (for Carbonaceous) consist in 6 different sub-classes which represent the main population of the asteroid main belt (up to 60% in mass, (DeMeo and Carry, 2013)). They represent the most primitive asteroids. Their surface is thought to be covered by dark material containing up to 5% of organic matter. Among C-complex asteroids, some subclasses are hydrated such as Cgh and Ch. Finally, the X-complex class consist of asteroids bearing water ice, probably at their surface (Campins et al., 2010), and could be related to comets.

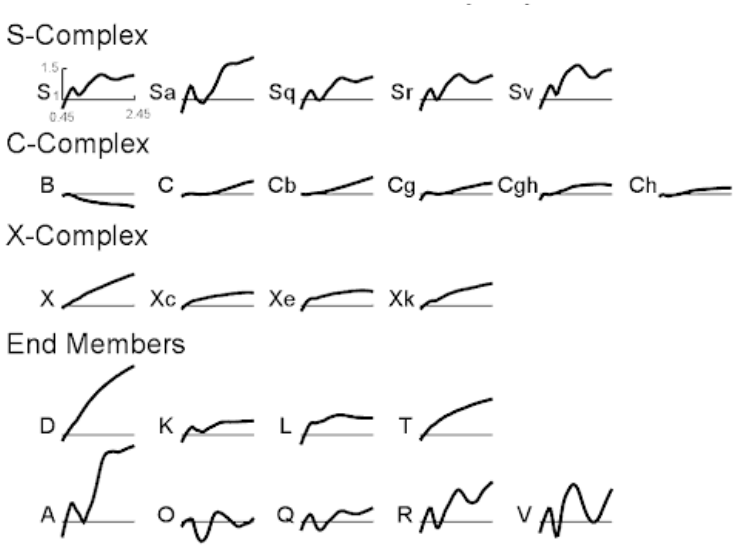

Figure 1-2: Different classses of asteroids and their representative reflectance spectra (ref)

The difference between asteroids and comets mostly lies in the composition and the surface activity of the body. Asteroids contains less ice and volatiles in general than comets although the separation gets tenuous as some asteroids in the main belt have shown some surface activity reminiscent of cometary activity (Hsieh and Jewitt, 2006, Hsieh, 2012 #2512), providing a link toward the existence of an asteroid-comet continuum.

1.2.2. Comets

Comets are small external solar system bodies coming from two main reservoirs: The Kuiper belt and the Oort cloud (predicted by the orbit of long-period comets). Their sizes and the fact that they mostly reside in the outer cold regions of the solar system (with temperature <30K) implies that they underwent little or no thermal modifications, making comets one of the most preserved objects in the solar system.

Cometary formation comes within the scope of a larger mechanism in the young solar system evolution, as described by e.g. the Nice model (Morbidelli et al., 2014; Walsh et al., 2012). This model suggests outward resonance of Jupiter and Saturn led to their migration and ultimately instability in the outer protoplanetary disk. This results in an outward and inward migration of small solar system bodies, leading to the Late Heavy Bombardments (LHB) on inner planets and the current orbital distribution of most planetary and cometary bodies in the outer solar system (Figure 1-3).

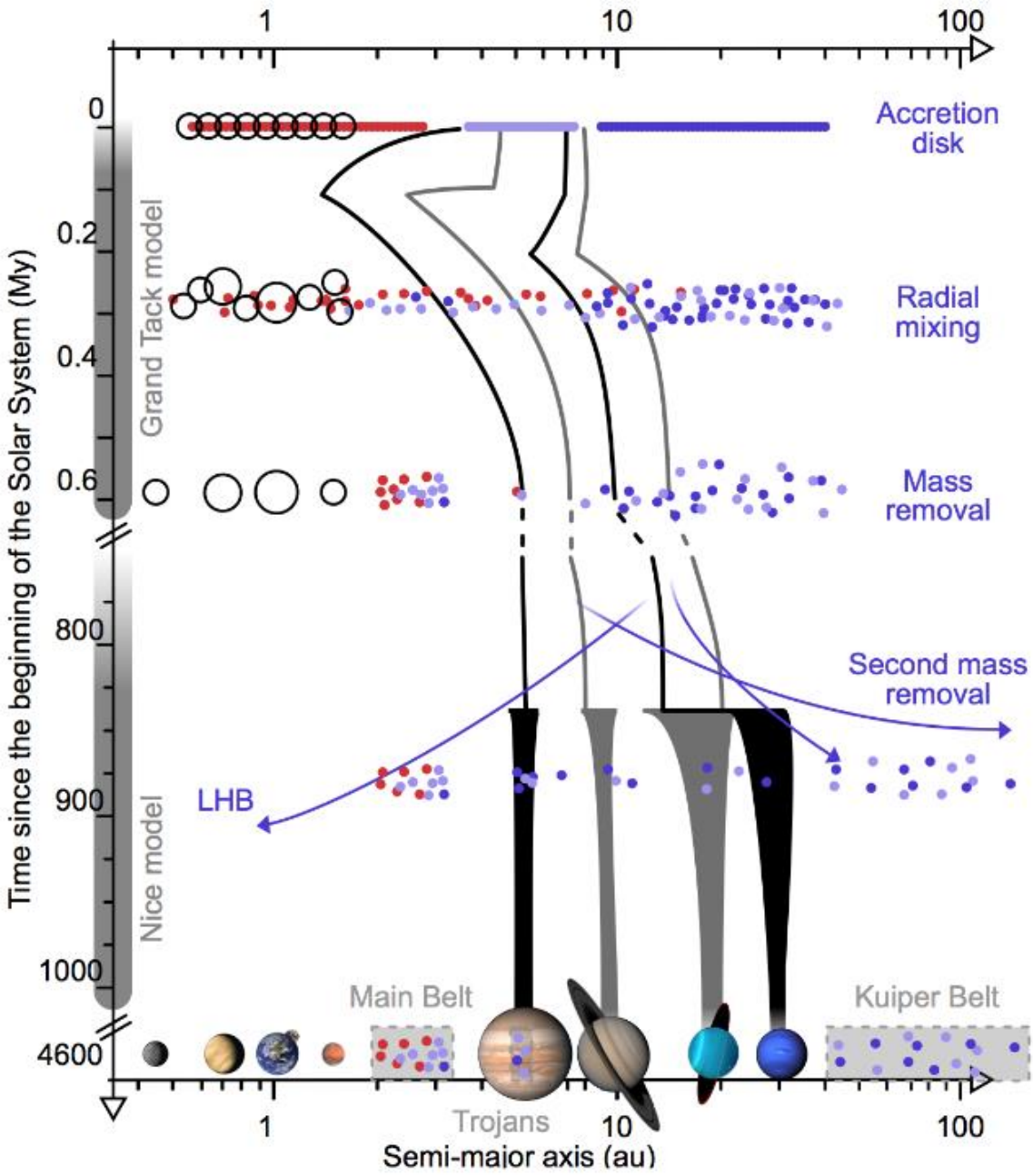

Figure 1-3: Giant planet migration effect on the distribution of mass in the early solar system as predicted by the Nice model, from (DeMeo and Carry, 2014).

Comets presents an irregularly-shaped surface which mostly consists in volatile ices (mostly water, CO, CO_2…) and dust. They are often divided in short and long-period comets. Long period comets (>200 years) are thought to originate from the Oort cloud while short periods comet (<200 years) would come from the Kuiper Belt, located outward Saturn orbit. Comet orbit can be perturbed by gravitational interaction with neighboring giant planets, leading to an elliptic trajectory bringing them to the inner solar system. By getting closer to the sun, the surface temperature of comets will rise and result in several transformation processes at their surface. Ices are heated and eventually sublimate when comets are close enough to the Sun (typically less than 3 AU). Sublimation of the ices will drag surface dust leading to the development of the comet's coma, formation of a dust tail, accompanied by an ion tail formed by interaction with the Solar

wind. These phenomena have been defined as cometary activity. Observation of surface activity similar to cometary activity on Main Belt asteroids (Hsieh et al., 2012) suggests the boundary between some asteroid and cometary bodies could be blurred. The possibility of an asteroid-comet continuum has been discussed in the last decade (Gounelle, 2011; Hsieh, 2017).

The possibility of aqueous alteration occurring on comets has been raised after potential identification of hydrated phases on 9P/Tempel 1 surface after the Deep Impact mission (Lisse et al., 2006). Aqueous alteration in cometary surface conditions has been explored experimentally (Nakamura-Messenger et al., 2011; Takigawa et al., 2019). Results indicate that liquid water with a high pH could in particular alter amorphous silicates on timescales as short as hours while alteration through gas-mineral interaction has shown to be not inefficient. As some comets could sustain the temperature and pressure conditions to permit basic liquid water to circulate on their surface (Suttle et al., 2020a; Watanabe et al., 2014), in-situ cometary aqueous alteration is therefore a possibility.

1.3. Dust in the solar system

Interplanetary dust has been first observed through zodiacal light observations, although such techniques mostly allow near earth observation for particles of a specific size range. This dust has two main sources: asteroids and comets (see Figure 1-4). Asteroidal dust is thought to be generated through impact on asteroidal bodies. This can happen during collision of two asteroids in regions of the main belt or through meteoritic impacts on their surface. Cometary dust is generated during cometary activity: surface grains can be dragged by gas sublimation during the comet entry in the inner solar system producing a dust coma and releasing dust on its orbit.

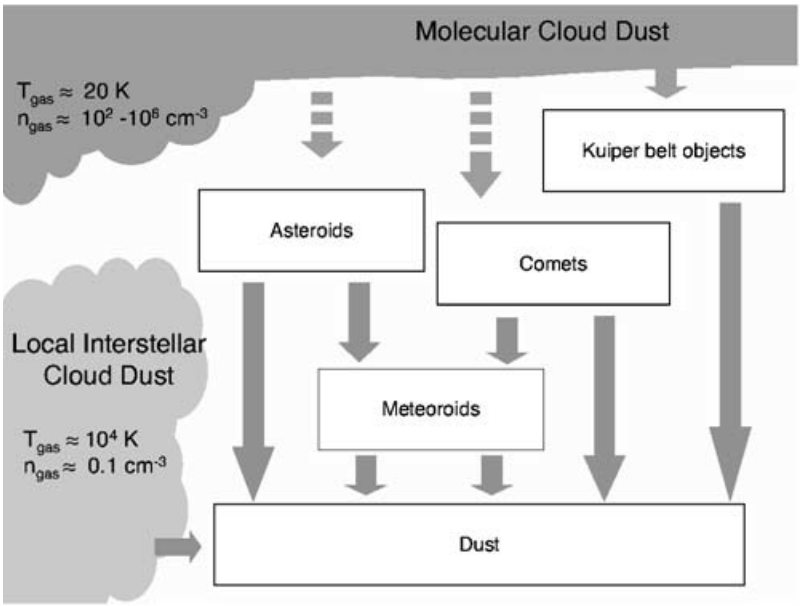

Figure 1-4: The different sources of interplanetary dust from Mann et al. (Mann et al., 2006).

Asteroidal dust is brought to the inner solar system through the Poynting-Robertson effect. This effect is due to solar radiations and is known to slow the orbital speed of free floating interplanetary particles. Thus, asteroid dust enters the Earth's atmosphere with relatively low velocities (<15 km.s^{-1}), allowing limited alteration from atmospheric entry heating for some of them. For comets, it was originally thought that, due to their important eccentricity and inclination, cometary dust with size larger than 70 µm reaching the Earth would fully vaporize during atmospheric entry because of the high velocity of the grains (Love and Brownlee, 1991).

Conversely, recent modelling of dust circulation in the solar system showed that cometary dust orbits could circularize through Poynting-Robertson effect (Carrillo-Sánchez et al., 2015; Nesvorný et al., 2011b) and therefore enter Earth's atmosphere with lower velocities close to 15 $km.s^{-1}$, for particles ranging from 100 µm to 200 µm. Such velocities would allow some cometary dust to reach Earth's surface without being strongly modified by the atmospheric entry process.

1.3.1. Interplanetary Dust Particles (IDPs)

First samples from interplanetary dust were collected in the Earth stratosphere by NASA's ER-2 airplane (Brownlee et al., 1971). A large amount of interplanetary dust particles (IDPs) with sizes smaller than 50 µm have been collected since the first flight and have been categorized based on their chemical characteristics. "Chondritic" IDPs are the particles which exhibit elemental compositions close to the one of carbonaceous chondrites (CC) meteorites. IDPs which present composition differing from the chondritic values are simply referred as "non-chondritic" IDPs.

Among chondritic IDPs, several groups can be identified based on their mineral content. The IR characterization of silicates by Sandford et al. (1985) revealed 3 dominant groups in IDPs. Ol group presents an olivine-dominated mineralogy, Px group a pyroxene-dominated mineralogy and LLS (Latticed Layer Silicate) presents a strong phyllosilicate signature. IDPs presenting anhydrous mineralogy (Px and Ol groups) represent about 40% of the total population.

Another classification based on the texture of chondritic IDPs have been established (Bradley, 2005; Mackinnon and Rietmeijer, 1987). Two main types of chondritic IDPs have been characterized: Chondritic Smooth (CS) and Chondritic Porous (CP) IDPs. CS-IDPs are compact grains mostly composed of phyllosilicates. They are thought to be related to carbonaceous chondrite meteorites and could have been produced on icy asteroids that potentially presented aqueous activity at their surface. Chondritic porous IDPs display a fluffy texture with important porosity (Bradley, 2003). They are mostly constituted of submicrometer-sized crystalline silicate (olivine and pyroxene) and do not contain hydrous phases. They also contain polycrystalline aggregate (such as Glass with embedded Metals and Sulfides (GEMS)), silicate glasses, iron sulfides, FeNi metals. Silicates display Mg-rich composition with enstatite and forsterite being the dominant phases. Another important characteristic of CP-IDPs is the large amount of organic matter in grains that can go up to 45% in mass (Keller et al., 1994). All these characteristics suggests a cometary origin for CP-IDPs (Bradley, 1988; Bradley, 2005; Brownlee et al., 1994; Keller et al., 2005; Keller et al., 1992).

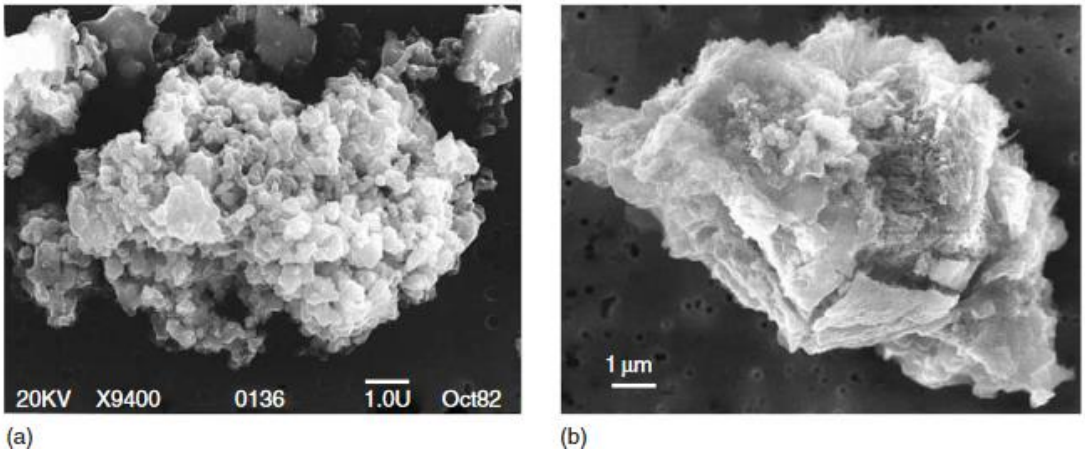

Figure 1-5: Secondary electron images of two types of Interplanetary Dust Particles by Bradley et al. (2005). (a) Anhydrous Chondritic Porous (CP) IDP. (b) Chondritic Smooth (CS) IDP presenting hydrated minerals.

1.3.2. Micrometeorites (MMs)

1.3.2.1. The first collection of extraterrestrial grains on Earth

The main mass of extraterrestrial material accreted on Earth is carried by particles with sizes 200 μm (Love and Brownlee, 1993). Therefore, they are powerful objects to investigate the chemistry of extraterrestrial material as well as better constrain its impact on early Earth chemistry. Micrometeorites (MMs) represent the fraction of interplanetary dust that survive the atmospheric entry and reach Earth's surface. While IDPs measure up to ~50μm, are collected mostly in the polar caps, MMs with sizes ranging between ~20 μm and several millimeters.

The first micrometeorites were collected in deep-sea sediments, using magnetic extraction to collect cosmic spherule (with the Challenger expedition in 1873, and still going on more recently (Prasad et al., 2013)). However, such collection methods imply the extraterrestrial grains underwent long period of exchange with the surrounding environment in conditions where chemical alteration or physical modification will occur.

A more recent method to collect extraterrestrial dust on Earth is to search in cold environment, such as polar regions of the globe. In 1984 and 1987, M. Maurette (CSNSM Orsay) collected micrometeorites in the cryoconite (dust made of sand, organics and bacteria) of Greenland icecap, where natural melting process in summer concentrated the extraterrestrial grains at the bottom of blue lakes, or in "cryoconite holes", making them more easily accessible than for previous collection methods (Maurette et al., 1986; Maurette et al., 1987). Along with usually found melted micrometeorites (cosmic spherules), unmelted micrometeorites were collected for the first time, although they represent only a small fraction of the recovered cosmic dust (~1%) (Maurette et al., 1987). Overall, collected particles showed evidence of strong water and even biological alteration due to their long residence time in surface water. The lack of Fe/Ni bearing phases, such as sulfides, usually found in extraterrestrial inorganic material, is another evidence these grains experienced an aqueous alteration.

Between 1987 and 1996, micrometeorite collections were performed by the CSNSM team in Antarctica, where extraterrestrial grains are collected by melting ice of the Antarctic blue ice cap. The first collections from Maurette et al. (1991) were carried out at 2 kilometers from the coast, at Cap Prudhomme, near the Dumont d'Urville French station. This collection allowed the recovery of an important amount of large micrometeorites (with sizes >25μm) with up to 20% of collected particles being extraterrestrial (Engrand and Maurette, 1998). Since 1995, US, Japanese and Italian/French teams also started to collect micrometeorites in Antarctica with different collection methods (e.g. Folco et al., 2005; Nakamura et al., 1999; Rochette et al., 2008; Taylor et al., 1998; Yada and Kojima, 2000). Micrometeorites were collected in water tanks used to supply drinking water of the South Pole and Dome Fuji stations. Extraterrestrial particles have also been collected in the Yamato Mountain in Antarctica (Terada et al., 2001), and in sediment traps at the surface of the Transantarctic Mountains (Folco et al., 2005; Rochette et al., 2008).

In 2000, the CSNSM team started a new expedition program led by J. Duprat in the central regions of Antarctica. Collections of micrometeorites are now carried out near the French-Italian station Concordia at Dome C (Figure 1-6). The station is located 1100km inland (75◦06'S 123◦20'E), on the Antarctic plateau which rises 3230 m above sea level. Conditions at Dome C allows a unique preservation of the extraterrestrial grains. Wind configuration protects the surface snow from terrestrial dust as they mostly go toward the coast of the continent and 3.5km of ice separates the surface snow from the continental floor. Temperature at Dome C vary from -

30 °C to -80°C, avoiding the potential aqueous alteration process occurring in the presence of liquid water.

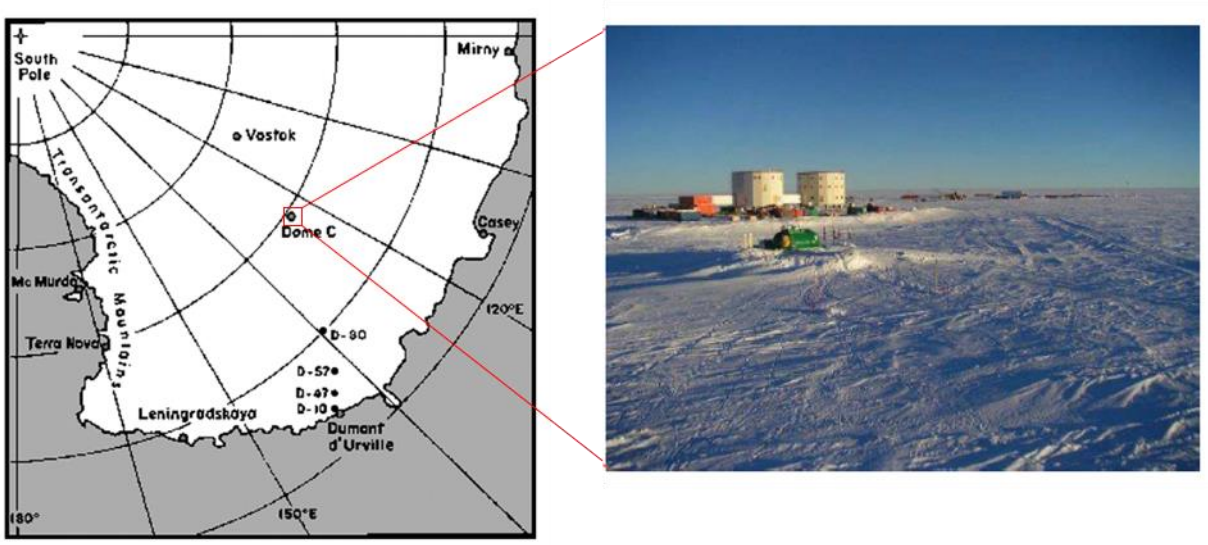

Figure 1-6: (left) Location of the Concordia station at Dome C in central Antarctica. (right) Photo of the Concordia station.

Extraterrestrial particles are collected in the Antarctic snow in trenches (5-8m deep) dug at a few kilometers from the station (Duprat et al., 2007), in order to minimize any anthropic contamination from the nearby human activities. The fact that micrometeorites were collected in snow also implies that the particles endured less mechanical stress than when preserved in ice, like for the Cap Prudhomme collections. This allows in particular a better preservation of the most fragile and porous particles that can easily be destroyed during the collection process. The snow accumulation rate is also low, and well recorded in the region of Dome C, facilitating the dating of snow layers chosen for extraction of the grains.

A recent study by Rojas et al. (Rojas et al.) monitoring the accretion rate of micrometeorites at Dome C (Antarctica) indicates that the flux of extraterrestrial material on Earth is dominated by sub-millimeter particles, mostly originating from Jupiter family comets (Carrillo-Sánchez et al., 2016; Nesvorný et al., 2011a). The difference between the measured surface flux of interplanetary particles and the dust models' prediction can be explained by a fraction of the most fragile MMs being destroyed during atmospheric entry.

The collection process of micrometeorites at Dome C has been optimized to minimize contamination of the recovered samples (Duprat et al., 2007; Rojas et al., 2021). Snow is transported from the trench using clean sealed barrels and brought to the station to melt it in a stainless-steel low temperature melter (see (Duprat et al., 2007; Rojas et al., 2021) for more details about the collection protocol). The particles can be in contact with the melted snow water for up to 20h. The resulting melted snow water is then sieved on a mesh nylon filter to retrieve the dust particles (with sizes > 20µm). This extraction method allows limited mechanical stress during the extraction, allowing a better preservation of the most porous and fragile particles. The low aqueous alteration of the recovered samples is also attested by the ubiquitous presence of Fe-Ni sulfides in the recovered micrometeorites. In previous collections from Cap Prud'homme, aqueous alteration of the particles was important and most grains were depleted in Ca, S and Ni due to important water circulation (Engrand and Maurette, 1998; Kurat et al., 1994). This depletion in soluble phases is not observed in the Concordia collection, suggesting limited

alteration of the MMs, as already expected by the low temperature preservation. The collection process of the Concordia collection also allowed the recovery and identification of a new interplanetary materials, already observed in Japanese AMMs collection, UltraCarbonaceous Antarctic Micrometeorites (UCAMMs) (Duprat et al., 2010; Nakamura et al., 2005a).

1.3.2.2. Micrometeorites classification and characteristics

Micrometeorites are interplanetary particles, with sizes larger than IDPs. While IDPs measure up to 50μm, micrometeorites have sizes ranging between 50 μm and 500 μm. MMs represent the fraction of interplanetary dust that survive the atmospheric entry and reach Earth's surface. Recent study by Rojas et al. (Rojas et al.) monitoring the accretion rate of micrometeorites indicates the flux of extraterrestrial material on Earth is dominated by sub-millimeter particles, mostly originating from Jupiter family comets (Carrillo-Sánchez et al., 2016; Nesvorný et al., 2011a). The difference between the measured surface flux of interplanetary particles and the dust models' prediction can be explained by a fraction of the most fragile MMs being destroyed during atmospheric entry.

Micrometeorites classification have been originally based on the heating they endured during atmospheric entry (Genge et al., 2008). This classification has been adapted by Dobrică (PhD Thesis, 2010) and is summarized in Table 1-1.

Table 1-1: Micrometeorite classification adapted by Dobrică (PhD Thesis, 2010)

Heating range	Type	Description
Unmelted MMs (uMMs)	Fine-grained fluffy **FgF**	Porous aggregates of sub-micrometre minerals Similar to CP IPDs Chondritic composition
	Fine-grained compact **FgC**	Compact aggregates of sub-micrometre minerals Chondritic composition
	Hydrated Fine-grained compact **H-FgC**	Hydrated fine-grained Compact micrometeorite Chondritic composition
	Coarse-grained **Cg**	Anhydrous silicate with varying sizes > 1μm, often cemented by a glassy matrix Variable composition
	Ultracarbonaceous **UCAMM**	Dominated by OM Small aggregates of minerals with CI compositions Composition enriched in C and N compared to CI
Partially melted	Scoria **Sc (Xtal)**	Blistered surface with magnetite shell Relict silicates and interstitial glass
Melted	Cosmic spherules **CS**	Melted texture. Initial composition modified by strong atmospheric entry heating. Potential presence of relict minerals

Scoria (Sc) and Cosmic spherules (CS) are the particles that are the most altered by atmospheric entry (Figure 1-7e and Figure 1-7f). The temperatures reached during atmospheric entry heating led to strong chemical modification of the original content of these micrometeorites such as loss of volatils and iron mobilization to form a magnetite shell in Sc. CS have been completely melted and have a distinctive rounded shape. The unmelted micrometeorites (uMM) have escape strong modification due to less significant heating during atmospheric entry (Duprat et al., 2007; Engrand et al., 2007a), making them better candidates to study the original composition of interplanetary dust.

Unmelted micrometeorites have elemental compositions close to carbonaceous chondrites (CCs), more specifically CM and CR types, and are thought to be from cometary origin. Fine-grained fluffy (FgF) MMs are very porous and fragile micrometeorites and have been found for the first time in the Concordia collection (Duprat et al., 2007). FgF display elemental composition close to the chondritic values for both minor and major elements (Dobrica, 2010). Overall, FgF are reminiscent of CP-IDPs, sharing similar mineralogy and elemental compositions. Fine-grained compact (FgC) MMs are very similar to FgF but have less porosity. Crystalline MMs or Coarse-grained (Cg) are dominated by large silicate grains, usually cemented by a glassy matrix.

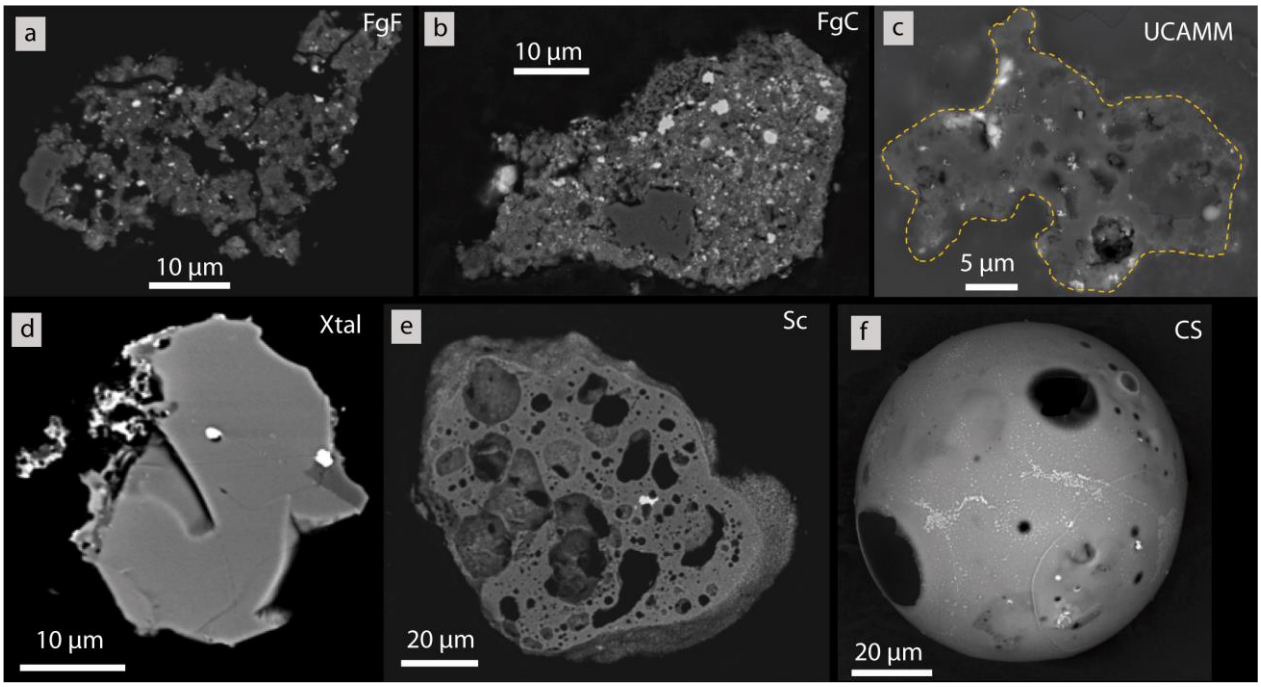

Figure 1-7: Backscattered electron images of the external surface of micrometeorites from the Concordia Collection (images from Dobrică (PhD Thesis, 2010).

Finally, Ultracarbonaceous Antarctica micrometeorites (UCAMMs) are MMs dominated by organic matter. They are the most recently discovered type of micrometeorites and have been found and described in several collections (Dartois et al., 2018; Dobrică et al., 2010; Dobrică et al., 2012; Dobrica et al., 2008; Duprat et al., 2010; Guérin et al., 2020; Nakamura et al., 2005a; Noguchi et al., 2015; Yabuta et al., 2017, Engrand, 2015 #1638). As this work mostly focuses on UCAMMs, an overview of their chemical and petrological characteristics is done in an independent section (see 1.3.2.3).

1.3.2.3. UltraCarbonaceous Antarctica Micrometeorites (UCAMMs)

UCAMMs have been discovered relatively recently compared to other MMs types (Dobrica et al., 2010). They are relatively rare in the Concordia collection (<1% of the collected particles), and could be identified only because of the high proportion of extraterrestrial to terrestrial particles (>50%) in the Concordia collection, which allows the characterization of every collected particle. UCAMMs represent the extraterrestrial object with the largest carbon to silicon ratio (Dartois et al., 2018), making them unique objects to study extraterrestrial organic matter (Duprat et al., 2010; Nakamura et al., 2005b). In UCAMMs, the organic matter (OM) can represent up to 99% of the volume of the particles in the most extreme cases, a value that is higher than for the most carbon-rich IDPs. This extended organic matter usually embeds small patches of minerals or mineral assemblages (Dobrică et al., 2012; Engrand et al., 2015b).

The large amount of organic content easily accessible in UCAMMs allowed a unique and powerful characterization of its organic matter. The first noticeable characteristic of the organic content of UCAMMs has been observed in the SEM/EDS spectra of bulk particles with the Kα line of carbon being much higher than the oxygen Kα line (Nakamura et al., 2005b). Investigation of the isotopic content of the OM of UCAMMs showed very high deuterium enrichment with δD rising up to 29,000 ± 3000 per mil, values which have not been observed in other types of extraterrestrial matter (see Figure 1-8, (Dartois et al., 2013; Duprat et al., 2010)). Infrared spectroscopy characterization of the organic matter of UCAMMs showed that they also contain very high nitrogen content with atomic nitrogen to carbon ratios going up to 0.2, values higher than for organics in meteorites or CP-IDPs. UCAMMs' infrared spectra also generally display a weaker C=O absorption band, indicating a lower oxygen content in UCAMM's OM compared to what is observed in the Insoluble Organic Matter (IOM) extracted by acid treatment of carbonaceous chondrites (CCs) (Dartois et al., 2013).

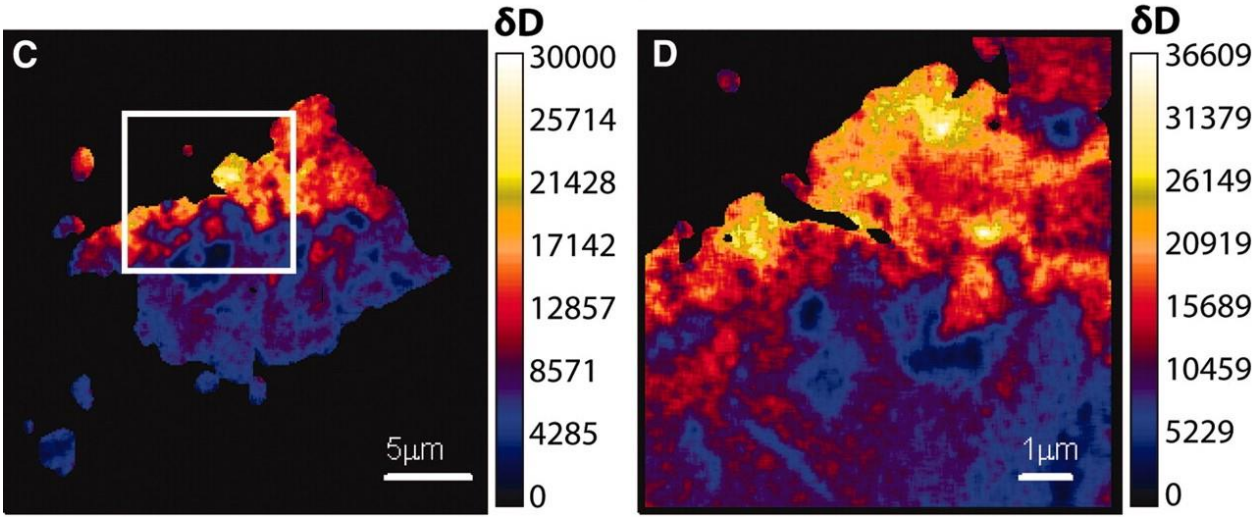

Figure 1-8: NanoSIMS (secondary ion mass spectrometry) isotopic maps of UCAMM DC06-119 showing the deuterium excess δD (‰) in the organic matter. From Duprat et al. ***(2010)***

Scanning Transmission X-ray Microscopy coupled with X-ray Near-Edge Absorption Structure (STXM-XANES) is used to study the composition and structure of organic matter in ultrathin sections of UCAMMs (see Chapter 4). The mineral component of UCAMMs can by studied by Transmission Electron Microscopy (TEM) (see Chapter 4).

UCAMMs presented and studied in this work originate from the Concordia collection, collected during the expeditions of 2006 (referred as DC06), 2016 (DC16) and 2019 (DC19). UCAMMs recovered in Antarctica have been brought back to the CSNSM, Orsay where they are preserved under nitrogen atmosphere before preliminary sorting and analysis.

Chapter 2

2. Analytical methods

Micrometeorites presented in this work have been analyzed with several techniques in order to get both a general and more precise characterization of the inorganic and organic content of extraterrestrial particles. This chapter presents the analytical steps from AMMs sorting and characterization to sample preparations for the different analyes and the corresponding data processing methods used. The main analytical techniques used in this work include Scanning Electron Microscopy (SEM), Transmission Electron Microscopy (TEM), Scanning Transmission X-ray Microscopy coupled with X-ray Absorption Near Edge Structure (STXM-XANES), Raman spectroscopy and mid and far Infrared (MIR and FIR, respectively) Microscopy.

2.1. Micrometeorites sorting and sample preparation

2.1.1. Micromanipulation and extraction

AMMs recovered during Antarctica expeditions are brought back to Orsay in nylon mesh filters (>20µm) in dry nitrogen atmosphere and stored in a clean room in order to minimize terrestrial contamination either during the extraction process or storage. Filters are then observed under a binocular microscope to identify potential extraterrestrial particles based on their size, texture and morphology. The particles are then picked using a white bristles nylon brush, which is previously humidified to facilitate transport from the filter to the sample holder. Individual particles are then handpicked and placed each in an independent sample holder. In the first sample holders used, particles were deposited on a cavity glass slides containing individual particles, numbered for reference.

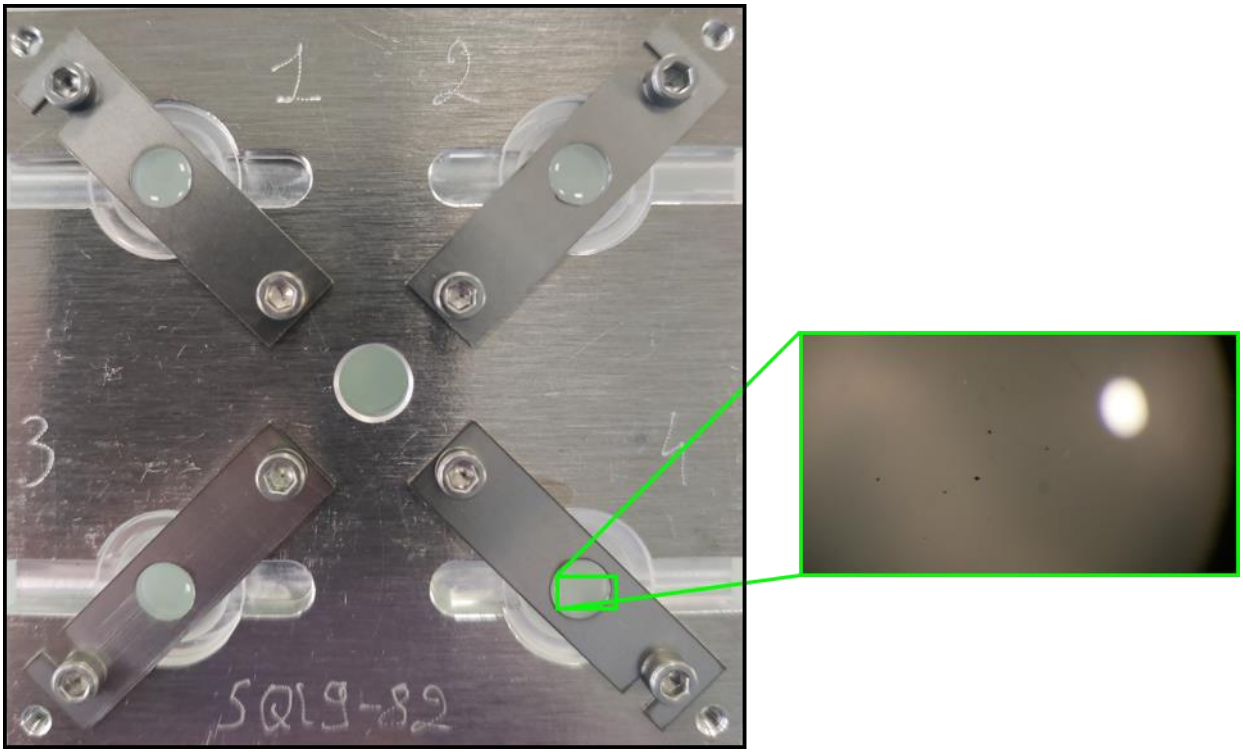

Figure 2-1: (left) Picture of the quartz sample holder used to store potential extra-terrestrial particles. The name of the stub is located at the bottom ('SQ19-82', Figure 2-1). (right) Zoomed picture of a particle after fragmentation in quartz sample holder. Each alveolus is numbered and contains a fragment particle.

New samples holders have been designed, with aluminium plates each containing four different quartz sockets containing individual particles. This allows a more efficient storage and

better preservation of the extracted particles before their first characterization. A picture of each particle deposited in a quartz holder is taken along with size measurements of the extracted particle. Each particle is also numbered (eg. SQ19-12-03: "Support Quartz"-Quartz holder-, year of extraction is 2019, 12th sample holder, 3rd particle of the plate). The particles are then fragmented using a scalpel to allow multiple analysis in parallel of the fragments. The number of fragments after the fragmentation process is documented in an online database, along with pictures of the original particle before and after fragmentation.

2.1.2. Sample preparation for Scanning Electron Microscopy (SEM) characterization

The first analysis consists in the confirmation of the extraterrestrial nature of the extracted grains using Scanning Electron Microscopy (SEM). Fragments from different particles are placed on a one inch aluminum disk covered with double-sided carbon tape (referred here as 'stub'). The fragments need to be put on a conductive substrate to facilitate charge evacuation during analysis. Each stub can contain up to about 40 fragments and allows the efficient characterization of large number of particles. Particles on the stubs are numbered according to their preparation date and their location on the stub for an easier follow-up (ex. ST20-11-25; ST-stub, year 2020, 11th stub of the year, 25th fragment on the stub). Particles numbered on stubs are also linked directly to their quartz sample holder number in order to facilitate the follow up of different grains. Data on the different numbered particles (sizes, images, number of fragments) and resulting fragments analyses (Secondary Electron images, Back-Scattered Electron Image and EDS spectrum, see Figure 2-2 and Figure 2-3) are stored in an online database were information is easily accessible to the group members.

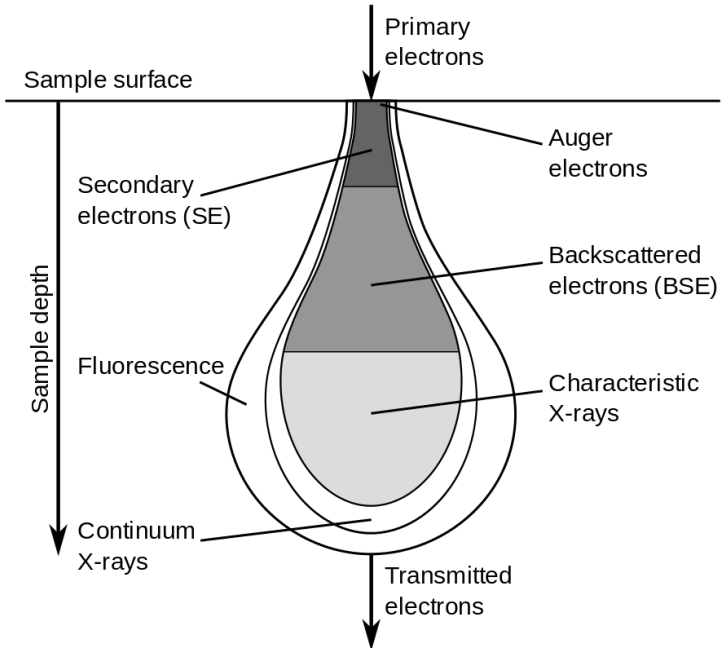

Figure 2-2: Interaction of an electron beam with the sample surface in the case Scanning Electron Microscopy. Secondary electrons (SE) probe the sample surface and allows a precise topographic imaging while backscattered electrons (BSE) are directly sensible to the atomic number within the samples. The characteristic X-rays emitted by the sample during electron-sample interaction also allows the realization of elemental maps.

The preliminary characterization of the particles is based on their images and EDX spectra (Energy Dispersive X-rays spectroscopy) obtained during the SEM analysis. Most of the particles

of the Concordia collection have been analyzed using a LEO 1350 SEM equipped with a Bruker EDX spectrometer.

The preliminary characterization of the particles is based on their images and EDX spectra (Energy Dispersive X-rays spectroscopy) obtained during the SEM analysis. SEM-EDX analysis allows the recording of elemental cartography of the grains as well as semi-quantitative analysis (Figure 2-3). Among the criteria to establish an extraterrestrial origin are the following:

- A chondritic distribution of the elements (composition dominated by O, Mg, Si, Fe, with possible minor peaks at Na, Al, S, Ca, Mn, Ni).
- A fine-grained texture of the particles, reflecting the mechanical aggregation of the small grains (with sizes > 50-100 nm) in the early solar nebula.
- The potential presence of partial or complete magnetite shell at the surface of the particles, which can be formed during atmospheric entry.
- The presence of Fe or Ni in the EDX spectrum, under the form of metal or sulfides
- In the case of UCAMMs, the SEM identification is also based on the Kα peak of Carbon, being higher than other X-ray lines in UCAMMs EDX spectrum.

Once all the fragments of a stubs have been characterized with SEM and their potential extraterrestrial nature has been confirmed, sample preparation for further analysis can be done directly from the stub's fragment, such as with Focused Ion Beam (FIB) section preparation (see 2.1.3), or on complementary fragments stored in the quartz holders. In the case of UCAMMs, additional characterizations with infrared and Raman microscopy (and if possible the measurement of isotopic composition by NanoSIMS) is necessary in order to confirm their extra-terrestrial nature. Sample preparation for infrared and Raman characterizations is described in 2.1.4.

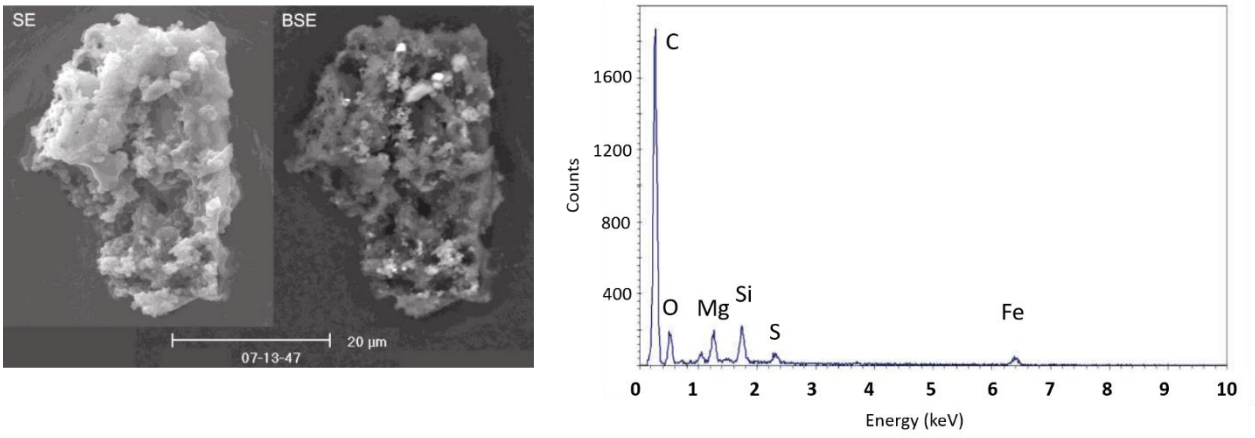

Figure 2-3: (left) Secondary Electron (SE) and Back-Scattered Electron(BSE) images of the UCAMM DC06-09-119. (right) corresponding EDX spectrum with the dominant Kα emission of carbon for UCAMMs.

2.1.3. STXM-XANES and STEM sample preparation

Sections of UCAMMs' fragments with about 100 nm thicknesses were prepared by Focused Ion Beam (FIB) by D. Troadec at IEMN (Lille). These FIB sections have been directly extracted from the fragments deposited on the stub previously analyzed by SEM. The FIB technique allows the extraction of ultrathin sections from the UCAMMs fragments without alteration of the textural integrity of the sample. Compared to ultramicrotome sample preparations, the FIB prevents nanoscale deformations sometimes encountered in microsectioned materials. The FIB sections

were worked out with gallium milling. Although the milling was performed at low current and voltage in order to minimize the potential induced artifacts, slight redeposition of Ga nanoparticles and sputtered material can sometimes be visible on the surface of the FIB sections. Nevertheless, the controlled low current prevented local compositional change or formation of amorphous layers.

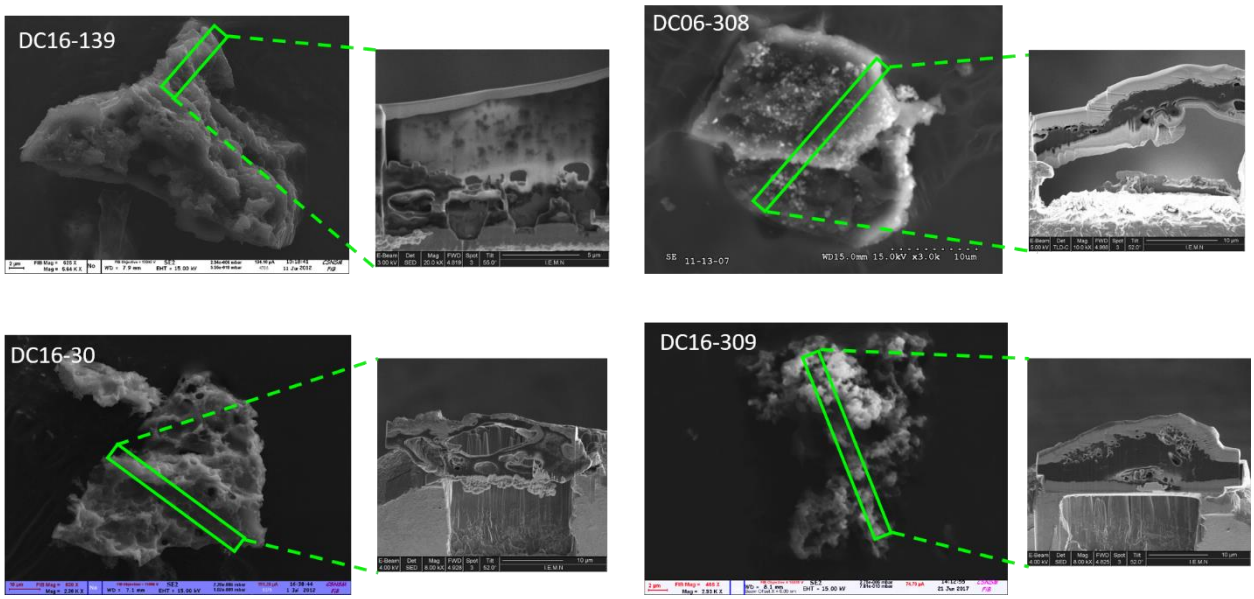

Figure 2-4: Secondary electron images of four UCAMM fragments, with the corresponding FIB sections (green boxes show the region selected for the extraction of the FIB sections)

Resulting FIB sections are about 100 nm thick, and can be analyzed with both Scanning Transmission Electron Microscopy (STEM) and Scanning Transmission X-Ray Microscopy – X-ray absorption near-edge structure (STXM-XANES) without further preparation. STXM-XANES and STEM analysis are complementary as they focus on the organic and mineral content of the particles respectively, allowing complete hyperspectral analyses of the different phases present in the FIB sections. The different analyses conditions and the resulting data processing for both STXM-XANES and STEM data are more thoroughly described in sections 0 and 2.3.

2.1.4. Sample preparation for Fourier-Transform Infrared (FTIR) and Raman microscopy

Sample preparation for Fourier-transform infrared (FTIR) and Raman microscopy is relatively simple compared to the making of FIB sections. As the minimum sampling size of FTIR analysis is of the order of several micrometer square, along with sufficient thickness, the FIB sections samples are often too thin to be measured with a sufficient signal-to-noise with these techniques. For this reason, another fragment of the same particle is retrieved from the quartz holder of the original particle. We performed infrared spectroscopy in transmission mode, so the particles need to be transferred to specifically designed diamond cell to gently flatten the fragment to a thickness of a few micrometers. This is a necessary step not only to reach a thickness where infrared radiation can be transmitted, but also considerably limits the scattering effect that will strongly affect the infrared spectra. This involves a flattening process between two diamond windows, monitored under a binocular where the shape and area of the fragment is followed during the crushing process, in order to obtain the optimal thickness for transmission infrared microscopy. The same sample preparation is used for Raman analyses, as there are no constrains

on the thickness and size of the samples. Raman measurements have been usually done on the region overlapping the ones recorded during FTIR analyses.

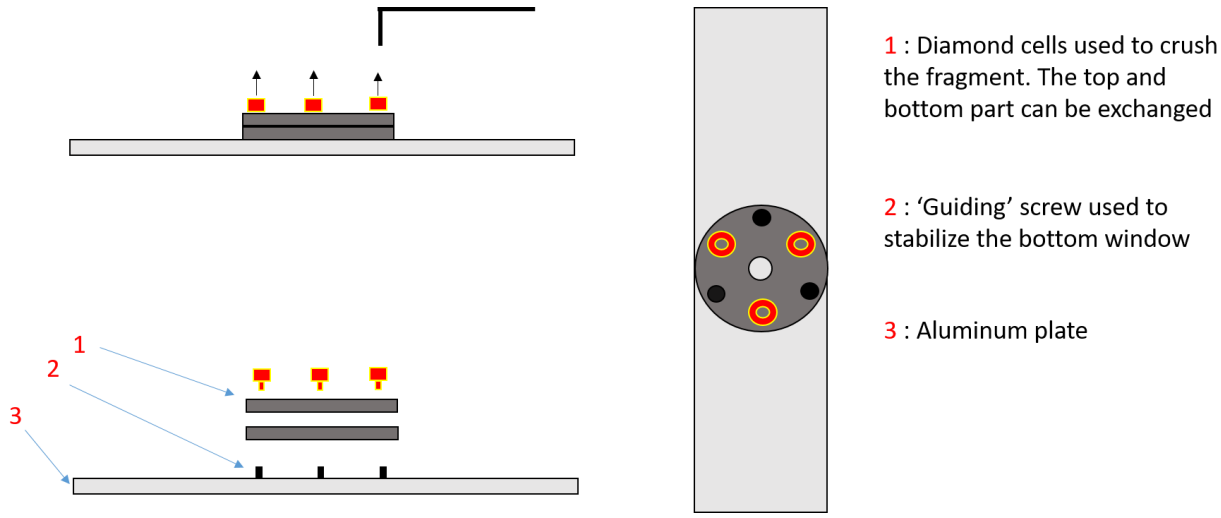

Figure 2-5: Drawing of the custom-made diamond cells used for FTIR and Raman analyses. The two diamond windows are independent and can be switched easily. Particle crushing is performed using the screws on top that will settle on the underlying aluminum plate. The low overall thickness of the sample holder (plate + 2 windows) allows manipulation under both binocular and the FTIR microscope.

The diamond cells are designed to hold two independents windows than can be switched between top and bottom position. The fragment is deposited on the bottom window before closing the cell and slowly tightening the screw in order to flatten the particle surface. These manipulations can be done both under a binocular or the optical microscope of a FTIR spectrometer. Infrared and Raman analyses conditions and data-processing are reviewed in section 2.4.

2.1.5. Sample preparation for IR nanospectroscopy (AFM-IR)

Sample preparation for IR nanospectroscopy (atomic-force microscope coupled with IR spectroscopy - AFM-IR) is one of the key parameters we investigated during this set of analyses. As a matter of fact, AFM-IR analyses can be strongly influenced by the geometry and the general shape of the studied sample. Parameters such as thickness, flatness, stiffness and adhesion to the underlying substrate may generate artifact in the gathered AFM-IR data. AFM-IR analyses in this work focuses on mineral characterization. For this work, three different types of samples preparation have been tested in order to determine the most efficient and clean methods to obtain the more reproducible infrared signal.

- Sample polishing to achieve a µm thick samples (using tripod polishing)
- Thick mineral polished sections
- Extraction of these polished minerals from the epoxy and pushed into an indium foil.

2.2. Scanning Transmission X-ray Microscopy coupled with X-ray absorption near-edge structure (STXM-XANES)

2.2.1. General principle

X-Ray absorption spectroscopy is used to investigate the electronic state and chemistry of matter, by using photons at energies where the core shell electrons of atoms in the investigated sample can be excited (in the range of 0.1 to 100 keV). In the case of the present study, photons were generated through synchrotron radiation at the SOLEIL, France and the ALS Barkeley

facilities. The photon energy can be tuned using a crystalline monochromator (see Figure 2-6) and the beam focalized using Bragg-Fresnel lenses (Zone plate in Figure 2-6).

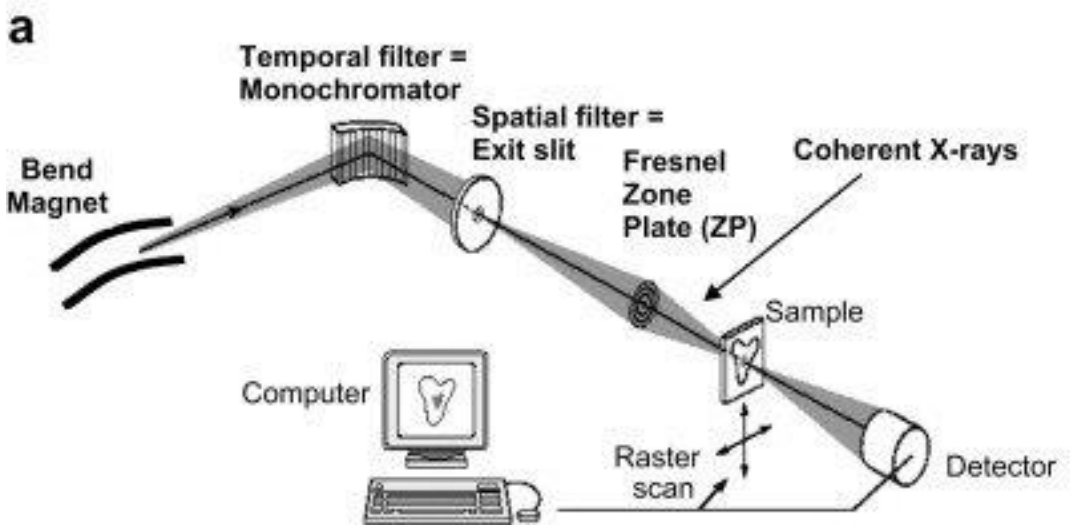

Figure 2-6: Simple diagram of the configuration of a STXM beam line. Image from (Ade and Hitchcock, 2008)

X-ray spectroscopy is based on the ionization of a core electron of an atom. The X-ray will excite the core electron above ionization threshold. Ionization of a core shell electron leads to a sudden increase in the absorption spectrum, the so-called absorption edge (see Figure 2-7). The energy of the absorption reveals the nature of the element and the pre-edge absorption can exhibit structures that give information about the chemistry and bonding of the investigated element in the sample (see Figure 2-7).

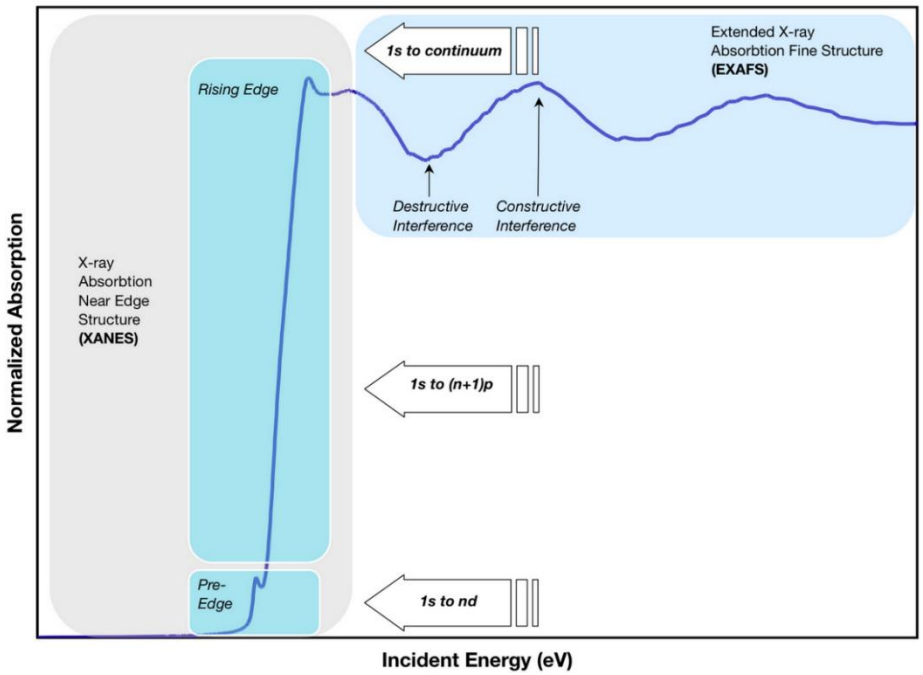

Figure 2-7: Representation of the different spectroscopic characteristics of an absorption edge in a X-Ray spectrum. Pre-edge structure contains information about bonding and chemistry of the investigated element. (Image CC BY-SA 3.0)

The spectroscopy presented in this work corresponds to X-ray absorption near-edge structure (XANES) and focuses on the analysis of the pre-edge region of the X-Ray transmission

spectrum as described above. Depending on the speciation at the K-edge of the atoms in the different phases of the sample section, differential absorption will occur for XANES at the respective ionization energy of the different elements. We focus on the characterization of the organic content of micrometeorites, therefore the STXM-XANES analysis are performed at the C- and N- K-edges for the present study.

2.2.2. Analysis conditions and data processing methods

STXM-XANES data were collected on the beamline 11.0.2 at ALS Berkeley (for two micrometeorites: DC06-18 and DC06-65) and on the HERMES beam line at the synchrotron SOLEIL for six other micrometeorites (mettre les noms, ou la ref au chapiter STXM?). In STXM lines, the optics are flushed with a very low pressure flow of O_2 allowing the photo-oxidation of eventual carbon contamination depositing with time on the optics. Energy calibrations are performed before the measurements, using as references the 3p Rydberg peak at 296.96 eV for the C K-edge of gaseous CO_2 and the 1s -> π* photo-absorption resonance of gaseous N_2 at 400.8 eV for the N K-edge.

First, each UCAMM FIB section was mapped at selected energies corresponding to the background absorption and to major functional groups (280 eV, 285 eV, 288.6 eV, 290.3 eV) to identify the organic content of the FIB section. This method allows fast acquisitions, large scale, and high spatial resolution (pixel size = 50nm). Sample stacks correspond to images collected at a higher resolution (0.1 eV), and better spatial resolution (35 nm) over a smaller area of the section Once the regions of interest are identified, hyperspectral absorption image stacks are acquired at high spectral resolution. For these absorption images, the energy range at the –C K-edge (270 eV - 355 eV) was defined with 100 meV resolution over the fine structure energy window of interest covering the pre-edge to the main edge absorption fine structure (282-295 eV) and with 1 eV for the pre and post-edge energy ranges. For Nitrogen, image stacks were collected over the energy range from 370 eV to 449 eV with 100 meV resolution for the fine structure energy range and and 1 eV for the pre and post edges. We defined the pixel size between 30 and 50 nm and the dwell time was set to 1 to 2ms per pixel. The energy of absorption is related to the chemical bonding of the atoms, and is used to identify the different functional groups. The peaks intensity variations are used to calculate the relative amounts of the different functional groups. The recorded data are processed with the aXis2000 software (ver. Oct 2018) to extract spectra and images (http://unicorn.mcmaster.ca/aXis2000.html). Once individuals sample stacks are collected, the first step consists in realigning the successive images to compensate for potential slight image acquisition drifts. The alignment function of aXis2000 is used. A reference area with a well identified contrast can also be set manually in the reference sample stack to improve the alignment process. Several alignment loops are then completed for each sample stack until the maximum displacement between two adjacent images gets lower than 5 pixels, typically. Images are converted to Optical Density (OD) by subtracting the background OD spectra, measured in holes present in the FIB sections.

Once the images are aligned and converted to OD, the main chemical phases present in the section can be identified, in particular in areas where they clearly dominate. Then a “stack fit” procedure is used. This aXis function selects all the pixel of the sample stack containing a given spectrum, corresponding to the main phases, allowing to produce functional group mapping involving C and N of the FIB section. False color maps identifying the phases with similar spectra over the range from 280 eV to 410 eV are presented in the results section (Chapter 3), obtained with the “stack fit” aXis tool. Shifts in the energy recorded during the C (+0.4 eV) and N (-0.1 eV)

calibration have also been corrected for, using the "Calibrate" function of aXis2000. A residue of the hyperspectral map is also calculated to assess that all present phases are represented by the selected set of spectra.

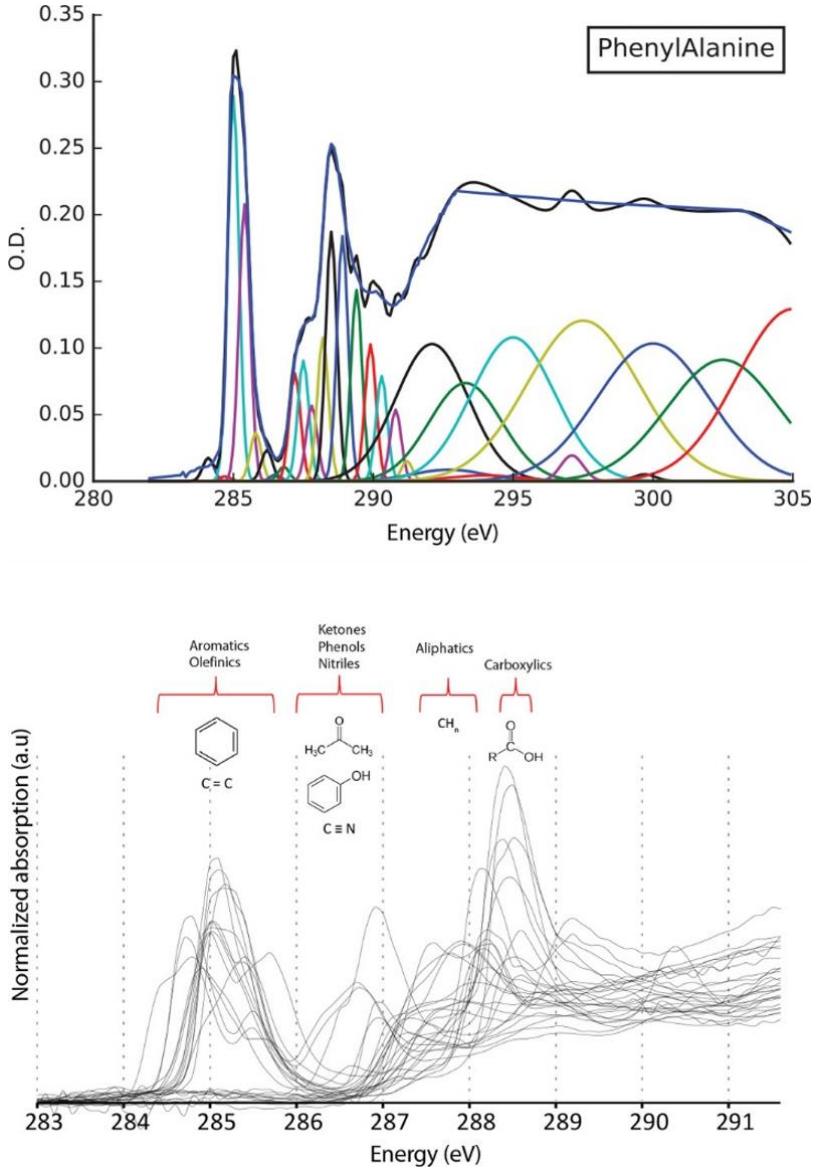

Figure 2-8: Example of phenylalanine fit with the set of Gaussian used to fit the carbon K-edge of STXM-XANES spectra in this study. Quantification methods and image from Le Guillou et al. (2018)

After the XANES spectra acquired at the C-, and N- edges are calibrated, data are processed using the Quantorxs code (Le Guillou et al., 2018). Data processing with Quantorxs enables estimating the N/C ratio values of the phases in the examined sample and also provides a relative quantification of carbon speciation. Before any deconvolution and quantification, the spectra need to be corrected for the contribution of other elements contributing to a background absorption. The pre-edge absorption level arises from the photoionization of valence electrons and the absorption and scattering of other elements present in the sample. The quantification is carried out by integrating the spectra from the pre-edge energy (282 eV for C, 397 eV for N) to the mean ionization energy (291.5 eV for C, 406.5 eV for N), once the pre-edge background correction has

been applied. The resulting integrated spectra are weighted by the relative absorption factors of carbon (3.67) and nitrogen (3.81) respectively. These factors correspond to the imaginary part (f2) of the complex atomic scattering factor at the ionization energy of the atoms (291.5 eV for C and 406.5 eV for N) as described by Henke et al. (1982; 1993). Once corrected by such absorption factors, a quantification of the atomic N/C ratio for each spectrum is performed with an estimated standard deviation of $1\sigma_{N/C}$= 0.02.

The second step consists in deconvolving the spectra to identify and quantify the relative proportions of the different functional groups at the C K-edge. As energy bands are overlapping in the edge region, a systematic functional deconvolution process is necessary to properly identify the different carbon configurations. A Gaussian fit is applied at the carbon edge, with the central position of the Gaussians kept at fixed energies established from the literature (De Gregorio et al., 2011). A basis set of 21 Gaussians are used to describe the different energy bands. The half-width at half maximum (HWHM) for each Gaussian is fixed at 0.2 eV and 0.3 eV (for carbon and nitrogen respectively) in order to perform a good fit even on the narrowest peaks. The Gaussian fit is then followed by a least square fitting on the sum of all the Gaussians between 282 eV and 305 eV for carbon. As multiple peaks overlap in the C K-edge region, the height of the Gaussians enable the quantification of 4 established "sets" of generic functional groups: aromatic-olefinic (284.4 eV, 284.7 eV, 285 eV and 285.4 eV), ketone-phenol-nitrile (286.2 eV, 286.5 eV and 286.8 eV), aliphatic (287.5 eV to 288 eV) and carboxylic-ester-acetal groups (288.5 eV to 289 eV).

2.3. Scanning Transmission Electron Microscopy (STEM) characterization

2.3.1. General principle

Electronic microscopy comes in the form of several acquisition methods. As the results presented in this work have been acquired using Scanning Transmission Electron Microscopy (STEM), a section will be dedicated to this mode of electronic microscopy analyses.

TEM analysis consists in the transmission of electron through an ultrathin sample section (such as FIB sections in this work, of thickness ranging from about 100 nm to 180 nm) with electron energy typically ranging from 60 keV to 400 keV. This interaction offers a high spatial resolution which can go down to a few Angströms, where atomic layering or atomic structure can be observed in crystalline samples. For TEM analysis, the ultrathin section is illuminated by a large and parallel electron beam that can project absorption or diffraction contrast onto a fluorescent screen. With this method one can record an image not only based on absorption contrast but also on diffraction difference between crystalline phases within the imaged sample.

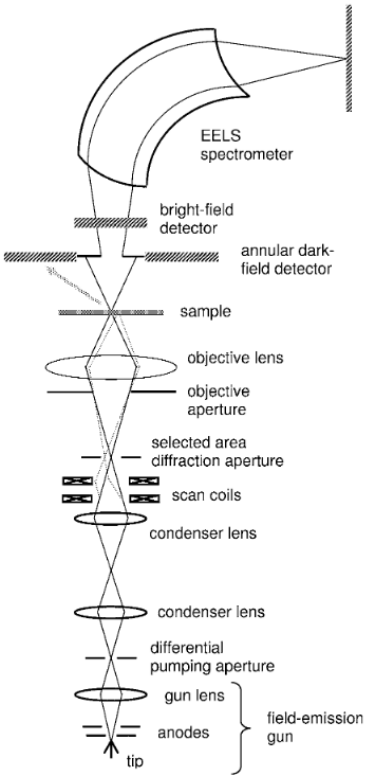

Figure 2-9: Diagram of the different component of a Scanning Transmission Electronic Microscope. Image from (Nellist, 2007)

In the case of STEM (Figure 2-9), the electron beam is focused and forms a much smaller illumination spot that is rastered over the sample in the regions of interest. This method allows the generation of hyperspectral EDX maps where each pixel contains an EDX spectrum.

The STEM mode combines a small probe size along with 'real-time' imaging, allowing a better overview and general characterization of the samples before further analysis of specific regions of interest. For each analyzed region of interest in this work, an HAADF (High Angle Annular Dark Field) image has been taken of each investigated mineral assemblage. HAADF images consist in collecting Rutherford scattered electron, producing a high resolution image based on the atomic number of atoms in the imaged assemblage. HAADF imaging can be done in parallel with EDX measurements during STEM analysis.

2.3.2. Analysis conditions and data processing methods

2.3.2.1. Data rebinning and phase identification

The mineral content of the FIB sections previously studied by STXM-XANES was analyzed using scanning transmission electron microscopy (STEM). Analyses have been performed on FEI Titan Themis 300 operating at UMET (Unité des matériaux et Transformations), Université de Lille. The analyses were made at 300 keV in HAADF mode coupled with EDX. These analyses allowed the study of mineral assemblages in UCAMMs at spatial resolution down to tens of nanometers. Electronic diffraction has also been acquired during the analysis of some complex mineral assemblages.

The data processing workflow is described in Figure 2-10. The reduction of the data implies rebinning of the raw data in order to increase the size of each pixel and therefore increase the EDX signal/noise ratio over the hyperspectral maps. For the different hyperspectral maps

presented here, a rebinning over 5 to 10 pixels was used (i.e. the total number of pixels was divided 5 to 10) depending on the original signal/noise ratio in the data. The binning factor has to be chosen carefully and not too high in order not to mix the potential nanometric phases. To avoid such a phase mixing, some of the hyperspectral maps were acquired over a longer time, in order to minimize the rebinning post-processing. Once the hyperspectral maps have workable signal to noise ratio, a singular values decomposition (SVD) is performed in order to identify the number of components present in the hyperspectral data (referred as 'variance ratio' in Figure 2-10). This first step helps constraining the parameters from the blind source separation leading to the generation of different model components and ultimately creating the masks of pixels associated with each identified phase. Several steps of linear combination of the spectra resulting from the mask of pixels are then calculated, with an increasing minimum pixel intensity threshold to generate new masks at each step and produce a new model from the initial data based solely on the identified component. This helps better isolating the 'pure' pixel phases before further data processing. Occasionally, the small sizes of some phases (typically phases smaller than 10 nm) could induce issues in the generation of the phases' masks as the total thickness of the FIB section then exceeds the studied phase contribution. In those cases, the first input of spectra before linear combination was done using manually selected pure phase ROI spectra, facilitating the component separation.

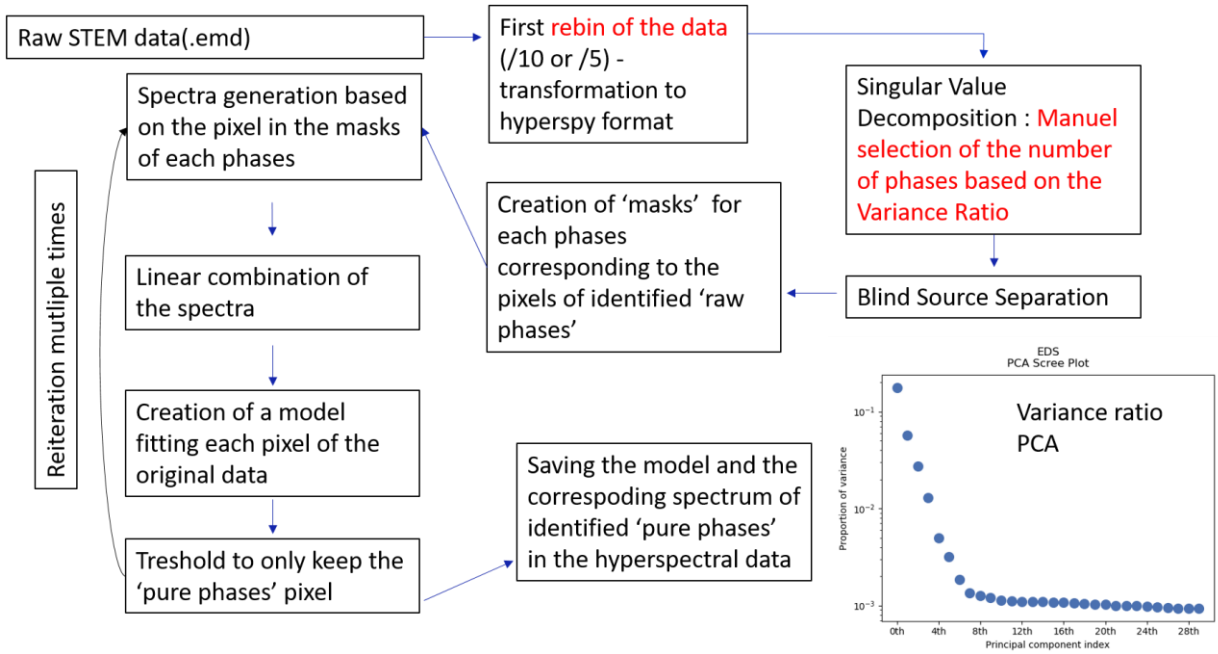

Figure 2-10: Workflow of the data processing method used to deconvolve hyperspectral data of STEM cartography.

2.3.2.2. Phase quantification

Once the final model for a given hyperspectral map has been calculated and the different phases were identified, the last step consists in the elemental quantification of the spectrum for each phases. Quantification of STEM EDX data is described by the Cliff-Lorimer equation:

$$\frac{C_A}{C_B} = k_{AB} \frac{I_A f(\chi_A)}{I_B f(\chi_B)} \left[1 + \frac{I_f^A}{I_A}\right]$$

Where C is the concentration of a given set of elements (here A and B), k_{AB} the Cliff-Lorimer coefficient (determined by the ionization cross-section, yield and other parameters that directly

depend on the measured elements), f(χ) is the absorption correction and I_f the fluorescence correction. Those last parameters can usually be neglected for ultrathin sample with thicknesses < 50 nm. In the case of the FIB sections analyzed for this work, the thickness of the samples was larger than 100 nm and thus the reabsorption cannot be ignored in the quantification calculation.

In order to quantify the reabsorption contribution, the local thickness and/or density of a hyperspectral map must be determined. This is done using the most Fe-rich phases of each hyperspectral map. As described earlier, the energy range of electron used for STEM analysis usually covers the K X-ray emission line for most major element found in meteorites. It also covers both the Kα (6,403 keV) and Lα (0.75 keV) X-ray lines of Fe that can be used to determine the local thickness of the sample. Indeed, the lower energy Lα X-ray line of Fe will be more absorbed than the higher energy Kα X-ray line. As the reabsorption is directly related to the energy of the X-ray lines, the local thickness value can be determined by iterating the quantification of Fe-rich phases using the Kα or the Lα X-ray lines of Fe at various sample thicknesses until both give the same result. For every assemblage presented in this work, the local thickness has been determined using the Fe-rich phase(s) of each assemblage.

In this work, I will also present organic matter STEM-EDX analysis of one FIB section of UCAMM DC06-18. Although EDX is usually not the method of choice for light element quantification, its high spatial resolution of STEM-EDX combined with the high organic content of UCAMM allows a good semi-quantitative and qualitative analysis of the organic matter chemistry around the inorganic phases in the studied FIB sections.

2.4. FTIR and Raman microscopies

2.4.1. Fourier Transform Infrared (FTIR) Microscopy

2.4.1.1. Infrared radiation and dipole moments changes

Infrared spectroscopy is the analysis of the interaction of infrared light with the investigated samples. It allows a qualitative and quantitative analysis of both inorganic and organic content of matter.

Infrared spectra probe the vibrational spectrum of the samples. Molecular bonds naturally experience several types of rotation and vibration based on their geometry that can be well predicted for e.g. diatomic to triatomic molecules (see Figure 2-11). IR analysis is based on Infrared light being selectively absorbed by the functional groups in the investigated sample, leading to a transition from the ground vibrational state to an excited vibrational state. A condition to observe an IR signature of a functional group is a clear change in the dipole moment of the molecule. For example, the symmetric stretching mode of the CO_2 molecules (Figure 2-11a) does not induce a change in the dipole moment during the vibration and is therefore 'IR-inactive'. The anti-symmetric stretching mode of CO_2 (Figure 2-11b) induces a change in the dipole moment of the molecule and is therefore referred as IR-active.

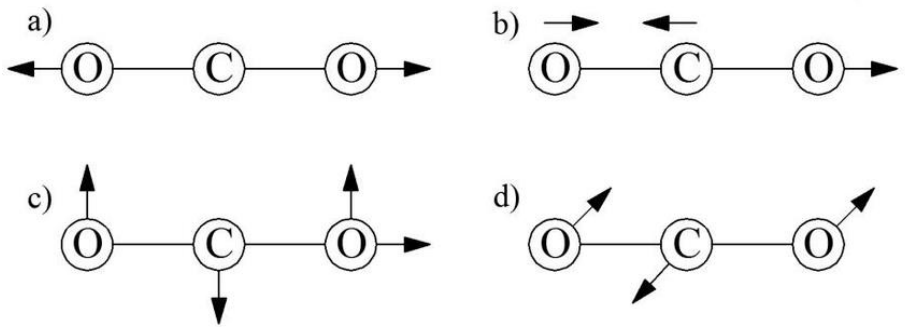

Figure 2-11: Inactive and active vibration modes of carbon dioxide. Infrared active modes are the one inducing a net change in the dipole moment of the molecule (image from (Olbrycht et al., 2016)).

Infrared spectroscopy is an important tool to characterize vibrational modes in matter and has been widely used for inorganic and organic analyses. Each frequency observed in an IR spectrum is characteristic of specific functional groups and allows a precise characterization of the samples. One limitation of infrared spectroscopy lies in its spatial resolution, which is constrained by the minimum size of the diffraction spot of the IR beam spot of a few µm in size. In the case of this work, IR was generated through synchrotron radiation, allowing analyses with the best spatial resolution (~6 x 6 μm^2), close to the diffraction limit.

2.4.1.2. Analysis condition and data processing

The data presented in this work have been collected on the SMIS beamline at SOLEIL synchrotron, France. IR analyses have been realized on several chondritic AMMs and UCAMMs to characterize their organic and inorganic contents. All the infrared measurements have been acquired in transmission mode, and the samples have been crushed to a thickness of a few µm and flattened to permit infrared radiation to go through the samples. The sample preparation for transmission IR analyses is described in section 2.1.4. As the range of frequency needed to analyze both the organic and mineral content of the measured samples is not covered by a single instrument, two FTIR microscopes with different detectors ranges have been used. Mid-IR (MIR) covers wavenumbers from 900 to 4000 cm^{-1} and holds most of the organic signatures, and the far-IR range (FIR) (100 to 700 cm^{-1}) covers mostly inorganic frequency (mostly silicates in this work). MIR analyses have been performed with a Continuum2/Thermo Nicolet 8700 Bench (with IR generated through synchrotron beam or internal source) and FIR analyses on Nicplan/Thermo Fischer iS50 with an internal source of IR radiations and a bolometer as detector. Spectra were usually collected with 2 or 4 cm^{-1} resolution and 512 to 1024 scans.

The first step of data processing for IR spectra consists in stitching the MIR and the FIR spectra. This can only be done if the sample region analyzed by both IR measurements overlap. If the area measured in MIR is smaller than the FIR coverage, several spectra can be coadded and averaged to correspond to the same spatial coverage. When the two spectra represent the same area of the sample, they can be connected. Sometimes, a small adjustment scaling factor must be applied to the far IR part of the spectrum in order to better stitch the two parts of the spectrum. The low S/N side parts of each spectrum are also cropped before the merging. An example of this process is presented in Figure 2-12.

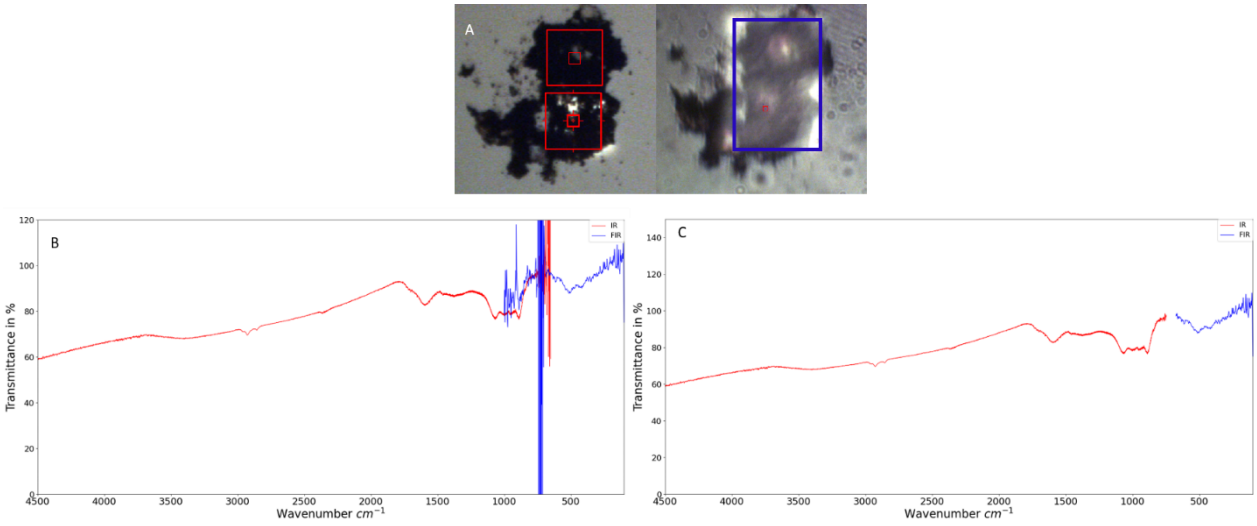

Figure 2-12: (A) Areas covered by the mid-IR measurement (red squares, left) and the far IR measurement (blue square, right). In order to cover the same area, two mid-IR spectra must be averaged. (B) Merged spectrum of the sample before cropping and scaling with the MIR part in red and the FIR part in blue (C) Final version of the total spectrum with both measurements merged and corrected.

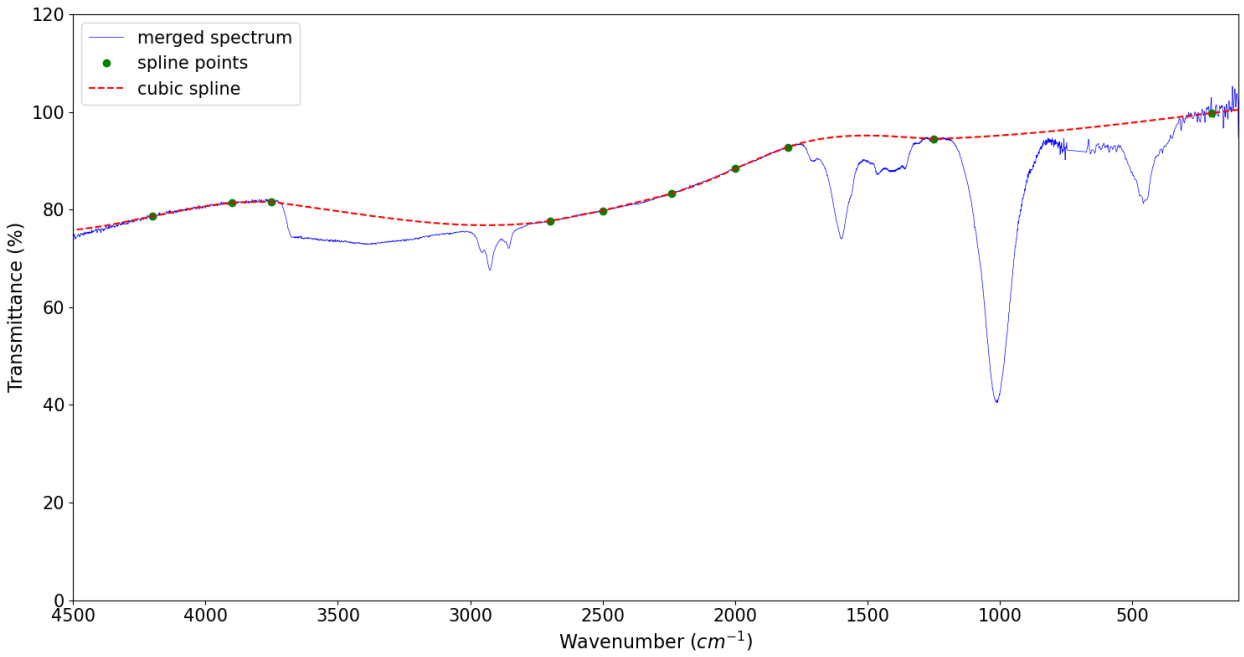

Figure 2-13: Cubic spline fit of a merged MIR-FIR spectrum. The blue line corresponds to the data, green points to the set of values used for the fit and the red dotted line corresponds to the cubic spline fit generated.

The second step of IR data processing is the baseline correction which is performed on the merged spectra. Baseline correction is a preprocessing technique used to correct the samples spectra from thin film interferences or extract specific vibrational absorption from the continuum. A baseline correction in this work has been applied using a cubic spline fit going through a set of frequencies selected over the region of the spectra exempt of absorption features. An example of such a baseline correction is shown in Figure 2-13. The same fitting procedure has been applied to all the IR spectra shown in this work.

2.4.1.3. Characterization of organic content of AMMs from IR spectra

Deconvolution of the mid-infrared (MIR) spectra of the different AMMs can give information on both organic to silicate ratio in the measured sample as well as aliphatic ramification within the organic content of AMMs. This deconvolution is realized in several steps after the baseline correction previously described has been applied. The first processing consists in measuring the surface area below the absorption bands of aliphatic carbons (between 2800 and 3050 cm^{-1}) and silicates (780 to 1200 cm^{-1} for olivine or pyroxene absorption bands, 900 to 1100 cm^{-1} for phyllosilicates, see Figure 2-14).

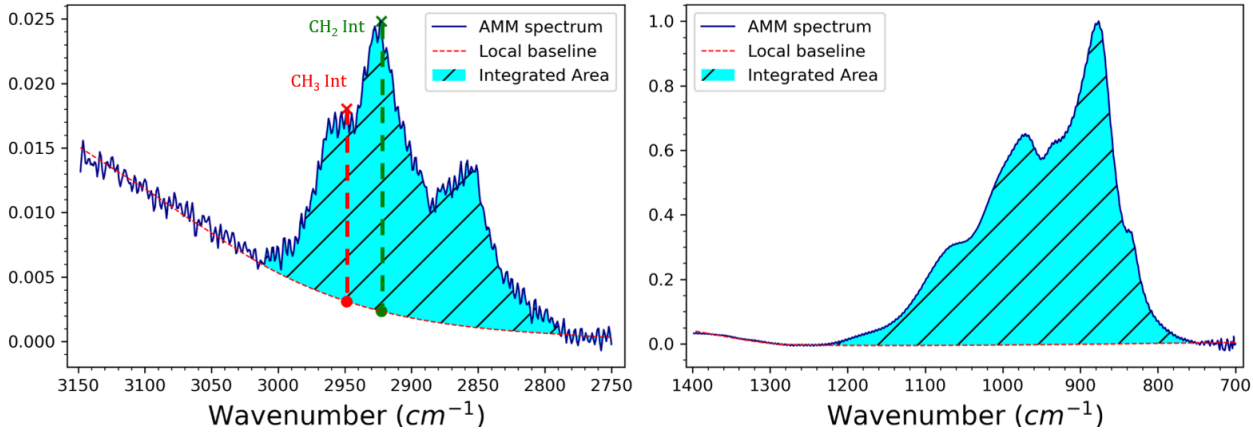

Figure 2-14: Example of area calculation under the aliphatic (left) and silicate(right) absorption peaks. The vertical lines on the left corresponds to the value of the CH_2 and CH_3 direct intensity measurements.

The area below the peaks is measured by applying a local baseline under the respective peaks, and integrating the area between the two curves. The CH_2/CH_3 ratio can be estimated based on the asymmetric stretching of these modes at 2930 and 2950 cm^{-1}. This has been performed with two different methods. First, by measuring the maximum height of the peaks of asymmetric CH_2 and CH_3 after local baseline correction (at 2960cm^{-1} and 2928 cm^{-1} respectively, Figure 2-14). In order to assess the relevance of direct intensity calculation, another characterization of the aliphatic absorption has been done using a set of Gaussians to fit both the asymmetric and symmetric vibration modes of aliphatic CH_2 and CH_3 at fixed wavelength listed in Table 2-1. A Gaussian located between the asymmetric and symmetric modes and corresponding to a probable Fermi Resonance with the bending mode was added for a better goodness of the fit, following the approach of Dartois et al (2005) (see Figure 2-15). The CH_2/CH_3 calculation in this case has been performed using the asymmetric modes of CH_2 and CH_3, which are better defined than the symmetric modes, as the fitting procedure is subject to more uncertainty for the symmetric modes, partially because of the presence of the CH_2 Fermi resonance band. The obtained integrated absorbance under the Gaussian fit is then corrected for the cross section of the column to extract the relative proportion of CH_2 and CH_3 in the investigated sample. By comparing the intensity ratio with the calculated proportion of CH_2 and CH_3 obtained by the Gaussian fit, one can better assess the relevance of direct intensity measurement of aliphatic absorptions to evaluate the relative proportion of CH_2 and CH_3.

Table 2-1: Wavelength positions used for the Gaussian fit and the corresponding vibrational modes and integrated cross section.

Wavelength (cm^{-1})	Aliphatic vibrational modes at 2900 cm^{-1}	A (cm/group)[a] - $x10^{-18}$
2961	CH_3 asymmetric	12.5 ± 1.0
2928	CH_3 asymmetric + Fermi resonance	8.4 ± 0.1
2876	CH_3 symmetric	2.0 ± 0.1
2854	CH_2 symmetric	2.4 ± 0.1

[a](Dartois et al., 2004)

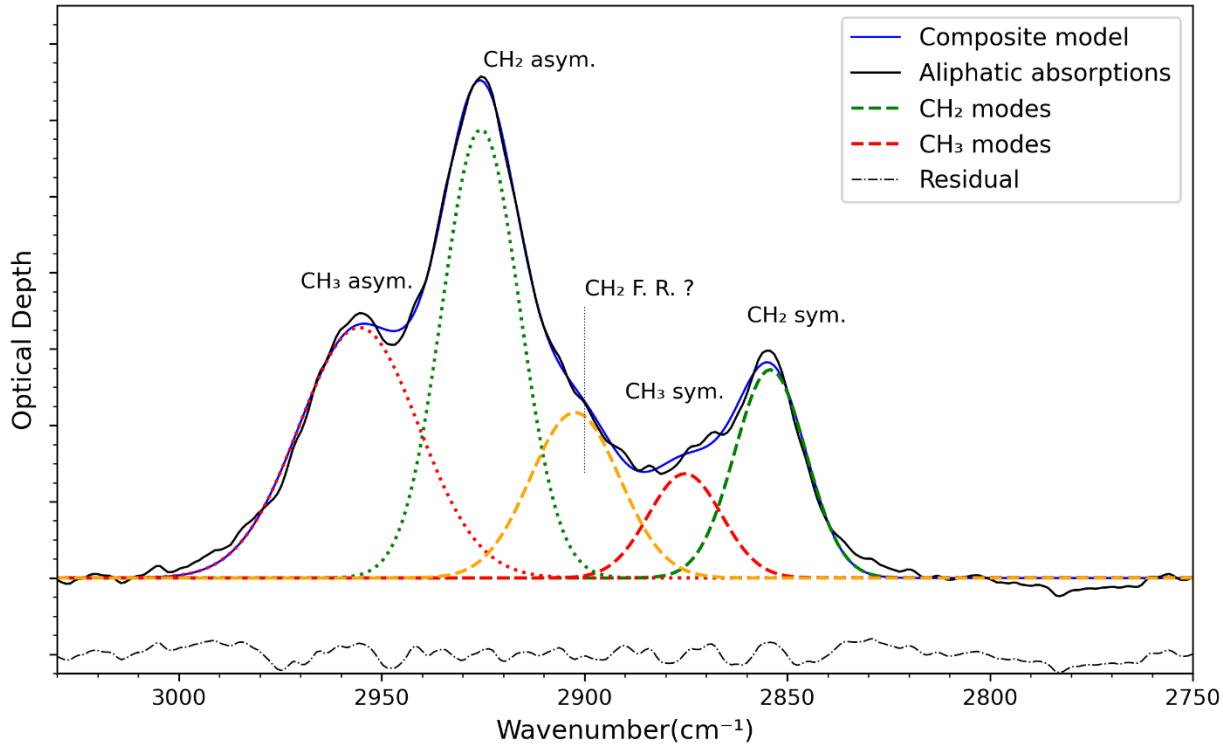

Figure 2-15: Example of the set of Gaussians used to fit the aliphatic absorption of AMMs infrared spectra. The dashed line at the bottom correspond to the residue between the fit and the spectrum.

2.4.2. Raman spectroscopy

2.4.2.1. General principle

The Raman spectroscopy, similarly to IR, is based on molecular vibrations. As for IR, it is a non-destructive analysis when properly used. It only necessitates a small amount of material and little sample preparation. It can be used to analyze both inorganic and organic content of a sample. The technique consists in illuminating a sample with a (generally visible) monochromatic radiation and measuring the scattered radiation. The interaction between the sample and the incident photons will lead to differential scattering as described in Figure 2-16.

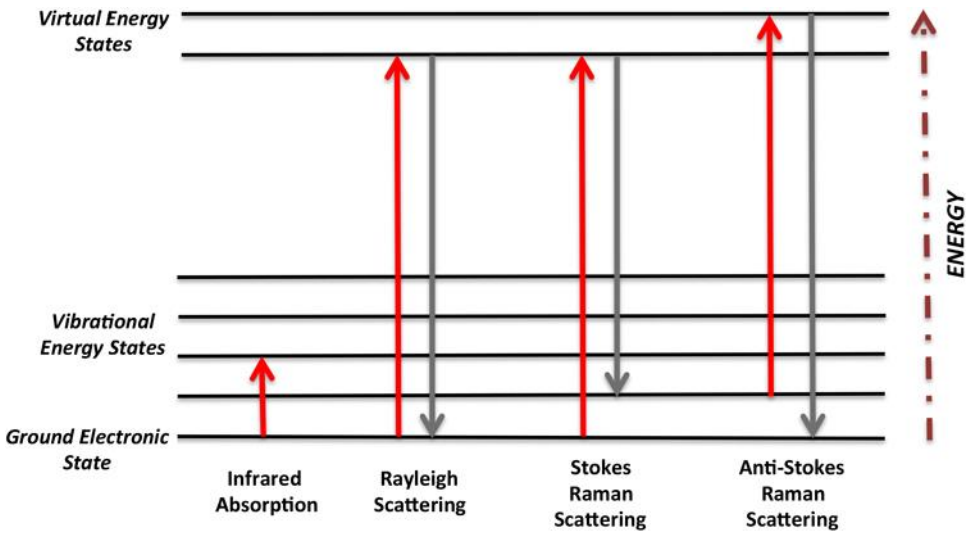

Figure 2-16: Photon-matter interaction measured in Raman spectroscopy. The Rayleigh scattering corresponds to scattered radiation with the same energy then the incident photons. Raman spectrum exploits the inelastic Stokes and Anti-Stokes scattering. Image from (Baker et al., 2016)

Due to a coupling with the vibrational energy levels in the investigated sample, part of the incident radiation will be scattered at a different energy than the incident one. This is referred as inelastic scattering or Raman scattering. It can be either a positive shift (Stokes scattering) or negative shift (Anti-Stokes) in energy. A Raman spectrum corresponds to the intensity of the different energy shifts between incident and scattered radiations.

An important parameter of the Raman analysis is the wavelength of the incident radiation. In the case of this study (532 nm), the frequency of the incident radiation is close to the frequency of the electronic transition of organic matter in the investigated sample. This can induce a resonance process between the sample and the incident radiation that will excite the electrons to higher electronic states. This induces a better emission (up to a factor of 10^6 compared to non-resonance Raman, (Smith and Dent, 2005)), allowing the measurement of micrometric samples. However, this stronger emission in resonance can lead to strong fluorescence signature in some carbon-rich samples, which have been sometimes encountered during our analysis.

The main Raman spectral features associated to organic matter characterized in this work are the two mains bands present in Raman analysis of polyaromatic carbons, referred to as 'D' and 'G' bands, respectively centered at about 1350 cm^{-1} and 1600 cm^{-1} (Tuinstra and Koenig, 1970). These bands are generated by the E_{1g} and A_{1g} stretching vibrational modes of aromatic carbon (Figure 2-17) and the physical activation process of these bands is still debated. The characterization of the organic content of micrometeorites in this work consists in a comparison with multiples measurements previously performed on reference samples and extraterrestrial samples.

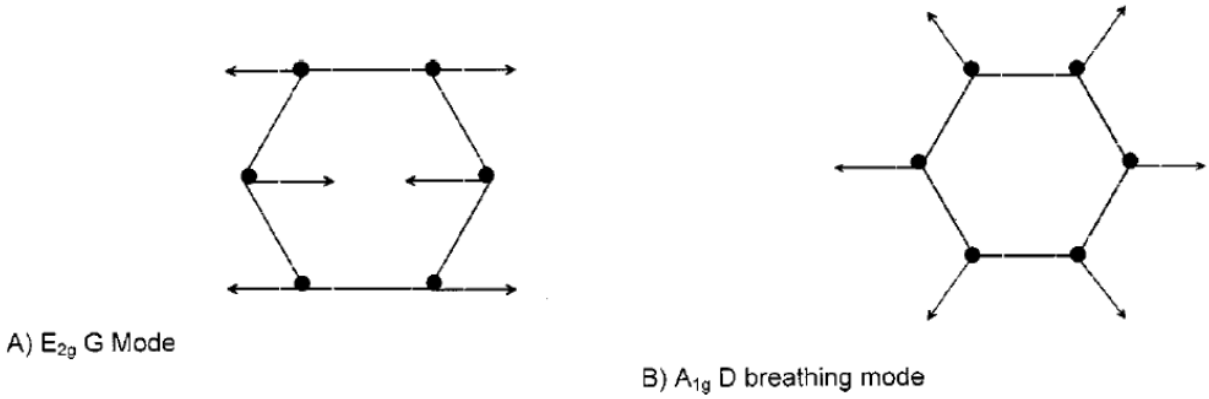

Figure 2-17: Raman-active stretching mode of G (A) and D (B) bands of polyaromatic carbon.

2.4.2.2. Analysis conditions and data processing

Raman analysis of this work were performed at the SMIS beamline of SOLEIL synchrotron (the Raman is not coupled with the synchrotron beam). Spectra were recorded on a Thermo Fisher DXR Raman spectrometer during two sessions in June 2019 and July 2020. Samples were analyzed with the same parameters as previous AMMs Raman measurement (Dartois et al., 2013; Dartois et al., 2018; Dobrică et al., 2011). The exciting laser had an incident wavelength of 532nm and the incident power was set to 0.1 to 0.5 mW in order to prevent sample alteration during analysis. 10 to 20 scans with an integration time of 20s were coadded for the generation of each spectrum. Punctual measurements as well as spectral mapping have been carried out on every sample.

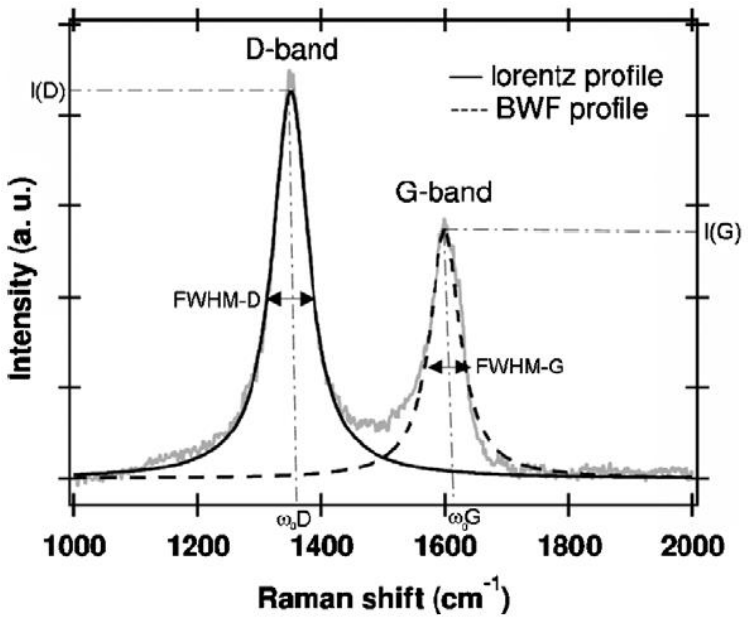

Figure 2-18: Example of the fitting parameters for the D and G bands of polyaromatic carbon. Image from (Bonal et al., 2006)

As stated above, he main Raman bands observed in the samples of the present work consist in D (default) and G (graphite) bands of polyaromatic carbons. The characterization of the organic content of AMMs is based on the determination of the spectral parameters of these two main

carbon bands. The method used here consists in fitting the D and G bands with a Lorentzian and Breit-Wigner-Fano (Ferrari and Robertson, 2000) spectral profiles, in order to retrieve their main spectral parameters (see Figure 2-18): the peak maximum positions (ω_D and ω_G), the intensity of the bands (I_D and I_G) and their full width at half maximum ($FWHM_D$ and $FWHM_G$).

Before data processing, Raman spectra are selected based on their signal/noise ratio, the potential presence of a diamond cell substrate peak contribution and the potential presence of a strong fluorescence signature. The second step consists in smoothing the data with Savitzky-Golay filter over several points to reduce the noise of the spectrum when necessary. Finally, a multi component model is built to fit the spectrum and extract the spectral parameters of the different D and G components. The composite model is built as follows:

- The first component consists in a baseline correction applied between 600 and 2000 cm^{-1} to correct for background effects and underlying residual fluorescence.
- The second component is a lorentzian profile with input parameters corresponding to the position of the D band.
- The third component is a Breit-Wigner-Fano asymmetric profile with input parameters corresponding to the position of the G band.

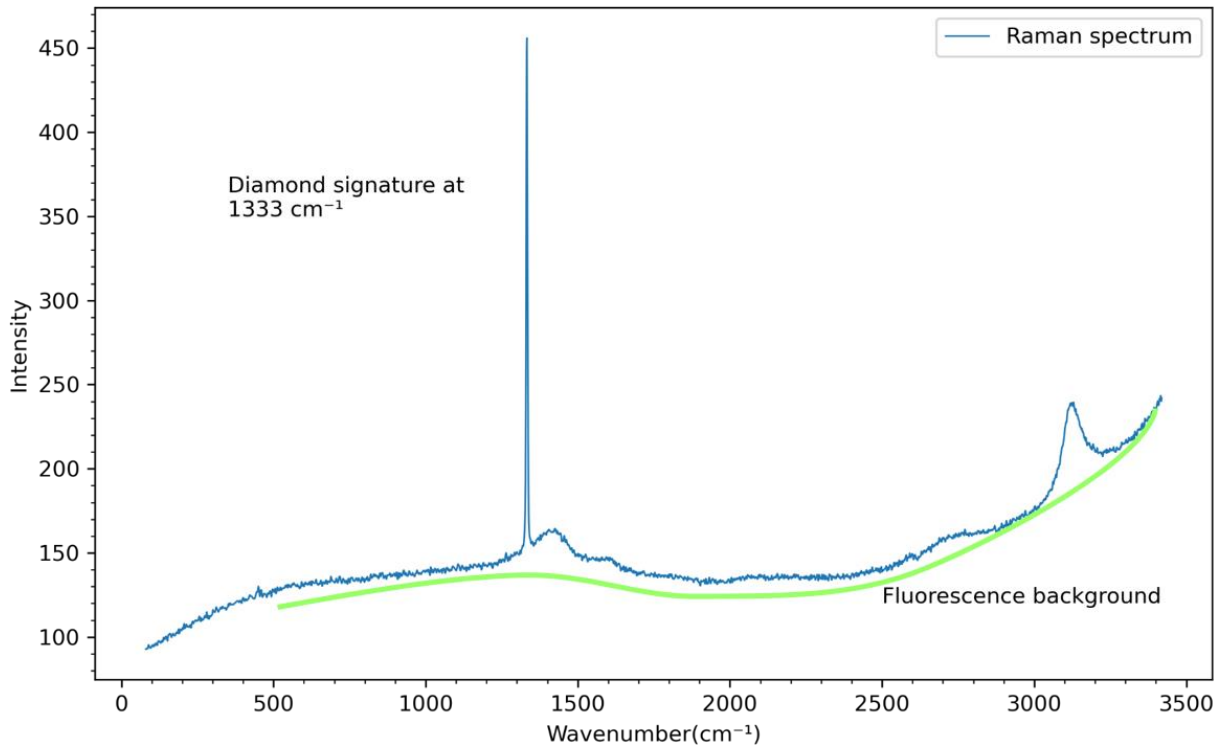

Figure 2-19: Spectral components encountered in some Raman spectra. Fluorescence is due to Raman resonance, and the strong diamond signature comes from the sample holder used for IR analysis, when the sample is too thin or transparent to the incident lasers. Spectra with either a strong diamond contribution or fluorescence have been left out of further processing.

The resulting model contains the spectral parameters of each processed spectrum. This process has been applied on both spectral maps and their averaged spectrum for each sample.

2.5. AFM-IR: IR nanospectroscopy

2.5.1. General principle

AFM-IR is a relatively recent technique that combines the high spatial resolution of the Atomic Force Microscopy (AFM) with an Infrared analysis (Dazzi et al., 2012; Dazzi et al., 2005). Although IR measurement is a universal tool for chemical characterization, as discussed previously one of its limitation for small regions of interest such as those found in micrometeorites resides in its spatial resolution limited by the optical diffraction limit of infrared radiations. The development of the AFM-IR has strongly improved the scale at which infrared analysis can be done: the technique consists in irradiating an area of the sample with a light generated by a tunable IR laser (QCL – Quantum Cascade Laser) (Figure 2-20).

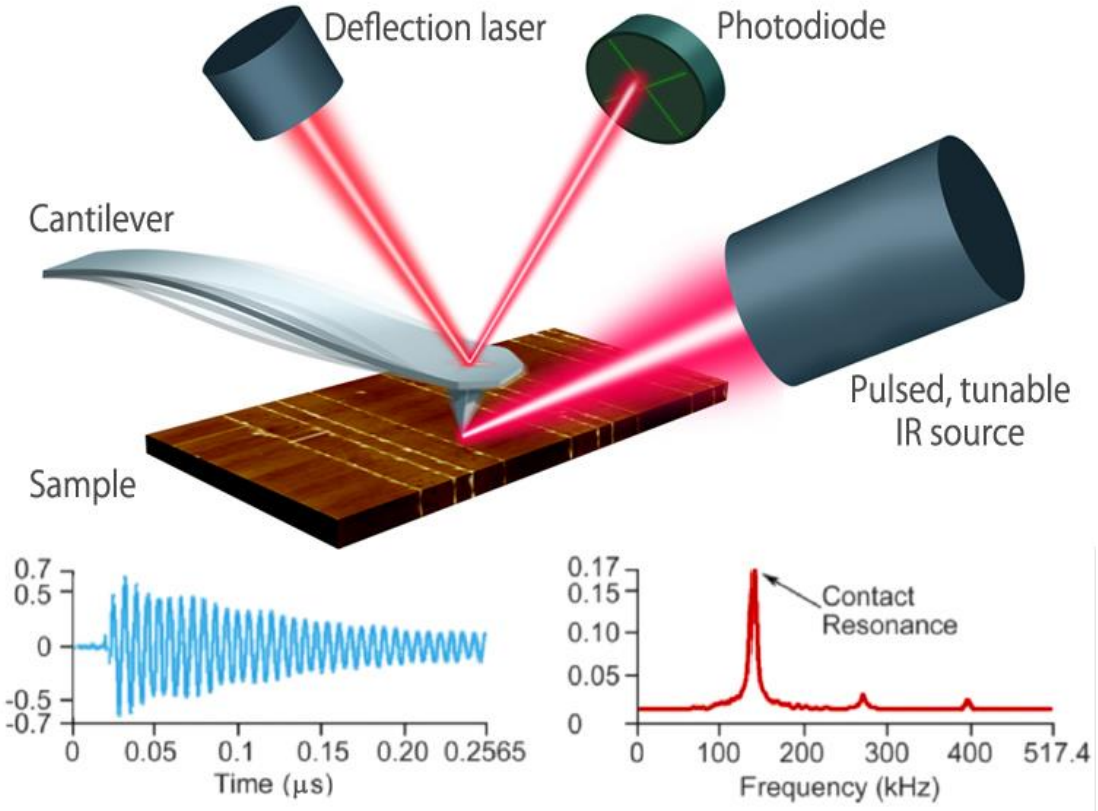

Figure 2-20: Representation of the AFM-IR set-up where an IR laser illuminate a sample, causing photo thermal expansion that is directly measured monitored the cantilever ring-down amplitude. The cantilever oscillation plotted against the laser wavenumber generate the IR spectrum. Image is from anasysinstrument.com.

If the laser is set to a wavelength that the sample will absorb, a photo-thermal expansion of the material will result from the light being converted to heat in the sample. This rapid thermal expansion can be measured by the tip of an AFM cantilever that will detect the irradiated volume expansion that can be shown to be directly proportional to the absorption coefficient of the sample. The cantilever oscillations are monitored with a four-quadrant detector for each wavelength of interest in order to produce a complete IR spectrum. The spatial resolution is therefore now set by the AFM precision, overcoming the IR optical diffraction limit. Two modes of operation are available: spectra taken at a fixed location or mappings over several μm^2 at a fixed wavelength.

The AFM-IR technique is still under development but has already applications in many domains such as microbiology and material science. The range of the tunable QCL lasers adapted

to this technique covers most of the organic portion of the infrared spectrum (typically from 900 to 2000 cm^{-1}) and has been mostly used to characterize organic material. The analysis of the organic content of a UCAMM has already been successfully demonstrated (Mathurin et al., 2019) although optimal sample preparation for this type of measurement is still challenging. The characterization of inorganic content with AFMIR, however, remains an ongoing research topic. For mechanical reason, photo-thermal expansion of mineral phases appears more complex to apprehend than for organic material.

2.5.2. Data processing

The AFM-IR data presented in this work will focus on the characterization of AFM-IR spectra measured on mineral phases in order to investigate the ability of AFM-IR to probe inorganic material. Several sample with different mineralogy and sample preparation methods (see 0) have been measured. The resulting spectra have been processed using the Orange software ((Demšar et al., 2013), version 3.27.1).

A preliminary step for data processing of AFM IR spectra is sometimes necessary. Some spectra recorded during the analysis exhibited 'jump' at fixed wavelength (1171 cm^{-1}, 1477 cm^{-1} and 1675 cm^{-1}), which correspond to transitions between different QCL Lasers. These jumps can be easily fixed and the spectrum before and after 'break-correction' are displayed in Figure 2-21. When the set of spectrum has been corrected for these kind of jumps, the next step consists in a general preprocessing of each of the spectra. This involves selecting only the spectra with high enough signal/noise ratio, before applying a Savitzky-Golay filter with identical parameters to the entire set of spectra. Once AFM-IR spectra have been preprocessed with the same procedure, they can be compared to each other to investigate the effect of different acquisition parameters.

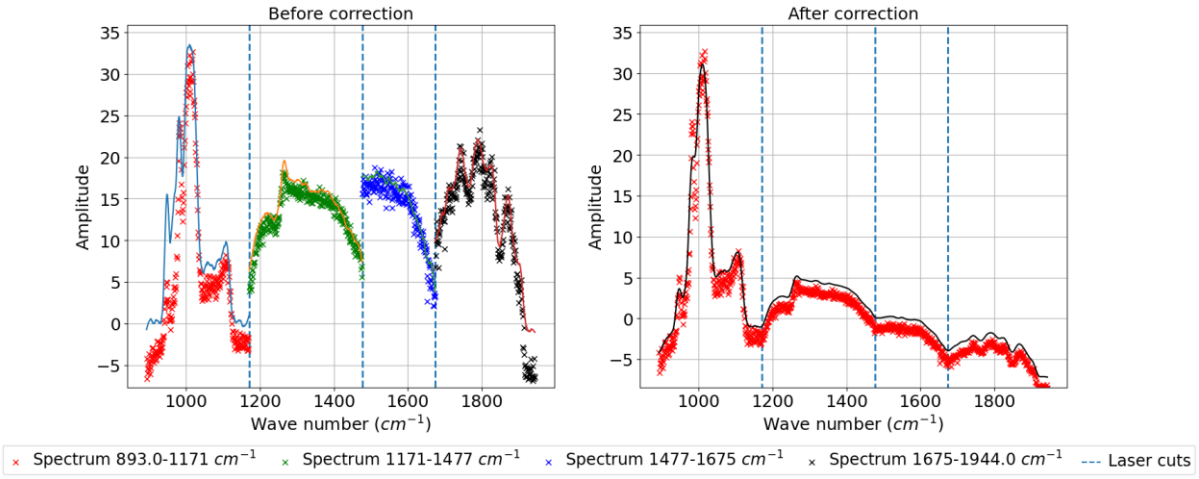

Figure 2-21: 'Break-correction' process applied to AFM IR spectra presenting 'jumps' in the original spectrum. The 'reference' part is the spectrum on the left while a multiplicative factor is applied to the successive part of the spectrum from left to right. The final reconstructed spectrum is display on the right plot.

Chapter 3

3. Characterization of chondritic AMMs by FTIR and Raman microscopies

3.1. Introduction

Ultracarbonaceous Antarctic micrometeorites (UCAMMs) represent only ~1% of the particles in the Concordia collection. They show unique characteristics strongly suggesting that they have a cometary origin. Most of the chondritic AMMs (~99% of the Concordia MMs) could also have a cometary origin, in agreement with models predicting that about 80% of the cosmic dust originates from comets (Nesvorný et al., 2011b). We thus characterized the organic and mineralogical content of several chondritic AMMs retrieved during 2006 and 2016 collection expedition at Dome C.

Previous characterizations of both organic and mineral content of AMMs revealed similarities with the grains from the comet Wild2 retrieved during the Stardust mission (Dobrică, 2010; Dobrică et al., 2009). Overall AMMs and Stardust grains have a composition close to CI values, and both contain refractory phases (Dobrică, 2010; Zolensky et al., 2006), such as Calcium Aluminum Inclusions (CAIs) observed in Stardust samples. These refractory phases are mostly found in chondritic meteorites where they can account for up to 13% of the volume (MacPherson, 2005). Those phases are thought to form in the inner solar system through condensation of a solar composition gas (Grossman, 1972). The presence of such phases in cometary materials may indicate large scale radial mixing where inner solar system material could have been brought to the external region of the solar system to be accreted on cometary parent body. Fragments of chondrule-like objects have also been occasionally observed in micrometeorites and in Wild 2 grains (Dobrică, 2010; Dobrică et al., 2009; Nakamura et al., 2008a). As chondrule texture type indicates crystallization in the inner solar system region from a melt, the presence of those phases in cometary material further attest from radial transport of these objects toward the external regions of the solar system (Simon et al., 2008; Zolensky et al., 2006).

AMMs and Wild 2 grains also share similarities in their mineralogical content. Both displays mostly silicates with abundant olivine and pyroxene grains. Overall silicates in Wild 2 and AMMs display a pyroxene to olivine ratio close to unity (Nakamura et al., 2008b). Silicates have varying composition in both Wild 2 and AMMs. Olivine are mostly Mg-rich with composition ranging from Fo_{99} to Fo_{4} in Stardust particles (Leroux et al., 2008; Zolensky et al., 2008; Zolensky et al., 2006) and Fo_{100} to Fo_{48} for AMMs (Dobrică et al., 2009). Although they present varying Mg-content, olivines in both Wild 2 grains and AMMs show a strong frequency peak at Fo_{99}. For pyroxene, the range in Mg-content is also relatively important in both Wild 2 samples and AMMs with values ranging between En_{58-100} and En_{65-99} respectively. In the same trend as for olivine, a strong frequency peak is observable at En_{99} indicating a mineralogy dominated by Mg-rich pyroxenes.

AMMs and Wild 2 grains also present abundant Fe-sulfides in their mineralogy. AMMs mostly contain sulfides under the form of troilite, thought to be the first sulfur-bearing mineral to form in the protoplanetary disk out of sulfurization of Fe-Ni metals. However, some sulfides present higher Ni content and some pentlandite-like stoichiometry have been observed (Engrand et al., 2007b). For Stardust grains, the collection method led to a depletion in S within sulfides due to the thermal event occurring during impact with the aerogel (Zolensky et al., 2006). Unaltered sulfur from Wild2 have stoichiometry corresponding to the one of troilite, similarly to AMMs.

In this chapter, we will focus on the characterization of the organic matter and mineral content of 10 AMMs through both Raman and mid-IR/far-IR analyses. Results will be compared with previous analyses on AMMs and on cometary grains from Wild 2 comet.

3.2. FTIR and Raman of chondritic AMMs

3.2.1. Mid- and far- Infrared analysis of AMMs

3.2.1.1. Qualitative analysis of IR signatures

Ten AMMs from the Concordia collection (Figures 1 and 2) retrieved during the Antarctic expeditions of 2006 (DC06-11-70, DC06-09-157, DC06-09-82 and DC06-05-64) and 2016 (DC16-08-164, DC16-14-141, DC16-11-301 and DC16-11-343) have been analyzed to cover the absorption range of mineral (100 – 1400 cm^{-1}) and organic phases (700 – 4000 cm^{-1}) during two different sessions at the SOLEIL synchrotron SMIS beamline in June 2019 and July 2020. Mid- and far- IR spectra of the different fragment of AMMs have been merged and processed following the procedure described in Chapter 2. The images of the fragments from the different AMMs analyzed are displayed in Figure 3-1 (hydrated chondritic AMMs) and Figure 3-2 (non-hydrated chondritic AMMs).

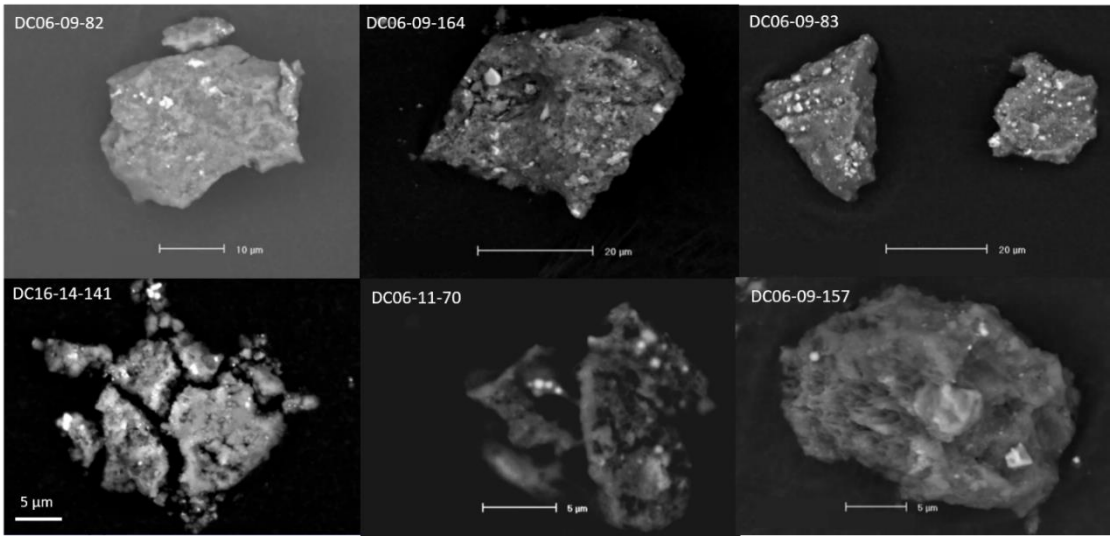

Figure 3-1: Back-scattered Electron (BSE) images of the fragments of 6 hydrated AMMs selected for FTIR analysis.

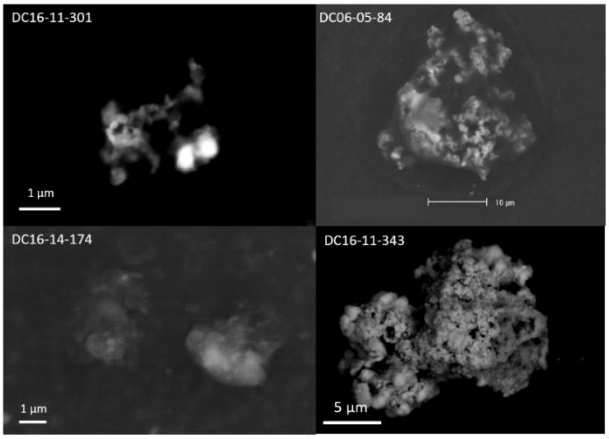

Figure 3-2: Back-scattered Electron images of the fragments of the 4 anhydrous chondritic AMMs studied in this work

The infrared spectra of the different AMMs are displayed in Figure 3-3 with a focus on the silicate absorption region in Figure 3-4. The spectra in blue correspond to the hydrated chondritic AMM fragments while the spectra in red correspond to non-hydrated chondritic AMMs. The IR spectra of the different AMMs always show absorption bands in the silicate region. The hydrated AMMs (in blue in Figure 3-4) present the characteristic phyllosilicate absorption with a large triangularly shaped band picking between 1005 and 1010 cm^{-1}. In the far IR part of the hydrated AMMs spectra, 2 peaks around 445 cm^{-1} and 460 cm^{-1} are visible. These absorption features could correspond to that of saponite (Beck et al., 2014). The hydrated AMMs do not display other dominant absorption peaks in their spectra over the silicate absorption range. However, small absorption features are visible at 880 cm^{-1}, 1448cm^{-1} and 1460 cm^{-1} for DC06-09-83. DC16_09_164 also present a slight shoulder at 880 cm^{-1} and diffuse peaks at 1448 cm^{-1} and 1460cm^{-1}. Such wavelengths correspond to carbonate absorption but precise identification of the nature of the carbonate could not be further identified.

The silicate absorption pattern for anhydrous AMMs is more complex and absorptions bands from different phases are overlapping. The main absorptions bands are summarized for the 4 chondritic AMMs in Table 3-1 and indicated in Figure 3-4 for the main ones. The IR profile observed over the silicate range is not identical for the 4 micrometeorites. DC16-14-174, DC16-11-301 and DC06-05-84 display their main absorption peaks around 890 cm^{-1} and 1065cm^{-1} while DC16-11-343 displays a large absorption band at 877cm^{-1} and a slight shoulder at 1060cm^{-1}. The 1060cm^{-1} absorption correspond to orthoenstatite (Jaeger et al., 1998) and is observed in all four samples. A less intense band observed around 888 cm^{-1} (corresponding to asymmetric stretching ν_{as} of SiO_4 in forsterite) is also present in all four spectra. The slight shift of the band to 877 cm^{-1} observed in DC16-11-343 could indicates the presence of fayalite (Fe-rich olivine) instead of Mg-rich forsterite, causing a slight shift of the vibration wavelength toward lower values with increasing Fe content (Jaeger et al., 1998). Overall, the mid-IR spectra of the non-hydrated AMMs suggest the presence of a mixture of Mg-rich silicates mostly dominated by pyroxenes for DC06-05-84, DC16-14-174 and DC16-11-301, and with the presence of Fe-rich olivines for DC16-11-343. The far IR part of the spectra also display the characteristic absorptions bands of both olivine and pyroxene, the most intense peaks being located around 350 cm^{-1} and 490 cm^{-1} for pyroxene and 415 cm^{-1} and 505cm^{-1} for olivine. Slight shifts in the maximum values of the peaks, probably due to high-Fe olivine, are observed for olivine-related peaks in DC16-11-343 in the same fashion as observed in the mid-IR spectrum.

Some unusual thin peaks have also been observed at 1350 cm^{-1}, 1365cm^{-1}, 2680 cm^{-1} and 2813 cm^{-1} in DC06-09-157, DC06-09-83, DC16-09-164 and DC16-14-174 (see Figure 3-3). Such absorption wavelength could correspond to carboxylic -CH and have been categorized as contamination. The organic absorption in AMMs are mostly composed of C=C/-OH absorptions located around 1600 cm^{-1} and aliphatic carbon absorption (CH_2 and CH_3 vibrational modes) located around 2950 cm^{-1}. The detailed absorptions of aliphatic bands for the different AMMs are summarized in Figure 3-5, except for AMMs DC06-05-84 and DC06-11-70 that did not display significant aliphatic absorptions. The main absorptions consist in symmetric and asymmetric vibrations of CH_2 and CH_3 (located around 2928 cm^{-1} and 2962 cm^{-1} respectively).

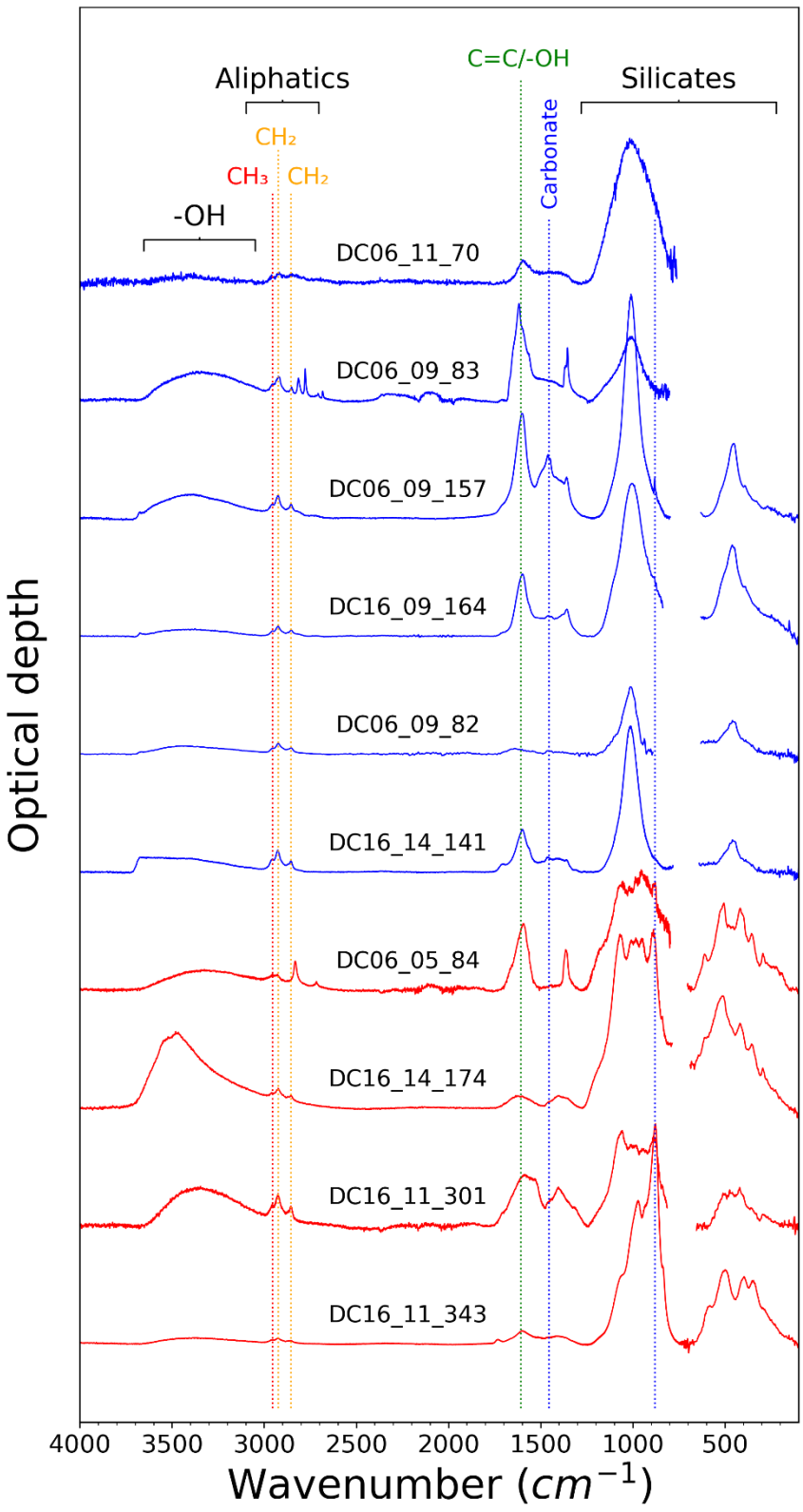

Figure 3-3: Merged far and mid infrared spectra (after baseline correction) of 10 AMMs from the Concordia collection collected during Antarctic expeditions in 2006 (DC06) and 2016 (DC16). Blue spectra correspond to hydrated chondritic AMMs containing phyllosilicates and red spectra correspond to non-hydrated chondritic AMMs.

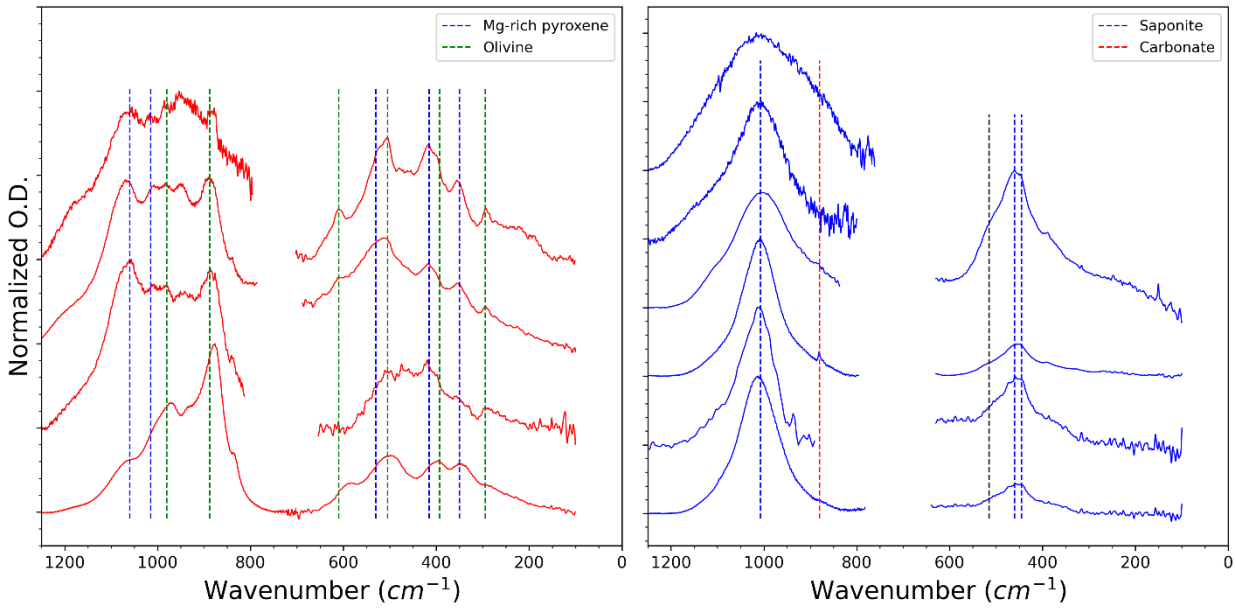

Figure 3-4: Z Zoom over the silicate absorption range of the IR spectrum in the different chondritic (right) and hydrated (left) AMMs. The main bands for Mg-rich pyroxene, olivine, saponite and carbonate are indicated in the spectra.

Table 3-1: Peak positions in the silicate range for non-hydrated Chondritic AMMs. Wavelenght in bold font correspond to strong peaks in the spectra. Values for forsterite and ortoenstatite from Jaeger et al. (1998).

Chondritic AMMs	Silicates bands position in IR spectra over the 200 – 1100 cm^{-1} range															
DC16_14_174	294	**352**	398	**416**	-	-	**504**	527	-	611	-	**884**	950	985	1015	1070
DC16_11_301	294	**351**	-	**415**	-	-	**505**	-	-	612	840	**888**	950	984	1008	**1070**
DC06_05_84	295	353	393	419	460	475	-	530	-	-	839	**888**	939	982	1012	**1060**
DC16_11_343	-	**348**	**396**	398	-	-	**498**	-	**591**	-	838	**877**	935	**972**	-	1060
Forsterite	295	361	378	395	-	-	512	-	-	609	840	884	950	980	1000	-
Ortoenstatite	-	354	393	408	465	-	-	540	-	-	862	900	938	-	1020	1063

Overall, the AMMs display similar absorption patterns for this part of the spectra with the asymmetric CH_2 absorption peaks being the most intense in every case. The same intensity difference for CH_2 and CH_3 is visible in the symmetric vibration bands (located around 2855 cm^{-1} and 2876 cm^{-1} respectively) although their lower intensity and the overlapping presence of the CH_2 Fermi Resonance mode at 2900 cm^{-1} makes their characterization more difficult.

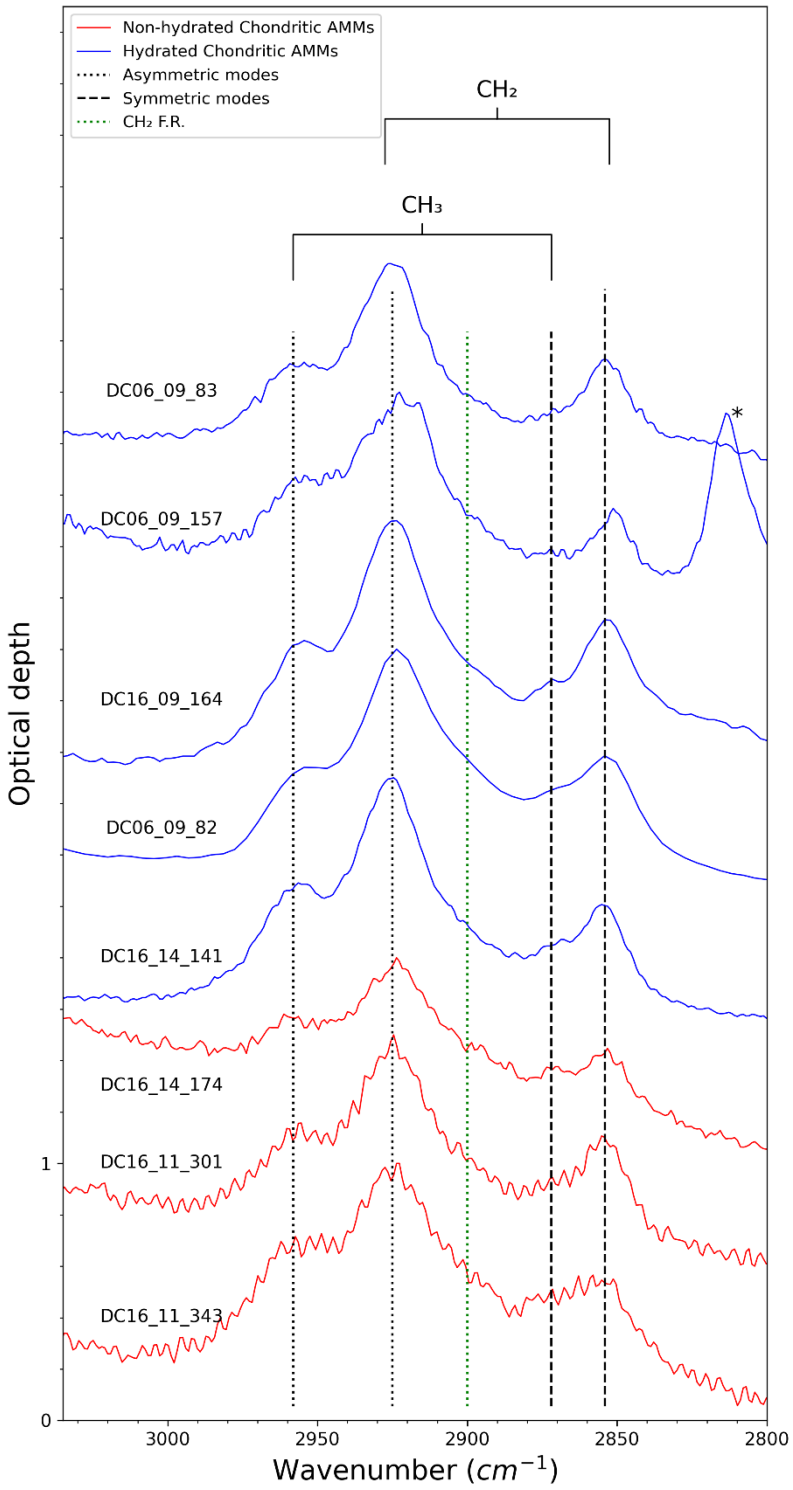

*Figure 3-5: Zoom on the aliphatic absorptions region of the MIR spectra for the different AMMs. The spectra have been normalized to the asymmetric mode of CH_2 and vertically shifted for clarity. AMMs DC 06_06_84 and DC 06_11_70 are not displayed because of their low aliphatic content. CH_2 F. R. : CH_2 Fermi resonance. *The peak at 2815cm^{-1} observed in DC06-09-157 has been characterized as contamination.*

3.2.1.1. Si/C ratio and aliphatic characterizations

The mid IR spectra of AMMs can give relative quantifications of the silicate to carbon ratio. The integrated areas under the silicate and the aliphatic absorption bands have been measured for the different AMMs and are summarized in Table 3-2. The integrated areas for the CH_2 and CH_3

peaks were measured following the method described in chapter 2: a set of 5 Gaussians were fitted under the aliphatic absorption bands and the area under the asymmetric modes of CH_2 and CH_3 were calculated and corrected in order to extract the value for the CH_2 and CH_3 groups.

Table 3-2: Band Area (BA) calculation for the peaks of silicate and aliphatic carbon in the different AMMs. When no value is indicated, the aliphatic band absorption was not intense enough to be quantified. The peak intensities (Int) are also indicated.

AMMs	BA(Sil)	BA(CH_2+CH_3)	Int CH_2	Int CH_3	BA(CH_2+CH_3)/BA(Si)
Chondritic non-hydrated AMMs					
DC16-11-343	164,21	2,11	0,023	0,015	0,013
DC16-11-301	257,26	18,03	0,267	0,140	0,070
DC16-14-174	202,71	3,83	0,052	0,026	0,019
DC06-05-84	204,50	3,55	-	-	0,017
Chondritic hydrated AMMs					
DC06-09-82	109,55	9,29	0,133	0,070	0,085
DC16-14-141	93,77	9,77	0,136	0,061	0,104
DC16-09-164	120,17	4,38	0,053	0,028	0,036
DC06-09-83	80,17	9,75	0,176	0,091	0,122
DC06-09-157	116,14	5,66	0,076	0,035	0,049
DC06-11-70	207,38	-	-	-	-

The aliphatic absorption around 2950 cm^{-1} can also give information about the ramification of the aliphatic carbon in the measured sample. The ratio of the intensities of the peaks at 2925 cm^{-1} (CH_3) and 2960 cm^{-1} (CH_2) has also been calculated to infer the ramification and length of aliphatic chains in the organic matter, following the data processing method described in the previous chapter.

The aliphatic CH_2 and CH_3 intensities and the integrated values for the silicate and aliphatic carbon bands are summarized in Table 3-2. The corresponding ratios and displayed against each other in Figure 3-6. The aliphatic to silicate ratios calculated from the IR spectra of the AMMs show rather large variations with values ranging from 0.035 to 0.122. Overall, hydrated chondritic AMMs exhibits larger aliphatic to silicate areas ratios than non-hydrated chondritic AMMs, with an average of 0.07 and 0.03 respectively. Calculation performed for most of both chondritic and hydrated AMMs show a CH_2/CH_3 ratio with values around 2.0. The measured CH_2/CH_3 ratio from intensities in AMMs seems independent from the aliphatic to silicate ratio variations observed within the AMM sample set.

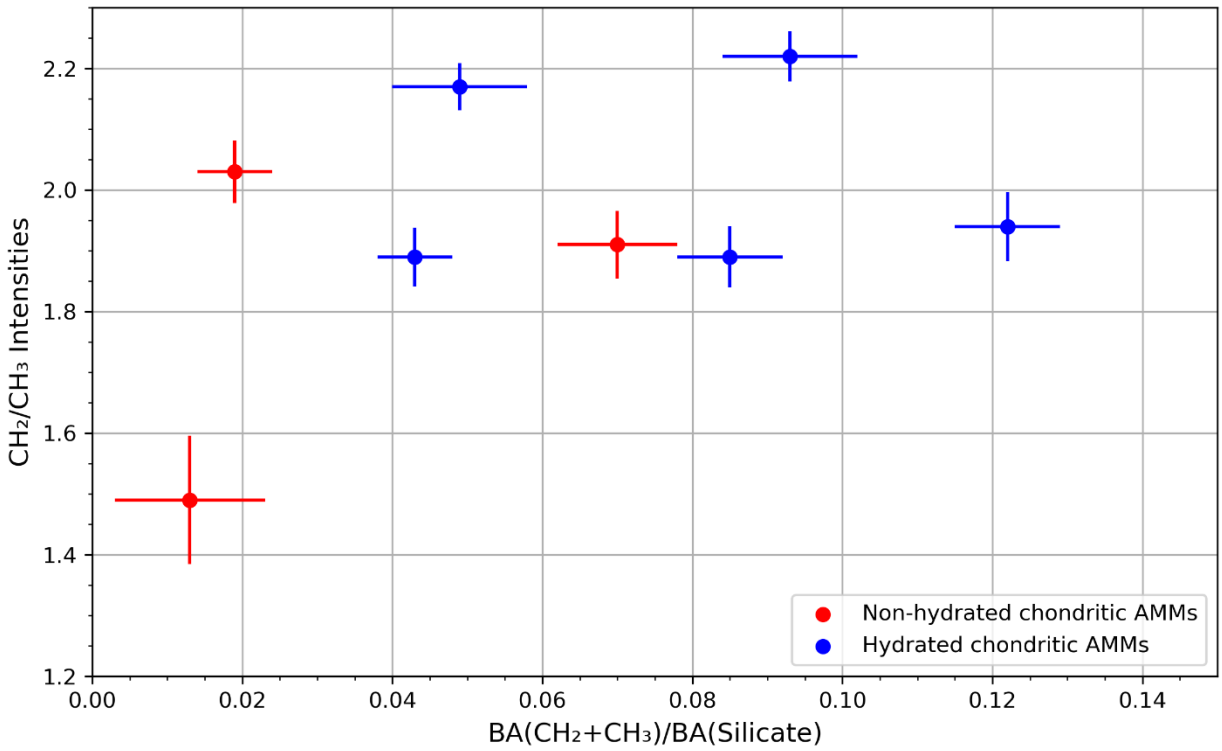

Figure 3-6: Ratio of CH_2/CH_3 intensities versus the corresponding aliphatic to silicate integrated band area (BA) ratio.

For this work, direct peak intensity calculations for the CH_2 and CH_3 bands (which is often used in the literature) have been compared with the quantification of the CH_2 and CH_3 groups from the integrated areas of the same bands (Figure 3-7). In order to have a direct comparison with carbonaceous dust from the diffuse interstellar medium as well as a sample with a clear different aliphatic content than the one found in AMMs, the value for the infrared galaxy IRAS 08572+3915 (Dartois et al., 2007) is also plotted in Figure 3-7.

Results summarized in Figure 3-7 show a good correlation between the intensity ratio and the $N(CH_2)/N(CH_3)$ that are quantified from of the integrated areas through the Gaussian fit corrected by the integrated cross sections of the functional groups (see Chapter 2). Consistently with results obtained by Dartois et al. (2007), the IRAS 08572 spectrum shows a CH_2/CH_3 ratio close to unity, indicating a highly aliphatic organic matter. For chondritic AMMs, the ratio directly calculated from the intensities of the bands is also correlated with the ratio of $N(CH_2)/N(CH_3)$ in the samples. Linear regression models indicate coefficients of 0.72 and 0.82 for (for calculations with no forced intercept (in black, Figure 3-7) and an intercept forced to 0 (in pink) respectively) between intensities and quantitative results obtained by area calculations.

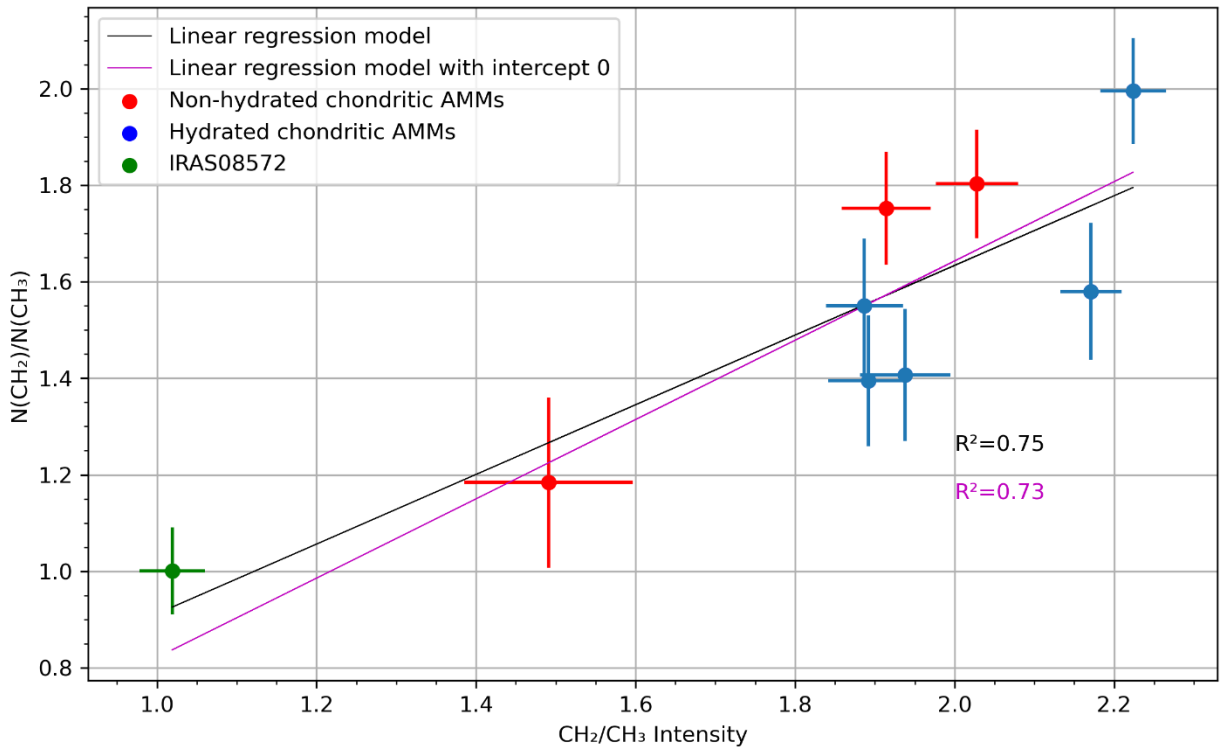

Figure 3-7: Measured CH_2/CH_3 intensities compared to the $N(CH_2)/N(CH_3)$ ratio extracted from Gaussian area calculation of CH_2 and CH_3 asymmetric modes. The two lines represent linear regression results with a fixed intercept at 0 (pink) and with no intercept fixed (black)

The obtained direct CH_2/CH_3 intensity ratios for AMMs can be compared with previous analysis from different extraterrestrial materials. Results obtained in this work are consistent with previous analysis on AMMs where intensities ratios obtained ranged from 1.76 to 2.6 (Battandier et al., 2018). Interplanetary Dust Particles (IDPs) analyzed with the same method revealed a larger variations of aliphatic content with values CH_2/CH_3 intensity ratio varying from 1 to 5.6, probably partly resulting from the heterogeneity within the sample set and from possible contamination with silicon oil, which is the collecting media for IDPs (Flynn et al., 2003). Analysis of the organic content of IDPs and of IOM extracted from meteorites has also been performed using the Gaussian fit and column density calculations. Chondritic IOM (for CI and CM meteorites) exhibits a $N(CH_2)/N(CH_3)$ ratio ranging from 1.7 to 3.5 (Orthous-Daunay et al., 2013). For Tagish Lake meteorite (an unclassified CC), CH_2/CH_3 ratio for IOM are similar to the one found in IOM from CI and CM with values comprised between 1.79 and 2.70 (Yesiltas and Kebukawa, 2016). For IDPs, similarly to direct intensity measurements, the $N(CH_2)/N(CH_3)$ ratios are variable and range from 2.5 to 6.1 (Matrajt et al., 2005; Merouane et al., 2014). Overall, chondritic AMMs shows less variation in their $N(CH_2)/N(CH_3)$ ratios than other extraterrestrial materials with values constantly fluctuating around 2. Generally, aliphatic content of the organic matter encountered in the solar system is characterized by a $N(CH_2)/N(CH_3)$ ratio strictly superior to 1.2, a minimum value which is measured in chondritic IOM. The aliphatic content in the diffuse interstellar medium measured through the 3.4 µm absorption bands of IRAS08572 exhibits a $N(CH_2)/N(CH_3)$ close to unity indicating more aliphatic branched organic carbon. This implies that, if the solar system initially accreted carbonaceous matter similar to the one observed in IRAS, this organic carbon has been reprocessed in order to increase the length of the aliphatic chains. Thermal metamorphism or aqueous alteration occurring on a parent body could lead to such

transformation of the organic content initially accreted. The large CH_2/CH_3 values encountered in IDPs (up to 6.1) seem hard to reconcile with the value obtained for other solar system organic material. Such large amount of CH_2 can be explained by different factors. The first important bias is the silicon oil used to recover the IDPs before analysis. Although careful cleaning of the samples is performed, the interaction between the porous IDPs and the silicon oil probably do not permit complete elimination of all potential contamination. Another important source of error is the methods used to perform the Gaussian fit under the aliphatic absorption at 3.4 µm. If maximum widths and positions of the fitted bands are not constrained enough, an overestimation of the contribution of CH_2 absorption band and ultimately lead to unreasonable values of $N(CH_2)/N(CH_3)$ from extracted from the fits.

3.2.2. Raman signature of organic matter in AMMs

The organic content of the AMMs has also been investigated using Raman spectroscopy. The analysis conditions and the data processing method are described in Chapter 2. The different averaged spectra of the AMMs measured at 532nm are displayed in Figure 3-8. The spectra have been normalized to their maximum intensity over the D and G Raman bands to ease comparison. Overall, all AMMs display the characteristic D and G bands of polyaromatic carbon (located around 1350 cm^{-1} and 1600 cm^{-1} respectively), although hydrated AMMs DC16-14-141 and DC06-09-82 display a relatively low amount of carbon and have a lower signal/noise (s/n) ratio than the other spectra, making the determination of their spectral parameters subject to more uncertainty. The number of spectra used for each averaged spectrum along with the extracted spectral parameters are summarized in Table 3-3.

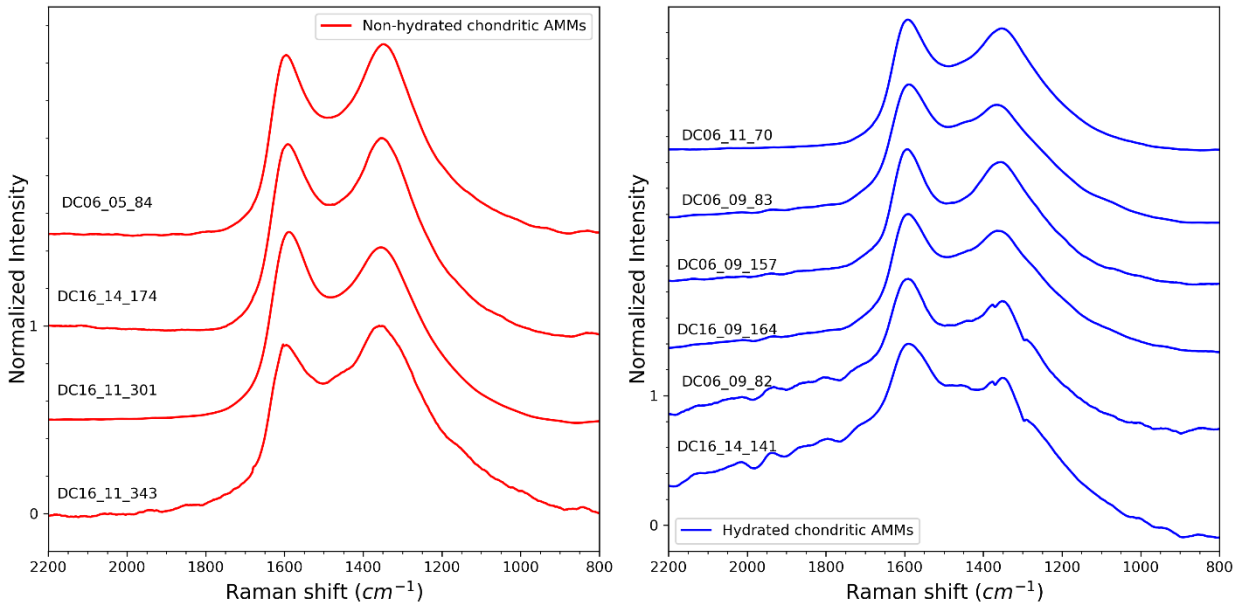

Figure 3-8: Zoom over the D and G absorption bands of polyaromatic carbon in chondritic non-hydrated (left, red) and chondritic hydrated (right, blue) AMMs. Spectra have been normalized to their maximum and shifted vertically to ease comparison.

The spectral parameters of the spectrum have been calculated for both individuals and averaged spectra for each AMM. Table 3-3 only present the spectral parameters of the D and G bands obtained for the average spectra of each AMMs. The number of spectra used to calculate the average was constrained by the amount of spectra exhibit sufficient s/n ratio for D and G bands in each sample as well as the coverage of the particle. The results of the individual averaged

spectrum in each AMMs is shown in Figure 3-9 and Figure 3-10. Spectral parameters of AMM DC16-14-141 could not be properly obtained because of the low s/n in the spectra, therefore, the AMM is not listed in the different comparison figures. Figure 3-11 present the values of both hydrated and chondritic AMMs in a global figure.

Table 3-3 : Spectral parameters of D and G bands extracted from the averaged Raman spectra of both non-hydrated and hydrated chondritic AMMs. (N: number of spectra used to calculate the average, I_D/I_G: intensity ratio, ω: band position, FWMH: full-width at half-maximum.)

AMMs	N of spectra averaged	I_D/I_G	ω_D (cm^{-1})	ω_G (cm^{-1})	FWHM-D (cm^{-1})	FWHM-G (cm^{-1})
Non-hydrated chondritic AMMs						
DC16-11-343	5	1.17	1346.7	1612.9	230.5	133.3
DC16-11-301	84	0.95	1346.9	1601	253.5	134.2
DC16-14-174	77	1.10	1342.9	1611.3	213.4	124.5
DC06-05-84	11	1.06	1343.2	1611	212	143.9
Hydrated chondritic AMMs						
DC06-09-82	9	1.03	1361.1	1590.9	252.1	140.5
DC16-09-164	42	1.21	1353.6	1586.2	287.6	128.7
DC06-09-157	33	1	1351.1	1597.3	249.2	105.7
DC06-09-83	132	1.01	1360	1597.6	317.6	119.3
DC06-11-70	69	0.98	1348.6	1603.9	246.1	120.9

Spectral parameters of each individual AMMs are summarized in Figure 3-9 and Figure 3-10. Each plot displays the spectral parameters of the averaged spectrum (stars) along with spectral parameters of the individual spectra (dots). Non-hydrated chondritic AMMs (in red) displays a D band position with values ranging from 1340 cm^{-1} to 1350 cm^{-1} and D-band FWHM comprised between 200 cm^{-1} and 250 cm^{-1}.

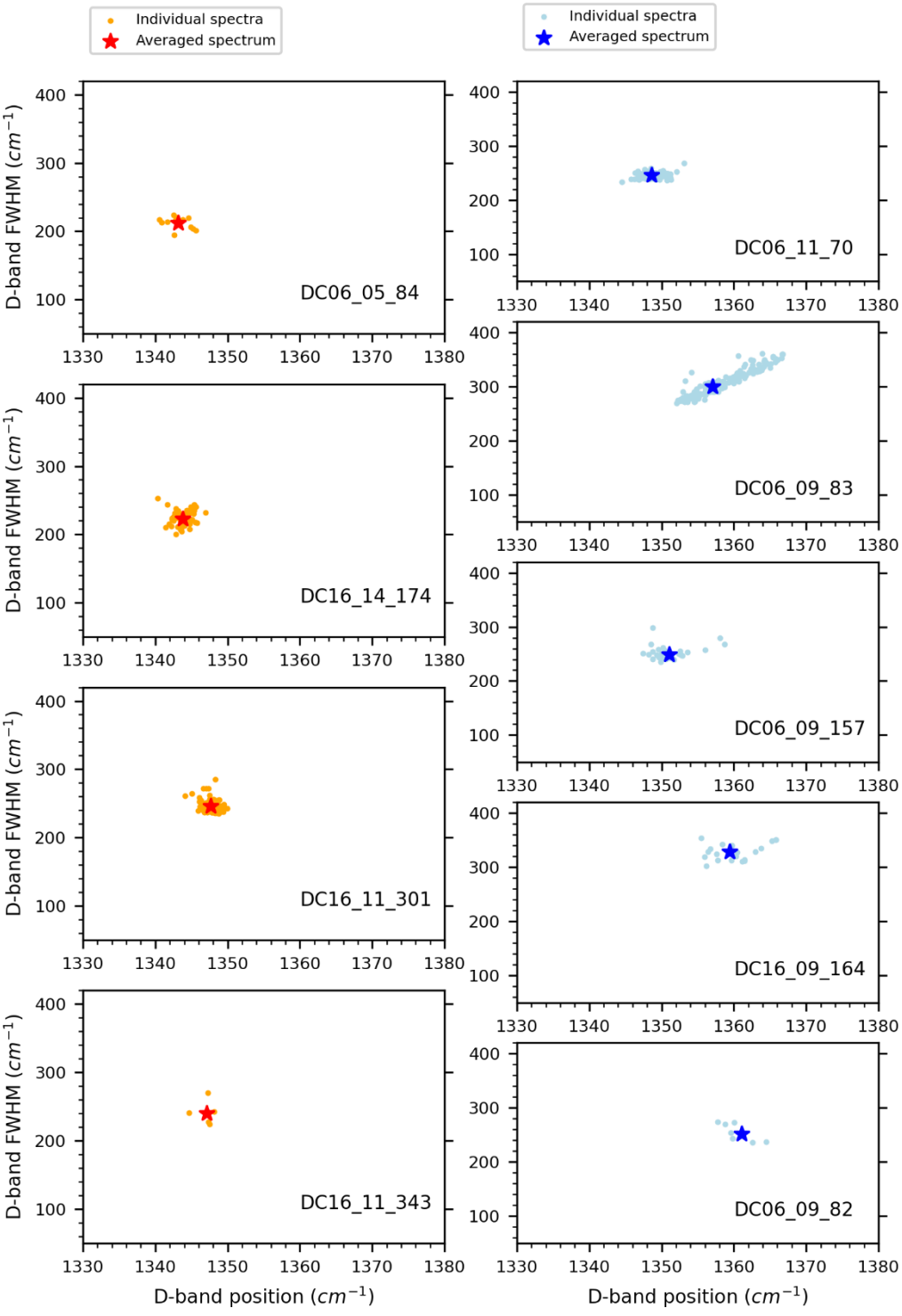

Figure 3-9: D-band position (cm-1) versus D-band FWMH for non-hydrated (left) and hydrated chondritic AMMs (right). The stars represent the spectral parameters obtained for the averaged spectrum while dots represent the spectral parameters for individual spectra.

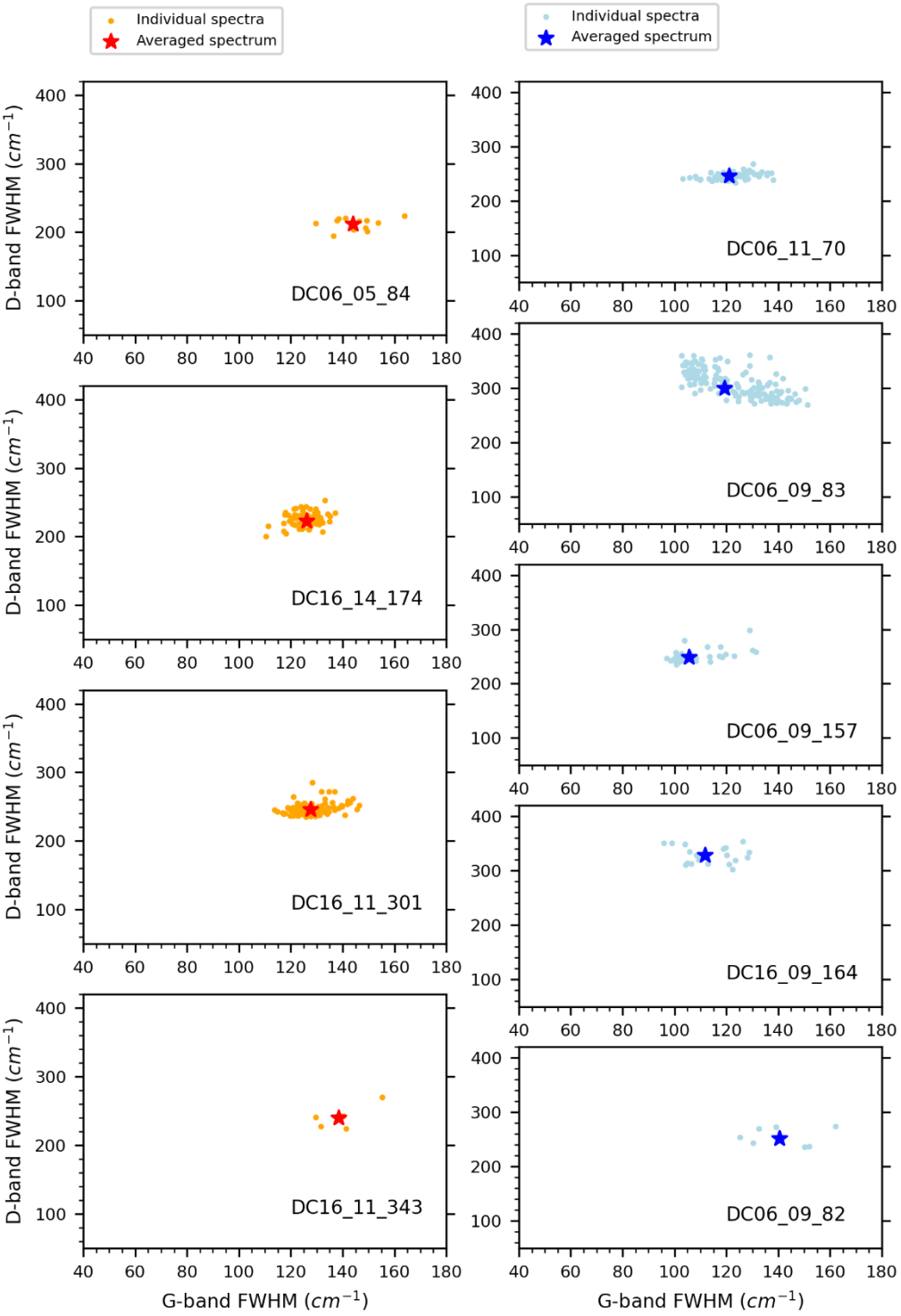

Figure 3-10: G-band full width at half maximum (FWHM, in cm⁻¹) versus D-band FWMH for non-hydrated (left) and hydrated chondritic AMMs (right). The stars represent the spectral parameters obtained for the averaged spectrum while dots represent the spectral parameters for individual spectra.

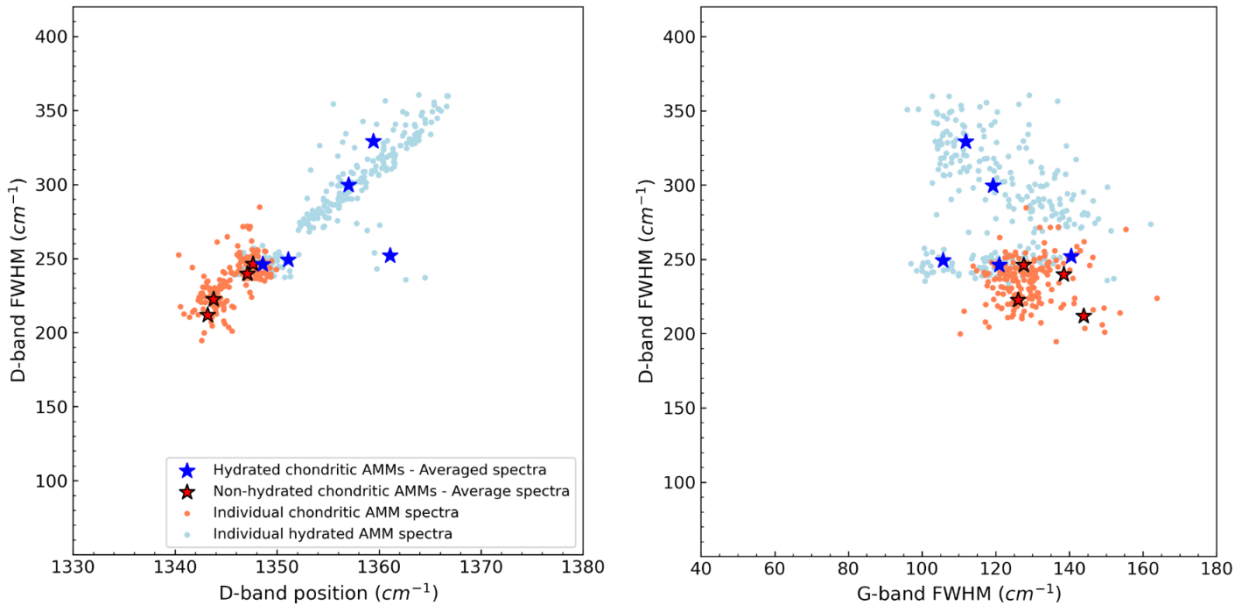

Figure 3-11: Raman D band full width at half maximum (FWHM) vs position of the D band (left) and G band FWHM (right) for the sample set of AMMs in this study. Stars represent the spectral parameters obtained from the averaged spectrum of each AMM while the dot represent individual spectra parameters.

Overall, individual spectra display parameters close to the average spectrum value, indicating a relatively homogenous structural order of the polyaromatic organic matter in those samples. For hydrated chondritic AMMs, the center of D-band is slightly shifted toward higher values, ranging between 1350 cm^{-1} and 1360 cm^{-1}. The FWMH of the D-band in hydrated samples also presents higher values comprised between 240 and 330 cm^{-1}. Another interesting pattern observable in hydrated chondritic AMMs is the larger dispersion of the spectral parameters of the individual spectrum compared to non-hydrated chondritic AMMs. Hydrated chondritic AMMs individual spectra shows larger variation, especially for D-band positions indicating a more heterogeneous polyaromatic content of the organic matter of hydrated AMMs than for non-hydrated AMMs. The ratio of the intensity of the D and G band also provides information on the extent of thermal modifications encountered by the organic material in the investigated samples. Intensity values for both chondritic and hydrated AMMs display ratio (I_D/I_G) ranging from 0.95 to 1.21.

Spectral parameters obtained for the AMMs in this study are consistent with previous Raman characterization of AMMs. The intensity ratio is consistent with results obtained by Dobrică (2011) and Battandier (2018), which carried analyses in similar conditions on AMMs. An additional observation to previous work is that the spectral parameters variations for individual spectra are also more important in hydrated AMMs than in non-hydrated chondritic AMMs. If non-hydrated samples were dehydrated during atmospheric entry, this would suggest than atmospheric entry heating had a limited impact on the spectral parameters of the organic matter in the investigated samples. The observed larger variations within hydrated AMMs organics spectral parameters could point out to different thermal (in addition to aqueous) history for non-hydrated and hydrated AMMs or a direct inheritance from different organic precursors.

The intensity ratio of the D and G band is systematically lower than 1.2 while the FWHM of the D-band is superior to 200 cm^{-1} (250cm^{-1} for hydrated AMMs). Such values indicate that the organics in AMMs were not strongly thermally altered, such as the IOM extracted from carbonaceous chondrites (CCs). Meteorites that experimented organic maturation through parent

body processes exhibit larger intensity ratio of the D and G bands as well as FWHM-D progressively decreasing toward 100 cm^{-1} for the most altered chondrites (Bonal, 2006; Bonal et al., 2007). The values measured in AMMs indicate that they did not experiment thermal metamorphism as intense as the one encountered in ordinary chondrites (OCs). The organic content of cometary particles from 81P/Wild 2 comet have also been characterized with Raman spectroscopy. Their spectral parameters along with those of other extraterrestrial materials are summarized in Figure 3-12.

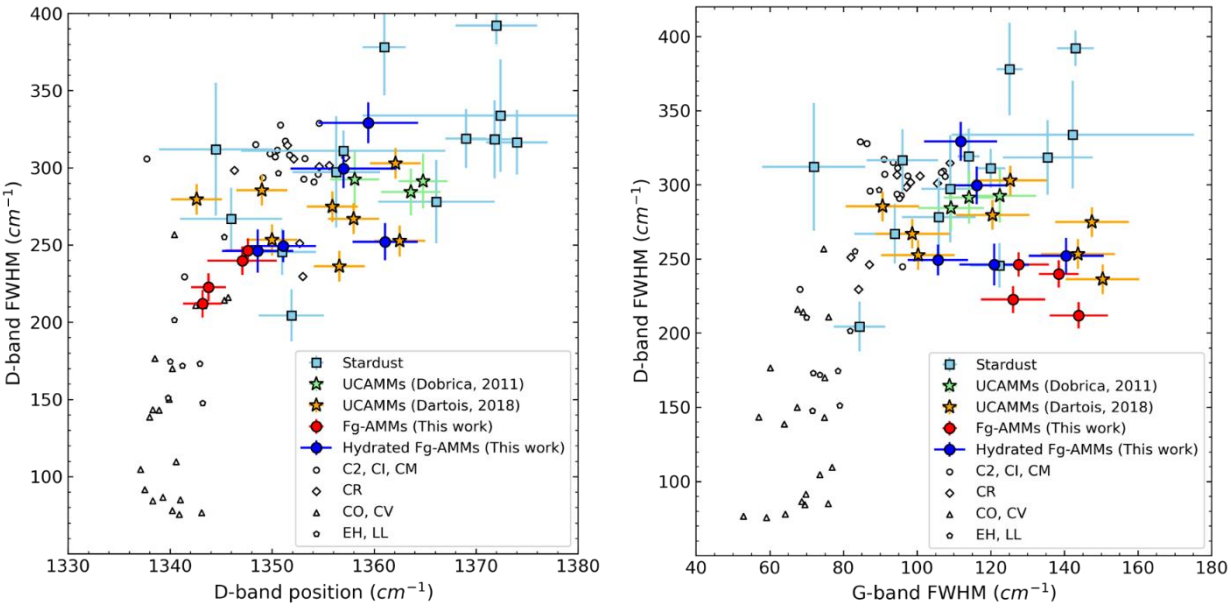

Figure 3-12: Figure reproduced from Dartois et al. (2018) displaying the FWHM of D-band versus D-band position (left) and FWHM of G band (right) for several extraterrestrial samples. The fitted trend on the left plot represents the organic matter primitivity: extraterrestrial organic matter with D-band width > 250 cm^{-1} are considered the most primitives. Data are from Busemann et al. (2007) (C2, CI and CM (circles), CO and CV (triangle), EH and LL (half circles)), Rotundi et al. (2008) (Wild 2, blue square) and Dobrică et al. (2011) (UCAMMs, green star)

When comparing the values obtained for AMMs in this work with previous analysis on extraterrestrial material (as shown in Figure 3-12), it appears that the spectral parameters for AMMs, both non-hydrated and hydrated, lie within the region delimited by the most primitive meteorites along with Ultracarbonaceous Antarctic Micrometeorites (UCAMMs, which will be more thoroughly discussed in Chapter 4), carbonaceous chondrites (CI, CM, in circles) and comet 81P/Wild 2 particles. All the AMMs measured in this work have spectral parameters closer to those of CCs and 81P/Wild 2 particles in general, further settling the relationship between micrometeorites and cometary samples (ref Elena 2009). From this work, it appears that slight differences exist between hydrated and non-hydrated AMMs. Non-hydrated AMMs overall exhibit values closer to that of the less altered CO, CV and C2, CI, CM meteorites while the hydrated AMMs spectral parameters cover the range of those of cometary particles from 81P/Wild 2. This could point out to different parent bodies for these two types of micrometeorites. Interestingly, the Raman parameters of organic matter of hydrated AMMs seems more closely related to 81P/Wild 2 particles than for non-hydrated AMMs. This further raises the on-going question of the possibility of aqueous alteration on cometary bodies (Guérin et al., 2020; Suttle et al., 2020b). Overall, the organic matter of hydrated AMMs seems more variable than for non-hydrated AMMs. This can be explained by two different scenarios. If the two AMMs types initially had identical organic precursor, different alteration history must have occurred in order to lead to the

nowadays observed difference in their organic matter. This alteration could be limited thermal events in the case of non-hydrated chondritic AMMs, which could homogenize the organic signature of the AMMs. The hydrated AMMs on the other hand, display more variability that could potentially be generated through aqueous alteration of the organic precursor. The other possibility is that the originally accreted organic materials were already different for the two AMMs types, implying that their parent body formed at different location in a chemically heterogeneous protoplanetary disk.

3.2.3. Mineral content of AMMs from the Concordia collection from Raman analysis

Raman analysis of the 10 AMMs in this study also allowed the characterization of some minerals present in these particles. In this section, a summary of the different mineral phases encountered in the AMMs' Raman spectra is presented. Because the polyaromatic carbon signature mostly dominate the Raman spectrum in AMMs, being intrinsically more intense and masking the underneath less intense mineral Raman signatures often, only a few individual spectra sometimes displayed mineral signatures over the 100 cm^{-1} to 1000 cm^{-1} range. Overall, 2 types of minerals have been observed in the measured sample set of AMMs. The magnetite is the most present phases and both types of AMMs displayed its signature. Some AMMs spectra with clearly identified magnetite are shown in Figure 3-13.

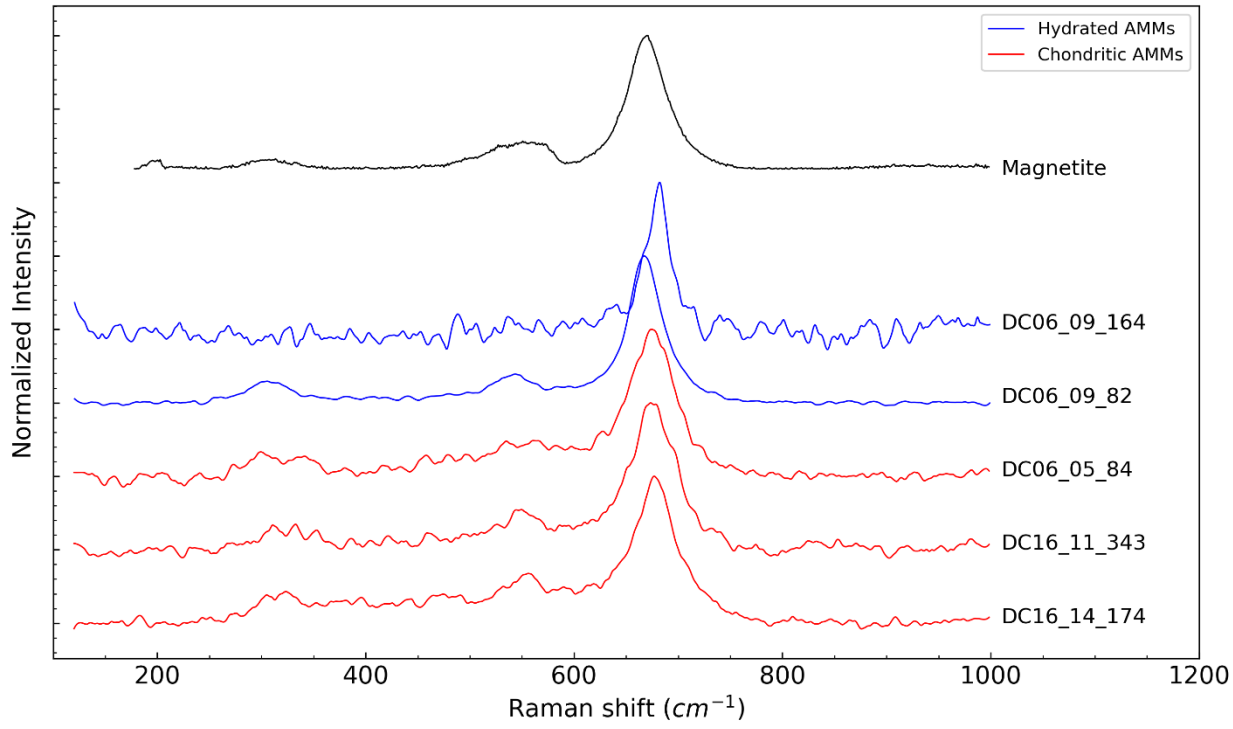

Figure 3-13: Spectra of both hydrated (blue) and chondritic (red) AMMs displaying the peak attributed to magnetite. The standard magnetite spectrum is displayed in black (Lyon Raman database: www.geologie-lyon.fr/Raman)

The magnetite-bearing spectra visible in Figure 3-13 display slight variations in the maximum of the peak around 670 cm^{-1}. The value for the pure magnetite spectrum corresponds to 675 cm^{-1} while the maximum in the investigated spectra range from 665cm^{-1} (for DC06-09-82 spectrum) to 680cm^{-1} (for DC06-09-164 spectrum). The potential presence of another mineral phase inducing those shifts have been ruled out by the absence of other peaks over 100 – 1200 cm^{-1} range. The observe variation in the peak maximum could therefore result from different orientations of the magnetite minerals measured.

The Raman signatures of hematite (showing several peaks between 200 cm^{-1} and 400 cm^{-1}) and of fayalite (Fe-rich olivine) have been identified in one AMM (DC06-09-164) and are displayed in Figure 3-14.

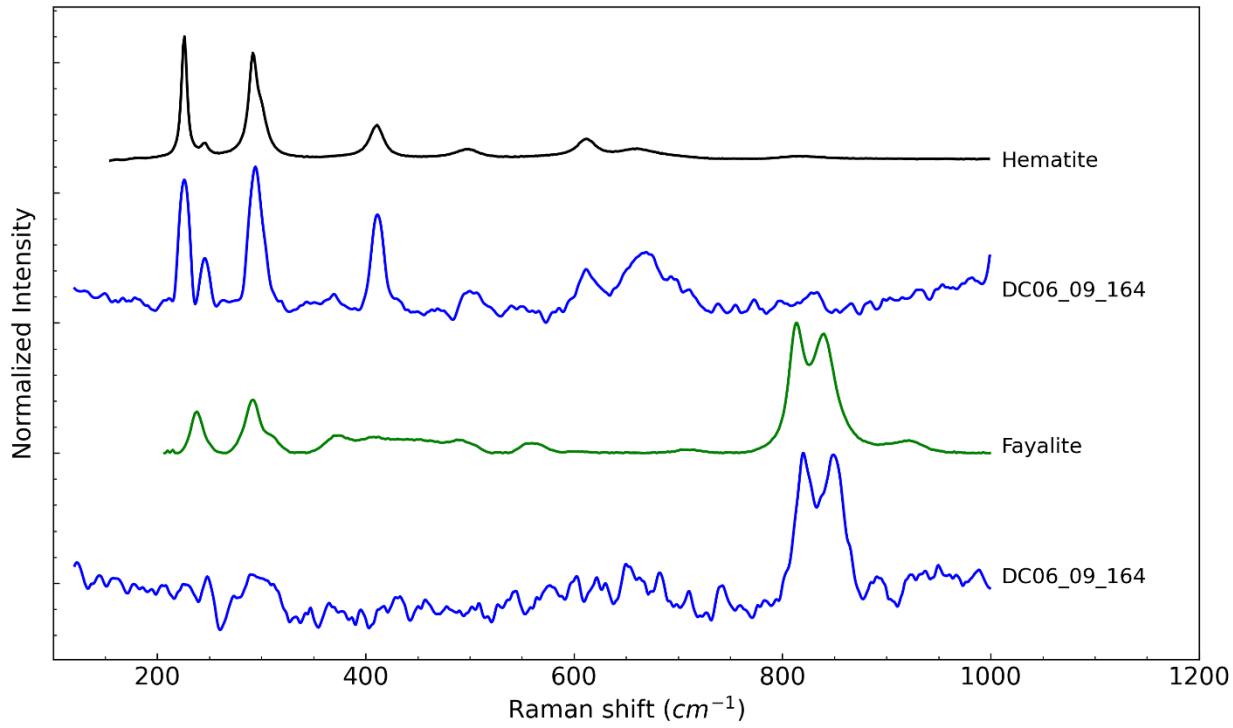

Figure 3-14: Punctual mineral phases corresponding to fayalite and hematite found in DC06-09-164. Pure mineral spectra are from RRUF (https://rruff.info/) and Lyon spectral database (www.geologie-lyon.fr/Raman).

From Raman analysis, the mineral diversity observed is less important than the one observed in the infrared spectrum of AMMs. Raman analysis mostly display oxides phases such as hematite and magnetite. Although a Fe-rich olivine related peak has been observed in DC06-0-164, silicate phases clearly visible in the mid and far IR spectra are not visible in the Raman spectra in the chondritic AMMs sample set, because the Raman spectral signatures are dominated by that of the polyaromatic organic carbon, at low laser power.

3.3. Conclusion

Raman and infrared characterization of the organic matter from AMMs further support the relationship between micrometeorites and cometary materials. The aliphatic content deduced from the 3.4 µm absorption bands of the infrared spectra is relatively constant from one AMM to another and seem independent from the hydration state of the micrometeorite. Area calculation with correction for integrated cross section give values around 2 for the calculated $N(CH_2)/N(CH_3)$ ratios. This values are consistent with solar system aliphatic content in general and corresponds to what have been measured in the organic matter of different extraterrestrial material. The feasibility of direct intensity calculations of CH_2 and CH_3 absorption has also been assess in this work. A factor of around 0.75 must be applied to the calculated CH_2/CH_3 intensity ratio in order to directly compared it with column density calculatios. The deconvolution of the Raman spectra of the different AMMs resulted in spectral parameters corresponding to pristine organic content. When plotted against different extraterrestrial materials, the spectral parameters from the Raman spectra of AMMs show a relatively good agreement with those of OM of primitive meteorites and cometary materials retrieved during the Stardust mission. Interestingly, the spectral parameters

of hydrated and non-hydrated AMMs displays some slight differences. The non-hydrated AMMs show less variability in the individual spectra measured than hydrated chondritic AMMs. They also exhibit lower value for D-band fwhm than hydrated AMMs. Overall, from Raman analysis, it seems than hydrated chondritic AMMs better represent the organic content of cometary material from Stardust. If the larger variations observed within the hydrated chondritic AMM is in fact the result of aqueous alteration, this raises the question of the possible role of aqueous alteration in the formation and/or alteration of cometary organic matter.

Chapter 4

4. The complex organic and minerals association in UCAMMs

Ultracarbonaceous Antarctica Micrometeorites (UCAMMs) are micrometeorites dominated by the organic matter which can account for up to 99% in volume of the particle. This organic matrix that extend over several microns embed small inorganic phases. Inorganic components of UCAMMs corresponds to both crystalline and amorphous phases with complex sub-micrometric mineralogical associations. The sample collection and extraction methods for micrometeorites (including UCAMMs) are described in chapter 2 as well as the description of the data processing method used (for all four methods presented in this chapter). UCAMMs presented in this work have been collected during the 2006 (DC06), 2016 (DC16) and 2019 (DC19) expeditions in Antarctica. A general overview of the UCAMMs characteristics is summarized in chapter 1.

In this section, the characterization of the organic content of UCAMMs will be described using FTIR, Raman and Scanning Transmission X-ray Microscopy coupled with X-ay Absorption Near-Edge Structure (STXM-XANES). The second part will focus on the characterization of inorganic content of eight different UCAMMs using FTIR and more spatially resolved STEM analysis.

The mineralogical and organic characterizations through STEM and STXM microscopies presented in this work will be published in an article: *STXM-XANES and TEM analysis of UltraCarbonaceous Antarctic MicroMeteorites (UCAMMs).* B. Guérin, C. Engrand, C. Le Guillou, H. Leroux, E. Dartois, J. Duprat, S. Bernard, K. Benzerara, L. Delauche, D. Troadec., Geochimica Cosmochimica Acta.

4.1. UCAMMs samples overview

Data presented in this chapter result from different analytical techniques on 10 different UCAMMs: 2 UCAMMs were characterized by IR and Raman, 8 UCAMMs were characterized by STXM-XANES and STEM (their IR and Raman characteristics have been previously published in Dartois et al. (2018)).

The infrared and Raman measurements of the two UCAMMs DC16-07-98 and DC19-GL-86 (Figure 4-1 and Table 4-1) have been performed at the SOLEIL synchrotron.

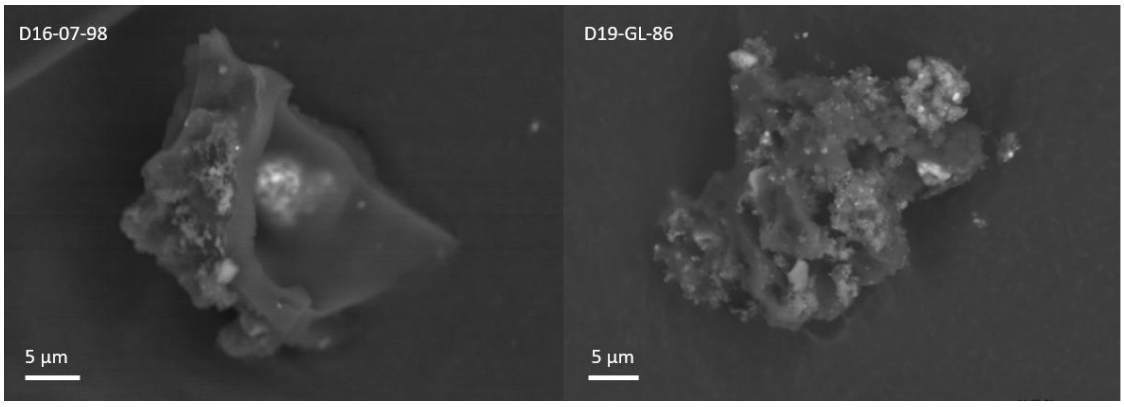

Figure 4-1: Backscattered electron images of fragments of the two Ultracarbonaceous Antarctic Micrometeorites (UCAMMs) DC16-07-98 and DC19-GL-86. Complementary fragments of these two UCAMMs were analyzed with FTIR and Raman microscopies at the SOLEIL synchrotron.

The STEM and STXM-XANES analysis of the eight other UCAMMs (Table 4-1) required the extraction of a FIB section from the fragments prior to the analysis. The sample preparation process as

well as data processing methods are described in Chapter 2. The fragments of eight UCAMMs (displayed in Figure 4-2 and summarized in Table 4-1) have been analyzed with both TEM and STXM-XANES allowing the characterization of both their organic and inorganic content at a better spatial resolution than for FTIR and Raman analysis, which can go down to tens of nanometers. The region analyzed with STEM and STXM-XANES in FIB sections are summarized in Figure 4-3.

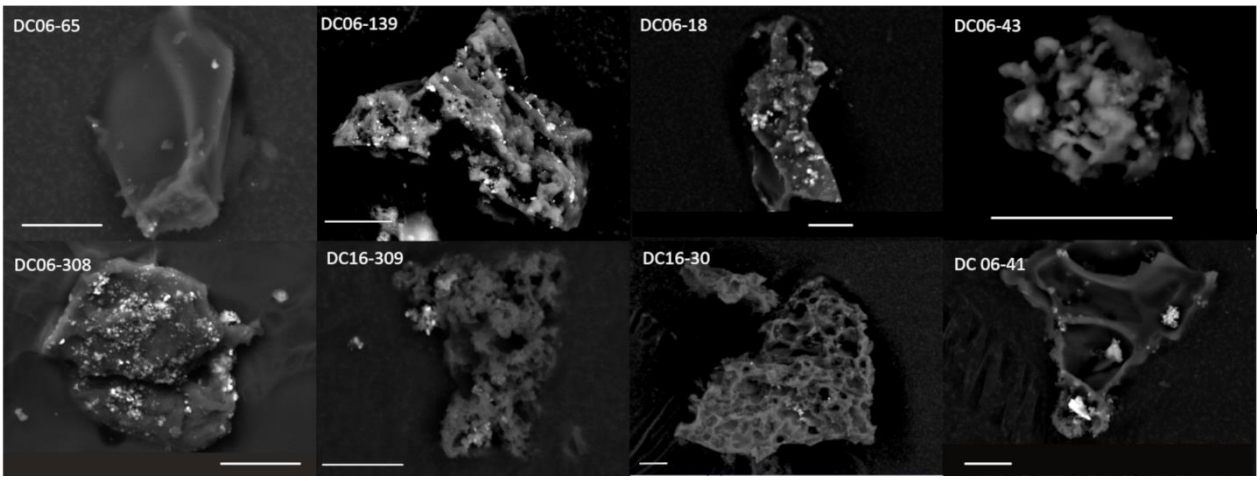

Figure 4-2: Back-scattered electron images of fragments of Ultracarbonaceous Antarctic Micrometeorites used for the analyses with STXM-XANES and STEM. Scale bar are 10 microns.

Table 4-1: List of the UCAMMs analyzed, with corresponding sizes of the original micrometeorites and performed analytical methods.

UCAMMs	Full name	Initial size (µm)	Analytical methods
DC16-98	DC16_07_98	50x80	Mid and far IR, Raman
DC19-86	DC18_GL_86		Mid and far IR, Raman
DC06-308	DC06_11_308	65x91	STEM, STXM-XANES
DC06-41	DC06_07_41	80x200	STEM, STXM-XANES
DC16-30	DC16_11_30	150x150	STEM, STXM-XANES
DC16-309	DC16_14_309	60x70	STEM, STXM-XANES
DC06-139	DC06_04_139	50x90	STEM, STXM-XANES
DC06-43	DC06_04_43	24x28	STEM, STXM-XANES
DC06-18	DC06_07_18	87x53	STEM, STXM-XANES
DC06-65	DC06_05_65	44x33	STEM, STXM-XANES

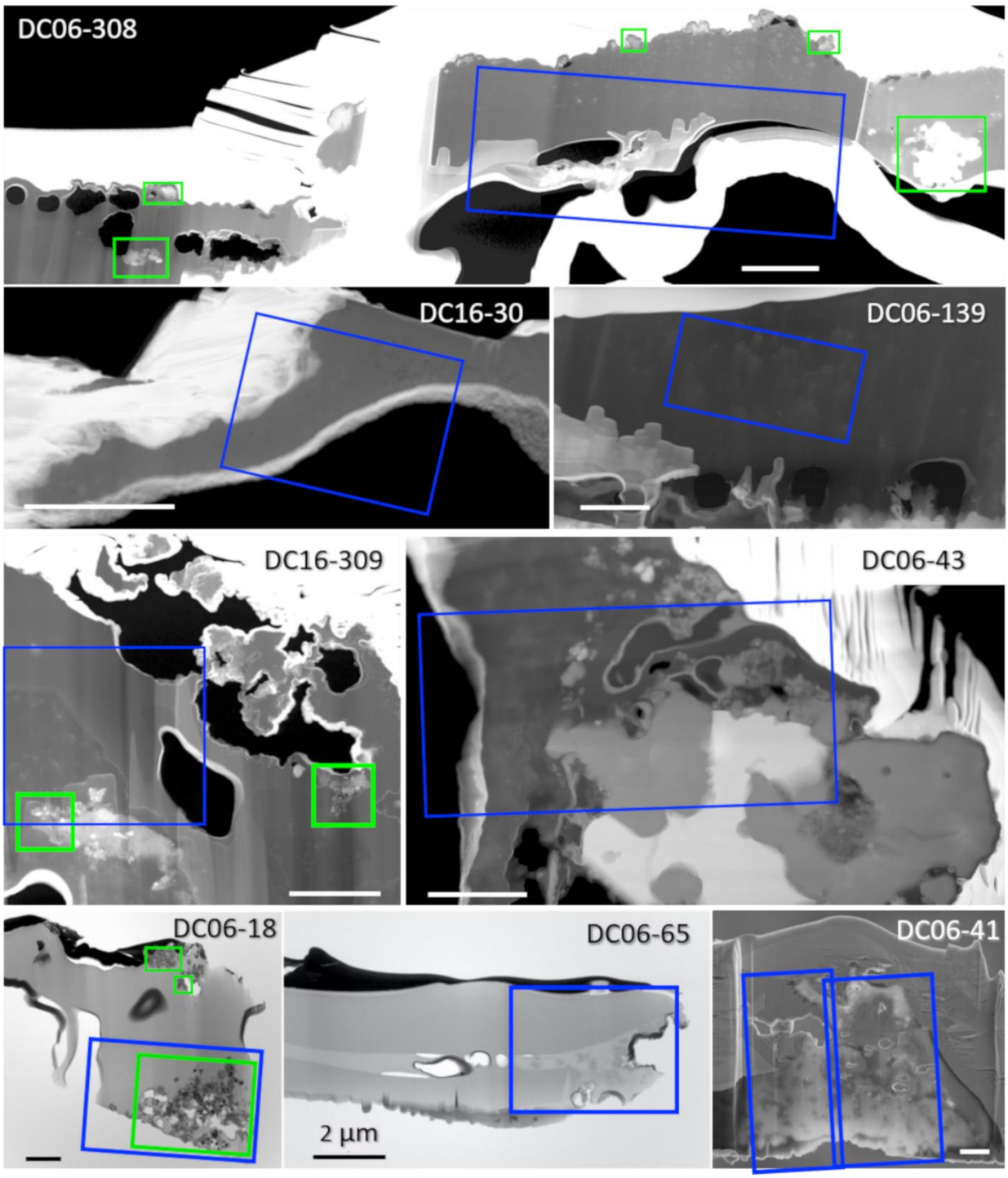

Figure 4-3: Electron microscope images of the eight UCAMM FIB sections analyzed with STEM and STXM-XANES: STEM High-angle annular dark field (HAADF) images for DC06-308, DC16-30, DC06-139, DC16-309, DC06-43); Bright field STEM images for DC06-18 and DC06-65, SEM image of DC06-41 at 5 kV (the FIB section was lost before STEM) . The platinum layer deposited on top of the sample during the FIB process appears in white in the HAADF images, in black in the bright field STEM images, and in smooth gray in the SEM image. The blue boxes show the locations of the STXM-XANES maps shown in Figure 4-9. The green boxes show the locations of mineralogy characterizations by STEM/EDX presented in this work. Scale bar is 2 µm.

4.2. The organic content of UCAMMs: FTIR, Raman and SXTM-XANES analysis

4.2.1. FTIR analysis

Mid and far infrared along with Raman measurements have been realized on two recently identified UCAMMs, DC16-07-98 and DC19-GL-86. Data collection and processing followed the protocol described in Chapter 2. The merged far and mid infrared spectra of the two UCAMMs are shown in Figure 4-4.

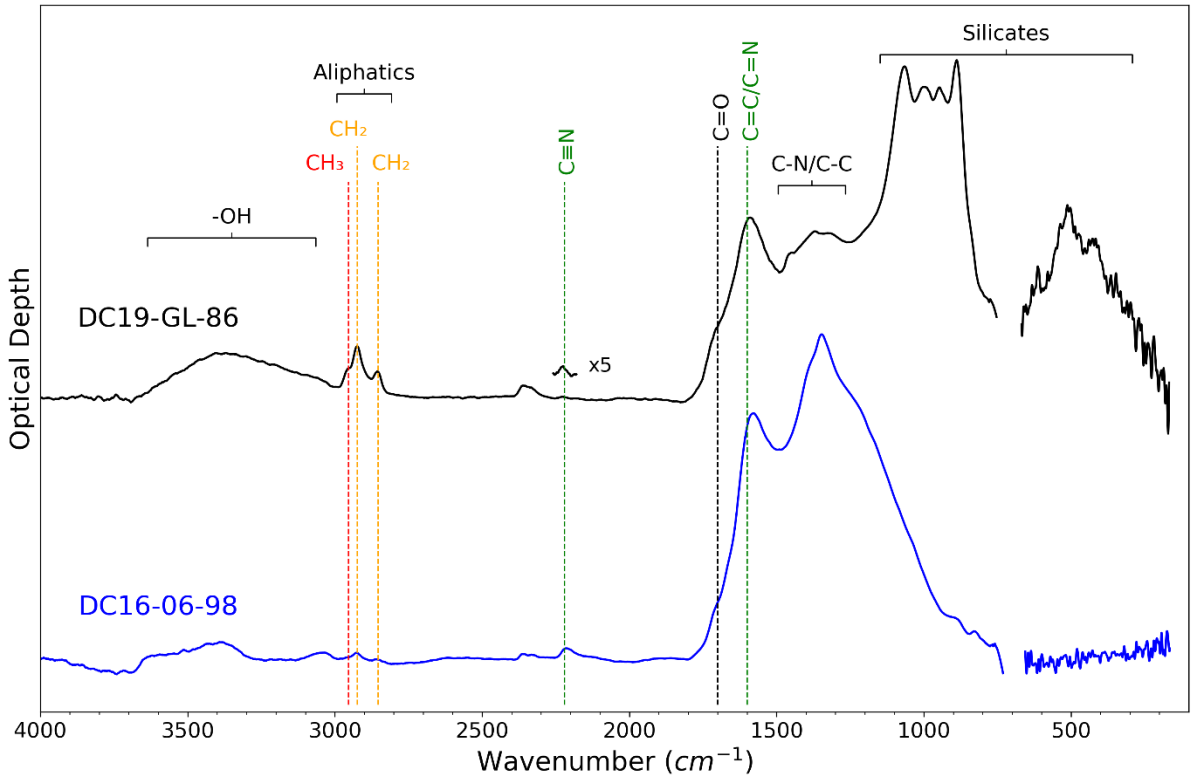

Figure 4-4: Merged far and mid-infrared spectra after baseline correction of 2 UCAMMs from the Concordia collection collected during Antarctic expeditions in 2016 (DC16) and 2019 (DC19).

The merged mid and far-infrared spectra of the two analyzed UCAMMs display noticeable differences in their organic absorption bands. DC16-98 (blue spectrum in Figure 4-4) displays its largest absorption peaks around 1230 cm^{-1} to 1500 cm^{-1}. Several peaks overlap in this region but the two mains absorption can be attributed to C-N/C-C vibration modes, which comes in the form of a broad peak over the 1100 cm^{-1} to 1400 cm^{-1} range. The second observed peak toward increasing wavenumber can be attributed mainly to aromatic C=C and C=N. This peak is more intense than the C-N/C-C absorption for DC19-86. A slight shoulder is also visible for both spectra around 1710-1720 cm^{-1} and corresponds to C=O contribution. The nitrile absorption peak at 2220 cm^{-1} (C≡N) is also detected in both UCAMMs, confirming, in addition to the C=N and C-N, their high nitrogen content. The nitrile absorption in DC19-86 has been zoomed on for better visualization (x5). Aliphatic absorptions on the 2850cm^{-1} – 3000cm^{-1} range are visible for both UCAMMs although DC19-86 presents a stronger signature. Overall the organic related absorptions observed in both UCAMMs are consistent with previous infrared analysis of UCAMMs (Dartois et al., 2013; Dartois et al., 2018). Aliphatic absorptions are usually very weak in UCAMMs IR spectra and have not be characterized yet (Dartois et al., 2013; Dartois et al., 2018). The

aliphatic absorption peaks for DC19-86 are however strong enough to quantify the CH2/CH3 ratio using the same procedure applied on AMMs as described in Chapters 2 and 3 and shown in Figure 4-5. This was not possible for DC16-98 as the aliphatic signature is not intense enough.

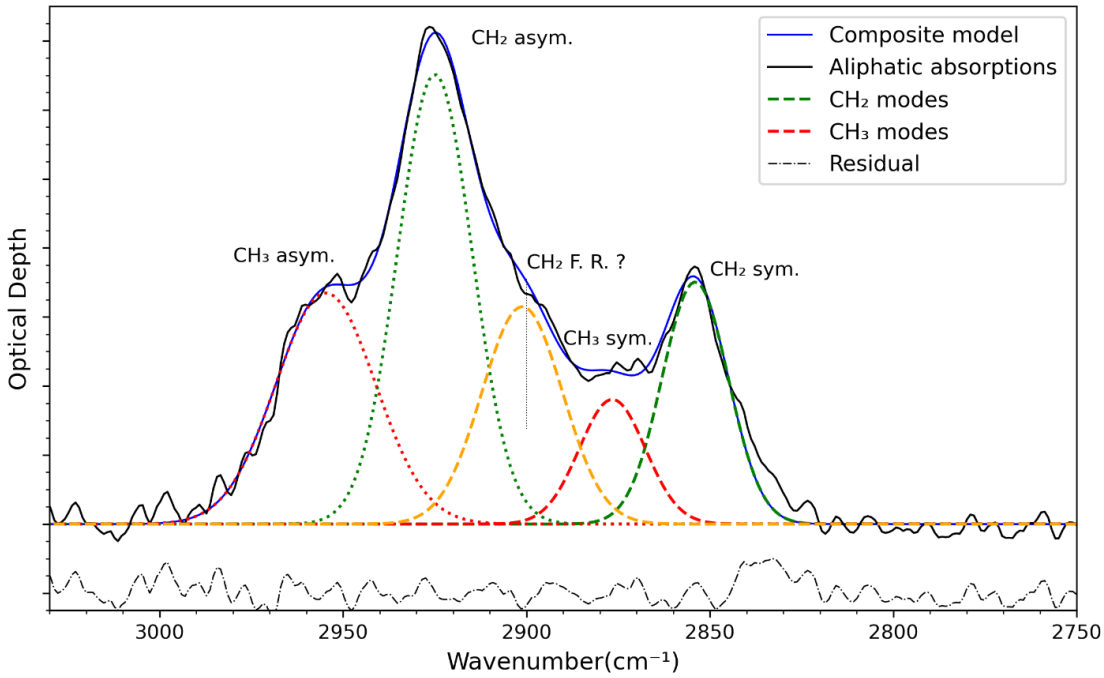

Figure 4-5: Composite Gaussian fit applied to the aliphatic absorption peaks of DC19-86. The method used is more thoroughly described in Chapter 2.

The Gaussian area calculations for DC19-86 gave results similar to what was obtained for non-hydrated and hydrated chondritic AMMs (Chapter 3). CH_2/CH_3 peak maximum ratio calculation gives a ratio of 1.97. The calculation through Gaussian modeling and area calculation gives column density ratio $N(CH_2)/N(CH_3)$ of 1.57, taking into account the integrated cross section absorption of CH_3 and CH_2. Those values are similar to the ones obtained for AMMs with the same methods.

4.2.2. Raman analysis

Figure 4-6 displays the averaged Raman spectra of the two UCAMMs over the area covered by the FTIR measurements. As expected for carbon-rich samples such as UCAMMs, the D and G bands of polyaromatic carbon are by far the dominant features in all the UCAMMs' Raman spectra. Both averaged spectra also display a small peak around 2220 cm^{-1}, corresponding to nitrile absorption (C≡N), similarly to what is observed in the infrared spectra. The same fitting procedure applied to AMMs and described in Chapter 2 was applied to the D and G bands of polyaromatic carbon in the UCAMMs' spectra. Results are summarized in Table 4-2 and Figure 4-7.

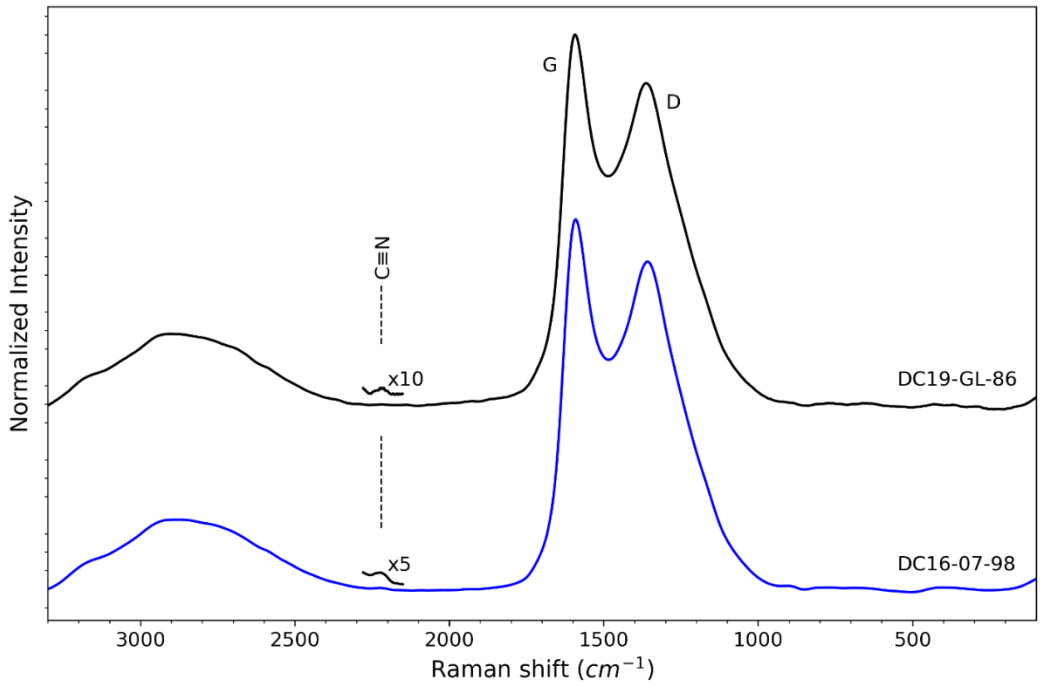

Figure 4-6: Average Raman spectrum of UCAMMs DC19-86 and DC16-98.. A zoom over the nitrile absorption range is shown as small absorption peaks were visible in both UCAMMs.

Table 4-2: Spectral parameters of the averaged spectra of the two UCAMMs analyzed with Raman microscopy obtained through the composite model.

UCAMMs	Number of spectra	I_D/I_G	ω_D (cm^{-1})	ω_G (cm^{-1})	FWHM-D (cm^{-1})	FWHM-G (cm^{-1})
DC16-06-98	35	0.95	1348.5	1604.3	268.2	114.6
DC19-GL-86	88	0.94	1351.8	1604.7	276.3	111.5

Both UCAMMs display I_D/I_G intensity close to unity, consistently with previous Raman measurement on UCAMMs, pointing out the disordered polyaromatic network in the OM of UCAMMs. The FWHM of D band for UCAMM DC19-86 and CD16-98 have values of 276.3 and 268.2 respectively. Values >250 cm^{-1} for D-band FWHM are associated with primitive meteorites. Spectral parameters of Stardust samples and UCAMMs lies in the upper part of both plots of Figure 4-8, pointing out the similarities between the organic content of those two samples. The G-band FWHM for UCAMMs lies at the top of the G-band FWHM vs D-band FWMH plot, with widths larger than for most meteorites and overlap with the values obtained for Stardust samples (Rotundi et al., 2008) and some IOM from the most primitive meteorites. Wider D-bands indicate a more pristine organic material for UCAMMs than for most meteorites and further emphasize the relationship between cometary particles and UCAMMs. The positions of the G-band are however located at higher values for both UCAMMs than for Stardust and most meteorites (1604 cm^{-1} for UCAMMs, around 1590 cm^{-1} for Stardust and pristine meteorites). This seems inconsistent with overall results as G-band position is thought to shift toward higher values with increasing thermal processing of the organic content..

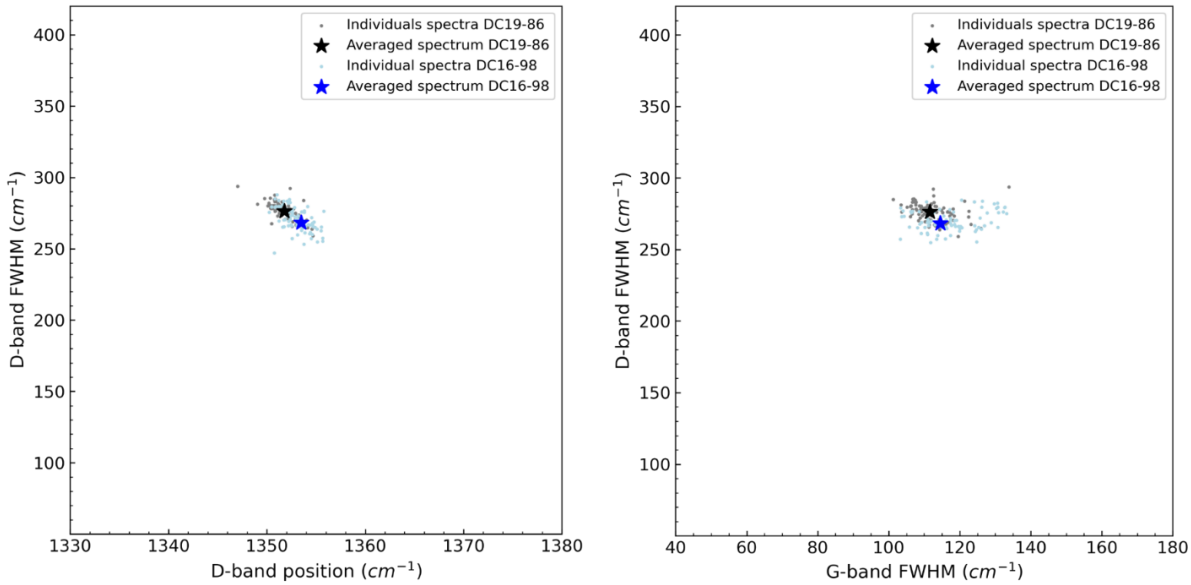

Figure 4-7: Raman D band full width at half maximum (FWHM) versus position (left) and G band FWHM (right) diagrams.

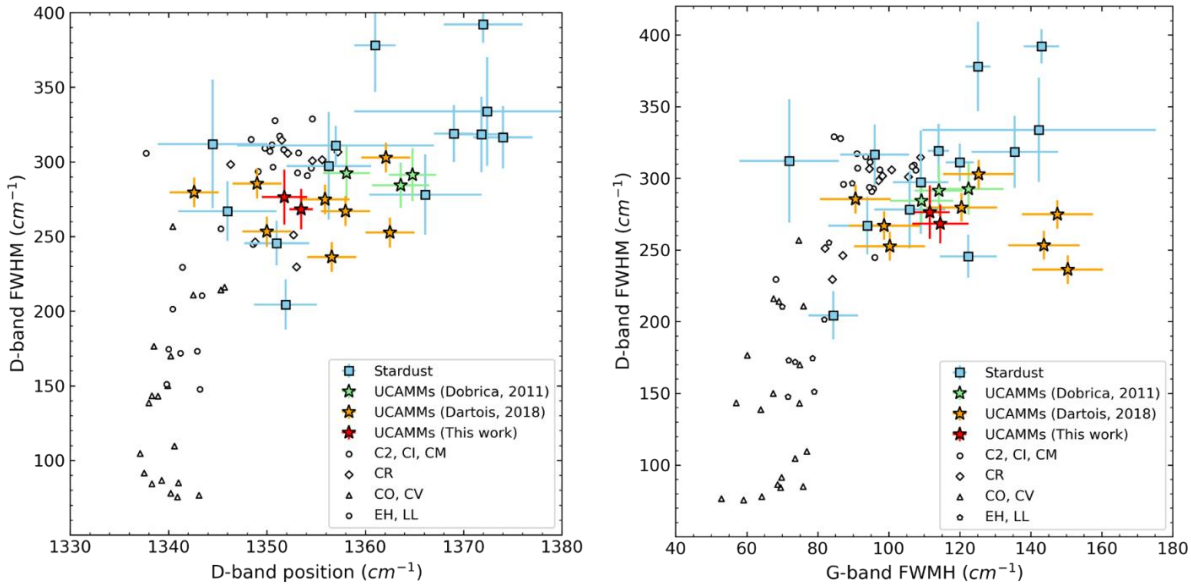

Figure 4-8: Figure adapted from Dartois et al. (2018) displaying the FWHM of D-band versus D-band position (left) and FWHM of G band (right) for several extraterrestrial samples. The fitted trend on the left plot represents the organic matter primitivity: extraterrestrial organic matter with D-band width > 250 cm^{-1} are considered the most primitives. Data are from Busemann et al. (2007) (C2, CI and CM (circles), CO and CV (triangle), EH and LL (half circles)), Rotundi et al. (2008) (Wild 2, blue square), Dobrică et al. (2011) (UCAMMs, green star) and Dartois et al. (2018).

Overall, spectral parameters of the Raman spectra of UCAMMs are close to the one obtained for both Stardust samples and IDPs (Rotundi et al., 2008; Rotundi et al., 2007). These similarities further confirm the pristine nature of the organic matter of UCAMMs as well as their probable relationship with comets.

4.2.3. STXM-XANES

Analyses with STXM-XANES allow the characterization of the organic matter with a higher spatial resolution than FTIR and Raman analysis and can go down to tens of nanometers. The analytical conditions and data processing methods are described in Chapter 2. The STXM-XANES hyperspectral

maps were acquired at the C and N K-edges for the 8 UCAMMs listed in Table 4-1. Three main kinds of organic matter (OM) can be identified by their different carbon and nitrogen speciation in the eight UCAMMs analyzed in this work. In Figure 4-9, the 3 identified types of OM are represented in blue, green and red in false color images resulting from the deconvolution of hyperspectral images acquired at the carbon and nitrogen K-edges. Figure 4-10 and Figure 4-11 present the corresponding spectra at the carbon and nitrogen K-edges, respectively.

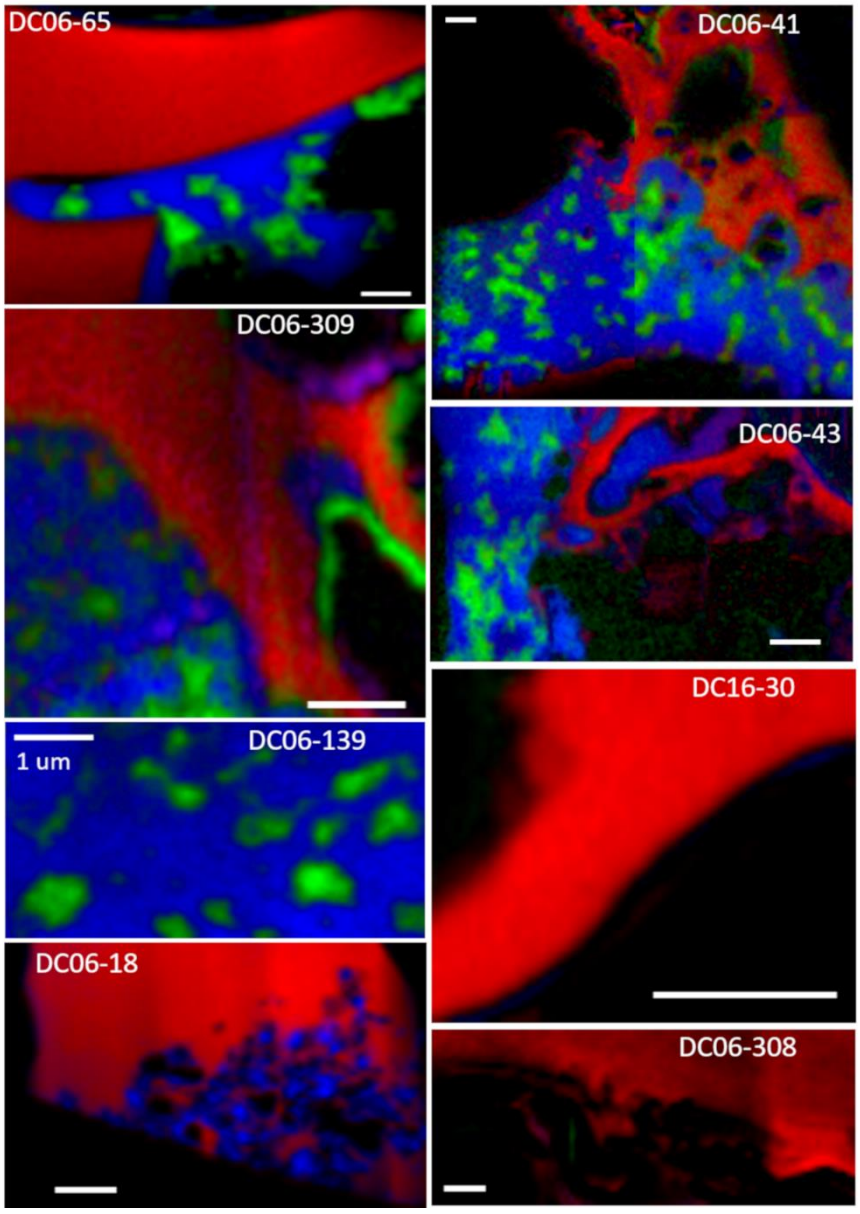

Figure 4-9: Carbon K-edge XANES spectra for the three different types of OMs observed in the eight UCAMMs, in maps corresponding to the areas shown as blue boxes in Figure 3: type I (in blue), type II (in green), and type III (in red). The absorption peak attributions were made according to De Gregorio et al. (2011).

The characteristic peaks of type I OM (in blue in Figure 4-9) are found at 284.8 eV (aromatic and olefinic groups, C=C), 286.4 eV (ketone and phenol, C=O) and 288.4 eV (carboxyl, O=C-O) (see Figure 4-10). Type II OM (in green in Figure 4-9) displays functional groups similar to type I OM although the first peak is shifted to 285 eV, indicating a larger contribution of aromatic with respect to olefinic

carbon. The N/C atomic ratio calculated for type I and II OMs ranges between 0.01 and 0.05 (1σ=0.02) and is below detection limit in some cases. For type III OM, the main absorption peaks are located at 284.8 eV and 286.4 eV, corresponding to aromatic carbon and nitrile (N≡C), respectively. Note that in type III OM spectra, there is no drop around 285.8 eV, corresponding to the contribution of imine (C=N), as seen in Figure 4-11. The type III spectra also display a smaller peak at 284.4 eV (alkene, C=C) than for types I and II, and the spectra do not show dominant oxygen-related peaks, although a small C=O-related absorption could contribute to the observed continuum in the spectra. The carboxylic contribution is lower, as for type II OM. The atomic N/C atomic ratios for type III OM are higher than for type I and II OMs ($0.07 \pm 0.02 < N/C_{III} < 0.20 \pm 0.02$, with an outlier at $N/C_{III} = 0.03 \pm 0.02$ for DC16-30). Discrimination between nitrile and ketone absorption, both located at around 286.4 eV in the carbon K-edge spectrum, is based on the STXM-XANES spectrum at the nitrogen K-edge (370 eV - 449 eV). If a significant nitrile absorption peak is visible at the nitrogen edge, the 286.4 eV peak is attributed to nitrile. Type I and II OM in UCAMMs do not show significant nitrogen absorption, pointing toward N-content of these phases below the detection limit. For type III OM spectra, the main peaks are located at 398.8 eV and 399.8 eV and correspond to imine and nitrile absorptions (Figure 4-11). Another smaller peak can be observed at 401.5 and can be attributed to the amide group. The N/C atomic ratios of the different organic matter types and the presence (or not) of mineral phases in the FIB section of each UCAMMs are summarized in Table 4-3.

Table 4-3: N/C atomic ratios of the different types of organic matter in the analyzed UCAMMs (from STXM-XANES quantificaton) and brief description of the mineral content observed (or not) within their FIB sections

	N/C atomic ratio (STXM-XANES)			**Minerals in FIB sections (STEM analyses)**
UCAMM	OM I	OM II	OM III	
DC06-308	-	-	0.20	Isolated mineral patches
DC06-41	0.02	0.01	0.12	n.a. (FIB section damaged after STXM)
DC16-30	-	-	0.03	No minerals
DC16-309	0.01	<0.01	0.07	Isolated mineral patch (Silicate, FeS, Phyllosilicate-like)
DC06-139	0.03	0.02	-	No minerals
DC06-43	0.04	0.03	0.08	Large mineral assemblage (Silicate, FeS), GEMS-like inclusions
DC06-18	<0.01	-	0.11	fine-grained mineral assemblages (Silicate, FeS), GEMS-like inclusions
DC06-65	0.03	0.05	0.20	No minerals

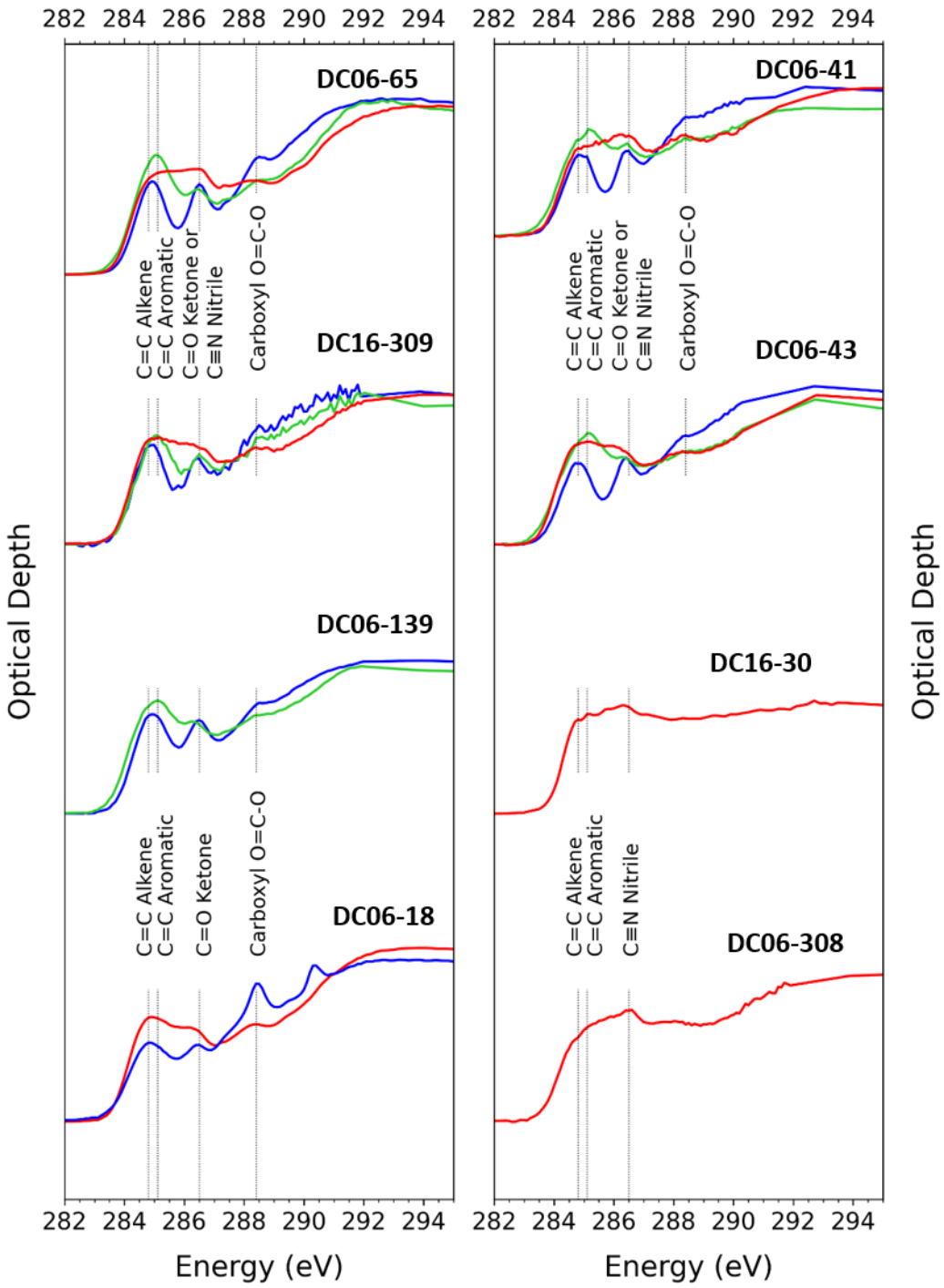

Figure 4-10: Carbon K-edge XANES spectra for the three different types of OMs observed in the eight UCAMMs, as illustrated in Figure 3: type I (in blue), type II (in green), and type III (in red). The absorption peak attributions were made according to (De Gregorio et al., 2011).

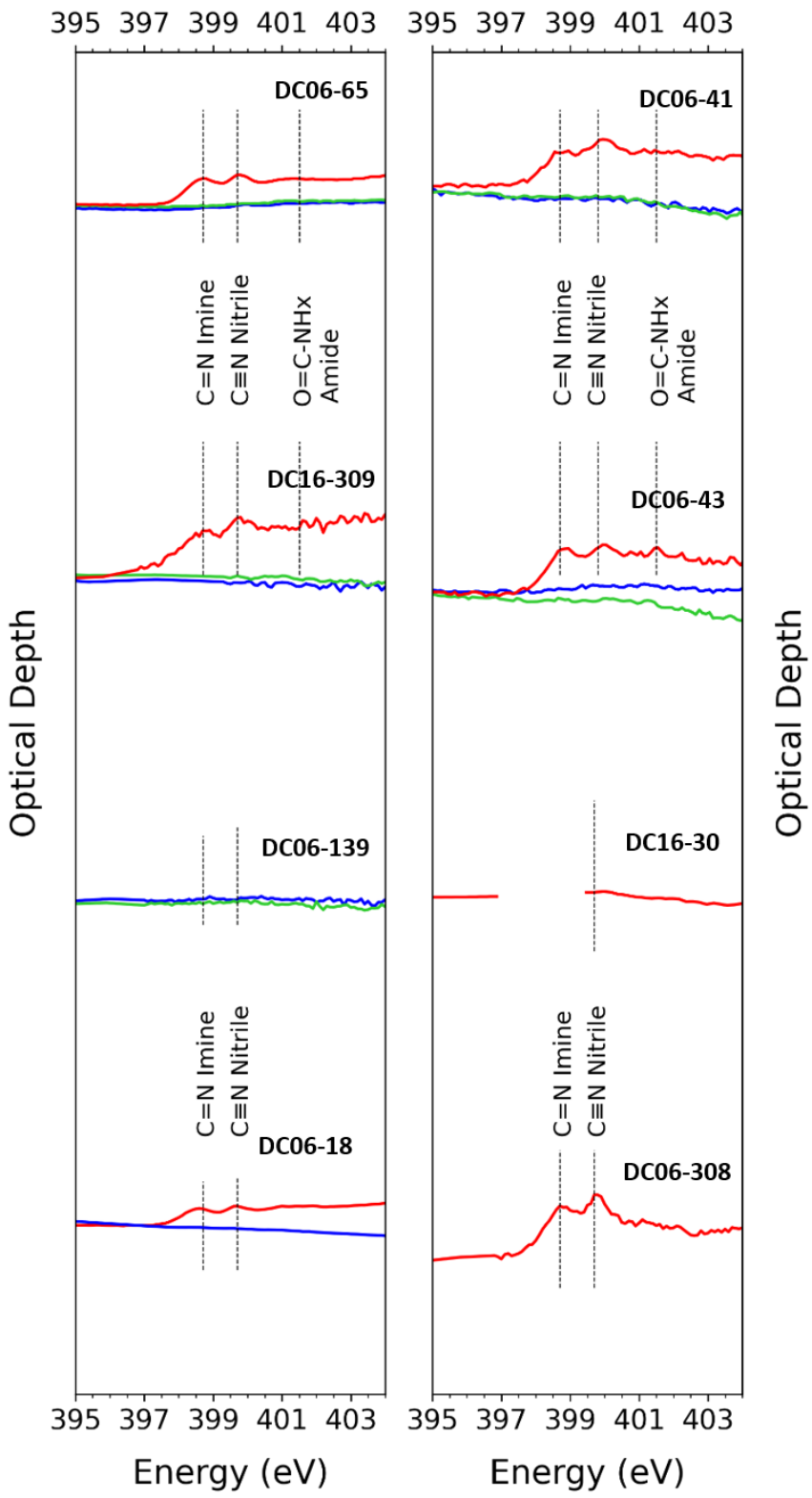

Figure 4-11: Nitrogen K-edge XANES spectra for the three different types of OMs observed in the eight UCAMMs, as illustrated in Figure 3: type I (in blue), type II (in green), and type III (in red). The absorption peak attributions were made according to (De Gregorio et al., 2011)

4.2.4. TEM imaging and EDX analysis of the organic matter

As the same FIB sections were used for both STXM-XANES and (S)TEM analysis, higher resolution images and EDX maps were acquired in the area analyzed by STXM-XANES, to characterize the fine structures and chemical heterogeneities at the nanometer scale. We present a combination of false color image with a detailed HAADF image of the three types of organic matter observed in the FIB section of UCAMM DC 16-309.

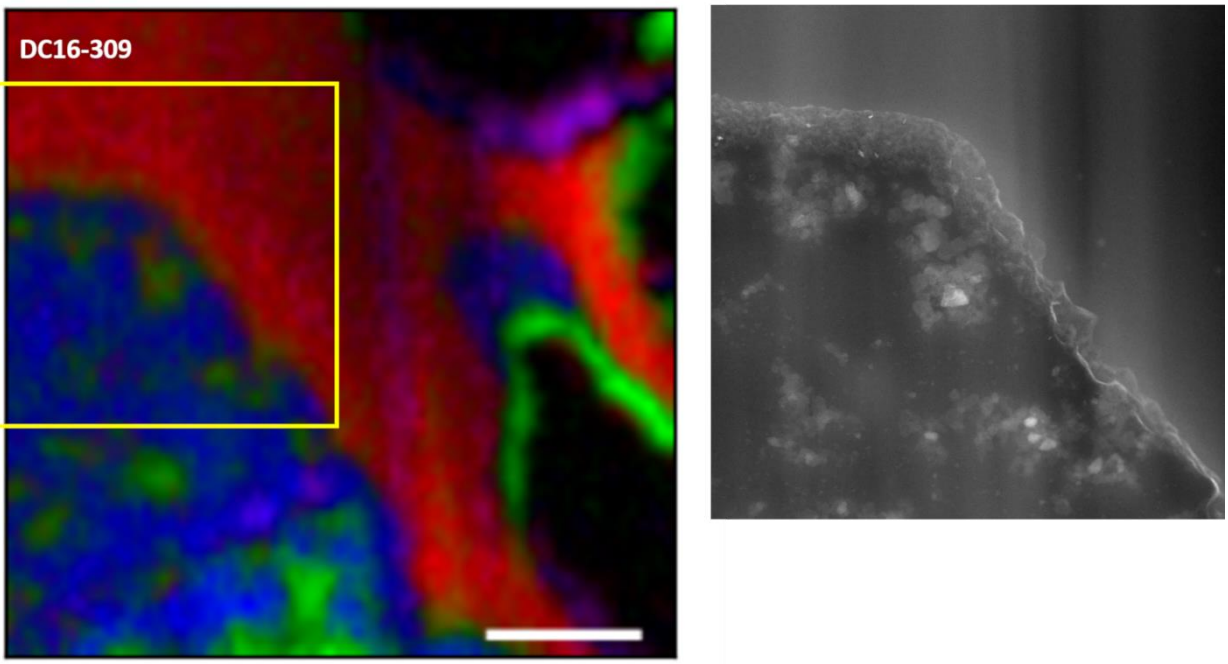

Figure 4-12: (left) False color STXM-XANES image obtained by the spectral deconvolution of hyperspectral maps acquired at the C and N K-edges for UCAMM DC16-309 (scalebar is 1 µm). The three type of organic matter are present in the image. The smooth area of OM on the top of the image corresponds to type III OM (in red) while the bottom left structure corresponds to type I (in blue) containing the dusty patches of type II OM (in green). (Right) detail HAADF image of the top left area analyzed by STXM-XANES in UCAMM DC16-309 (yellow square).

The three types of OM are not systematically found in all UCAMMs' FIB sections. STEM imaging of the organic matter in DC16-309 clearly shows that organic matter of types I, II and III observed in STXM-XANES have different textures (see Figure 4-12). Type I and II OMs are generally associated together in the form of sub-micrometric patches (“dusty patches”) of type II OM embedded in a type I OM (see DC06-41, DC16-309, DC06-139, DC06-43 and DC06-65 in Figure 4-9) (Charon et al., 2017 ; Engrand et al., 2015a). In contrast, type III OM always presents a smooth texture. The STEM image in Figure 4-13 reveals the presence of a foamy-like layer between the organic matters of types I and III (detailed HAADF image). From the EDX map, it appears that the ‘foamy-like’ phase contains small amount of Fe (in red, Figure 4-13 middle). The presence of iron does not correlate with either oxygen or sulfur in this phase. Areas resembling inorganic phases are also present in most of the dusty patches that represent type II OM. The EDX analysis of these inorganic phases indicates that they contain Na, S and a small amount of Si Figure 4-13. EDX spectrum extracted from the region containing these inorganic phases do not display a clear stoichiometry but these brighter phases could correspond to small NaS_2 minerals.

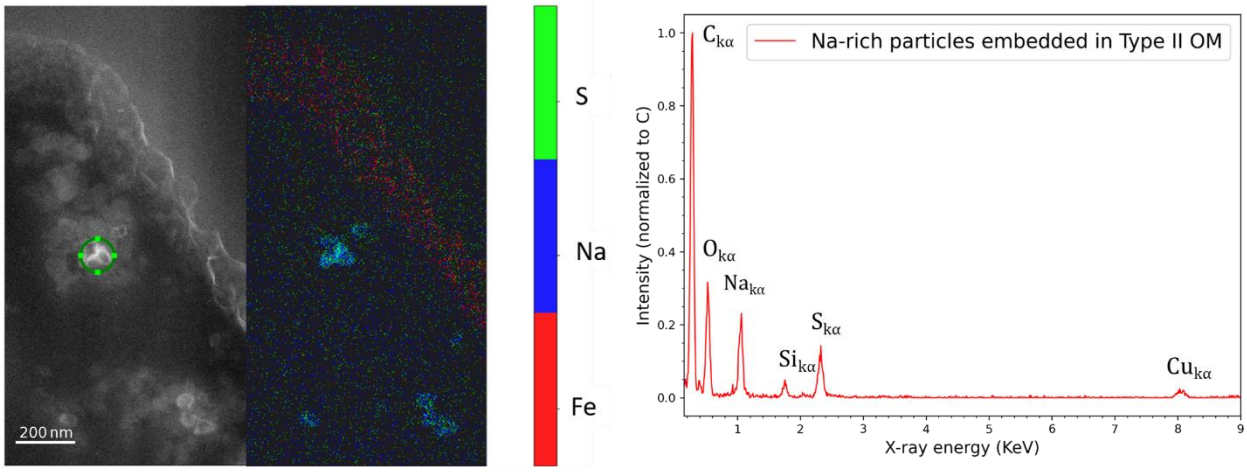

Figure 4-13: (A) HAADF images of the EDX map of the organic matter of UCAMM DC16-309.The green circle corresponds to the location of the spectrum displayed in (c). (B) Elemental map showing Fe (in red), S (in green) and Na (in blue) based on X-ray lines intensities. Each element is normalized to its maximum for better visualization. (C) EDX spectrum extracted from the green ROI of the HAADF image normalized to carbon intensity. The Cu signal is due to the grid substrate.

EDX spectra of the three types of OM have been acquired by selecting ROIs in the EDX hyperspectral maps, and are displayed in Figure 4-14. The spectra have been normalized to the maximum C intensity in each phase. The N-enrichment of the type III OM is visible in the spectrum in Figure 4-14, with a clear decrease of the N and O contents from type III to type I, and then to type II.

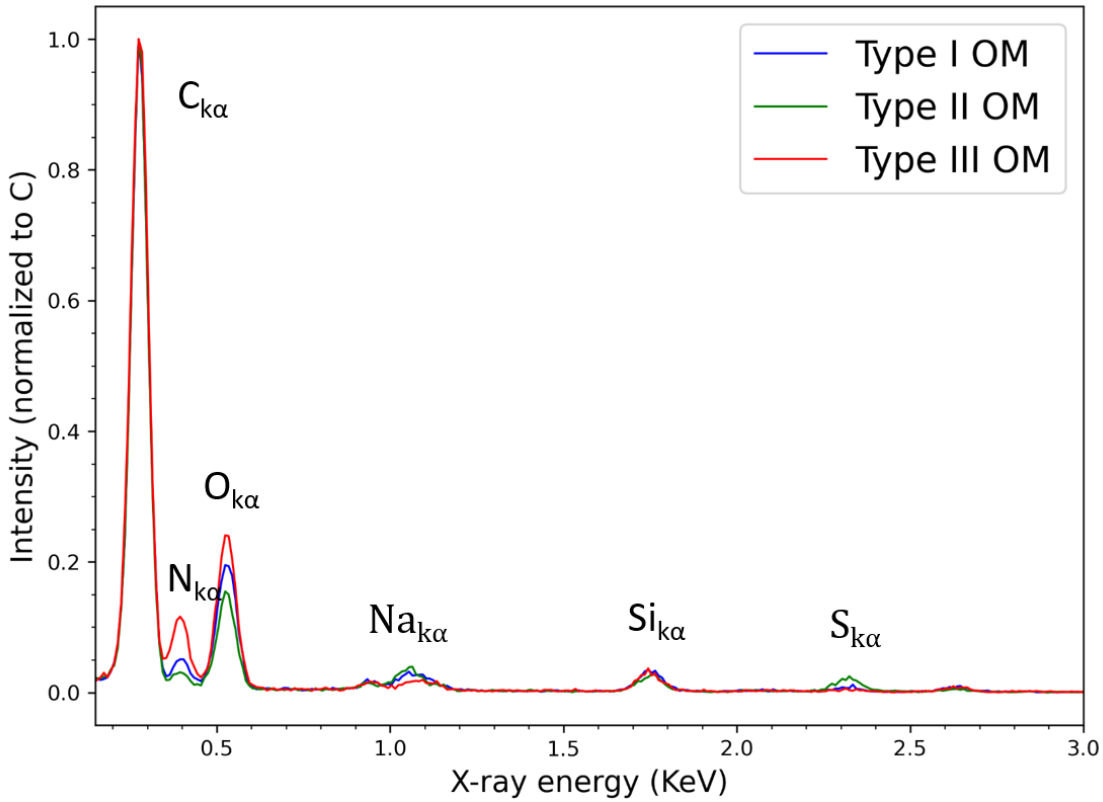

Figure 4-14: EDX spectra of the three types of organic matter in DC16-309. Each spectrum has been normalized to its maximum carbon intensity for easier comparison.

Gradients in composition around GEMS-like assemblages are observed in DC06-18 as illustrated in Figure 4-15, Na and N increase toward the mineral assemblages at the 50 nm level.

Organic matter appears to be found in small amounts inside the fine-grained inclusion shown in Figure 4-15 and exhibits a N/C atomic ratio that can reach a value up to 0.5.

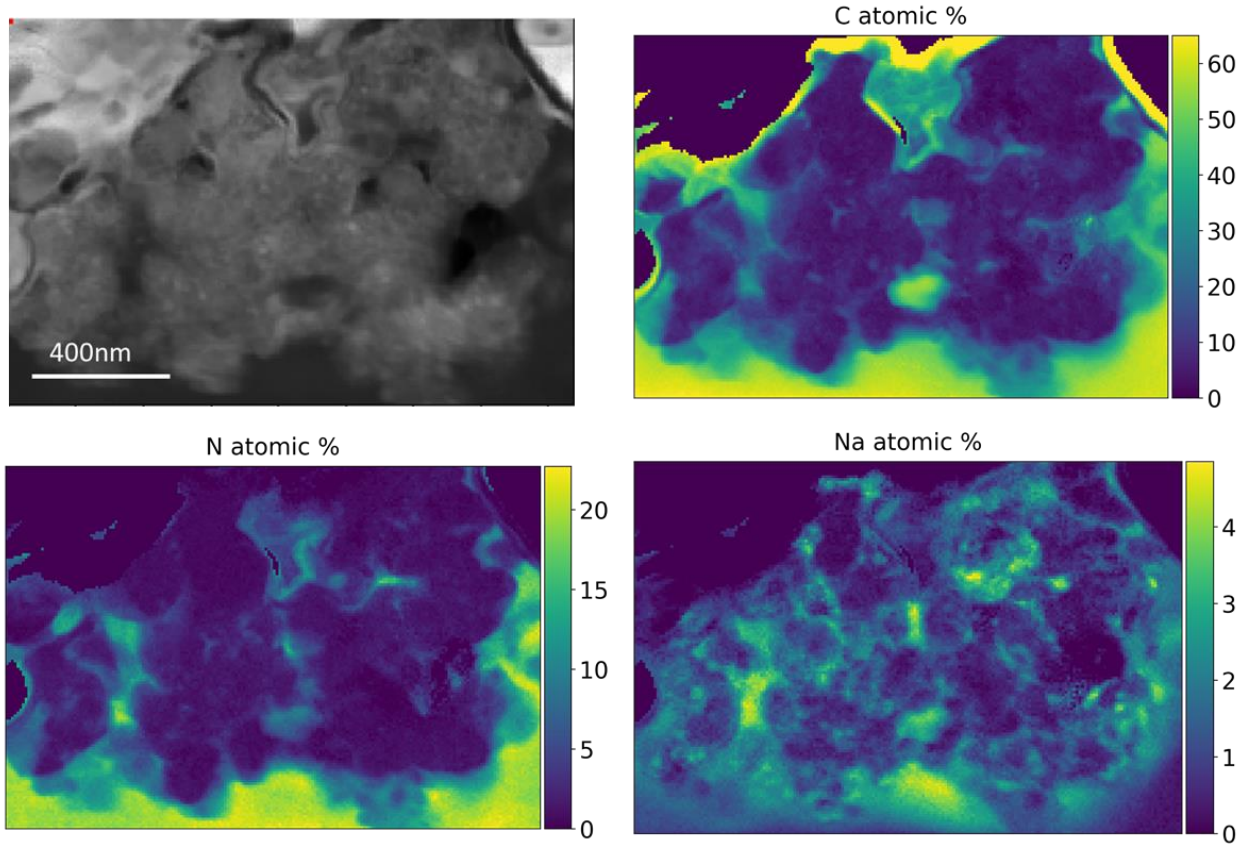

Figure 4-15: HAADF image and quantified EDX maps (at%) of a GEMS-like assemblage in UCAMM DC06-18, which is located at the top of the FIB section, probably close to the external surface of the UCAMM.

4.3. The inorganic content of UCAMMs: FTIR, Raman and STEM analysis

The inorganic content of UCAMM has been investigated with several analytical techniques. First, an overview of the inorganic content of the two UCAMMs analyzed with FTIR and Raman is presented. The STEM analysis allowed the characterization of the inorganic component at a high spatial resolution and the analysis of the several mineral assemblages in UCAMM DC06-308 and DC16-309 will be presented.

4.3.1. Inorganic signature in FTIR and Raman spectra of UCAMMs

The infrared spectra of UCAMM DC16-98 does not display any silicate-related absorptions over the 100 cm^{-1} – 1200cm^{-1} range showing non mineral contribution in this UCAMM fragment. The IR spectrum of UCAMM DC19-86 on the other hand displays several absorptions peaks in the silicate region. A zoom over the silicate absorption region in DC19-86 is displayed in Figure 4-16. The absorption in D19-86 can be explained by the presence of both Mg-rich pyroxene (Figure 4-16, in blue) or Mg-rich olivine (Figure 4-16, in green). The main absorption peaks related to pyroxene, and more specifically ortho-enstatite are located around 350 cm^{-1}, 530 cm^{-1}, 998 cm^{-1} and 1060 cm^{-1}. The peaks attributed to olivine are located around 294 cm^{-1}, 415 cm^{-1}, 505 cm^{-1}, 610 cm^{-1}, 888 cm^{-1} and 945 cm^{-1} and corresponds to forsterite absorptions. The identification of the peaks has been done based on Jaeger et al. (1998).

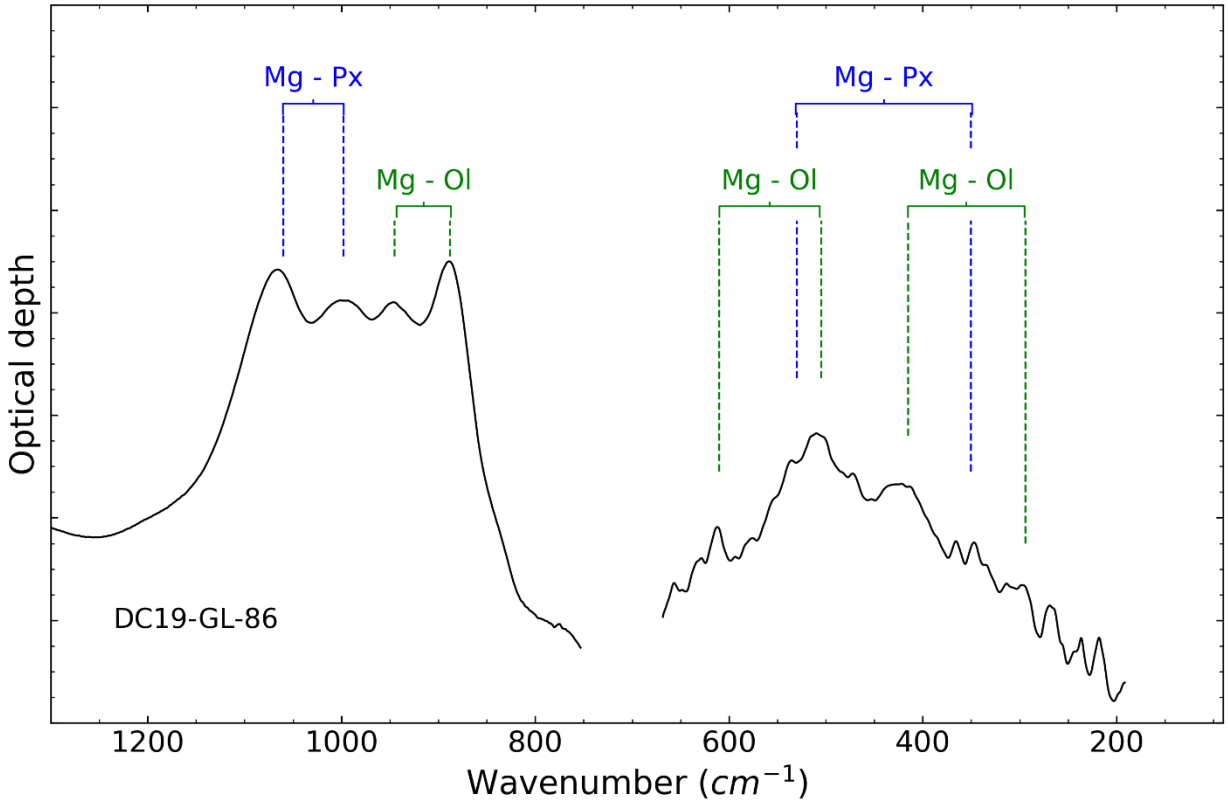

Figure 4-16: Zoom of the infrared spectrum over the 100 cm^{-1}- 1200 cm^{-1}absorption range for UCAMM DC19-86. The spectrum for DC16-98 is not displayed as it has no mineral-related absorption over the silicate range (see Figure 4-4).

4.3.2. STEM analysis of DC06-308 and DC16-309

(S)TEM analysis revealed that only four out of the eight FIB sections contain inorganic inclusions embedded in an abundant carbonaceous matter (DC06-308, DC06-43, DC16-309 and DC06-18; see Figure 4-3). The FIB sections of DC16-30, DC06-139 and DC06-65 do not contain any mineral phases, and we could not investigate the mineralogy of DC06-41 by TEM, as the FIB section was lost after STXM-XANES analysis. We focus hereafter on the description of inorganic phases of DC06-308 and DC16-309.

4.3.2.1. Mineralogy of DC06-308

DC06-308 revealed several mineral assemblages showed in Figure 4-18, Figure 4-20, Figure 4-21 and Figure 4-22. The locations of the different hyperspectral maps are shown in Figure 4-17. A peculiar attention was paid to the first mineral assemblage presented in Figure 4-18 as they displayed a more complex mineralogy than the other inorganic patches that presented more homogeneous textures and compositions.

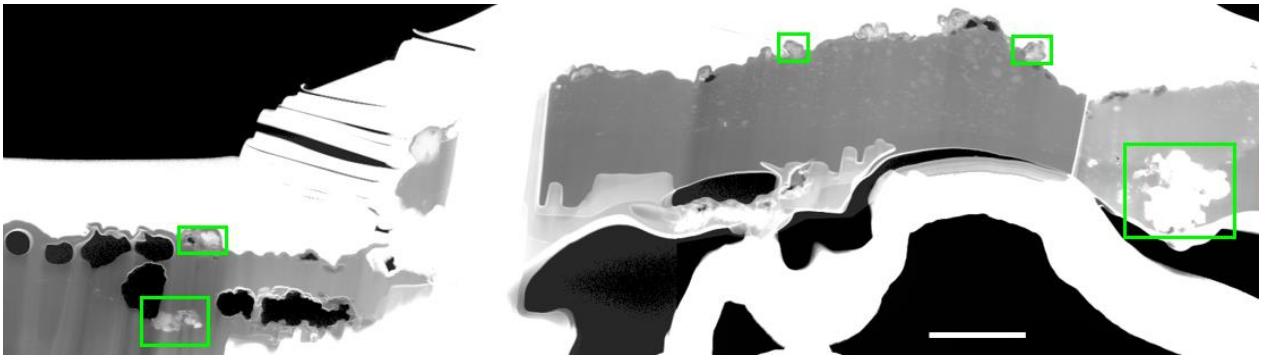

Figure 4-17: Location of the different EDX hyperspectral maps realized on DC06-308 and presenter in Figure 4-18, Figure 4-20, Figure 4-21 and Figure 4-22. Scale bar is 2 µm.

In the assemblages of Figure 4-18, the different phase maps produced by PCA indicate a fine grain texture, with several phases intimately mixed. The two assemblages display a Si-rich groundmass (quoted here as "Si-rich matrix") embedding Mg-rich olivines and Mg-rich low-Ca pyroxenes. A Ca-rich pyroxene has also been observed in one assemblage (Figure 4-18 A), and seems closely associated with a Fe-sulfide. Fe oxides are usually decorating the edge of the assemblage for most mineral phases, along with Fe-sulfides in some cases (Figure 4-18 B). Spatial heterogeneities can be present at a very small scale, down to a few nm.

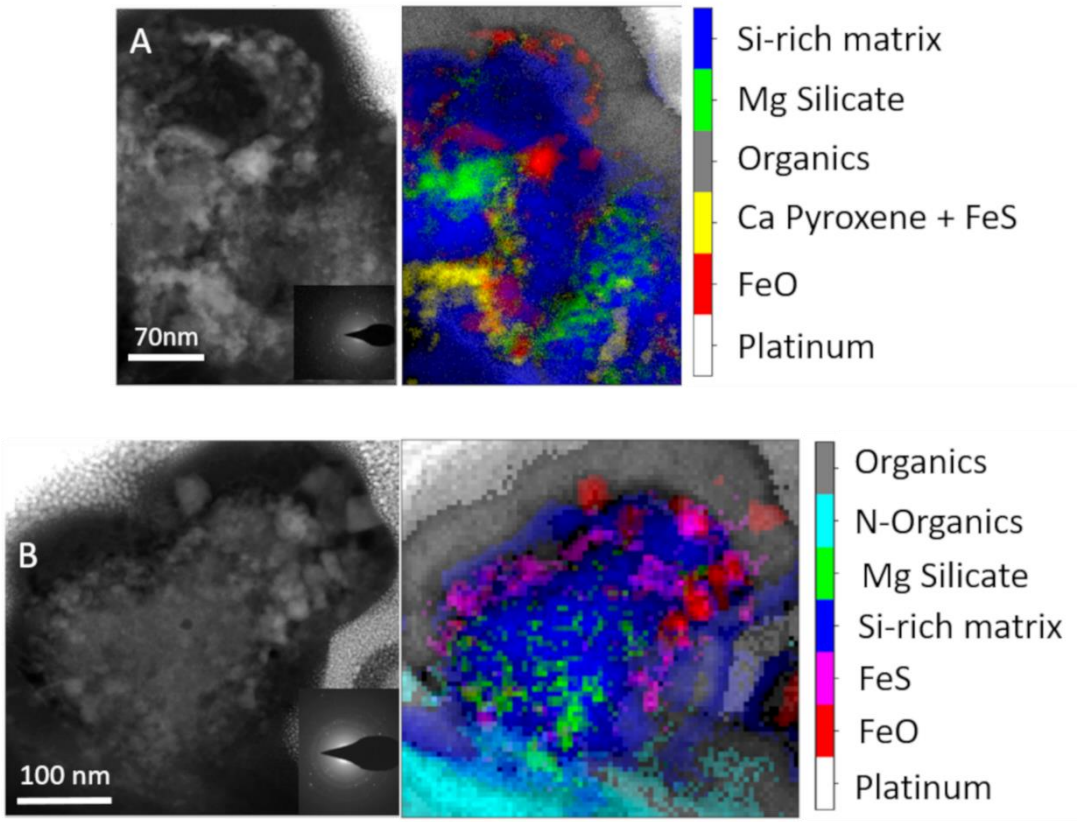

Figure 4-18: (A and B, left) High Angle Annular Dark Field (HAADF) image of 2 mineral assemblages in DC06-308 (A and B, right) False color images corresponding to the EDX maps of the different phases identified by Principal Component Analysis (PCA). The phases are ordered by decreasing number of counts in the respective spectra

Electron diffraction patterns (visible at bottom right of HAADF images of Figure 4-18 and in Figure 4-19) point out to both crystalline and amorphous components in the mineral assemblages. One

or two rings formed by diffraction of poorly crystalline material can be observed. The rings often contain diffractions spots indicating the presence of multiple small crystals with varied crystallographic orientations. Attribution of the different diffractions spots has been done based on the identified phases in the EDX hyperspectral maps. A summary of the different diffraction distances observed as well as their identification is done in Figure 4-19.

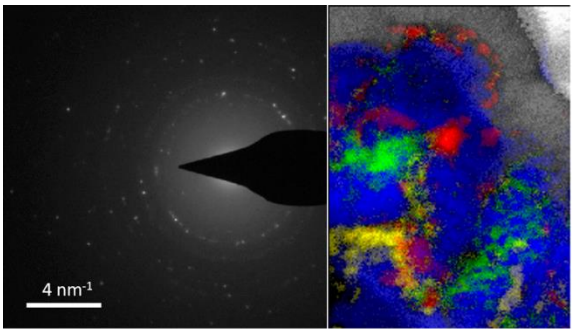

D-spacing (Å)	Potential phases
1.12	Magnetite/Troilite/Pyrrhotite
1.32	Pyrrhotite/Troilite
1.40	Enstatite/Augite/Pyrrhotite/Troilite/Magnetite
1.52	Enstatite
1.7	Magnetite/Troilite/Pyrrhotite
1.84	Hematite
2.09	Pyrrhotite/Troilite/Magnetite
2.61	Enstatite/Augite/Pyrrhotite/Troilite/Magnetite

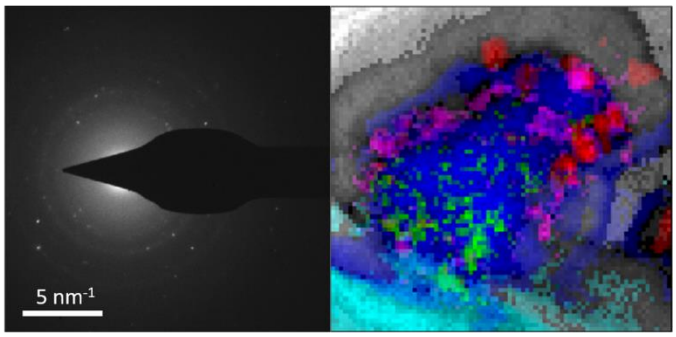

D-spacing (Å)	Potential phases
1.09	Magnetite/Pyrrhotite/Troilite
1.3	Pyrrhotite/Troilite/Magnetite
1.49	Enstatite/Magnetite
1.76	Troilite/Pyrrhotite/Magnetite
2.10	Pyrrhotite/Troilite
2.61	Pyrrhotite/Troilite/Enstatite

Figure 4-19: Diffraction pattern observed in two different complex mineral assemblage of DC06-308. The attribution of the different D-spacing was realized based on the phases observed in EDX hyperspectral maps.

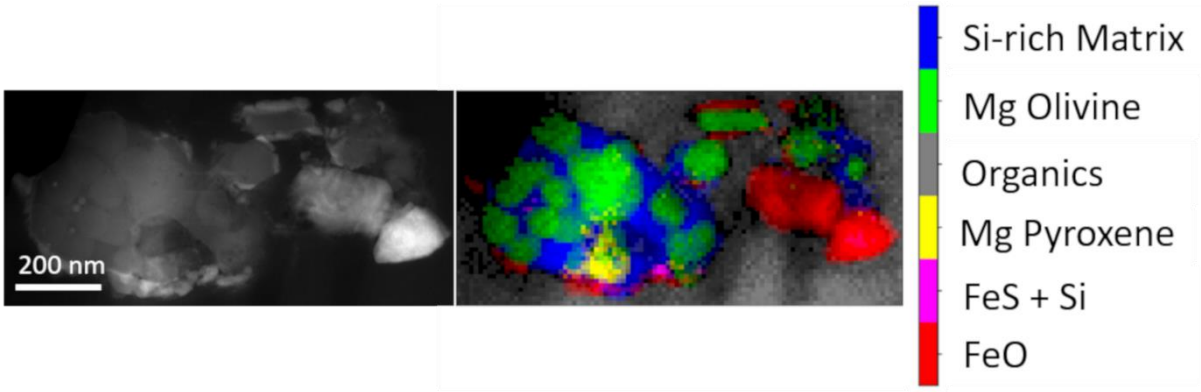

Figure 4-20: HAADF image (right) and EDX phase distribution (left, false color) of a crystalline assemblage in DC06-308 dominated by Mg-rich olivine grains cemented by an amorphous silica-rich matrix, with Fe oxides and Fe sulfides at the border of the object.

The mineral assemblage in Figure 4-20 shows a hypocrystalline-like texture consisting of Mg-olivines cemented by a Si-rich matrix. Some thin Fe-oxide phases are visible on the edge of the assemblage as well as a larger Fe-oxide crystal next to the main assemblage. Two other simple assemblage have been observed and are displayed in Figure 4-21 and Figure 4-22. The first ones, showed in Figure 4-21, consist in large Mg-rich silicate displaying rather large Fe-sulfides at their surface. The silicate do not display any compositional heterogeneity as observed in the assemblages showed in Figure 4-18. Figure 4-22 displays a large Fe-sulfides which shows oxidation signs on its edge

with the presence of a peripheral Fe oxide. This could result from surface oxidation of the sulfur during atmospheric entry.

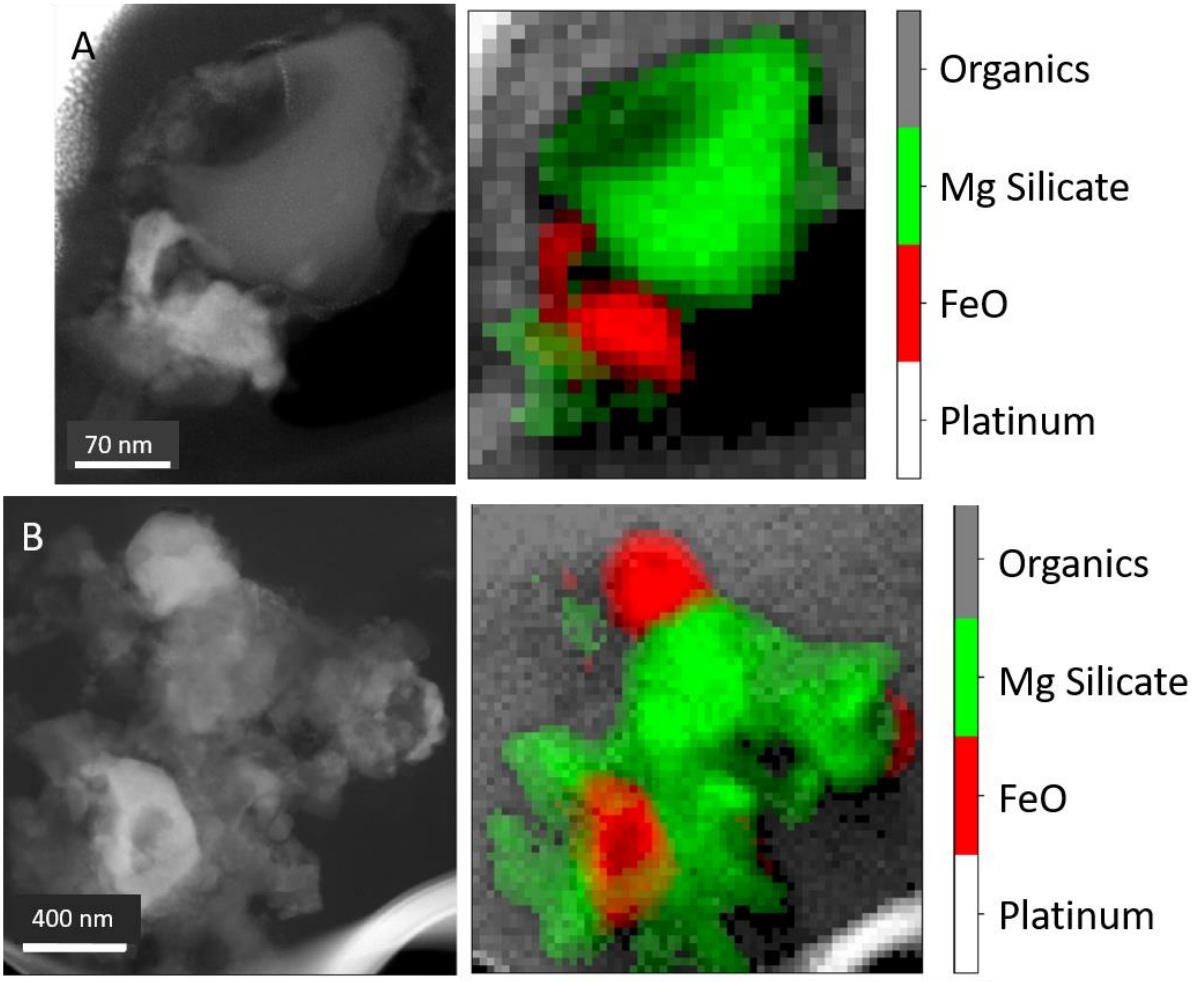

Figure 4-21: (A and B, left) High Angle Annular Dark Field (HAADF) image of 2 simple mineral assemblages in DC06-308 (A and B, right) False color images corresponding to the EDX maps of the different phases identified by Principal Component Analysis (PCA). The phases are ordered by decreasing number of counts in the respective spectra

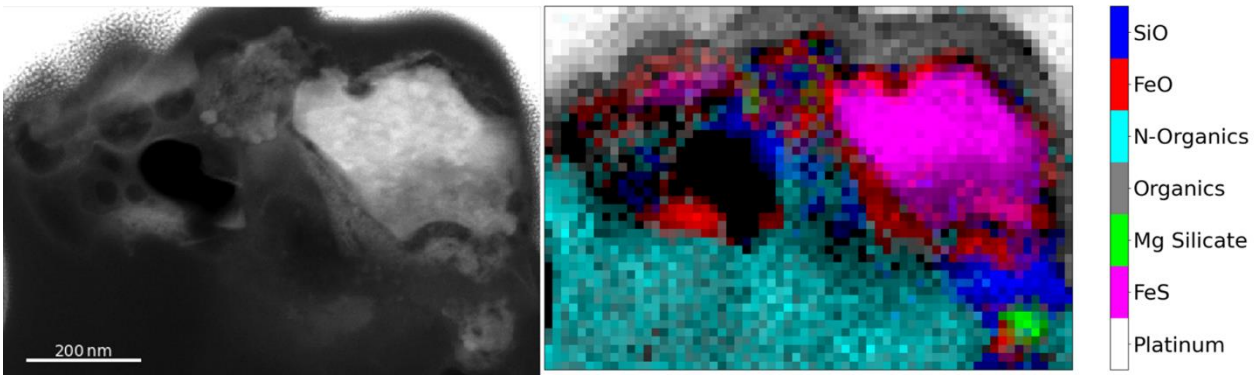

Figure 4-22: (left) High Angle Annular Dark Field (HAADF) image of a complex mineral assemblages in DC06-308 located on the top edge of the FIB section. (right) False color images corresponding to the EDX maps of the different phases identified by Principal Component Analysis (PCA). The phases are ordered by decreasing number of counts in the respective spectra.

Compositions of the different phases from the mineral assemblages in DC06-308 are summarized in Figure 4-25. One silicate (in green in Figure 4-18A) is close to a forsterite composition with high Mg/(Fe+Mg) (Fo_{95}) ratio while another silicate phase (in green in Figure 4-18B) has a non-stoichiometric composition and a higher Fe concentration (Mg/(Fe+Mg) = 0.7). Silicates in Figure 4-20 are both Mg-rich and have compositions corresponding to forsterite and enstatite (in green and yellow, respectively). The matrix that cements the mineral grains is amorphous and shows Si-rich compositions (square symbols in Figure 4-25). Overall Fe sulfides in DC06-308 are Ni-poor and have a composition matching that of troilite (Figure 4-25B). The simpler inorganic assemblages, displayed in Figure 4-21, both display stoichiometric compositions of Mg-rich pyroxene.

4.3.2.2. Mineralogy of DC16-309

The analysis of DC16-309 revealed a mineral with a fibrous texture similar to that of a phyllosilicate with a total size of around 2.4 µm (Figure 4-24A). The global composition of this fibrous phase is close to that of the Si-rich matrix found in other assemblages except for a high Al/Si atomic ratio. A mineral with enstatite composition is also associated with the phyllosilicate-like phase. A mineral assemblage close to this fibrous phase contains large low-Ni Fe sulfides (hundreds of nanometers) and smaller Fe oxides (Figure 4-24A). This mineral assemblage is embedded in type I OM.

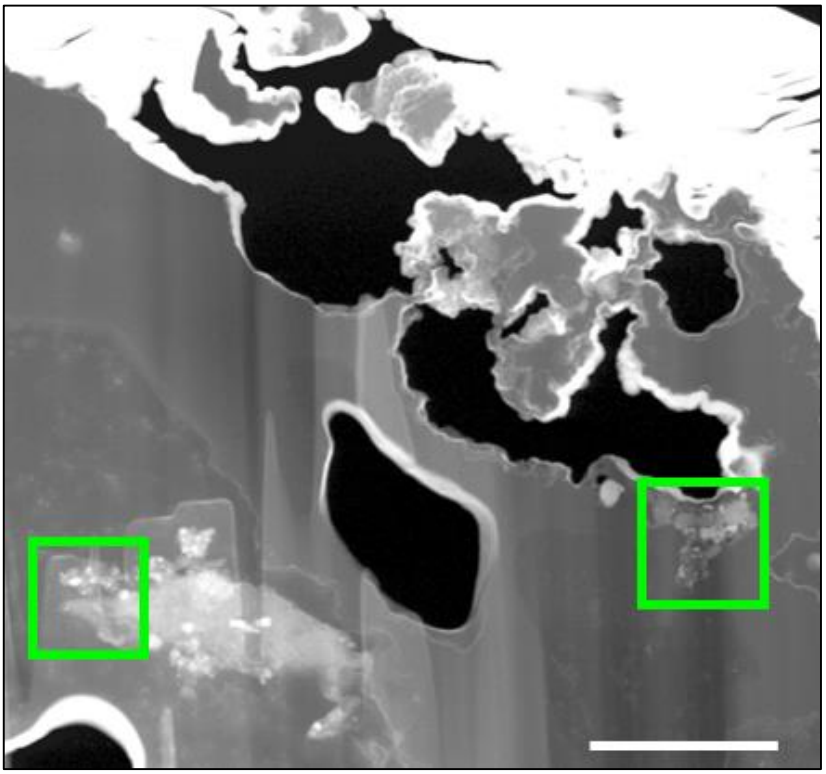

Figure 4-23: Location of the different EDX hyperspectral maps realized on DC16-309 and presenter in Figure 4-24. Scale bar is 2 µm.

DC16-309 exhibits another complex mineral assemblage (Figure 4-24B) made of Ca- and Mg-rich silicates, Mg-rich silicate, Fe-sulfides and oxides (~100 nm) and smaller FeNi sulfides (tens of nm). The Ca-rich and Mg-rich phases are closely associated. Fe oxides and sulfides are distributed at the edge of the assemblages or under the form of larger crystals.

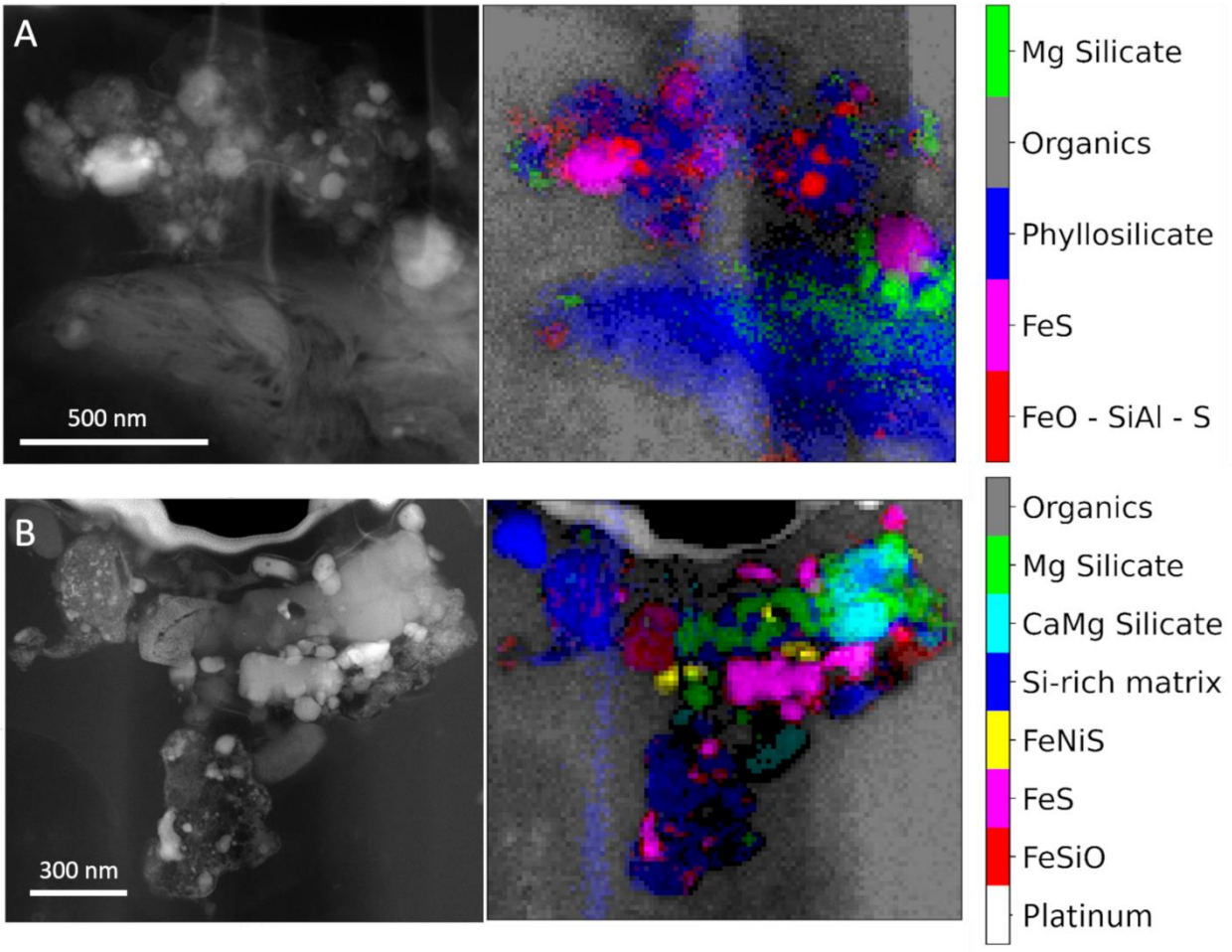

Figure 4-24: (left) High angle annular dark field (HAADF) images and (right) False color images corresponding to the map of the different phases identified by Principal Component Analysis of the EDX hyperspectral maps.. (A) Phyllosilicate-like phase (fibrous phase) decorated with a mineral assemblage. (B) Mineral assemblage located at the border of a vesicle. Both assemblages are embedded in the organic matter.

The small sized Mg-rich silicates in DC16-309 display non-stoichiometric compositions possibly due to the sampling of several phases under the electron beam. The mineral associated with the phyllosilicate matches an enstatite composition (Figure 4-25). The nature of the Mg-rich silicate in the second assemblage (Figure 4-24B) is not clear (Figure 4-25). The matrix data (square symbols in Figure 4-25) show Si-rich compositions. Fe sulfides in DC16-309 present two distinct compositions. Fe sulfides associated with the phyllosilicate present low-Ni/Fe values with a composition close to that of pyrrhotite (Figure 4-25B). Similar compositions are found in Fe-sulfides of the second assemblages with low-Ni concentration. A second population of sulfides in this assemblage (Figure 4-24B) exhibits a large Ni/Fe ratio with composition close to that of pentlandite (Figure 4-25B). They are smaller in size and are only found in this assemblage. A small mineral with stoichiometry close to that of Na_2S has been observed within dusty patches of DC16-309, although no diffraction or proper characterization could be made due to the loss of the DC16-309 FIB section after the first STEM session. From EDX spectra, the stoichiometry is closer to that of sulfide rather than that of sulfate.

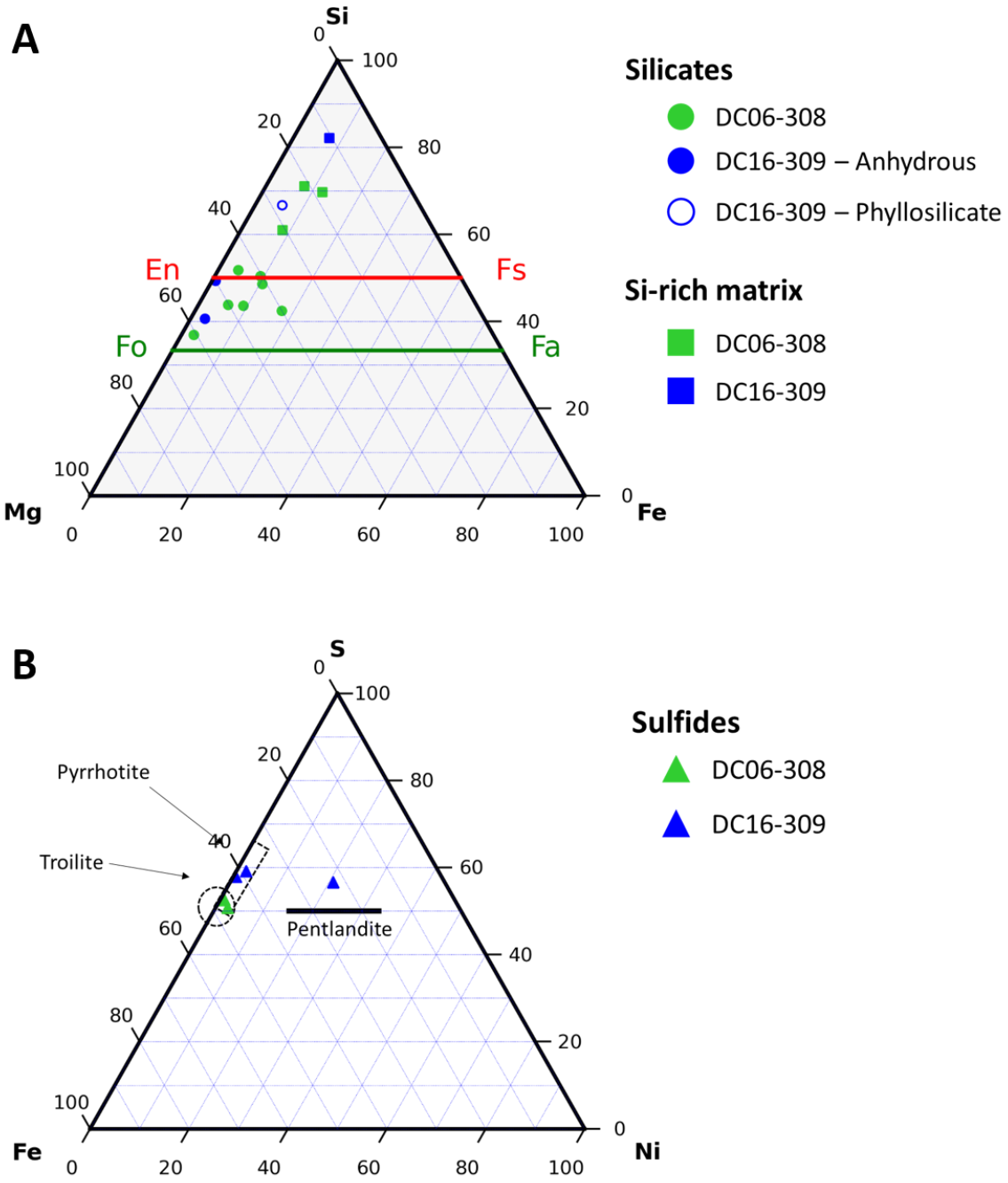

Figure 4-25: (A) Ternary diagram displaying the composition (in at%) of silicate mineral and matrix in assemblages found in DC06-308 and DC16-309. (B) Ternary diagram displaying the composition (in at%) of Fe sulfides and metals in assemblages from UCAMMs DC06-308 and DC16-309.

Chapter 5

5. UCAMMs in the context of extraterrestrial samples

5.1. Comparative mineralogy among cometary particles

It has been estimated that the Earth accretes around 30 000±20 000 tons of sub-millimetric extraterrestrial material every year, with 25% to 50% of this flux reaching Earth surface (Love and Brownlee, 1993; Rojas et al., 2021). Dynamic models predict that most of this cosmic dust originates from active Jupiter-family comets (Nesvorný et al., 2010; Plane, 2012). Chondritic anhydrous (CA-IDPs), also called chondritic porous IDPs (CP-IDPs) in the literature (Ishii et al., 2008), and UCAMMs, are the two cosmic dust populations that show the strongest evidence to originate from comets (Dartois et al., 2013; Dartois et al., 2018; Duprat et al., 2010; Nakamura et al., 2005b). These samples can be analyzed in the laboratory, and the results directly compared with the analyses from space missions that investigated comets 1P/Halley, 9P/Tempel1, 81P/Wild2 (sample return) and 67P/Churyumov-Gerasimenko (Giotto, Vega, Deep Impact, Stardust and Rosetta missions, respectively).

The individual mineral phases in the 11 UCAMMs analyzed so far (this work, (Dobrică et al., 2012)) mostly consist in small mineral assemblages and scarcer isolated minerals embedded in an abundant carbonaceous matrix (excepted for DC06-43 for which the analyzed fragment contain a 10µm-sized aggregate of minerals) (Charon et al., 2017; Engrand et al., 2015a). In this work, the composition of the small mineral assemblages in UCAMMs DC06-308 and DC16-309 and of isolated mineral phases in DC 06-18 was investigated by transmission electron microscopy (see Chapter 4). Whereas the analyses of UCAMMs DC06-308 and DC16-309 and DC06-18 revealed mineral compositions in agreement with previous observations (Charon et al., 2017; Dobrică et al., 2012; Engrand et al., 2015a), one phyllosilicate-like phase was unexpectedly found in DC16-309 (See Chapter 4).

Crystalline minerals from this study consist of low-Ca Mg-rich pyroxenes (with stoichiometry ranging between En_{60} and En_{97}) and Mg-rich olivines (stoichiometry comprised between Fo_{75} and Fo_{99}) with rare Ca-rich pyroxenes and Fe(Ni) sulfides. In UCAMM DC06-308, a hypocrystalline-like assemblage was identified, and other such assemblages were also described in Dobrică et al. (2012). The bulk composition of this assemblage in DC06-308 is CI-like. The bulk composition of the other assemblages studied in DC06-308 and DC16-309 is enriched in Si compared to CI (Figure 5-1). Si-rich compositions are also found in primitive phases in primitive meteorites (Le Guillou and Brearley, 2014; Le Guillou et al., 2015; Le Guillou et al., 2019; Leroux et al., 2015; Vollmer et al., 2020; Zanetta et al., 2021), in GEMS in CP-IDPs (Keller and Messenger, 2011), and in comet 67P/Churyumov-Gerasimenko (Bardyn et al., 2018).

Fe sulfides are often decorating silicate mineral with composition matching that of troilite and/or pyrrhotite (low-Ni Fe sulfides), but occasionally pentlandite crystals have been observed. Glassy phases are also observed in 3 UCAMMs (Charon et al., 2017; Dobrică et al., 2012; Engrand et al., 2015a) that resemble GEMS found in primitive IDPs (Keller and Messenger, 2011). Secondary minerals have also been observed in UCAMMs (Dobrică et al., 2012) such as small iron oxides, carbonates and sphalerite. Small Na-rich crystals with stoichiometry close to Na_2S have been observed located within the dusty patches in DC16-309.

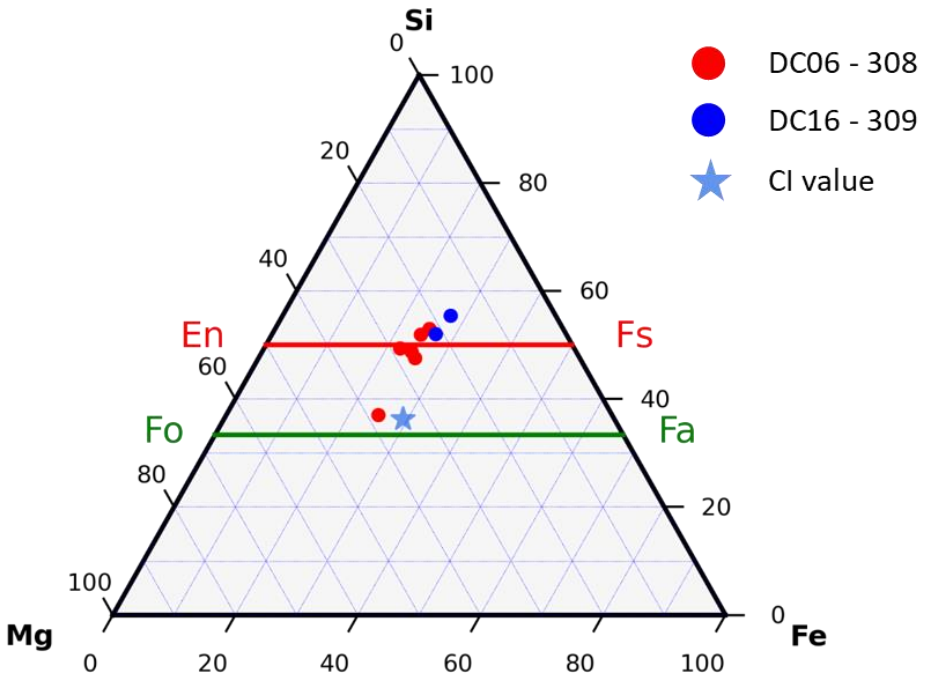

Figure 5-1: Ternary diagram showing the bulk composition (in at%) of the different assemblages analyzed in DC06-308 and DC16-309. The light blue star represents the CI value from Lodders (2010). The red point close to the CI value represents the composition of the hypocrystalline-like assemblage.

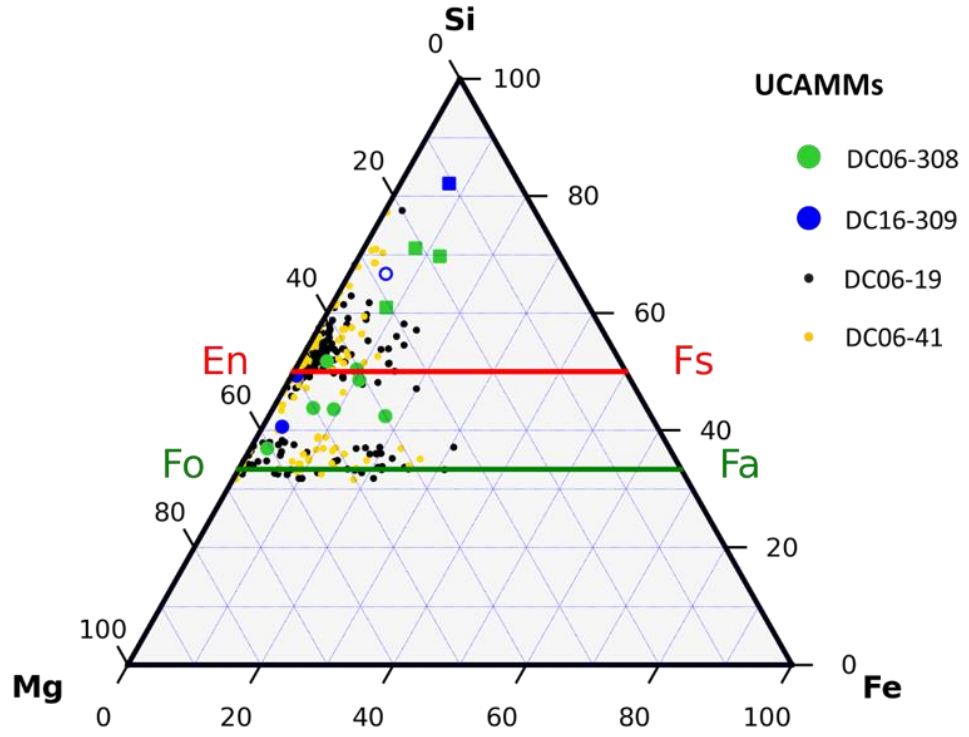

Figure 5-2: Ternary diagram showing the composition (in at%) of the silicate phases in the different assemblages present in DC06-308 and DC16-309 along with previous measurements from DC06-19 and DC06-41 from Dobrică et al. (2012).

Compared to chondritic porous IDPs (CP-IDPs), UCAMMs mineralogy show similar main mineral components (Mg-rich crystalline silicate, FeS and GEMS) and accessory phases alike what

is observed in CP-IDPs (Dobrică et al., 2012; Ishii et al., 2008; Levasseur-Regourd et al., 2018). In addition to metal-poor GEMS found in UCAMM DC06-09-19 (Dobrica et al. 2012), GEMS-like objects have been found in UCAMMs DC06-18 and DC06-43 among the 4 UCAMM-bearing minerals investigated in this study. The GEMS-like inclusions are either contained in type I phase or type III. Si-rich glass and GEMS-like objects present in UCAMMs only contain rare Fe metal inclusions compared to what is observed in CP-IDPs.

Overall, the occurrence of pyroxene and olivine mineral grains lead to pyroxene/olivine ratio equal or larger than 1 for UCAMMs (Dobrică et al., 2012). A pyroxene-dominated mineralogy is also seen in chondritic porous anhydrous IDPs (Donahue, 1999).

Direct measurements of Halley comet during Vega-1, Vega-2 and Giotto missions brought the first insight into the cometary dust composition (Jessberger et al., 1988; Kissel et al., 1986; Kissel and Krueger, 1987). The composition of the dust from comet 67P/Churyumov-Gerasimenko (67P/C-G) was recently analyzed by the COSIMA instrument during the Rosetta mission (Kissel et al., 2009). No mineralogical characterization was possible with the instruments on board, but a bulk Si-rich composition compared to the Solar composition was observed in 67P/C-G dust particles, with Mg/Si and Fe/Si atomic ratios of 0.11 ± 0.03 and 0.29 ± 0.1, respectively (Bardyn et al., 2018). These values are compatible with that of the Si-rich matrix measured in the UCAMM mineral assemblages in DC06-308 and DC16-309 (see Chapter 4 and Figure 5-2).

Analysis of the mass spectra of Halley particles suggested a lack of Fe-rich pyroxene and olivine and the survival of Mg-rich silicate, a mineralogy close to that observed in UCAMMs (Jessberger et al., 1988). The large occurrence of pyroxenes is also seen in Stardust samples (Zolensky et al., 2006) although olivines with wide compositional range are also common in Stardust tracks (Frank et al., 2014). Spectral analysis of comet Hale-Bopp also revealed a Mg-rich silicate mineralogy, containing both olivine and pyroxenes (Malfait, 1999 ; Wooden et al., 2000; Wooden et al., 1999). Spectral analysis of the comet 9P/Tempel 1 during Deep Impact mission exposed a mineralogy dominated by Mg-rich silicates with a pyroxene/olivine ratio close to unity along with the presence of carbonate and potential phyllosilicate (Lisse et al., 2006). Mineralogical zonations in disks have been observed (Bouwman et al., 2008; Olofsson et al., 2009; van Boekel et al., 2005), but no systematic trend with radial distance to the star has been found up to now. As both CP-IDPs and UCAMMs are thought to originate from comets, a Px/Ol ratio close to 1 may be an indication of cometary origin. With high spatial resolution in the observation of disks, ground-based interferometers such as MATISSE, and the James Webb Space Telescope, will give new insight into mineralogical zonations in protoplanetary disks.

As stated before, UCAMM DC06-308 presents a mineral assemblage exhibiting an hypocrystalline-like texture similar to what was observed in Dobrică et al. (2012), and reminiscent of chondrule fragments observed in Stardust samples (Nakamura et al., 2008a). It resembles a chondrule-like object, with porphyritic olivines embedded in a Si-rich matrix. This assemblage could have formed through a chondrule-forming event where dust particles were melted, until crystallization of mineral phases with equilibrated compositions. This event could not have happened after the incorporation of the minerals in the organic matter of UCAMMs (i.e. typically not during atmospheric entry), as it would have required temperatures above 1200°C which would have strongly modified or destroyed this organic matter. The presence of such high-temperature assemblages within cometary dust is compatible with the presence of crystalline silicates and points toward radial mixing in the protosolar disk where high temperature material

were transported outward to the outer solar system (Birnstiel et al., 2012; Bockelée-Morvan et al., 2002; Ciesla, 2009).

Secondary minerals such as carbonate (Dobrică et al., 2012), and the phyllosilicate candidate found in this study, are also observed in UCAMMs (see Chapter 4). Spectral observation of the ejecta subsequently to Deep Impact mission on comet 9P/Tempel 1 was interpreted to contain about 5% of carbonates and up to 9% of phyllosilicate (Lisse et al., 2007a; Lisse et al., 2006), although this remains controversial (Harker et al., 2005). Wooden et al. (2004) and Lisse et al. (2007b) also claimed that a phyllosilicate signature in comet Hale-Bopp could not be ruled out. However, definitive in-situ detection of cometary phyllosilicate has not been achieved yet. Analyses of Fe-sulfides in Stardust tracks revealed the presence of pyrrhotite, pentlandite and orthorhombic cubanite (Berger et al., 2011). The combination of these sulfides points toward aqueous alteration at low temperature (<210°C). This aqueous alteration could have happened on an asteroidal parent body, requiring a later transport mechanism of the altered components to the comet-forming region. Alternatively, aqueous alteration on the comet could be considered (see paragraph 5.4).

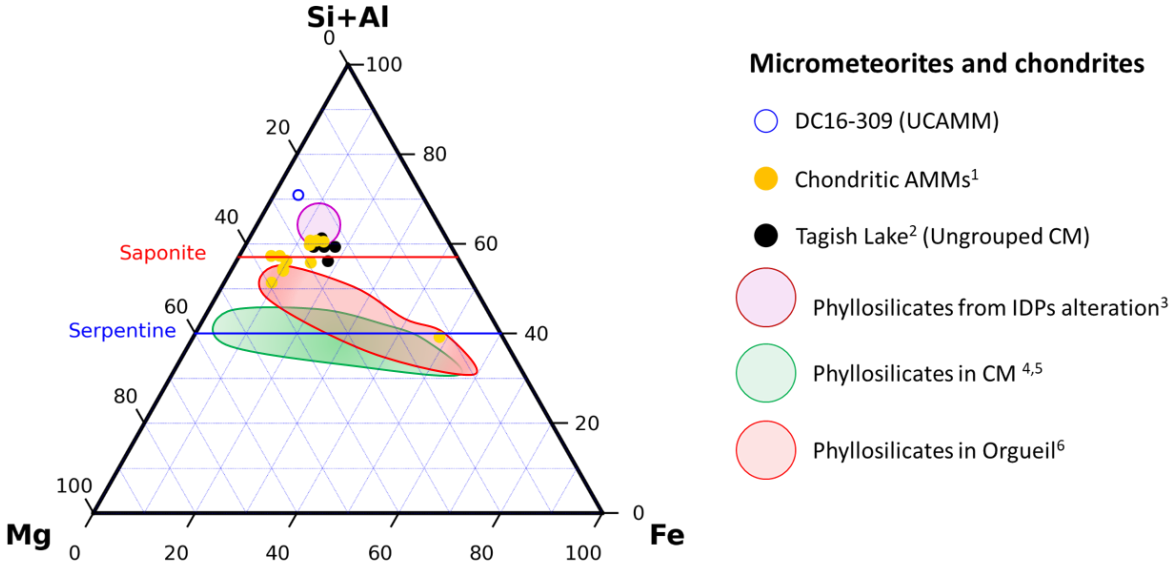

Figure 5-3: Ternary diagram displaying the composition (in at%) of the phyllosilicate-like mineral in DC16-309 (open blue circle) along with that of phyllosilicates from carbonaceous chondrites (red and green fields), Antarctic micrometeorites (AMMs) and phyllosicilates formed from aqueously altered GEMS in IDPs (Nakamura-Messenger et al., 2011). Data for AMMs from data Dobrica et al (2018) and Noguchi et al. (2002); data for CCs from Tomeoka and Buseck (1988), Bunch and Chang (1980), Browning et al. (1996), and Noguchi et al. (2002).

The composition of the phyllosilicate-like mineral in DC16-309 exhibits an unusual composition with a high Al/Si ratio of 0.22. It does not match that of saponite or serpentine stoichiometry and is Al-rich and Fe-poor compared to phyllosilicates in carbonaceous chondrites (CCs). Hydrous silicates exhibiting compositions relatively close to the one in DC16-309 are from Tagish Lake, or the ones obtained by aqueous alteration of GEMS in IDPs reported by Nakamura-Messenger et al. (2011) simulating the conditions of potential aqueous alteration on comets.

Concerning the occurrence of small Na-rich crystals with stoichiometry close to Na_2S in dusty patches in DC16-309, it might be related to the possible presence of ammonium sulfate in 67P/C-G. Indeed, the 3.2 µm band of the 67P/C-G nucleus is compatible with the presence of

ammonium salt (NH_4^+), which constitutes a good spectral fit to the reflectance spectra (Poch et al., 2020), and would explain the nitrogen depletion in the coma (Altwegg et al., 2020). Among matching candidates, ammonium sulfate ($(NH_4^+)_2SO_4^{2-}$) has been proposed.

5.2. Comparison of the different types of organic matter in extraterrestrial materials

5.2.1. Molecular signature and elemental composition of UCAMMs' organic matter

The C/Si elemental ratio presents a gradient in the solar system (Bergin et al., 2015; Lee et al., 2010). Dust presenting high C/Si ratio can be interpreted as originating from outer regions of the Solar System. It has been proposed by Dartois et al. (2018) to use this gradient to assess the heliocentric distances formation for the UCAMMs (which have a C/Si atomic ratio up to 30). When plotted with meteorites, IDPs and interstellar medium (ISM) values, UCAMMs display the highest C/Si ratio, that is even higher than for the average ISM value (see figure 8 in Dartois et al., 2018). This carbon abundance suggests a mechanism of concentration of organic matter at large heliocentric distances, within a nitrogen rich ice matrix, and works against a direct inheritance of the UCAMMs' organic matter from the ISM.

The Rosetta/COSIMA mass spectra of cometary dust particles from 67P/C-G lead to a high C/Si ratio of $0.18\pm^{0.05}_{0.04}$ (Bardyn et al., 2017). These measurements inferred that 67P/C-G particles were made of up to 50 wt% of organic matter. This ratio is in the range of what is found for UCAMMs, which display very large organic/mineral ratio (up to 90 vol% of carbon). The solid organic component of comet 67P/C-G characterized by Rosetta/COSIMA exhibits similarities with insoluble organic matter (IOM) extracted from carbonaceous chondrites (Fray et al., 2017; Fray et al., 2016), although the H/C measurement in 67P particles (H/C=1.04±0.16) show that organics from 67P/C-G were less unsaturated that organic material in these IOMs (Isnard et al., 2018). This suggests that 67P/C-G organic material is more pristine than the IOMs extracted from carbonaceous chondrites.

For comet 81P/Wild 2, Stardust analysis revealed on the contrary a low carbon content (Brownlee, 2014). This can partly be explained by the collection method of the Stardust mission, which probably volatilized a large part of the organic species during the impact with the aerogel. Matrajt et al. (2008) identified rare carbonaceous phases in Stardust samples, with an amorphous nature and approximate solar C and D/H isotopic compositions. Among the rare carbon-rich phases detected in Stardust samples, De Gregorio et al. (2017) also revealed nanometric Cr-rich magnetite coated with conformal layers of poorly graphitized carbon (PGC). PGC layers formation is consistent with Fischer-Tropsch-types formation process, occurring on primary carbide condensates or metal grains. This process is consistent with nebular oxidation of reduced material, showing additional evidence of large-scale radial mixing in the early solar system, where high-temperature material could have been brought out to the outward solar system.

The N/C elemental ratio of UCAMMs reveals relatively high nitrogen content compared to carbon, with values up to 0.2. The STXM-XANES analyses of UCAMMs revealed the presence of three types of organic matter (quoted types I, II and III) with different nitrogen compositions (Figure 5-4), with two of them often being closely associated to each other, as type II OM only appears embedded in type I OM. Atomic N/C ratios are variable in type III OM, with values ranging from 0.08 (for mildly heated particles) to 0.2, while type I and II N/C ratios range from below detection limit to 0.05. Type III OM being the main N carrier in the UCAMM organic matter, the

bulk N/C atomic ratios reported in Table 3 for each UCAMM should be lower than the N/C values determined for their type III OM, if samples are homogeneous. This is observed in most samples, except for DC06-18 and DC16-30 (see Table 5-1). As the N/C atomic ratios were measured on different UCAMM fragments, this suggests heterogeneity of N/C atomic ratios in UCAMMs. The elemental composition of type I and II OMs indicates a N/C atomic ratio compatible with that of IOM extracted from CCs ($0<N/C<0.05$). The N/C atomic ratio of 67P/C-G cometary dust is consistent with previous analysis in comets (81P/Wild 2, 1P/Halley) with values ranging between 0.02 and 0.06 (Fray et al., 2017), also compatible with that of type I/III OM in UCAMMs and of IOM from carbonaceous chondrites. The low N/C atomic ratio of Stardust organics could be biased by the collection methods, which implied high temperature heating of the samples during impact with the aerogel. In that case, the measured N/C atomic ratio measured in 81P/Wild 2 samples can be seen as a lower limit of the original nitrogen content of the cometary organic matter. The different N contents of the three OMs in UCAMMs suggest different origins for type I/II OMs and type III OM. UCAMMs' type I and II OMs embed high temperature crystalline minerals such as pyroxene and olivine. The association of high temperature phases with types I and II OMs possibly indicates a mechanism of formation similar to that of meteoritic IOM, possibly in the inner Solar System, also this is still debated (Alexander et al., 2017; Alexander et al., 2007; Gourier et al., 2008; Remusat et al., 2006). The type III OM presents higher N/C atomic ratios, harbors a smooth texture, is devoid of crystalline minerals and can extend over several μm^2 in area. GEMs-like inclusions are found associated with type III OM in some samples (DC06-09-19 from Dobrica et al. 2012, DC06-43, DC06-18). The production of such a N-rich organic matter from ices' irradiation by galactic cosmic rays (GCR) can be achieved at large heliocentric distances and could be a formation mechanism of type III OM (Augé et al., 2016; Dartois et al., 2013). N-rich ices can be retained by large enough bodies beyond a so-called "nitrogen snow line". Experimental high energy ion irradiations on accelerators of ice mixtures representative of solar system icy body surfaces can indeed produce residues showing infrared spectral features comparable to the ones recorded in the organic matter spectra of UCAMMs (Augé et al., 2019; Augé et al., 2016; Dartois et al., 2018; Rojas et al., 2020).

Recent analysis of the PanSTARRs comet based on N_2/CO measurement in the comet's coma indicates that its organic content could exhibit an elemental N/C atomic ratio around 0.15 (Biver et al., 2018), a value consistent with what is found in the type III OM of UCAMMs. However, this ratio for the PanSTARRs comet is derived from the CO and N_2 species, and the calculated N/C ratio might not be directly comparable with the OM in UCAMMs, which contain generally less oxygen in organics (e.g. less carbonyl) that CCs IOM (Dartois et al., 2018).

Table 5-1: Bulk N/C atomic ratios for five UCAMMs measured by electron microprobe, and N/C atomic ratios for their respective type III organic matter measured by STXM-XANES.

	Bulk N/C (EMPA)*	Type III N/C (STXM-XANES)
DC06-18	0.17 ± 0.04	0.11 ± 0.02
DC06-41	0.06 ± 0.02	0.12 ± 0.02
DC06-65	0.15 ± 0.04	0.20 ± 0.03
DC06-43	0.04 ± 0.03	0.08 ± 0.03
DC16-30	0.09 ± 0.06	0.03 ± 0.02

*from Dartois et al. (2018)

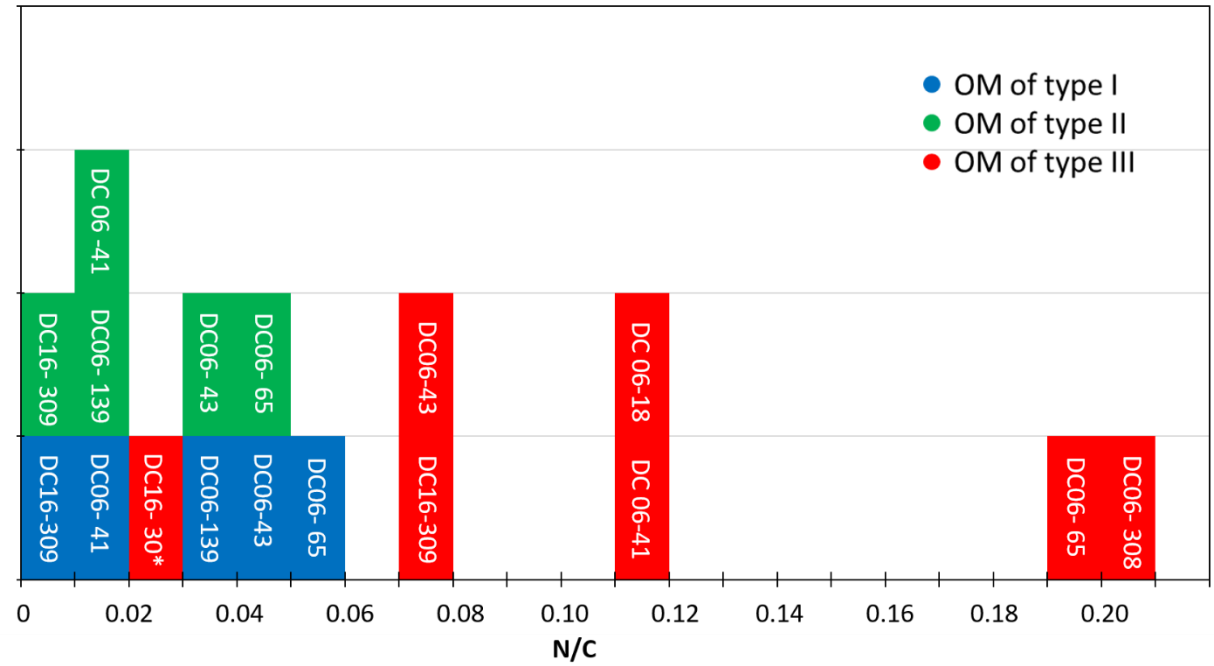

*Figure 5-4: Histogram of the distribution of N/C atomic ratios for the 3 different organic matter types found in each UCAMM presented in this study. *The low N/C atomic ratio for type III OM in DC16-30 could be explained by a higher heating during atmospheric entry, see section 5.3*

Analysis of Stardust samples allowed STXM-XANES characterization of different organic fragments of 81P/Wild 2 cometary dust. Among the samples presenting carbonaceous material, track 80 is thought to be the most pristine and more representative sample of indigenous cometary organics from Stardust collection (De Gregorio et al., 2011). It appears that organic matter of 81P/Wild 2 samples presents similar carbon speciation as type I in UCAMMs (see Figure 5-5). Both spectra display their main first peak at 284.8 eV, corresponding to the alkene carbon while type II is more aromatic (the first peak is shifted toward the 285 eV value). These spectra are also close to that of insoluble organic matter of carbonaceous chondrites (Alexander et al., 2017; Changela et al., 2018; Le Guillou et al., 2014; Vinogradoff et al., 2018). Type I OM of UCAMMS also display a very similar spectrum compared to the spectrum of carbonaceous chondrite IOM from QUE99177 (type CR2). The comparison with IOM from QUE9917 was specifically chosen because of its homogeneous IOM spectral signature (Le Guillou et al., 2014), and because of a possible cometary origin of CR chondrites. The main peaks at 284.8 eV and 286.4 eV are also present and some carboxylic absorption is also visible in the same trend as for 81P/Wild 2 samples. Regarding the N-rich OM of type III in UCAMM, no counterpart has been observed in 81P/Wild 2 samples or meteoritic IOM.

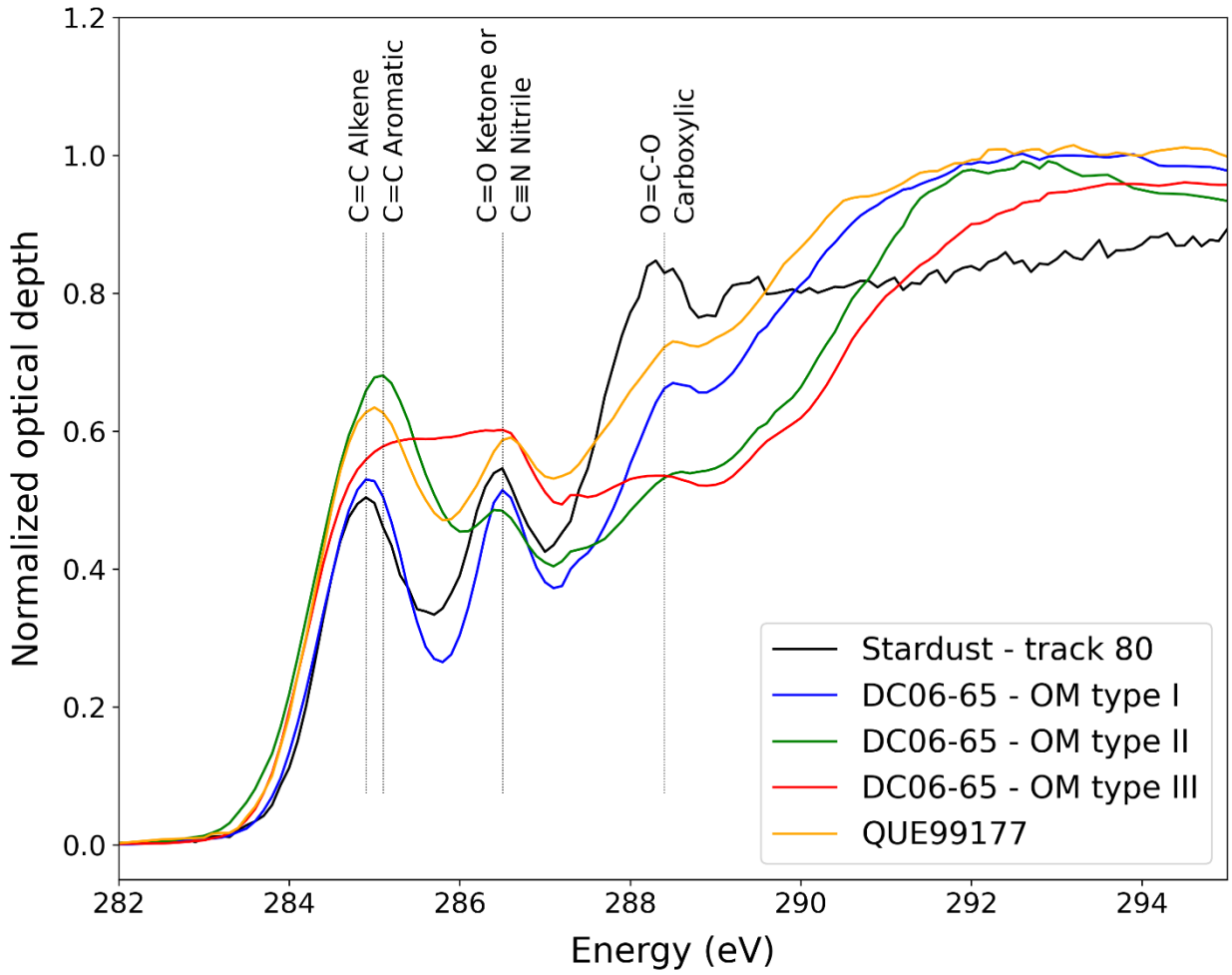

Figure 5-5: STXM-XANES spectra of the 3 different types of OM in UCAMM DC06-65 compared to spectra of organic pristine particle from track 80 in Stardust (81P/Wild 2) samples and IOM from QUE99177.

5.2.2. Mineral-organic interface

In the STXM-XANES spectra at the C-K edge, type II OM does not display the same drop in absorption between 285 eV and 286.5 eV as for type I OM. The presence of inorganic phases within the dusty patches in type II OM could explain this continuous absorption. This may possibly be explained by C=C-R configuration, with aromatic carbon linked to other carbon or heteroatoms such as N or O instead of hydrogen, shifting the absorption energy of aromatic carbon toward higher values (>285 eV).

GEMS-like inclusions can be present in type I or type III OM. These fine-grained phases could in turn contain organic matter, like what is observed in DC06-18 (see Chapter 4). In that case, the GEMS-like inclusions are enclosed in type III OM and the N content of the organic matter that is located inside the inclusion can reach N/C atomic ratios up to ~0.5. This value is higher than the maximum atomic N/C atomic ratio observed for type III OM, which is around 0.2 see Figure 5-4). In the case of the organic residue produced by irradiation, heating to 300°C was performed in order to reproduce the IR signature of UCAMMs, suggesting a mild thermal alteration of the precursor of type III OM in UCAMMs, maybe during atmospheric entry (Augé et al., 2016). In the case of DC06-18, the organic matter trapped inside the GEMS-like inclusion could have been protected from such a mild thermal event, and could thus have better preserved the initial N/C atomic ratio of the N-rich organic matter.

UCAMMs show a bulk Na enrichment compared to CI. The high bulk Na abundances of UCAMMs, and the high N/C ratio of their organic matter are exceptional in the sense that they are not observed in any other kind of extraterrestrial material analyzed in the laboratory. Na is common in comets, as evidenced by the observation of a sodium tail in comet Hale-Bopp (Cremonese et al., 1997), and of a systematic Na enrichment in particles collected and analyzed by COSIMA during the Rosetta mission around comet 67P/Churyumov-Gerasimenko (Bardyn et al., 2017). The host phase of Na in comets has however not been identified yet. Elemental maps of the organic matter of DC06-18 shown in Chapter 4 show an increase of the Na concentration close to GEMS-like phases, which appears sometimes correlated with an increase of the N concentration in the organic matter. The Na/Si atomic ratio is about twice that of CI in GEMS-like phases in DC06-18. The partial correlation of the Na and N abundances suggests the presence of at least two Na-bearing phases, one of them being correlated with the N content of the organic matter close to the inorganic phases. Alternatively, the Na halo observed in DC06-18 around the mineral assemblages could possibly be explained by a mild heating event inducing diffusion of Na from the GEMS-like phase, with an atomic Na/Si ratio ~ 2x CI, toward the organic matter.

The N/C atomic ratio in comets is lower than that of the Sun, which suggests the presence of a hidden nitrogen reservoir in comets. Semivolatile ammonium salts were recently identified in comet 67P/C-G, and could represent a significant fraction of the nitrogen present in comets (Altwegg et al., 2020; Poch et al., 2020). To match the reflectance spectra of 67/C-G, these ammonium salts are associated with a finely grinded Fe sulfide (Poch et al., 2020). The observed N and Na partial correlation in UCAMM DC06-18, and the identification of a mineral in type II OM with a composition close to that of Na_2S questions the relevance of testing Na_2S in a combination with ammonium salts to reproduce the reflectance spectra of 67P/ C-G.

5.3. Potential effect of atmospheric entry heating

Since UCAMMs are collected on Earth after atmospheric entry, one has to decipher the effect of heating during atmospheric entry from possible heating processes on their parent body. As UCAMMs can reach sizes from tens to several hundreds of μm, they are expected to experiment higher temperature rises than smaller particles such as IDP (tens of μm) during atmospheric entry. According to Love et al. (1994), MMs with sizes larger than 50 μm can reach temperatures above 800 °C during atmospheric entry heating.

The UCAMMs organic matter characteristics gives an upper limit to the extent of heating (<500°C) they could have experienced during atmospheric entry. Raman analysis of several UCAMMs (Dartois et al., 2018) displays large D and G FWHMs bands (above 140 cm^{-1}), attributed to carbon bonds, whose FWHMs is sensitive to the temperature indicating atmospheric entry heating temperature lesser than about 500°C based on simulations from Bonnet et al. (2015). The presence of a nitrile (2220 cm^{-1}) peak in the infrared spectra of some UCAMMs (Dartois et al., 2018) also constrains temperature to values lower than about 500°C during atmospheric entry, as the nitrile content would not be preserved at higher temperature. It is also important to note that the measured N/C atomic ratio in UCAMMs can be considered as a lower limit value, as even a limited heating could have reduced this ratio. The low nitrogen content of UCAMM DC16-30 type III OM (N/C = 0.03 ± 0.02, see Figure 5-4) could result from a more extensive heating during atmospheric entry. Indeed, as seen in Chapter 4, DC16-30 displays a vesicular texture that can be indicative of high-temperature heating. Overall, the relatively low oxygen content of organic matter of UCAMMs is also consistent with a limited heating during atmospheric entry.

High temperature heating effects are less constrained by the mineral content of UCAMMs than by organic matter, when considered apart from the fact that the mineral assemblages in UCAMMs are embedded in the organic matter. Bradley et al. (2014) experimented the effect of heating on IDPs and MMs. Heating MMs around 500°C leads to the mobilization of sulfides within amorphous silicate that will accumulate on the grain surface. Interaction with atmospheric O_2 may oxidize it to magnetite rim if temperatures reach 1200°C (Toppani et al., 2000). Heating experiments also show the formation of large Fe-sulfides (hundreds of nm) decorating silicate, although they were thought to result from gas-phase sulfidization in the solar nebula (Keller and Messenger, 2011). In UCAMMs, although primary minerals often display large decorative Fe-sulfides similar to those formed in heating experiments (Bradley and Ishii, 2017), no clear iron oxidation has been observed, except in the case of DC06-308, where the analyzed mineral inclusions are located at the surface of the particle (see Chapter 4). The observed Fe-oxide in this sample could thus result from mild heating during atmospheric entry processing, also indicated by a possible moderate thermal processing of fine-grained inorganic inclusions. The crystallization of chondrule-like material (see Dobrică et al. 2012, and Chapter 4) can however not have occurred during atmospheric entry flash-heating, which would have destroyed the organic content around it. In DC06-308, Na is below detection limit, whereas the Na/Si ratio is about chondritic in DC16-309. The Na depletion in DC06-308 can thus be explained by mild atmospheric entry heating. The presence of a potential phyllosilicate in DC16-309 also sets an upper limit to the reached temperature (<600°C) during atmospheric entry, as phyllosilicates are rapidly thermally decomposed (Greshake et al., 1998). The ubiquitous presence of Fe sulfides within UCAMMs mineralogy indicates an upper limit around 650°C for atmospheric entry heating temperature as they are easily removed during high temperature oxidizing event.

5.4. On the possibility of aqueous alteration of cometary particles

5.4.1. Sources of aqueous alteration on comets

Internal heating and radiogenic decay are the main sources of energy to explain liquid water formation and alteration on asteroid surfaces. However, if the cometary parent body internal heating or impact-generated heating are not efficient enough, an alternative scenario has to be proposed to explain the potential water activity on comets. Suttle et al. (2020a) proposed that aqueous alteration mostly occurs when silicate interacts directly with liquid water during comet's perihelion passage, generating enough heat and/or pressure to maintain the presence of liquid water on the subsurface of the cometary body. As alteration of silicate with basic water could lead to the formation of phyllosilicates within hours (Nakamura-Messenger et al., 2011), this process could explain the punctual presence or detection of hydrated mineral in cometary dust. However not all comets meet the conditions to sustain liquid water for long enough timescale during perihelion passage. According to Suttle et al. (2020a), only 6% to 9% of periodic comets could host possible conditions for subsurface aqueous alteration to occur.

5.4.2. Mineral alteration in UCAMMs

The secondary mineral phases such as a phyllosilicate candidate (this work) and carbonates (Dobrică et al., 2012) in UCAMMs could have formed out of hydrothermal alteration on a first parent body in the inner regions of the protoplanetary disk before being incorporated into comets. Whether secondary minerals observed in cometary materials are in-situ alteration products or heritage from asteroidal hydrothermal alteration is questioned here.

Experimental aqueous alteration of CP-IDPs showed that aqueous alteration of silicate could occur in interaction with either liquid or water vapor (Nakamura-Messenger et al., 2011;

Takigawa et al., 2019). When directly exposed to liquid water at basic pH and relatively low-temperatures (25°C to 160°C), amorphous silicates like GEMS can be altered on timescale of hours. The alteration of crystalline silicates like enstatite could require longer time scales or higher temperatures. Extrapolation to lower temperatures kinetics indicates that alteration could occur at around 0°C over extended timescales (on the order of weeks). The reaction rate when silicates are exposed to water vapor phases is much slower (100 -120 hours) as it is only driven by the formation on a thin water film at the surface of silicates if pressure and temperature are high enough. When comparing reaction rates of liquid/solid interaction and vapor-solid interaction, it is unlikely that water vapor led to strong alteration process in cometary dust although its orbital window is wider than for liquid water.

Concordia micrometeorites are collected by melting snow and filtering water (Duprat et al. 2007). It is necessary to examine a potential aqueous alteration during the collection of the UCAMMs in Dome C. During the extraction process, particles can stay in Antarctica water for up to 15 hours, at temperature lower than 20°C. Antarctic snow and water have variable pH comprised between 4.8 and 6.1 (Ali et al., 2010; Fujii, 1983). Nakamura-Messenger' experiments (2011) showed that pH is critical to the kinetic of alteration reaction. Their experiments were carried at higher pH values, to simulate cometary surface conditions (pH=11). Such large difference in acidity would critically slow down the reaction kinetic in the case of alteration with Antarctic water. Moreover, if aqueous alteration was dominant in Antarctica during the process of the Concordia collection, all samples would be extensively hydrated, which is not the case.

Yabuta et al. (2017) have proposed a formation of UCAMMs' organic matter through slight aqueous alteration. Mineralogical characteristics of UCAMMs tend to show minor aqueous alteration effects such as the low metal concentration in GEMS-like objects found in UCAMMs (Dobrică et al., 2012). Even with limited aqueous alteration, metals phases are the most easily mobilized phases and can be quickly depleted. The presence of Fe sulfides with compositions approaching that of pentlandite (See Chapter 4) points toward a small amount of hydrothermal alteration. Their localization at the periphery of silicate minerals is compatible with a small amount of fluid circulation within the carbonaceous matrix of UCAMMs. The presence of a phyllosilicate-like mineral exhibiting a fibrous texture in UCAMM DC16-309 is also attesting of an aqueous alteration event (See Chapter 4). The phyllosilicate candidate is enriched in Al and decorated with large Fe sulfides. Its composition is close to that of aqueously altered GEMS at basic pH obtained by Nakamura-Messenger et al (2011). The formation of DC16-309 phyllosilicate candidate could therefore result from an aqueous alteration in conditions close to those sustainable on cometary surface (pH=12, T=25°C) during perihelion. The heritage from a previously altered body can however not be discarded.

Characterization of organic and inorganic features from increasingly altered micrometeorites by Noguchi et al. (2017) confirm that UCAMMs could have possibly evolved through a weak aqueous alteration process on their parent body.

5.4.3. Organic matter alteration

If UCAMMs experimented aqueous alteration, their organic content should display chemical evidence of this process. The effect of hydrothermal alteration on insoluble organic matter (IOM) of carbonaceous chondrite as a part of its formation mechanism has already been described in several works (Alexander et al., 2007; Le Guillou et al., 2014; Vinogradoff et al., 2017). Hydrothermal alteration leads to increased aromatization of the organic carbon associated with the loss of aliphatic carbon, although the H/C ratio and the alteration degree of IOM do not show

correlation for several CMs chondrite (Alexander et al., 2007; Alexander et al., 2010). Alteration of IOM also leads to an increase in the concentration of oxygen within the organic content through chemical oxidation. It might lead to decrease in N/C and H/C ratios of the organic content as it gets oxidized, which is not necessarily observed in carbonaceous chondrite IOM of increasing oxidized types.

Among the three different types of OM that have been identified in UCAMMs (types I, II and III), type I and II share clear characteristics with IOM of CCs while type III organics of UCAMMs exhibits a different chemistry. It has already been proposed that in UCAMMs type I and II on one hand, and type III OM on the other hand, could have formed through distinct processes. Type I and II, associated with crystalline phases, may have formed in the same way as IOM, in region close to the sun and could have experimented hydrothermal alteration on a first parent body. The formation scenario for type III OM is different. It is suggested to have formed out of irradiation of N-rich ices in distant solar system regions (Augé et al., 2015). Whether these three phases experimented a subsequent aqueous alteration during comet's perihelion is still uncertain as several alteration steps could overlap in their signature.

5.5. On the formation of UCAMMs

UCAMMs are assembling components formed at different locations in the protoplanetary disk and their chronological history of formation might be complex to unveil. The crystalline components of UCAMMs such as olivines and pyroxenes formed at high temperature, likely in the inner solar system. The presence of chondrule-like objects in UCAMMs also points out to a formation of crystalline minerals (or mineral assemblages) in the inner regions of the Solar System. The crystalline minerals could not be inherited directly from the ISM as interstellar dust is largely amorphous (Kemper et al., 2004, 2005; Wright et al., 2016). These crystalline phases are associated and embedded within organic matter of type I and II in UCAMMs, indicating a potential close-by formation location and/or timing, after the high temperature crystalline phases, in process similar to the one that formed IOM of CCs. These mixtures of organics and mineral could have experimented hydrothermal alteration during the first steps of their formation and water circulation on the surface of a primitive parent body could explain some of the alteration features seen in some UCAMMs. This material then needs to be transported toward the outer solar system to explain the presence of minerals fragment (and of their associated organic matter) in cometary dust. In this cometary forming region, UCAMMs parent bodies could have accreted N-rich ices on theirs surfaces. Irradiation of these ices with energetic particles such as Galactic Cosmic Rays can lead to the formation of an organic residue that would form large patches of N-rich type III OM devoid of minerals.

From there, UCAMMs parent bodies could have started their cometary journey and at some moment being perturbed gravitationally and travel towards the inner solar system. During their perihelion, conditions on their surface could have been sufficient to maintain liquid water so that aqueous alteration might have occurred. However, it is hard to differentiate the original alteration (during or just after the first step of mineral formation) from the late ones, in this scenario, during the travel toward the inner solar system. If cometary particles exhibit components indicating a potential aqueous alteration, it is not clear whether it is a heritage from early hydrothermal alteration on an asteroidal parent body or a product from aqueous alteration event during comet's perihelion.

Chapter 6

6. Toward IR- Atom Force Microscopy - InfraRed (AFM-IR) analysis of minerals

In this chapter, the feasibility of AFM-IR characterization of minerals is investigated. Measurements were done on two different minerals, a Mg-rich olivine with different sample preparations (see Chapter 2 for more details about the different sample types), and a Mg-rich pyroxene (enstatite). Each sample was analyzed with varying analysis parameters to investigate their effect on the resulting spectra.

6.1. The mineral signatures and effect of sample preparation

Two different minerals were measured during this session: a Mg-rich olivine and a Mg-rich pyroxene. The two different spectra are presented in Figure 6-1. The samples in this case correspond to polished micrometer-thick sections. The spectra have been measured with similar analytical parameters. The two spectra display different absorption bands over the 900 cm^{-1} – 1300 cm^{-1} range. Although many of the peaks can not be directly compared to conventional FTIR absorption spectra of the respective minerals, they show that the AFM-IR measurements can be sensitive to two different mineral phases.

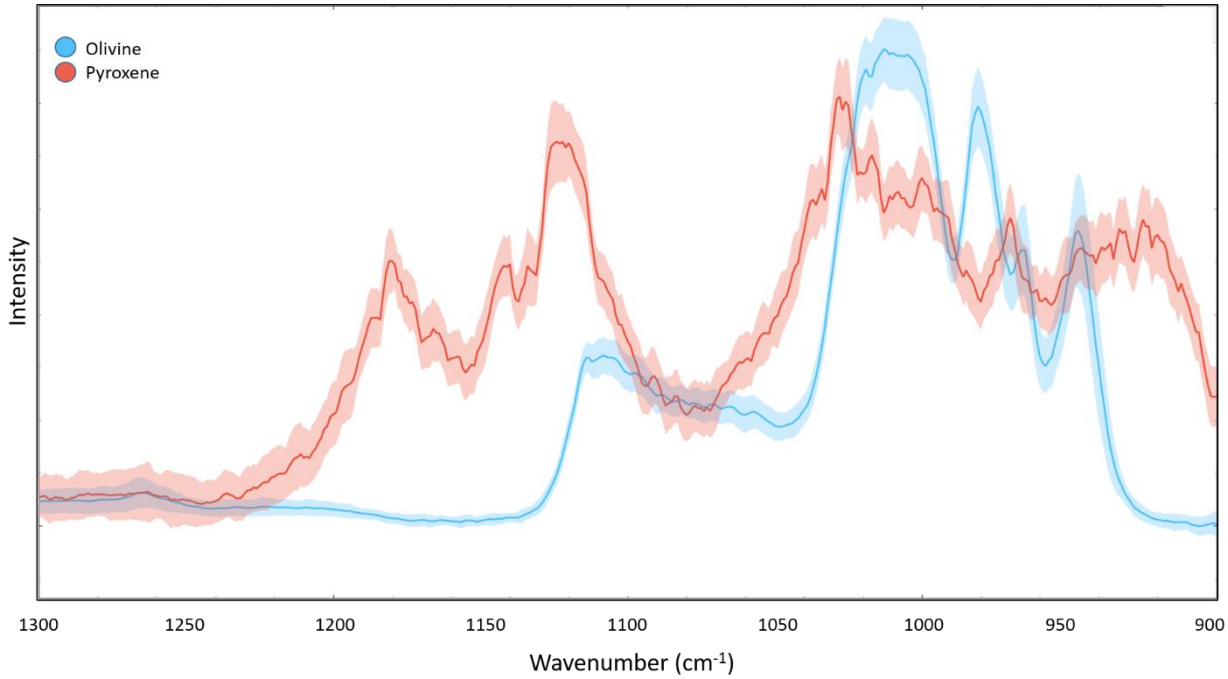

Figure 6-1: Comparison of pyroxene (red) and olivine (blue) absorption bands over the 900 cm^{-1} – 1300 cm^{-1} region for the polished micrometer-thick sample preparations. The light halo surrounding the different spectra represents the spectral variation for the averaged set of spectra.

Then, the effect of sample preparation on the recorded AFMIR spectrum is evaluated. This comparison is shown in Figure 6-2 for olivine only, as the overall quality of the spectra were better for this mineral phase. The exact crystallographic orientations of these olivine samples were not known, and constitute an additional parameter that should be taken into account.

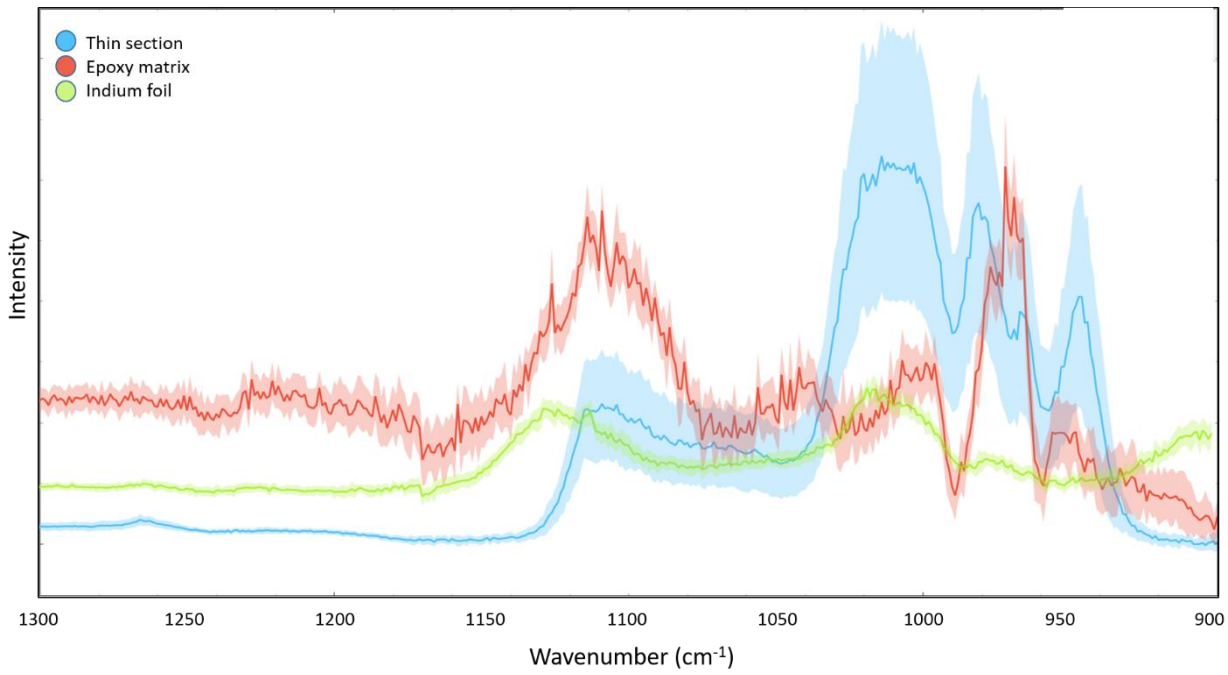

Figure 6-2: Comparison of the averaged spectra obtained for Mg-rich olivine with the 3 different sample preparation methods. Analyses were performed under similar analytical conditions. The crystallographic orientations of the olivine samples are not known. The light halo surrounding the different spectra represents the spectral variation for the averaged set of recorded spectra.

Two different regions of the olivine polished thin section sample were measured with similar analysis parameters and are displayed in Figure 6-3. The obtained spectra seem rather consistent over the olivine section in that case.

From Figure 6-2 it appears that the sample preparation is critical for the AFMIR analysis of silicates minerals. The three different sample preparation result in rather different AFMIR spectra, a complexity added by the orientation of the minerals, which is here unknown, and probably plays a role in the observed variations of the spectra. The thin section preparation (in blue, Figure 6-2) gave the more consistent results although the intensity of the absorption peaks is variable. For samples prepared in epoxy matrix (in red, Figure 6-2), most of the spectra displayed a low signal to noise (s/n) ratio. This might result from the interaction of the beam with the epoxy matrix embedding the mineral sections, leading to thermal expansion unrelated to the intended mineral analysis. In Figure 6-2, only the more consistent spectra from the samples in epoxy matrix are displayed as most of the measurement did not display any clear absorption. The observed peaks for epoxy matrix preparation however do not corresponds to the one observed in the thin section sample. The same mineral sections were then extracted from the epoxy to be put in Indium foil. The resulting AFM-IR spectra are displayed in green in Figure 6-2 for olivine and in Figure 6-4 for both minerals. Although the indium foil preparation allowed more consistent AFM-IR spectra than for epoxy matrix, the absorption peaks neither correlate with thin section spectra or sample in epoxy spectra in Figure 6-1. However, the indium foil sample preparation seems better than the epoxy for AFM-IR sample analyses as the generated spectra displayed a better s/n noise ratio and more consistent spectral band shapes. Although the absorption bands for olivine are not consistent from one sample preparation to another (Figure 6-1), the AFM-IR mineral signature is different for pyroxene and olivine for a given sample preparation (Figure 6-1 for polished thin section and Figure 6-4 for epoxy matrix).

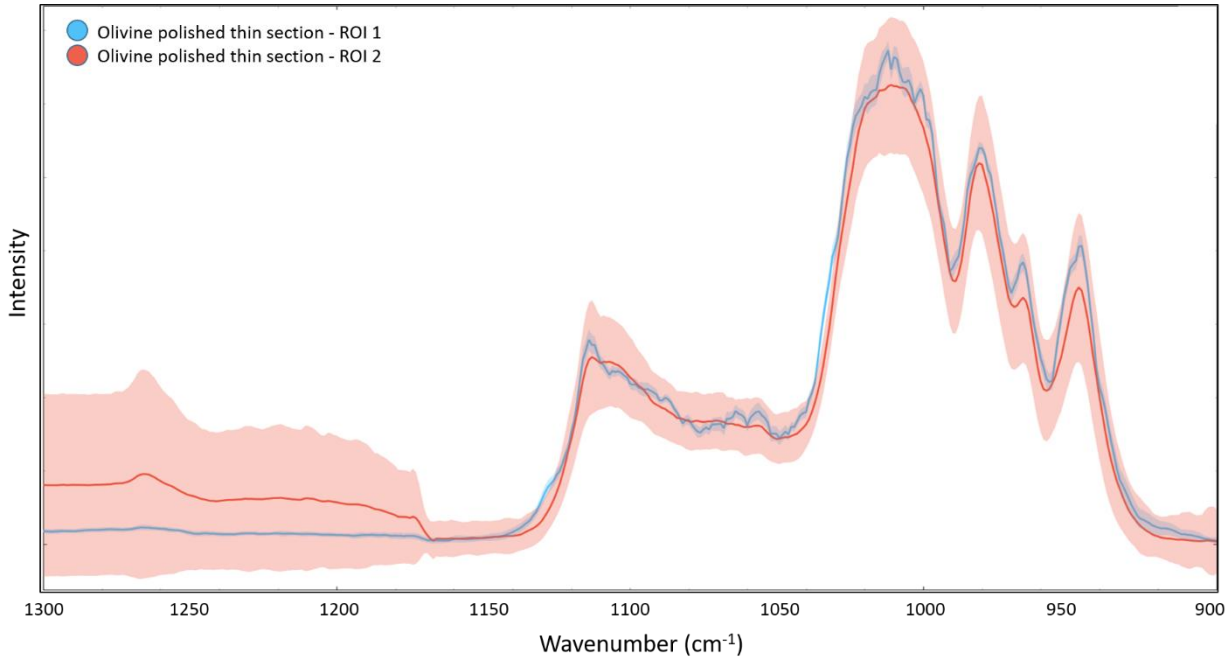

Figure 6-3: Comparison of the averaged spectra obtained for olivine polished thin section for two distinct regions of interest. Analyses were realized in similar analytical conditions. The light halo surrounding the different spectra represents the spectral variation for the averaged set of spectra.

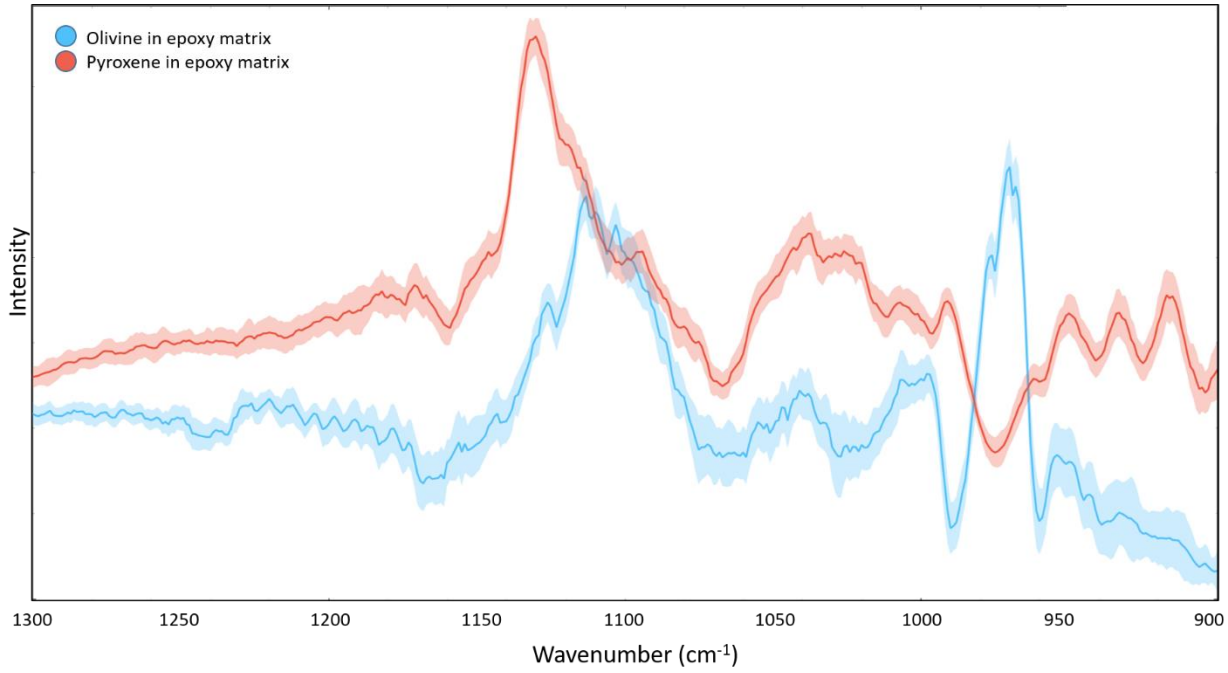

Figure 6-4: Comparison of pyroxene (red) and olivine (blue) absorption bands over the 900 cm $^{-1}$ – 1300 cm^{-1} region for the epoxy matrix sample preparations.

It appears that, even though AFM-IR is sensitive to different mineral IR signatures, the sample preparation method is critical in influencing the resulting measured spectra. The "matrix-based" sample preparations (either epoxy matrix or indium foil preparations) seems to give less consistent results than the polished thin sections. Part of the measured spectra for epoxy and indium foil matrix had very bad signal/noise ratios. This is probably resulting from the thermal expansion of the matrix overwriting the overall AFM-IR signature. This artifact is particularly

important in the epoxy matrix sample, as the organic nature of the matrix makes it more likely to be affected by a higher thermal expansion.

6.2. Effect of analysis parameters

In addition to sample preparation, the effect of analysis parameters must also be constrained. The AFM-IR technique allows the tuning of different parameters. The effects of the laser frequency, the setpoint of the cantilever and the type of cantilever are investigated here. The reference sample used is the olivine polished thin section (blue spectra, Figure 6-1) as this sample preparation method displayed the most consistent spectra overall. The first investigated parameter is the frequency of the laser and the resulting spectra are displayed in Figure 6-5.

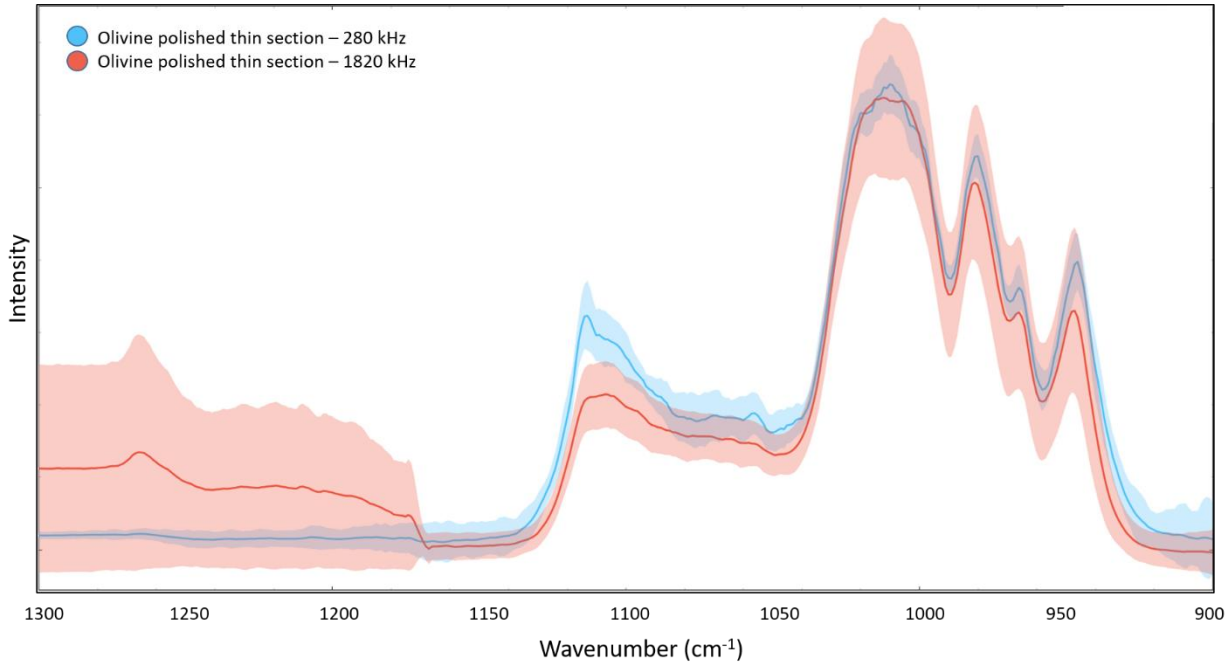

Figure 6-5: AFMIR spectra for olivine polished section at two laser frequencies. The light halo surrounding the different spectra represents the spectra variations for the averaged set of spectra.

The two spectra measured at different frequencies for the olivine polished thin sections are in good agreement with each other. The value of the laser frequency does not seem to impact the general AFMIR spectra in a strong way although small differences are observable. The peak at 1125 cm^{-1}, although visible in both spectra, is more intense and better defined with the laser frequency set to 280 kHz (in blue, Figure 6-5). At higher wavenumbers, the spectra generated at 1820 kHz show more variation in intensity than for the 280 kHz. A broad absorption band is also visible at 1260 cm^{-1}, which does not seem to be present in the 280 kHz spectrum. Overall, the laser frequency does not seem to impact strongly the main AFM-IR signatures of the measured olivine polished thin section.

The second parameter investigated here corresponds to the setpoint of the cantilever. This parameter controls the cantilever sensitivity threshold with regard to the sample's surface. We investigated the effect of three different setpoint values in this work: 0V, 1V and 3V (with a fixed cantilever type and fixed laser frequency). The resulting spectra for 3 different setpoints are show in Figure 6-6.

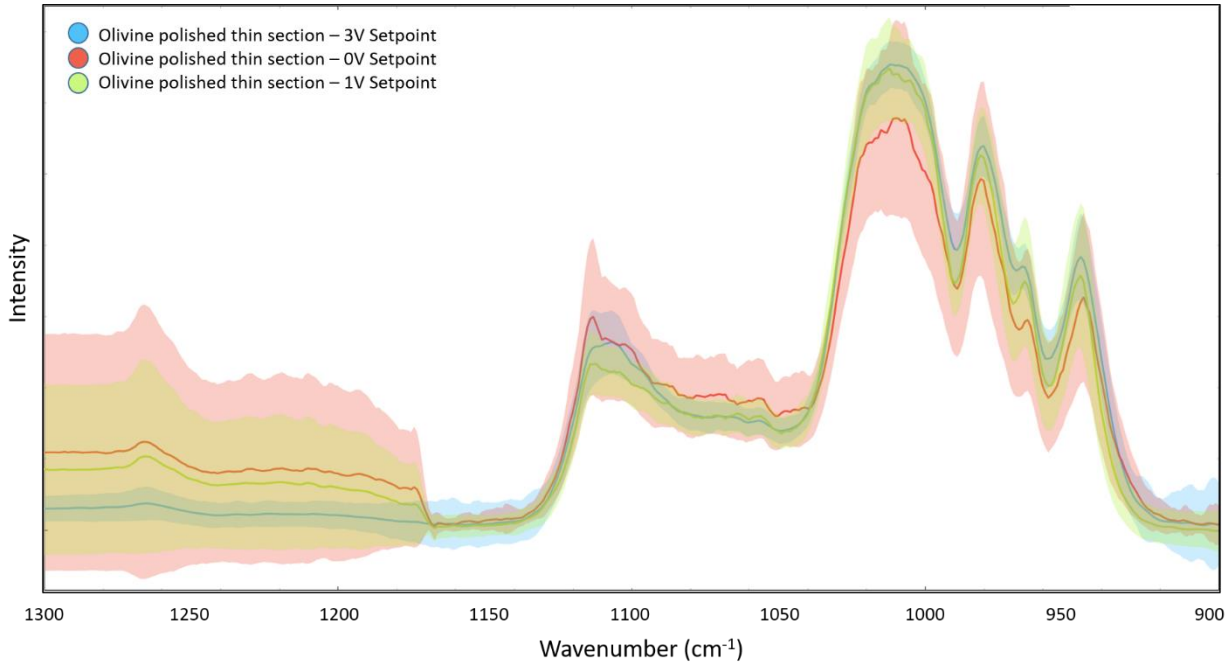

Figure 6-6: AFMIR spectra for olivine polished section at three cantilever setpoints. The light halo surrounding the different spectra represents the spectra variations for the averaged set of spectra.

Spectra measured with different setpoints are overall in good agreement. However, the variations seem more important with setpoints of 0V and 1V (in red and green in Figure 6-6, respectively). The 3V setpoint, in blue, shows rather tenuous variation compared to the other setpoints, reflecting possible better conditions analysis for this type of sample. The broad peak observed around 1260 cm^{-1} is already observed in the 280 kHz spectra and seems present regardless of the chosen setpoint value.

Finally, the effect of the choice of cantilever geometry has been evaluated. For each cantilever, spectra with varying laser frequencies, setpoints and at different regions of interest were measured. Here, we only display the resulting spectra for two different cantilevers of the same kind at a fixed set of parameters: a laser frequency of 1820 kHz and a setpoint of 3V. Figure 6-7 displays the resulting spectra for olivine polished thin section. The generated spectra display the same main absorption bands over the 900 cm^{-1}-1300 cm^{-1} absorption range. The spectra obtained with cantilever 2 (in red, Figure 6-7) seems to have more variation than for cantilever 1 (in blue), but overall, the absorption band and spectra general shapes are consistent regardless of the chosen cantilever.

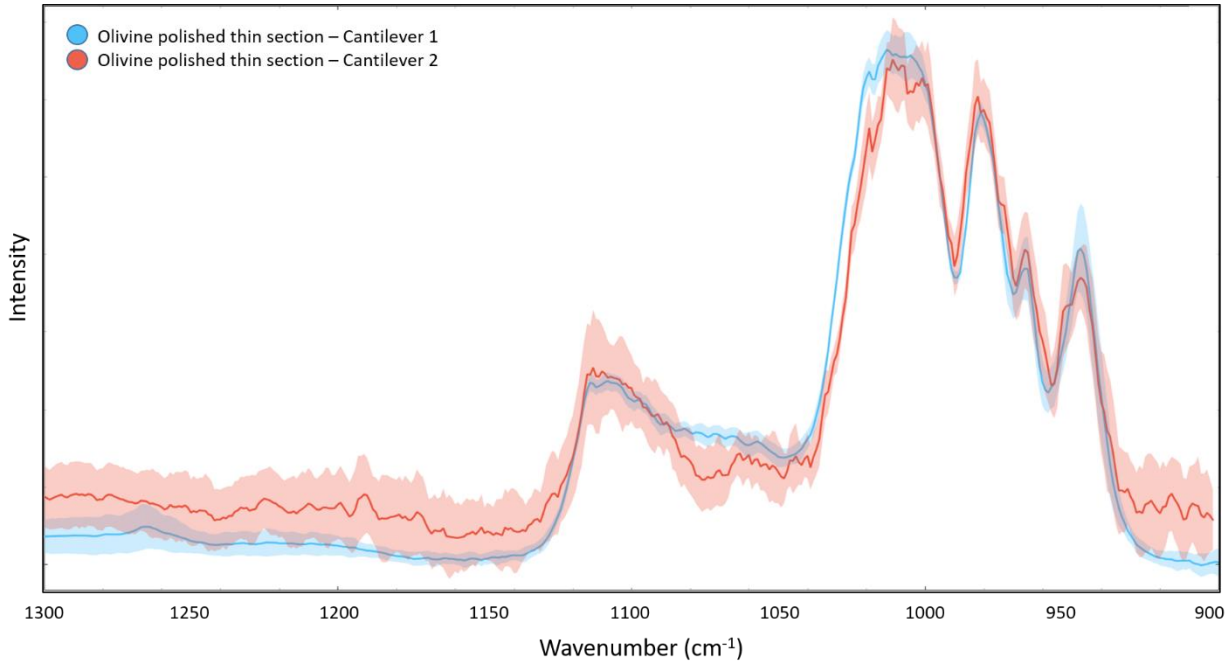

Figure 6-7: AFMIR spectra for olivine polished section with two different cantilever. The light halo surrounding the different spectra represents the spectra variations for the averaged set of spectra.

6.3. Conclusion

In this work, we studied the influence of sample preparations and analyses parameters on the measurement of two different mineral phases. The crystalline orientation of the minerals represents an unknown parameter here, but results indicates that the measured AFM-IR spectra could also dependent on the sample preparation and or support. "Matrix-based" samples where fragments of mineral were embedded in either epoxy or indium foil showed the largest variations in the measured spectra, particularly for epoxy matrix. This might be the result of the interaction between the illuminating laser spot and the matrix, leading to undesirable thermal expansion of the sample holder. However, the acquired spectra for two different minerals types display different bands for a fixed sample preparation method. This indicates that AFMIR can differentiate between two different mineral phases. The polished thin section however, gave rather good and consistent results, although the absorption bands observed in the spectra do not straightforwardly match with the classical FTIR absorption spectra or olivine or pyroxene. This work is a preliminary ttest study, as AFM-IR was first developed for the characterization of organic matter. The effect of crystal orientation and sample thickness still has to be further constrained.

Neither the choice of the cantilever nor the analysis parameters seem to have a significant impact on observed absorption bands in the spectra. However, the s/n ratio of most spectra seem to be dependent on the chosen analysis parameters. In order to optimize the s/n for potential AFMIR mineral analysis, the optimal conditions must be further investigated on a larger set of minerals with different thermal expansion behaviors.

Chapter 7

7. Conclusions and perspectives

The understanding of the formation mechanism of the solar system and its early evolution is closely related to the characterization of the small bodies from the cold external regions of the solar system. Those objects are thought to have better preserved their original characteristics than inner solar system bodies that could have undergone significant hydrothermal alteration. The samples retrieved from the 81P/Wild 2 comet by the Stardust spatial mission revealed the joint presence of organic matter (OM) close to that of primitive meteorites and of mineral phases which formed at high temperature in the internal region of the protoplanetary disk. In particular, typical components present in carbonaceous chondrites (CCs) such as refractory inclusion and chondrules, were found in 81P/Wild 2 sample. Such intimate mixture of mineral and organic phases strongly suggests the presence of a radial transport of material in the early solar system history that brought high temperature inorganic phases to the colder external region of the disk, where comets accreted. This also highlights the possibility of a physico-chemical continuum between asteroids and comets.

AMMs from the Concordia collection are unique samples to study this continuum and to have access to cometary materials as most of the dust falling on Earth is thought to derive from comets (Carrillo-Sánchez et al., 2016; Nesvorný et al., 2010). The micrometeorites presented in this work were collected close to the Concordia station in Antarctica over several campaigns (2006, 2016, 2019). The large majority of Concordia micrometeorites (> 90%) consist in chondritic particles showing similarities with the relatively rare group of CCs (although they cannot be related to a given group of CCs). Previous works from Dobrică et al. (2009) showed that these chondritic micrometeorites from the Concordia collection shared chemical and mineralogical characteristics with the sample recovered from 81P/Wild2 comet, supporting a genetic link between most micrometeorites and cometary materials. A rare family of Concordia micrometeorites (~1%) shows unusual characteristics, being dominated by isotopically anomalous and N-rich organic matter, with a minor mineral component. These Ultracarbonaceous Antarctic Micrometeorites (UCAMMs) can include more than 90 vol% of organic matter. Previous work from Dobrică et al. (2011, 2012) and Dartois et al. (2013, 1018) have studied the Raman and infrared signatures of UCAMMs organic matter, and have provided a first characterization of the minerals in a few UCAMMs by transmission electron microscopy.

In this work, I studied the organic and mineral characterizations of three types of micrometeorites: hydrated chondritic AMMs, non-hydrated chondritic AMMs and UCAMMs. All particles were studied by Fourier-transform infrared (FTIR) and Raman microscopies, in order to retrieve a global view of the composition of their organic matter, and of their mineral content. An in-depth analysis of 8 UCAMMs performed on complementary fragments of the same particles was done using scanning transmission X-ray microscopy coupled with X-ray absorption near edge spectroscopy (STXM-XANES) and scanning transmission electron microscopy (STEM) on thin sections made by focused ion beam (FIB) techniques, allowing the characterization of their organic and mineral content at a spatial resolution down to tens of nanometers. A preliminary study of the characterization of the mineralogical signature by infrared nanospectroscopy by AFM-IR (atomic force microscopy coupled with infrared spectroscopy) was also carried out. This relatively new technique was developed for the characterization of organic compounds, and the study of minerals by AFM-IR is under development.

Infrared and Raman characteristics of chondritic AMMs are consistent with the primitive nature of the organic content of micrometeorites. The characterization of the aliphatic CH components through the 3.4 μm absorption band (around 2920 cm^{-1}) showed that the organic materials within hydrated and non-hydrated chondritic AMMs have a methylene to methyl column density $N(CH_2)/N(CH_3)$ ratio around 2, after taking into account for their respective integrated cross sections. A comparison between the values obtained with this quantification method and with the ratio obtained from direct peak intensity measurements using the CH_3 and CH_2 peaks from literature studies indicates a fairly good linear relationship. The $N(CH_2)/N(CH_3)$ ratio around 2 is consistent with that measured in most organics in extraterrestrial samples, and tends to show an increase in the length of the aliphatic chains compared to carbonaceous matter detected in the interstellar medium (ISM), which has a ratio around 1 (Dartois et al., 2007). The Raman microscopy study of hydrated and non-hydrated chondritic AMMs pointed out differences between these two types of micrometeorites. Non-hydrated chondritic AMMs have spectral parameters of their D and G bands that have values close to the one observed within primitive meteorites. The spectral parameters for hydrated chondritic AMMs however tends to show spectral parameters closer to the one measured in the samples retrieved during the Stardust mission. The spectral parameters of individual spectra of the organic matter in hydrated chondritic AMMs also showed larger variations than for non-hydrated chondritic AMMs, for which the average spectral parameters are close to the values of the individual spectra taken over the area of the whole AMMs. This can result from three different scenarios: the first possibility is that hydrated and non-hydrated chondritic AMMS initially accreted different organic compounds, leading to the observed difference. If they accreted an initial organic material similar to that observed in non-hydrated AMMs, the observed difference can be explained by aqueous alteration of the particles, that would increase heterogeneity of the spectral parameters of the organic matter, at the scale probed by visible Raman microscopy measurements (~0.5-1 μm). Alternatively, if the organic content originally accreted was similar to the one observed in hydrated AMMs, it could have been transformed and homogenized by a thermal process that dehydrated the micrometeorites to result to the one observed in non-hydrated chondritic AMMs. This latter possibility is less likely, as the mineralogy of non-hydrated AMMs does not seem to proceed from the dehydration of hydrated chondritic AMMs.

Overall, the Raman and FTIR microscopy analysis of the organic component of hydrated and non-hydrated chondritic AMMs further emphasize the relationship between micrometeorites and cometary material. The best overlapping of the spectral parameters from Raman spectra of hydrated chondritic AMMs with 81P/Wild 2 materials tends to strengthen the possibility of water circulation on some cometary surface. This could also be explained by the possible asteroid-comet continuum, where cometary material retained the signature of aqueous alteration undergone during asteroidal hydrothermal history, prior to the beginning of cometary activity.

The FTIR characterization of the two UCAMMs identified in this study is in agreement with previous analyses, and the spectral parameters extracted from the Raman spectra correspond to what was previously observed in UCAMMs (Dartois et al., 2013; Dartois et al., 2018; Dobrică et al., 2011). UCAMMs shows Raman spectral parameters very close to the one measured in the cometary material from 81P/Wild 2 retrieved by the Stardust mission, further strengthening a genetic link between UCAMMs and cometary material. The individual spectra measured on the two UCAMMs also show variation ranges similar to those already observed in hydrated chondritic AMMs. The typical nitrile absorption band at 2220 cm^{-1}, expected in UCAMMs due to their high nitrogen content, is also visible for both particles in all Infrared or Raman spectra.

A more detailed characterization of the organic and inorganic content of UCAMMs at high spatial resolution was performed using STEM and STXM-XANES. The STXM-XANES hyperspectral maps reveal the presence of 3 different types of organic matter (OM) in UCAMMs. The OM types referred to as type I and type II are often associated under the form of type I matrix embedding type II OM patches. The STXM-XANES signature of types I & II OM are rather similar, although type II OM shows more contribution from aromatic carbon than for type I. These two types of OM display spectra that resemble that of insoluble organic matter (IOM) chemically extracted from carbonaceous chondrites, possibly indicative of similar formation mechanism and environment. These organic phases are also the ones that contains the crystalline mineral components of UCAMMs. Type III OM is the organic phases that bears most of the nitrogen content of UCAMMs. This OM phase generally has a smooth texture, can extend over several micrometers (it usually covers larger areas than the other types), and is devoid of crystalline minerals. It can occasionally contain glassy phases resembling GEMS (glass embedded with metals and sulfides) that were first identified in IDPs collected in the stratosphere. An estimation of the N/C atomic ratio of type III OM from the STXM-XANES absorptions at the C- and N- K edges gives values ranging from 0.08 to 0.21. This is more than twice the ratio measured in the classical IOMs from CCs. The inorganic content of UCAMM measured by STEM consists mostly in small mineral assemblages, with sizes of few hundreds of nanometers, or single minerals with sizes from 50 nm (and up to 1 μm in one UCAMM), embedded in the abundant carbonaceous matrix. Mineral phases in UCAMMs consist in Mg-rich silicates, either olivines or pyroxenes, iron sulfides and a few iron oxides (mostly Ni-poor). Some more complex assemblages, resembling GEMS in some cases, have been observed and consist in an Si-rich matrix embedding smaller mineral phases such as Mg-rich olivine or pyroxene, Fe-sulfides and rare Ca-rich pyroxenes. A hypocrystalline-like mineral assemblage with an igneous-like texture resembling a chondrule has also been observed. The unexpected presence of a mineral presenting a fibrous texture reminiscent of a phyllosilicate has been observed in one UCAMM. The bulk composition of most of the inorganic phases in UCAMMs showed Si-rich values compared to solar composition.

The N-enrichment observed in type III OM could be explained by a formation of this phase by irradiation of N-rich ices in the external region of the solar system (Augé et al., 2019; Augé et al., 2016; Rojas et al., 2020), implying a different formation location for the different constitutive organic phases observed in UCAMMs. This observation further supports the possibility of a large scale radial transport of material from the inner solar system to the outer region in its early history. The presence of high-temperature phases in UCAMMs, such as minerals, also supports a radial mixing of early solar system components. The presence of a potential hydrated phase within UCAMM further raises the question of aqueous alteration in cometary material. The presence of a hydrated mineral within cometary material could be the result of different formation mechanisms. The first possibility is the inheritance of this altered phase from an already processed parent body that experimented aqueous alteration before its components being incorporated into the UCAMMs' parent body. This could also be the results of an asteroid-comet continuum where asteroid bodies are ejected in the outer solar system after their first steps of thermal and/or aqueous alteration before starting their cometary activity. Finally, in-situ aqueous alteration on cometary surface could also be considered, as some comets are thought to experiment pressure and temperature conditions that would allow the presence of liquid water and could therefore sustain the conditions for direct in-situ alteration during perihelion. The relatively good agreement between the Raman spectral parameters of the organic content of hydrated chondritic

AMMs and UCAMMs could suggest a slight effect of aqueous alteration on the organic content of UCAMMs.

In order to better understand the relationship between AMMs, UCAMMs and cometary material formation processes, several complementary studies are suggested here.

The analysis of the mineral content of hydrated chondritic AMMs with STEM, as well as isotopic characterization of their phyllosilicates, could help better constrain the formation location and mechanism of these hydrated phases in cometary materials. This can be compared to the phyllosilicates observed in CM chondrites to try to better understand the relationship between primitive meteorites and cometary materials.

Aqueous and/or thermal alteration experiments of the organic content of AMMs could also help understanding the larger variation of the Raman spectral parameters observed in hydrated chondritic AMMs and UCAMMs. Identifying if these AMMs initially had similar organic material that was subsequently altered or accreted already different organic precursor could give better constrains on the formation mechanism of organic phases in comets.

Concerning the AFM-IR technique, the characterization of the mineral signature by this technique is under development, and needs further systematic comparison with conventional FTIR on a wide range of mineral samples to assess large scale coherence. These samples will need to be designed to better describe the measured AFM-IR spectra, including the possible diverse crystalline orientations of the minerals under scrutinity. Fine-grained powders are also good samples to characterize by AFM-IR to test for random orientation response of crystals.

Finally, the Hayabusa 2 mission that brought samples for Ryugu's asteroids back on Earth in January 2021 will also help better understand the potential relationship between asteroidal organic and mineral materials and the ones observed in cometary matter. The retrieved samples allow the characterization with the same techniques used for micrometeorites and a much precise characterization of asteroidal material of known origin.

8. Annexes

Synthèse en français

Introduction

Ce travail de thèse se concentre sur l'analyse de micrométéorites récoltées en Antarctique. L'essentiel de la matière extraterrestre atteignant la surface terrestre étant portée par des particules de 200 µm, sous forme de micrométéorites. Ces poussières extra-terrestres sont principalement issues des petits corps du système solaire tels que les astéroïdes et les comètes. Ces corps, de par leur petite taille ou leur formation tardive, n'ont subi que peu ou pas d'altération post-accrétionnelle, et ont donc retenu les caractéristiques physico-chimiques de la matière qu'ils ont originellement accrété. Les micrométéorites offrent donc l'opportunité de mieux caractériser cette matière primitive et potentiellement mieux comprendre les étapes de l'évolution du système solaire. Trois types d'AMMs ont été analysés durant ma thèse : les micrométéorites chondritiques (AMMs) hydratées et anhydres, et les micrométéorites ultracarbonées (UCAMMs). Les AMMs chondritiques sont des grains extraterrestres d'une centaine de micromètres présentant des caractéristiques minéralogiques proches de celle des chondrites carbonées ainsi que des échantillons cométaires ramenés par la mission Stardust. Elles représentent environ 30% de la collection de micrométéorites Concordia. Les UCAMMs sont plus rares et ne représentent que 1% des poussières analysées. Ce sont des grains principalement constitués de matière organique (MO) contenant de petits assemblages minéralogiques. La MO des UCAMMs est particulièrement riche en azote (ratio N/C élémentaire allant jusqu'à 0.2) et présente également des compositions isotopiques marquées par de forts enrichissements en deutérium. L'abondance et l'accessibilité de la MO des UCAMMs permet son analyse in-situ, contrairement à la matière organique insoluble (IOM) des météorites qui nécessite préalablement une extraction par traitement acide.

Analyses InfraRouges (IR) et Raman des AMMs chondritiques

Des fragments de dix micrométéorites chondritiques (AMMS) de la collection Concordia ont été caractérisés en spectroscopie infrarouge (IR) et spectroscopie Raman. Les mesures ont été réalisées sur la ligne SMIS au synchrotron SOLEIL, Orsay.

Les analyses IR révèlent une dichotomie minéralogique au sein de la population d'AMMs chondritiques qui présentent différents type d'absorptions dans la zone correspondant aux silicates (200 – 1300 cm^{-1}). 6 AMMs présentent une signature infrarouge correspondant à celles des phyllosilicates (avec principal pic d'absorption à 1010 cm^{-1}). Les 4 autres AMMs présentent des absorptions plus complexes, correspondant à des mélanges, en proportions différentes, d'olivines et de pyroxènes généralement riches en magnésium. Les absorptions liées aux groupements organiques dans les micrométéorites ne reflètent cependant pas la dichotomie minéralogique observée et des pics similaires sont observés dans les deux groupes d'AMMs chondritiques (hydratées et anhydres) : des absorptions autour de 2900 cm^{-1} liées aux groupements aliphatiques, une absorption a 1640 cm^{-1} associée au C=O ainsi qu'un pic autour de 1600cm^{-1} correspondant au C=C aromatiques.

Les analyses Raman ont été réalisées sur les même fragments que ceux utilisés pour les analyses IR préalablement décrites. Toutes les micrométéorites présentent des spectres Raman dominés par les bandes D et G du carbone. Les paramètres spectraux des spectres des différentes AMMs peuvent ainsi être extraits pour permettre leur comparaison avec d'autres objets extraterrestres. Les analyses des bandes D et G de la MO des AMMs reflètent également la dichotomie observée en infrarouge : les AMMs hydratées présentent des paramètres spectraux

différent des AMMs anhydres. Deux principales tendances sont observables dans les échantillons analysés :

- les paramètres spectraux des AMMs hydratées présentent de valeurs similaires à celles obtenues pour des objets primitifs, ayant subi peu d'altération thermique (largeur à mi-hauteur de la bande D >250 cm^{-1} centre de la bande D >1350 cm^{-1}). Les paramètres de la bande D du carbone des AMMs anhydres ont des valeurs inférieures (largeur < 250cm^{-1}, centre < 1350 cm^{-1}), plus proche de celle observées dans les chondrites carbonées (CCs) primitives.

-La variabilité des paramètres spectraux au sein d'une même micrométéorite est supérieure pour les AMMs hydratées. Les AMMs anhydres présentent des paramètres spectraux plus constants au sein de chaque AMMs, suggérant une matrice organique plus homogène que pour les AMMs hydratées.

Analyses des micrométéorites ultracarbonées (UCAMMs)

Les fragments de deux UCAMMs ont été analysés, dans les mêmes conditions que les AMMs chondritiques, en spectroscopie IR et Raman.

Les spectres infrarouges présentent des caractéristiques différentes dans la zone d'absorption des silicates (200 – 1300 cm^{-1}). Une des UCAMM analysée exhibe une signature infrarouge de silicate anhydre, identifié comme un pyroxène magnésien. Le fragment de la deuxième UCAMM ne présente aucune absorption dans la zone des silicates. Les absorptions liées aux groupements organiques sont en revanche similaires pour les deux UCAMMs, Les principales absorption liées au groupements organiques sont les suivantes : C=C/C=N autour de 1600 cm^{-1}, C≡N à 2200 cm^{-1} et une absorption variable à 2900 cm^{-1} correspondant aux CH_x aliphatiques.

Les analyses Raman des deux UCAMMs révèlent des spectres similaires, dominés par les bandes D et G du carbone. Un pic est également visible à 2200 cm^{-1} et correspond au nitrile (C≡N). La largeur à mi-hauteur et le centre de la bande D dans ces spectres présentent des valeurs supérieures à 250 cm^{-1} et 1350 cm^{-1}, respectivement. Ces valeurs sont proches de celles mesurées pour les AMMs hydratées, et coïncident avec les valeurs obtenues pour les objets primitifs tels que les échantillons de la comète 81P/Wild 2 et les chondrites primitives.

Huit UCAMMs différentes ont également été analysée via spectroscopie X en transmission (STXM-XANES) et microscopie électronique en transmission (STEM) afin de caractériser leur contenu organique et minéralogique. Pour réaliser ces analyses en transmission, des lames FIB (Focused Ion-Beam) d'une centaine de nanomètre d'épaisseur ont été préparés à l'IEMN, Lille.

Les analyses STXM-XANES révèlent la présence de 3 types de matières organiques, présentant des chimies différentes. Les types appelés type I et II ont des chimies similaires à celle de l'IOM des chondrites carbonées primitive. Elles présentent des ratios élémentaires en N/C inférieur à 0,05. La matière organique de type III arbore une texture plus lisse et s'étend souvent sur plusieurs µm. Elle présente une chimie du carbone différente des types I et II, avec une proportion de carbone aromatique plus faible. Sa principale caractéristique étant son très fort enrichissement en azote avec des N/C élémentaires allant jusqu'à 0,2. La majeure fraction d'azote de la MO des UCAMMs est donc portée par cette matière organique de type III.

Les analyses STEM des différentes lames FIB d'UCAMMs révèlent que deux d'entre elles possèdent des assemblages minéralogiques au sein de leur matrice organique. Ces assemblages consistent majoritairement en des aggrégats de différentes phases. La taille totale des assemblages varie de 100 nm au micron pour les plus grands. Les phases présentent au sein de ses assemblages sont généralement semblables d'un assemblage à l'autre : une matrice riche en silicium, contenant des petits minéraux magnésiens présentant une stœchiométrie proche de celle du pyroxène. Ces assemblages contiennent aussi des sulfures de fer (majoritairement de la pentlandite) ainsi que de ponctuels oxydes de fer. Un assemblage présentant une texture fibreuse,

similaire à celle d'un phyllosilicate, a aussi été identifié dans une des lames FIB d'UCAMM. Ce minéral présente une composition riche aluminium et silicium.

Conclusion

Les analyses IR et Raman des AMMs chondritiques hydratées et anhydres ont permis de souligner la similarité de leur contenu organique avec celui des chondrites carbonées primitives. Les paramètres spectraux obtenus pour les AMMs hydratées coïncident également avec les valeurs obtenues par les analyses des échantillons de la comètes Wild 2. Les micrométéorites étant supposé provenir majoritairement des comètes, ces observations soulèvent également la question de la possibilité d'altération aqueuse au sein des matériels cométaires et du rôle de la circulation d'eau dans les processus d'altération de la matière organique.

Les caractérisations du contenu des UCAMMs via STEM et STXM-XANES permet de mieux comprendre l'histoire de ces objets. La similarité entre la matière organique des UCAMMs et celle contenue dans les particules cométaires suggèrent un lieu de formation dans les régions externes du système solaire. L'irradiation de glace riche en azote dans les régions externes du disque protoplanétaire pourrait être à l'origine de la matière organique observé dans les UCAMMs. La présence conjointe de minéraux de haute température et de minéraux hydratés au sein de cette matière organique implique aussi un phénomène de transport efficace dans le jeune système solaire. La présence d'un potentiel phyllosilicate au sein d'une UCAMM suggère également la possibilité de phénomènes d'altération aqueuse sur les surfaces cométaires. La présence de cette phase hydratée pourrait également s'expliquer par un héritage d'un corps parent plus ancien ayant déjà subi des phénomènes d'altérations avant son incorporation au sein du corps cométaire.

STEM data from mineral assemblages in UCAMMs DC06-308 and DC16-309

Table 8-1 : Elemental compositions of the phases in the different mineral assemblages observed in DC06-308 and DC16-309.

Phase	Al	C	Ca	Cl	Cr	Cu	Fe	K	Mg	Mn	N	Na	Ni	O	P	S	Si	Ti	Zn
UCAMM DC06-308 – Assemblage 1																			
Fe Oxide	0,5	14,3	0,7	0,2	0,1	0,0	26,2	0,0	3,0	0,0	1,0	0,0	0,2	42,3	0,7	3,9	6,7	0,0	0,1
FeS – CaPx	0,2	21,4	2,5	0,3	0,0	0,0	14,0	0,0	3,6	0,0	1,9	0,0	0,0	30,6	0,8	20,2	4,2	0,0	0,2
Mg Silicate	1,3	9,1	1,5	0,1	0,2	0,0	3,2	0,1	18,4	0,1	1,3	0,0	0,0	48,3	0,4	1,1	14,7	0,0	0,1
Si-rich matrix	0,9	14,1	1,2	0,2	0,1	0,0	3,5	0,0	5,2	0,0	2,0	0,0	0,1	49,9	0,4	2,2	20,1	0,0	0,1
UCAMM DC06-308 – Assemblage 2																			
Fe Oxide	0,6	18,6	0,8	0,1	0,0	0,0	23,7	0,0	3,0	0,0	0,4	0,0	0,6	37,9	0,4	4,3	9,5	0,0	0,1
FeS + MgSiO	0,8	21,1	0,4	0,2	0,1	0,0	15,8	0,0	3,8	0,1	0,0	0,0	0,8	27,9	0,7	17,2	10,8	0,0	0,3
Si-rich matrix	1,2	11,9	0,8	0,1	0,1	0,0	3,6	0,0	9,9	0,0	0,5	0,0	0,1	50,5	0,4	0,9	19,8	0,0	0,1
Mg-Silicate	0,9	17,0	0,5	0,1	0,1	0,0	4,2	0,0	14,3	0,0	1,6	0,1	0,1	45,7	0,4	1,6	13,3	0,0	0,1
UCAMM DC06-308 – Assemblage 3																			
Fe Oxide	0,3	12,8	0,1	0,2	0,0	0,0	33,8	0,0	2,1	0,0	1,7	0,0	0,0	46,4	0,3	0,5	1,8	0,0	0,2
Fe Sulfides + SiO	0,0	17,5	0,1	0,0	0,2	0,0	19,4	0,1	1,9	0,0	3,4	0,0	0,2	37,7	0,0	14,3	4,8	0,1	0,3
Mg Pyroxene	0,9	5,8	0,5	0,0	0,5	0,0	5,8	0,0	14,1	0,1	1,9	0,2	0,8	53,6	0,3	0,4	15,0	0,0	0,0
Mg Olivine	0,4	8,8	0,0	0,1	0,1	0,0	1,3	0,0	21,3	0,2	2,8	0,0	0,0	51,4	0,1	0,4	13,0	0,0	0,1
Si-rich Matrix	3,0	13,8	0,3	0,2	0,2	0,0	1,9	0,3	5,1	0,1	4,2	0,2	0,1	52,4	0,2	0,7	17,3	0,0	0,1
UCAMM DC16-309 – Assemblage 1																			
FeS – SiO	1,1	34,3	0,0	0,8	0,1	0,0	14,1	0,0	1,5	0,1	4,0	0,8	1,1	24,0	0,5	14,2	3,0	0,0	0,5
FeS	0,0	24,3	0,1	0,1	0,0	0,0	24,3	0,0	0,1	0,0	0,0	0,0	1,1	11,9	0,1	37,0	0,9	0,0	0,1
FeNiS	0,0	33,3	0,0	0,1	0,0	0,0	9,5	0,0	1,4	0,1	1,8	0,1	8,3	17,6	0,0	25,3	2,4	0,1	0,0
Si-rich Matrix	1,9	15,4	0,4	0,3	0,2	0,0	2,6	0,1	2,5	0,0	1,3	0,7	0,2	53,6	0,2	1,0	19,3	0,0	0,2
CaMg Silicate	1,0	12,0	6,6	0,2	0,4	0,0	0,4	0,1	8,3	0,1	2,0	0,6	0,0	52,0	0,3	0,5	15,6	0,0	0,1
Mg Silicate	0,6	9,9	0,9	0,1	0,1	0,0	1,4	0,0	20,1	0,1	1,1	0,7	0,0	49,6	0,2	0,4	14,5	0,0	0,1
UCAMM DC16-309 – Assemblage 2																			
FeS - SiAlO	3,2	23,8	0,1	0,2	0,2	0,0	18,4	0,1	1,7	0,0	0,9	0,7	0,7	30,6	0,1	6,6	12,6	0,0	0,2
FeS	1,0	35,9	0,1	0,2	0,0	0,0	16,8	0,0	0,6	0,0	0,0	0,4	0,2	17,9	0,3	23,4	2,9	0,0	0,2
Phyllosilicate	3,3	22,0	0,0	0,3	0,2	0,0	2,3	0,1	6,3	0,0	1,6	0,6	0,0	46,2	0,3	1,1	15,2	0,0	0,4
Mg Silicate	1,8	20,3	0,1	0,2	0,2	0,0	2,9	0,1	12,8	0,0	0,9	0,8	0,0	44,0	0,3	2,7	12,6	0,0	0,3

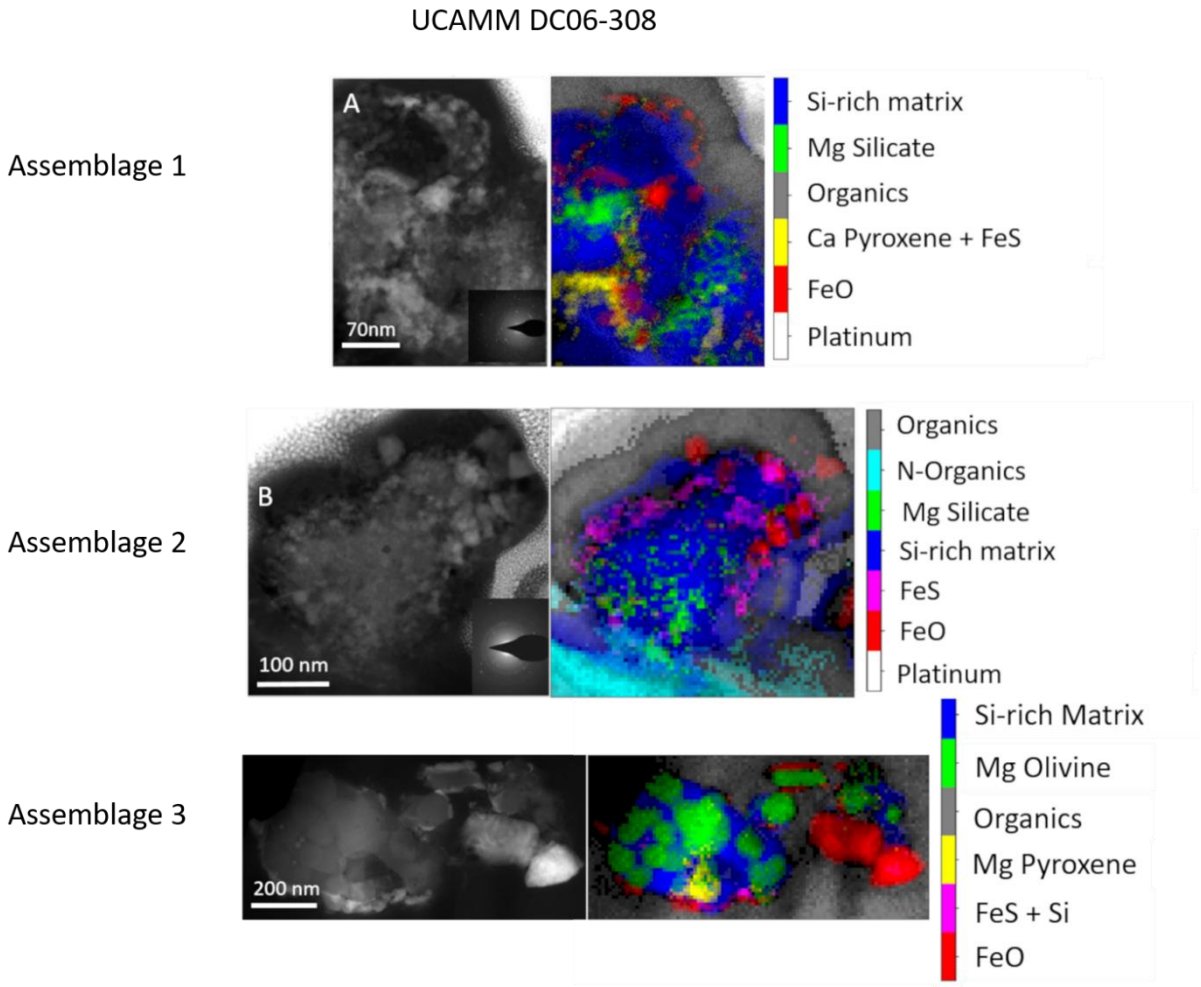

Figure 8-1: (left) High Angle Annular Dark Field (HAADF) image of 3 mineral assemblages in DC06-308. (right) False color images corresponding to the EDX maps of the different phases identified by Principal Component Analysis (PCA). The phases are ordered by decreasing number of counts in the respective spectra

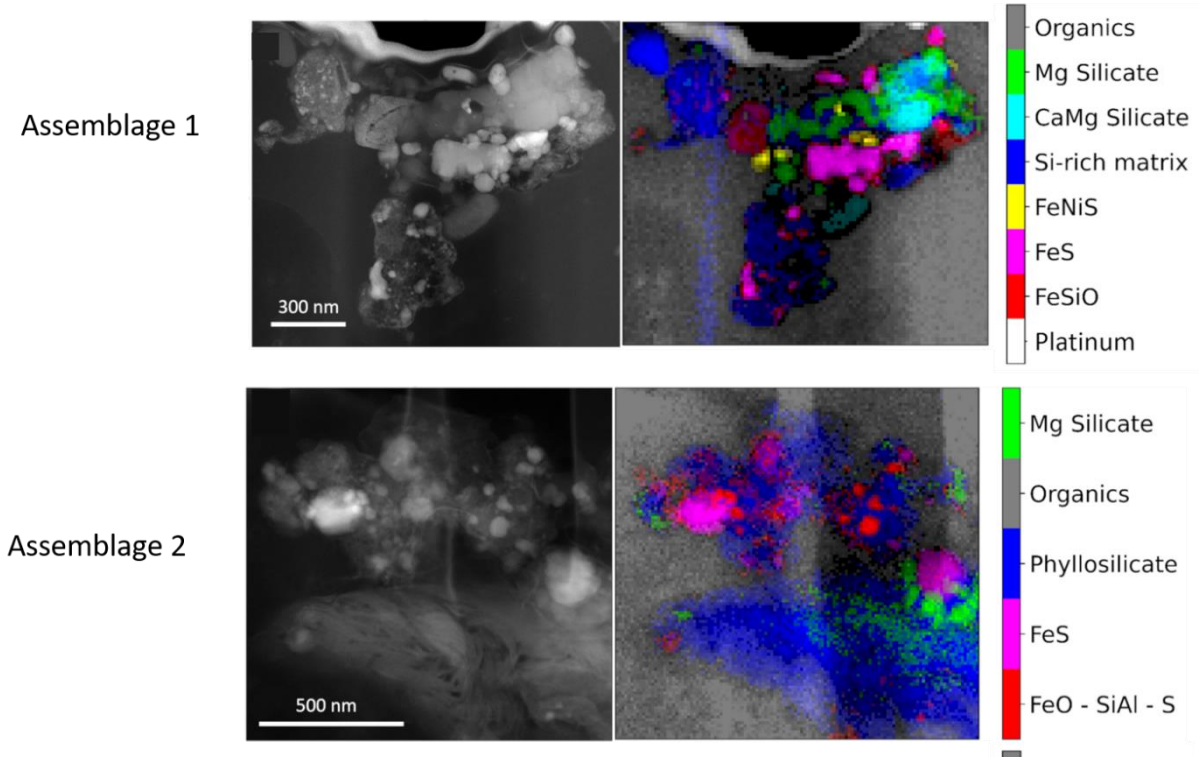

Figure 8-2: (left) High angle annular dark field (HAADF) images and (right) False color images corresponding to the map of the different phases identified by Principal Component Analysis of the EDX hyperspectral maps.. (A) Phyllosilicate-like phase (fibrous phase) decorated with a mineral assemblage. (B) Mineral assemblage located at the border of a vesicle. Both assemblages are embedded in the organic matter.

References

Ade, H. and Hitchcock, A.P. (2008) NEXAFS microscopy and resonant scattering: Composition and orientation probed in real and reciprocal space. Polymer 49, 643-675.

Alexander, C.M.O.D., Cody, G.D., De Gregorio, B.T., Nittler, L.R. and Stroud, R.M. (2017) The nature, origin and modification of insoluble organic matter in chondrites, the major source of Earth's C and N. Chemie der Erde - Geochemistry 77, 227-256.

Alexander, C.M.O.D., Fogel, M., Yabuta, H. and Cody, G.D. (2007) The origin and evolution of chondrites recorded in the elemental and isotopic compositions of their macromolecular organic matter. Geochimica et Cosmochimica Acta 71, 4380-4403.

Alexander, C.M.O.D., Newsome, S.D., Fogel, M.L., Nittler, L.R., Busemann, H. and Cody, G.D. (2010) Deuterium enrichments in chondritic macromolecular material—Implications for the origin and evolution of organics, water and asteroids. Geochimica et Cosmochimica Acta 74, 4417-4437.

Ali, K., Sonbawane, S., Chate, D., Siingh, D., Rao, P., Safai, P. and Budhavant, K. (2010) Chemistry of snow and lake water in Antarctic region. Journal of earth system science 119, 753-762.

Altwegg, K., Balsiger, H., Hänni, N., Rubin, M., Schuhmann, M., Schroeder, I., Sémon, T., Wampfler, S., Berthelier, J.-J., Briois, C., Combi, M., Gombosi, T.I., Cottin, H., De Keyser, J., Dhooghe, F., Fiethe, B. and Fuselier, S.A. (2020) Evidence of ammonium salts in comet 67P as explanation for the nitrogen depletion in cometary comae. Nature Astronomy.

Augé, B., Dartois, E., Boduch, P., Domaracka, A., Rothard, H., Brunetto, R., Engrand, C., Bardin, N., Delauche, L., Duprat, J., Silva Vignoli Muniz, G., Mejia, C. and Martinez, R. (2015) Irradiation of nitrogen rich ices by swift heavy ions, clues to the origin of ultracarbonaceous micrometeorites, Swift Heavy Ions in Matter, Darmstadt.

Augé, B., Dartois, E., Duprat, J., Engrand, C., Slodzian, G., Wu, T.D., Guerquin-Kern, J.L., Vermesse, H., Agnihotri, A.N., Boduch, P. and Rothard, H. (2019) Hydrogen isotopic anomalies in extraterrestrial organic matter: role of cosmic ray irradiation and implications for UCAMMs. A&A 627, A122.

Augé, B., Dartois, E., Engrand, C., Duprat, J., Godard, M., Delauche, L., Bardin, N., Mejía, C., Martinez, R., Muniz, G., Domaracka, A., Boduch, P. and Rothard, H. (2016) Irradiation of nitrogen-rich ices by swift heavy ions. Clues for the formation of ultracarbonaceous micrometeorites. A&A 592, A99.

Baker, M.J., Hughes, C.S. and Hollywood, K.A. (2016) Raman spectroscopy. Biophotonics: Vibrational Spectroscopic Diagnostics, 1-94.

Bardyn, A., Baklouti, D., Briois, C., Cottin, H., Engrand, C., Fischer, H., Fray, N., Gardner, E., Hornung, K., Isnard, R., Langevin, Y., Lehto, H., Le Roy, L., Ligier, N., Merouane, S., Modica, P., Orthous-Daunay, F.-R., Paquette, J., Rynö, J., Schulz, R., Silén, J., Siljeström, S., Stenzel, O., Thirkell, L., Varmuza, K., Zaprudin, B., Kissel, J. and Hilchenbach, M. (2018) Global Composition of Cometary Dust Particles from 67P/Churyumov-Gerasimenko as Deduced from the COSIMA/Rosetta Instrument, LPSC, p. #1531.

Bardyn, A., Baklouti, D., Cottin, H., Fray, N., Briois, C., Paquette, J., Stenzel, O., Engrand, C., Fischer, H. and Hornung, K. (2017) Carbon-rich dust in comet 67P/Churyumov-Gerasimenko measured by COSIMA/Rosetta. Monthly Notices of the Royal Astronomical Society 469, S712-S722.

Battandier, M., Bonal, L., Quirico, E., Beck, P., Engrand, C., Duprat, J. and Dartois, E. (2018) Characterization of the organic matter and hydration state of Antarctic micrometeorites: A reservoir distinct from carbonaceous chondrites. Icarus 306, 74-93.

Beck, P., Garenne, A., Quirico, E., Bonal, L., Montes-Hernandez, G., Moynier, F. and Schmitt, B. (2014) Transmission infrared spectra (2-25 mum) of carbonaceous chondrites (CI, CM, CV-CK, CR, C2 ungrouped): Mineralogy, water, and asteroidal processes. Icarus 229, 263-277.

Berger, E.L., Zega, T.J., Keller, L.P. and Lauretta, D.S. (2011) Evidence for aqueous activity on comet 81P/Wild 2 from sulfide mineral assemblages in Stardust samples and CI chondrites. Geochimica et Cosmochimica Acta 75, 3501-3513.

Bergin, E.A., Blake, G.A., Ciesla, F., Hirschmann, M.M. and Li, J. (2015) Tracing the ingredients for a habitable earth from interstellar space through planet formation. Proceedings of the National Academy of Sciences 112, 8965-8970.
Birnstiel, T., Klahr, H. and Ercolano, B. (2012) A simple model for the evolution of the dust population in protoplanetary disks. Astronomy & Astrophysics 539, A148.
Biver, N., Bockelée-Morvan, D., Paubert, G., Moreno, R., Crovisier, J., Boissier, J., Bertrand, E., Boussier, H., Kugel, F., McKay, A., Russo, N.D. and DiSanti, M.A. (2018) The extraordinary composition of the blue comet C/2016 R2 (PanSTARRS)★★★. A&A 619, A127.
Bockelée-Morvan, D., Gautier, D., Hersant, F., Huré, J.M. and Robert, F. (2002) Turbulent radial mixing in the solar nebula as the source of crystalline silicates in comets. Astronomy and Astrophysics 384, 1107-1118.
Bonal, L. (2006) Matière organique et métamorphisme thermique dans les chondrites primitives. Université Joseph-Fourier-Grenoble I.
Bonal, L., Bourot-Denise, M., Quirico, E., Montagnac, G. and Lewin, E. (2007) Organic matter and metamorphic history of CO chondrites. Geochimica et Cosmochimica Acta 71, 1605-1623.
Bonal, L., Quirico, E., Bourot-Denise, M. and Montagnac, G. (2006) Determination of the petrologic type of CV3 chondrites by Raman spectroscopy of included organic matter. Geochimica et Cosmochimica Acta 70, 1849-1863.
Bonnet, J.-Y., Quirico, E., Buch, A., Thissen, R., Szopa, C., Carrasco, N., Cernogora, G., Fray, N., Cottin, H., Roy, L.L., Montagnac, G., Dartois, E., Brunetto, R., Engrand, C. and Duprat, J. (2015) Formation of analogs of cometary nitrogen-rich refractory organics from thermal degradation of tholin and HCN polymer. Icarus 250, 53-63.
Bouwman, J., Th, H., Hillenbrand, L.A., Meyer, M.R., Pascucci, I., Carpenter, J., Hines, D., Kim, J.S., Silverstone, M.D., Hollenbach, D. and Wolf, S. (2008) The Formation and Evolution of Planetary Systems: Grain Growth and Chemical Processing of Dust in T Tauri Systems. The Astrophysical Journal 683, 479.
Bradley, J. and Ishii, H. (2017) An inconvenient reality: terrestrial alteration of interplanetary dust particles (IDPs) and micrometeorites (MMs), 80th Annual Meeting of the Meteoritical Society, p. 6260.
Bradley, J., Ishii, H., Wozniakiewicz, P., Noguchi, T., Engrand, C. and Brownlee, D. (2014) Impact of the terrestrial environment on the compositions of GEMS. LPI, 1178.
Bradley, J.P. (1988) Analysis of chondritic interplanetary dust thin-sections. Geochimica et Cosmochimica Acta 52, 889-900.
Bradley, J.P. (2003) Interplanetary Dust Particles. Treatise on Geochemistry 1, 711.
Bradley, J.P. (2005) Interplanetary dust particles, in: Davis, A.M., Holland, H.D., Turekian, K.K. (Eds.), Meteorites, Comets and Planets: Treatise on Geochemistry. Elsevier-Pergamon, Oxford, pp. 689-711.
Browning, L.N., McSween, H.Y. and Zolensky, M.E. (1996) Correlated alteration effects in CM carbonaceous chondrites. GCA 60, 2621-2633.
Brownlee, D. (2014) The Stardust mission: analyzing samples from the edge of the solar system. Annual Review of Earth and Planetary Sciences 42, 179-205.
Brownlee, D.E., Hodge, P.W. and Bucher, W. (1971) The physical nature of interplanetary dust as inferred by particles collected at 35 km, International Astronomical Union Colloquium. Cambridge University Press, pp. 291-295.
Brownlee, D.E., Joswiak, D.J., Love, S.G., Bradley, J.P., Nier, A.O. and Schlutter, D.J. (1994) Identification and analysis of of cometary IDPs, LPSC, pp. 185-186.
Bunch, T.E. and Chang, S. (1980) Carbonaceous chondrites-II. Carbonaceous chondrite phyllosilicates and light element geochemistry as indicators of parent body processes and surface conditions. GCA 44, 1543-1577.
Busemann, H., Alexander, C.M.O.D. and Nittler, L.R. (2007) Characterization of insoluble organic matter in primitive meteorites by microRaman spectroscopy. Meteoritics and Planetary Science 42, 1387-1416.

Campins, H., Hargrove, K., Pinilla-Alonso, N., Howell, E.S., Kelley, M.S., Licandro, J., Mothé-Diniz, T., Fernández, Y. and Ziffer, J. (2010) Water ice and organics on the surface of the asteroid 24 Themis. Nature 464, 1320-1321.
Carrillo-Sánchez, J.D., Nesvorný, D., Pokorný, P., Janches, D. and Plane, J.M.C. (2016) Sources of cosmic dust in the Earth's atmosphere. Geophysical Research Letters 43, 11,979-911,986.
Carrillo-Sánchez, J.D., Plane, J.M.C., Feng, W., Nesvorný, D. and Janches, D. (2015) On the size and velocity distribution of cosmic dust particles entering the atmosphere. Geophysical Research Letters 42, 6518-6525.
Changela, H.G., Le Guillou, C., Bernard, S. and Brearley, A.J. (2018) Hydrothermal evolution of the morphology, molecular composition, and distribution of organic matter in CR (Renazzo-type) chondrites. Meteoritics & Planetary Science 53, 1006-1029.
Charon, E., Engrand, C., Benzerara, K., Leroux, H., Swaraj, S., Belkhou, R., Duprat, J., Dartois, E., Godard, M. and Delauche, L. (2017) A C-, N-, O-XANES and TEM study of organic matter and minerals in ultracarbonaceous Antarctic micrometeorites (UCAMMs), LPSC, p. #2085.
Ciesla, F.J. (2009) Two-dimensional transport of solids in viscous protoplanetary disks. Icarus 200, 655-671.
Cremonese, G., Boehnhardt, H., Crovisier, J., Rauer, H., Fitzsimmons, A., Fulle, M., Licandro, J., Pollacco, D., Tozzi, G. and West, R. (1997) Neutral sodium from comet Hale-Bopp: a third type of tail. The Astrophysical Journal Letters 490, L199.
Dartois, E., Caro, G.M.M., Deboffle, D., Montagnac, G. and d'Hendecourt, L. (2005) Ultraviolet photoproduction of ISM dust. A&A 432, 895-908.
Dartois, E., Engrand, C., Brunetto, R., Duprat, J., Pino, T., Quirico, E., Remusat, L., Bardin, N., Briani, G., Mostefaoui, S., Morinaud, G., Crane, B., Szwec, N., Delauche, L., Jamme, F., Sandt, C. and Dumas, P. (2013) UltraCarbonaceous Antarctic micrometeorites, probing the Solar System beyond the nitrogen snow-line. Icarus 224, 243-252.
Dartois, E., Engrand, C., Duprat, J., Godard, M., Charon, E., Delauche, L., Sandt, C. and Borondics, F. (2018) Dome C ultracarbonaceous Antarctic micrometeorites. Infrared and Raman fingerprints. A&A 609, A65.
Dartois, E., Geballe, T.R., Pino, T., Cao, A.-T., Jones, A., Deboffle, D., Guerrini, V., Bréchignac, P. and D'Hendecourt, L. (2007) IRAS 08572+3915: constraining the aromatic versus aliphatic content of interstellar HACs. Astronomy and Astrophysics 463, 635-640.
Dartois, E., Marco, O., Muñoz-Caro, G., Brooks, K., Deboffle, D. and d'Hendecourt, L. (2004) Organic matter in Seyfert 2 nuclei: Comparison with our Galactic center lines of sight. Astronomy & Astrophysics 423, 549-558.
Dazzi, A., Prater, C.B., Hu, Q., Chase, D.B., Rabolt, J.F. and Marcott, C. (2012) AFM–IR: combining atomic force microscopy and infrared spectroscopy for nanoscale chemical characterization. Applied spectroscopy 66, 1365-1384.
Dazzi, A., Prazeres, R., Glotin, F. and Ortega, J.M. (2005) Local infrared microspectroscopy with subwavelength spatial resolution with an atomic force microscope tip used as a photothermal sensor. Opt. Lett. 30, 2388-2390.
De Gregorio, B.T., Stroud, R.M., Cody, G.D., Nittler, L.R., David Kilcoyne, A.L. and Wirick, S. (2011) Correlated microanalysis of cometary organic grains returned by Stardust. Meteoritics & Planetary Science 46, 1376-1396.
De Gregorio, B.T., Stroud, R.M., Nittler, L.R. and Kilcoyne, A.L.D. (2017) Evidence for Reduced, Carbon-rich Regions in the Solar Nebula from an Unusual Cometary Dust Particle. The Astrophysical Journal 848, 113.
DeMeo, F., Alexander, C., Walsh, K., Chapman, C. and Binzel, R. (2015) The compositional structure of the asteroid belt. Asteroids iv 1, 13.
DeMeo, F. and Carry, B. (2013) The taxonomic distribution of asteroids from multi-filter all-sky photometric surveys. Icarus 226, 723-741.
DeMeo, F.E. and Carry, B. (2014) Solar System evolution from compositional mapping of the asteroid belt. Nature 505, 629-634.

Demšar, J., Curk, T., Erjavec, A., Gorup, Č., Hočevar, T., Milutinovič, M., Možina, M., Polajnar, M., Toplak, M. and Starič, A. (2013) Orange: data mining toolbox in Python. the Journal of machine Learning research 14, 2349-2353.
Dobrică, E. (2010) Les micrométéorites CONCORDIA : des neiges antarctiques aux glaces cométaires. Université Paris Sud XI, Orsay, p. 167.
Dobrică, E., Engrand, C., Duprat, J., Gounelle, M., Leroux, H., Quirico, E. and Rouzaud, J.-N. (2009) Connection between micrometeorites and Wild 2 particles: From Antarctic snow to cometary ices. Meteoritics and Planetary Science 44, 1643-1661.
Dobrica, E., Engrand, C., Leroux, H. and Duprat, J. (2010) Investigation of Ultracarbonaceous Antarctic Micrometeorites by Analytical Transmission Electron Microscopy, Lunar and Planetary Science, p. 1613.
Dobrică, E., Engrand, C., Leroux, H. and Duprat, J. (2010) Investigation of ultracarbonaceous Antarctic micrometeorites by analytical transmission electron microscopy, LPSC, p. #1613.
Dobrică, E., Engrand, C., Leroux, H., Rouzaud, J.N. and Duprat, J. (2012) Transmission electron microscopy of CONCORDIA ultracarbonaceous Antarctic micrometeorites (UCAMMs): mineralogical properties. Geochimica et Cosmochimica Acta 76, 68-82.
Dobrica, E., Engrand, C., Quirico, E., Montagnac, G. and Duprat, J. (2008) New clues on composition and structure of carbonaceous matter in Antarctic micrometeorites. Meteoritics & Planetary Science 43, A38-A38.
Dobrică, E., Engrand, C., Quirico, E., Montagnac, G. and Duprat, J. (2011) Raman characterization of carbonaceous matter in CONCORDIA Antarctic micrometeorites. Meteoritics and Planetary Science 46, 1363-1375.
Dobrica, E., Ogliore, R.C., Engrand, C., Nagashima, K. and Brearley, A.J. (2018) Origins of Secondary Minerals in Micrometeorites, Microscopy and Microanalysis, pp. 2096-2097.
Donahue, T.M. (1999) New analysis of hydrogen and deuterium escape from Venus. Icarus 141, 226-235.
Duprat, J., Dobrică, E., Engrand, C., Aléon, J., Marrocchi, Y., Mostefaoui, S., Meibom, A., Leroux, H., Rouzaud, J.-N., Gounelle, M. and Robert, F. (2010) Extreme Deuterium Excesses in Ultracarbonaceous Micrometeorites from Central Antarctic Snow. Science 328, 742-745
Duprat, J., Engrand, C., Maurette, M., Kurat, G., Gounelle, M. and Hammer, C. (2007) Micrometeorites from central Antarctic snow: The CONCORDIA collection. Advances in Space Research 39, 605-611.
Engrand, C., Benzerara, K., Leroux, H., Duprat, J., Dartois, E., Bardin, N. and Delauche, L. (2015a) Carbonaceous phases and mineralogy of ultracarbonaceous Antarctic micrometeorites identified by C- and N-XANES/STXM and TEM LPSC, p. #1902.
Engrand, C., Benzerara, K., Leroux, H., Duprat, J., Dartois, E., Bardin, N. and Delauche, L. (2015b) Carbonaceous Phases and Mineralogy of Ultracarbonaceous Antarctic Micrometeorites Identified by C- and N-XANES/STXM and TEM, LPSC, Lunar and Planetary Science Conference, p. 1902.
Engrand, C., Briois, C., Thirkell, L. and Cottin, H. (2007a) A Concordia Antarctic micrometeorite used as a cometary proxy for the analyses of COSIMA onboard ROSETTA. MAPS 42 suppl., A42.
Engrand, C., Duprat, J., Maurette, M. and Gounelle, M. (2007b) Fe-Ni sulfides in Concordia Antarctic micrometeorites. LPSC XXXVIII, #1668 (CD-ROM).
Engrand, C. and Maurette, M. (1998) Carbonaceous micrometeorites from Antarctica. MAPS 33, 565-580.
Ferrari, A.C. and Robertson, J. (2000) Interpretation of Raman spectra of disordered and amorphous carbon. Physical Review B 61, 14095-14107.
Flynn, G.J., Keller, L.P., Wirick, S. and Jacobsen, C. (2003) A Preliminary Assessment of the Organic Content of Interplanetary Dust Particles. LPSC XXXIV, 1652-1653.
Folco, L., Rochette, P., Gattacceca, J. and Perchiazzi, N. (2005) Micrometeorites from Frontier Mountain, Antarctica. Meteoritics and Planetary Science 40, A49.
Frank, D.R., Zolensky, M.E. and Le, L. (2014) Olivine in terminal particles of Stardust aerogel tracks and analogous grains in chondrite matrix. Geochimica et Cosmochimica Acta 142, 240-259.

Fray, N., Baklouti, D., Bardyn, A., Briois, C., Cottin, H., Engrand, C., Fischer, H., Hilchenbach, M., Isnard, R., Le Roy, L., Modica, P., Paquette, J., Ryno, J., Stenzel, O., Siljeström, S. and Thirkell, L. (2017) Characterization of the refractory organic matter present in the dust particles of 67P/Churyumov-Gerasimenko, EGU General Assembly Conference, p. 12953.

Fray, N., Bardyn, A., Cottin, H., Altwegg, K., Baklouti, D., Briois, C., Colangeli, L., Engrand, C., Fischer, H., Glasmachers, A., Grün, E., Haerendel, G., Henkel, H., Höfner, H., Hornung, K., Jessberger, E.K., Koch, A., Krüger, H., Langevin, Y., Lehto, H., Lehto, K., Le Roy, L., Merouane, S., Modica, P., Orthous-Daunay, F.-R., Paquette, J., Raulin, F., Rynö, J., Schulz, R., Silén, J., Siljeström, S., Steiger, W., Stenzel, O., Stephan, T., Thirkell, L., Thomas, R., Torkar, K., Varmuza, K., Wanczek, K.-P., Zaprudin, B., Kissel, J. and Hilchenbach, M. (2016) High-molecular-weight organic matter in the particles of comet 67P/Churyumov–Gerasimenko. Nature 538, 72-74.

Fujii, Y. (1983) Seasonal variation of pH values in snow at Halley Base and Mizuho Station, Antarctica.

Genge, M.J., Engrand, C., Gounelle, M. and Taylor, S. (2008) The classification of micrometeorites. MAPS 43, 497-515.

Gounelle, M. (2011) The asteroid-comet continuum: in search of lost primitivity. Elements 7, 29-34.

Gourier, D., Robert, F., Delpoux, O., Binet, L., Vezin, H., Moissette, A. and Derenne, S. (2008) Extreme deuterium enrichment of organic radicals in the Orgueil Meteorite; revisiting the interstellar interpretation? Geochimica et Cosmochimica Acta 72, 1914-1923.

Greshake, A., Klöck, W., Arndt, P., Maetz, M., Flynn, G.J., Bajt, S. and Bischoff, A. (1998) Heating experiments simulating atmospheric entry heating of micrometeorites. Clues to their parent body sources. MAPS 33, 267-290.

Grossman, L. (1972) Condensation in the primitive solar nebula. Geochimica et Cosmochimica Acta 36, 597-619.

Guérin, B., Engrand, C., Le Guillou, C., Leroux, H., Duprat, J., Dartois, E., Bernard, S., Benzerara, K., Rojas, J., Godard, M., Delauche, L. and Troadec, D. (2020) STEM and STXM-XANES Analysis of FIB Sections of Ultracarbonaceous Antarctic Micrometeorites (UCAMMs), LPSC. Lunar and Planetary Institute, Houston, p. #2117.

Harker, D.E., Woodward, C.E. and Wooden, D.H. (2005) The dust grains from 9P/Tempel 1 before and after the encounter with Deep Impact. Science 310, 278-280.

Henke, B., Lee, P., Tanaka, T., Shimabukuro, R. and Fujikawa, B. (1982) Low-energy X-ray interaction coefficients: Photoabsorption, scattering, and reflection: E= 100–2000 eV Z= 1–94. Atomic data and nuclear data tables 27, 1-144.

Henke, B.L., Gullikson, E.M. and Davis, J.C. (1993) X-ray interactions: photoabsorption, scattering, transmission, and reflection at E= 50-30,000 eV, Z= 1-92. Atomic data and nuclear data tables 54, 181-342.

Hsieh, H.H. (2017) Asteroid–comet continuum objects in the solar system. Philosophical Transactions of the Royal Society A: Mathematical, Physical and Engineering Sciences 375, 20160259.

Hsieh, H.H. and Jewitt, D. (2006) A population of comets in the main asteroid belt. Science 312, 561-563.

Hsieh, H.H., Yang, B., Haghighipour, N., Kaluna, H.M., Fitzsimmons, A., Denneau, L., Novakovic, B., Jedicke, R., Wainscoat, R.J., Armstrong, J.D., Duddy, S.R., Lowry, S.C., Trujillo, C.A., Micheli, M., Keane, J.V., Urban, L., Riesen, T., Meech, K.J., Abe, S., Cheng, Y.C., Chen, W.P., Granvik, M., Grav, T., Ip, W.H., Kinoshita, D., Kleyna, J., Lacerda, P., Lister, T., Milani, A., Tholen, D.J., Veres, P., Lisse, C.M., Kelley, M.S., Fernandez, Y.R., Bhatt, B.C., Sahu, D.K., Kaiser, N., Chambers, K.C., Hodapp, K.W., Magnier, E.A., Price, P.A. and Tonry, J.L. (2012) Discovery of Main-Belt Comet P/2006 VW139 by Pan-STARRS1. LPI Contributions 1667, 6313.

Ishii, H.A., Bradley, J.P., Dai, Z.R., Chi, M., Kearsley, A.T., Burchell, M.J., Browning, N.D. and Molster, F. (2008) Comparison of comet 81P/Wild 2 dust with interplanetary dust from comets. Science 319, 447-450.

Isnard, R., Bardyn, A., Fray, N., Briois, C., Cottin, H., Paquette, J., Stenzel, O., Alexander, C., Baklouti, D., Engrand, C., Orthous-Daunay, F.-R., Siljeström, S., Varmuza, K. and Hilchenbach, M. (2018)

H/C elemental ratios of the refractory organic matter in cometary particles of 67P/Churyumov-Gerasimenko, European Planetary Science Congress, pp. EPSC2018-2416.
Jaeger, C., Molster, F.J., Dorschner, J., Henning, T., Mutschke, H. and Waters, L.B.F.M. (1998) Steps toward interstellar silicate mineralogy. IV. The crystalline revolution. Astronomy and Astrophysics 339, 904-916.
Jessberger, E.K., Christoforidis, A. and Kissel, J. (1988) Aspects of the major element composition of Halley's dust. Nature 332, 691-695.
Keller, L.P. and Messenger, S. (2011) On the origins of GEMS grains. Geochimica et Cosmochimica Acta 75, 5336-5365.
Keller, L.P., Messenger, S., Scott, E.R.D. and Reipurth, B. (2005) The Nature and Origin of Interplanetary Dust: High-Temperature Components, in: Krot, A.N. (Ed.), Chondrites and the Protoplanetary Disk, p. 657.
Keller, L.P., Thomas, K.L. and McKay, D.S. (1992) An interplanetary dust particle with link to CI chondrites. GCA 56, 1409-1412.
Keller, L.P., Thomas, K.L. and McKay, D.S. (1994) Carbon in primitive interplanetary dust particles, in: Zolensky, M.E., Wilson, T.L., Rietmeijer, F.J.M., Flynn, G.J. (Eds.), Analysis of Interplanetary Dust, AIP Conf. Proc. Amer. Inst. Physics Press, New York, pp. 159-164.
Kemper, F., Vriend, W.J. and Tielens, A.G.G.M. (2004) The absence of crystalline silicates in the diffuse interstellar medium. The Astrophysical Journal 609, 826-837.
Kemper, F., Vriend, W.J. and Tielens, A.G.G.M. (2005) Erratum: ``The Absence of Crystalline Silicates in the Diffuse Interstellar Medium'' (ApJ, 609, 826 [2004]). The Astrophysical Journal 633, 534-534.
Kissel, J., Altwegg, K., Briois, C., Clark, B.C., Colangeli, L., Cottin, H., Czempiel, S., Eibl, J., Engrand, C., Fehringer, H.M., Feuerbacher, B., Fischer, H., Fomenkova, M., Glasmachers, A., Greenberg, J.M., Grün, E., Haerendel, G., Henkel, H., Hilchenbach, M., von Hoerner, H., Höfner, H., Hornung, K., Jessberger, E.K., Koch, A., Krüger, H., Langevin, Y., Martin, P., Parigger, P., Raulin, F., Rüdenauer, F., Rynö, J., Schmid, E.R., Schulz, R., Silén, J., Steiger, W., Stephan, T., Thirkell, L., Thomas, R., Torkar, K., Utterback, N.G., Varmuza, K., Wanczek, K.P., Werther, W. and Zscheeg, H. (2009) COSIMA: High resolution time-of-flight secondary ion mass spectrometer for the analysis of cometary dust particles onboard ROSETTA, in: Schultz, R., et al. (Eds.), ROSETTA : ESA's Mission to the Origin of the Solar System. Springer Science, pp. 201-242.
Kissel, J., Brownlee, D.E., Buchler, K., Clark, B.C., Fechtig, H., Grun, E., Hornung, K., Igenbergs, E.B., Jessberger, E.K., Krueger, F.R., Kuczera, H., McDonnell, J.A.M., Morfill, G.M., Rahe, J., Schwehm, G.H., Sekanina, Z., Utterback, N.G., Volk, H.J. and Zook, H.A. (1986) Composition of comet Halley dust particles from Giotto observations. Nature 321, 336-337.
Kissel, J. and Krueger, F.R. (1987) The organic component in dust from comet Halley as measured by the PUMA mass spectrometer on board VEGA 1. Nature 326, 755-760.
Kurat, G., Koeberl, C., Presper, T., Brandstätter, F. and Maurette, M. (1994) Petrology and geochemistry of Antarctic micrometeorites. GCA 58, 3879-3904.
Le Guillou, C., Bernard, S., Brearley, A.J. and Remusat, L. (2014) Evolution of organic matter in Orgueil, Murchison and Renazzo during parent body aqueous alteration: In situ investigations. Geochimica et Cosmochimica Acta 131, 368-392.
Le Guillou, C., Bernard, S., De la Pena, F. and Le Brech, Y. (2018) XANES-based quantification of carbon functional group concentrations. Analytical chemistry 90, 8379-8386.
Le Guillou, C. and Brearley, A. (2014) Relationships between organics, water and early stages of aqueous alteration in the pristine CR3.0 chondrite MET 00426. Geochimica et Cosmochimica Acta 131, 344-367.
Le Guillou, C., Changela, H.G. and Brearley, A.J. (2015) Widespread oxidized and hydrated amorphous silicates in CR chondrites matrices: Implications for alteration conditions and H2 degassing of asteroids. Earth and Planetary Science Letters 420, 162-173.
Le Guillou, C., Zanetta, P., Leroux, H., Brearley, A., Zanda, B. and Hewins, R. (2019) Amorphous Silicates in Carbonaceous and Ordinary Chondrites, 82nd Annual Meeting of The Meteoritical Society, p. 6267.

Lee, J.-E., Bergin, E.A. and Nomura, H. (2010) The solar nebula on fire: A solution to the carbon deficit in the inner solar system. The Astrophysical Journal Letters 710, L21.
Leroux, H., Cuvillier, P., Zanda, B. and Hewins, R.H. (2015) GEMS-like material in the matrix of the Paris meteorite and the early stages of alteration of CM chondrites. Geochimica et Cosmochimica Acta 170, 247-265.
Leroux, H., Rietmeijer, F.J.M., Velbel, M.A., Brearley, A.J., Jacob, D., Langenhorst, F., Bridges, J.C., Zega, T.J., Stroud, R.M., Cordier, P., Harvey, R.P., Lee, M., Gounelle, M. and Zolensky, M.E. (2008) A TEM study of thermally modified comet 81P/Wild 2 dust particles by interactions with the aerogel matrix during the Stardust capture process. Meteoritics & Planetary Science 43, 97-120.
Levasseur-Regourd, A.-C., Agarwal, J., Cottin, H., Engrand, C., Flynn, G., Fulle, M., Gombosi, T., Langevin, Y., Lasue, J., Mannel, T., Merouane, S., Poch, O., Thomas, N. and Westphal, A. (2018) Cometary Dust. Space Science Reviews 214, 64.
Lisse, C.M., Dennerl, K., Christian, D.J., Wolk, S.J., Bodewits, D., Zurbuchen, T.H., Hansen, K.C., Hoekstra, R., Combi, M., Fry, C.D., Dryer, M., Mäkinen, T. and Sun, W. (2007a) Chandra observations of comet 9P/Tempel 1 during the Deep Impact campaign. Icarus 190, 391-405.
Lisse, C.M., Kraemer, K.E., Nuth Iii, J.A., Li, A. and Joswiak, D. (2007b) Comparison of the composition of the Tempel 1 ejecta to the dust in Comet C/Hale-Bopp 1995 O1 and YSO HD 100546. Icarus 187, 69-86.
Lisse, C.M., VanCleve, J., Adams, A.C., A'Hearn, M.F., Fernandez, Y.R., Farnham, T.L., Armus, L., Grillmair, C.J., Ingalls, J., Belton, M.J.S., Groussin, O., McFadden, L.A., Meech, K.J., Schultz, P.H., Clark, B.C., Feaga, L.M. and Sunshine, J.M. (2006) Spitzer spectral observations of the Deep Impact ejecta. Science 313, 635-640.
Lodders, K. (2010) Solar system abundances of the elements, in: Goswami, A., Reddy, B.E. (Eds.), Principles and Perspectives in Cosmochemistry. Springer Berlin Heidelberg, pp. 379-417.
Love, S. and Brownlee, D. (1993) A direct measurement of the terrestrial mass accretion rate of cosmic dust. Science 262, 550-553.
Love, S.G. and Brownlee, D.E. (1991) Heating and thermal transformation of micrometeoroids entering the Earth's atmosphere. Icarus 89, 26-43.
Love, S.G. and Brownlee, D.E. (1994) Peak atmospheric entry temperatures of micrometeorites. Meteoritics 29, 69-70.
Mac Low, M.-M. and Klessen, R.S. (2004) Control of star formation by supersonic turbulence. Reviews of modern physics 76, 125.
Mackinnon, I.D. and Rietmeijer, F.J. (1987) Mineralogy of chondritic interplanetary dust particles. Reviews of Geophysics 25, 1527-1553.
MacPherson, G.J. (2005) Calcium-Aluminum-rich Inclusions in chondritic meteorites, in: Davis, A.M., Holland, H.D., Turekian, K.K. (Eds.), Meteorites, Comets and Planets: Treatise on Geochemistry. Elsevier-Pergamon, Oxford, pp. 201-246.
Malfait, K.J. (1999) The properties and evolution of the dusty disks surrounding Herbig Ae/Be stars, Ph.D. Thesis, p. 832.
Mann, I., Köhler, M., Kimura, H., Cechowski, A. and Minato, T. (2006) Dust in the solar system and in extra-solar planetary systems. The Astronomy and Astrophysics Review 13, 159-228.
Mathurin, J., Dartois, E., Pino, T., Engrand, C., Duprat, J., Deniset-Besseau, A., Borondics, F., Sandt, C. and Dazzi, A. (2019) Nanometre-scale infrared chemical imaging of organic matter in ultra-carbonaceous Antarctic micrometeorites (UCAMMs). A&A 622, A160.
Matrajt, G., Ito, M., Wirick, S., Messenger, S., Brownlee, D.E., Joswiak, D., Flynn, G., Sandford, S., Snead, C. and Westphal, A. (2008) Carbon investigation of two Stardust particles: A TEM, NanoSIMS, and XANES study. Meteoritics & Planetary Science 43, 315-334.
Matrajt, G., Muñoz Caro, G.M., Dartois, E., D'Hendecourt, L., Deboffle, D. and Borg, J. (2005) FTIR analysis of the organics in IDPs: Comparison with the IR spectra of the diffuse interstellar medium. Astronomy and Astrophysics 433, 979-995.
Maurette, M., Hammer, C., Brownlee, D.E., Reeh, N. and Thomsen, H.H. (1986) Placers of cosmic dust in the blue ice lakes of Greenland. Science 233, 869-872.

Maurette, M., Jéhano, C., Robin, E. and Hammer, C. (1987) Characteristics and mass distribution of extraterrestrial dust from the Greenland ice cap. Nature 328, 699-702.
Maurette, M., Olinger, C., Christophe, M., Kurat, G., Pourchet, M., Brandstätter, F. and Bourot-Denise, M. (1991) A collection of diverse micrometeorites recovered from 100 tons of Antarctic blue ice. Nature 351, 44-47.
Merouane, S., Djouadi, Z. and Le Sergeant d'Hendecourt, L. (2014) Relations between aliphatics and silicate components in 12 stratospheric particles deduced from vibrational spectroscopy. The Astrophysical Journal 780, 174.
Morbidelli, A., Gaspar, H.S. and Nesvorny, D. (2014) Origin of the peculiar eccentricity distribution of the inner cold Kuiper belt. Icarus 232, 81-87.
Nakamura-Messenger, K., Clemett, S.J., Messenger, S. and Keller, L.P. (2011) Experimental aqueous alteration of cometary dust. Meteoritics & Planetary Science 46, 843-856.
Nakamura, T., Imae, N., Nakai, I., Noguchi, T., Yano, H., Terada, K., Murakami, T., Fukuoka, T., Nogami, K.-I., Ohashi, H., Nozaki, W., Hashimoto, M., Kondo, N., Matsuzaki, H., Ichikawa, O. and Ohmori, R. (1999) Antarctic micrometeorites collected at the Dome Fuji Station. Antarctic Meteorite Research 12, 183-198.
Nakamura, T., Noguchi, T., Ozono, Y., Osawa, T. and Nagao, K. (2005a) Mineralogy of ultracarbonaceous large micrometeorites, Meteoritics and Planetary Science, p. #5046.
Nakamura, T., Noguchi, T., Ozono, Y., Osawa, T. and Nagao, K. (2005b) Mineralogy of ultracarbonaceous large micrometeorites. Meteoritics 40 Suppl., #5046.
Nakamura, T., Noguchi, T., Tsuchiyama, A., Ushikubo, T., Kita, N.T., Valley, J.W., Zolensky, M.E., Kakazu, Y., Sakamoto, K., Mashio, E., Uesugi, K. and Nakano, T. (2008a) Chondrule-like objects in short-period comet 81P/Wild 2. Science 321, 1664-1667.
Nakamura, T., Tsuchiyama, A., Akaki, T., Uesugi, K., Nakano, T., Takeuchi, A., Suzuki, Y. and Noguchi, T. (2008b) Bulk mineralogy and three-dimensional structures of individual Stardust particles deduced from synchrotron X-ray diffraction and microtomography analysis. Meteoritics & Planetary Science 43, 247-259.
Nellist, P.D. (2007) Scanning Transmission Electron Microscopy, in: Hawkes, P.W., Spence, J.C.H. (Eds.), Science of Microscopy. Springer New York, New York, NY, pp. 65-132.
Nesvorný, D., Janches, D., Vokrouhlický, D., Pokorný, P., Bottke, W.F. and Jenniskens, P. (2011a) Dynamical model for the zodiacal cloud and sporadic meteors. The Astrophysical Journal 743, 129.
Nesvorný, D., Jenniskens, P., Levison, H.F., Bottke, W.F., Vokrouhlicky, D. and Gounelle, M. (2010) Cometary origin of the zodiacal cloud and carbonaceous micrometeorites. Implications for hot debris disks. The Astrophysical Journal 713, 816-836.
Nesvorný, D., Vokrouhlický, D., Pokorný, P. and Janches, D. (2011b) Dynamics of dust particles released from Oort cloud comets and their contribution to radar meteors. The Astrophysical Journal 743, 37.
Noguchi, T., Nakamura, T. and Nozaki, W. (2002) Mineralogy of phyllosilicate-rich micrometeorites and comparison with Tagish Lake and Sayama meteorites. EPSL 202, 229-246.
Noguchi, T., Ohashi, N., Tsujimoto, S., Mitsunari, T., Bradley, J.P., Nakamura, T., Toh, S., Stephan, T., Iwata, N. and Imae, N. (2015) Cometary dust in Antarctic ice and snow: Past and present chondritic porous micrometeorites preserved on the Earth's surface. Earth and Planetary Science Letters 410, 1-11.
Noguchi, T., Yabuta, H., Itoh, S., Sakamoto, N., Mitsunari, T., Okubo, A., Okazaki, R., Nakamura, T., Tachibana, S., Terada, K., Ebihara, M., Imae, N., Kimura, M. and Nagahara, H. (2017) Variation of mineralogy and organic material during the early stages of aqueous activity recorded in Antarctic micrometeorites. Geochimica et Cosmochimica Acta 208, 119-144.
Olbrycht, R., Kałuża, M., Wittchen, W., Borecki, M., Więcek, B. and De Mey, G. (2016) Gas identification and estimation of its concentration in a tube using hyperspectral thermography approach, Proc. 13th Quantitative Infrared Thermography Conf., pp. 605-610.
Olofsson, J., Augereau, J.-C., van Dishoeck, E., F., Merín, B., Lahuis, F., Kessler-Silacci, J., Dullemond, C., P., Oliveira, I., Blake, G., A., Boogert, A., C. A., Brown, J., M., Evans, N., J., Geers, V., Knez, C.,

Monin, J.-L. and Pontoppidan, K. (2009) C2D Spitzer-IRS spectra of disks around T Tauri stars. A&A 507, 327-345.
Orthous-Daunay, F.R., Quirico, E., Beck, P., Brissaud, O., Dartois, E., Pino, T. and Schmitt, B. (2013) Mid-infrared study of the molecular structure variability of insoluble organic matter from primitive chondrites. Icarus 223, 534-543.
Plane, J.M.C. (2012) Cosmic dust in the earth's atmosphere. Chemical Society Reviews 41, 6507-6518.
Poch, O., Istiqomah, I., Quirico, E., Beck, P., Schmitt, B., Theulé, P., Faure, A., Hily-Blant, P., Bonal, L., Raponi, A., Ciarniello, M., Rousseau, B., Potin, S., Brissaud, O., Flandinet, L., Filacchione, G., Pommerol, A., Thomas, N., Kappel, D., Mennella, V., Moroz, L., Vinogradoff, V., Arnold, G., Erard, S., Bockelée-Morvan, D., Leyrat, C., Capaccioni, F., De Sanctis, M.C., Longobardo, A., Mancarella, F., Palomba, E. and Tosi, F. (2020) Ammonium salts are a reservoir of nitrogen on a cometary nucleus and possibly on some asteroids. Science 367, eaaw7462.
Prasad, M.S., Rudraswami, N.G. and Panda, D.K. (2013) Micrometeorite flux on Earth during the last ~50,000 years. Journal of Geophysical Research: Planets 118, 2013JE004460.
Reipurth, B. (2005) The early sun: evolution and dynamic environment, Chondrites and the Protoplanetary Disk, p. 54.
Remusat, L., Palhol, F., Robert, F., Derenne, S. and France-Lanord, C. (2006) Enrichment of deuterium in insoluble organic matter from primitive meteorites: A solar system origin? Earth and Planetary Science Letters 243, 15-25.
Rochette, P., Folco, L., Suavet, C., van Ginneken, M., Gattacceca, J., Perchiazzi, N., Braucher, R. and Harvey, R. (2008) Micrometeorites from the Transantarctic Mountains. PNAS 105, 18206-18211.
Rojas, J., Duprat, J., Dartois, E., Wu, T.-D., Engrand, C., Augé, B., Mathurin, J., Guérin, B., Guerquin-Kern, J.-L., Boduch, P. and Rothard, H. (2020) Isotopic Analyses of Ion Irradiation-Induced Organic Residues, Clues on the Formation of Organics from UCAMMs, LPSC. Lunar and Planetary Institute, Houston, p. #1630.
Rojas, J., Duprat, J., Engrand, C., Dartois, E., Delauche, L., Godard, M., Gounelle, M., Carrillo-Sánchez, J., Pokorný, P. and Plane, J. (2021) The micrometeorite flux at Dome C (Antarctica), monitoring the accretion of extraterrestrial dust on Earth. Earth and Planetary Science Letters 560, 116794.
Rotundi, A., Baratta, G.A., Borg, J., Brucato, J.R., Busemann, H., Colangeli, L., D'Hendecourt, L., Djouadi, Z., Ferrini, G., Franchi, I.A., Fries, M., Grossemy, F., Keller, L.P., Mennella, V., Nakamura, K., Nittler, L.R., Palumbo, M.E., Sandford, S.A., Steele, A. and Wopenka, B. (2008) Combined micro-Raman, micro-infrared, and field emission scanning electron microscope analyses of comet 81P/Wild 2 particles collected by Stardust. Meteoritics & Planetary Science 43, 367-397.
Rotundi, A., Ferrini, G., Baratta, G.A., Palumbo, M.E., Palomba, E. and Colangeli, L. (2007) Combined Micro-Infrared (IR) and Micro-Raman Measurements on Stratospheric Interplanetery Dust Particles. Dust in Planetary Systems 643, 149-153.
Rotundi, A. and Rietmeijer, F.J.M. (2008) Carbon in meteoroids: Wild 2 dust analyses, IDPs and cometary dust analogues. Earth Moon and Planets 102, 473-483.
Sandford, S.A. and Walker, R.M. (1985) Laboratory infrared transmission spectra of individual interplanetary dust particles from 2.5 to 25 microns. ApJ 291, 838-851.
Simon, S.B., Joswiak, D.J., Ishii, H.A., Bradley, J.P., Chi, M., Grossman, L., Aléon, J., Brownlee, D.E., Fallon, S., Hutcheon, I.D., Matrajt, G. and McKeegan, K.D. (2008) A refractory inclusion returned by Stardust from comet 81P/Wild 2. Meteoritics and Planetary Science 43, 1861-1877.
Smith, E. and Dent, G. (2005) Introduction, basic theory and principles. Modern Raman spectroscopy-A practical approach, 1-21.
Suttle, M., Folco, L., Genge, M. and Russell, S. (2020a) Flying too close to the Sun–the viability of perihelion-induced aqueous alteration on periodic comets. Icarus 351, 113956.
Suttle, M.D., Folco, L., Genge, M.J. and Russell, S.S. (2020b) Flying too close to the Sun – The viability of perihelion-induced aqueous alteration on periodic comets. Icarus, 113956.

Takigawa, A., Furukawa, Y., Kimura, Y., Davidsson, B. and Nakamura, T. (2019) Exposure experiments of amorphous silicates and organics to cometary ice and vapor analogs. The Astrophysical Journal 881, 27.
Taylor, S., Lever, J.H. and Harvey, R.P. (1998) Accretion rate of cosmic spherules measured at the South Pole. Nature 392, 899-903.
Terada, K., Yada, T., Kojima, H., Noguchi, T., Nakamura, T., Yano, H. and Group, J.A.W. (2001) General Characterization of Antarctic Micrometeorites Collected by the 39Th Japan Antarctic Research Expedition. Meteoritics and Planetary Science Supplement 36, A206.
Tomeoka, K. and Buseck, P.R. (1988) Matrix mineralogy of the Orgueil CI carbonaceous chondrite. GCA 52, 1627-1640.
Toppani, A., Libourel, G., Engrand, C. and Maurette, M. (2000) Experimental simulation and modeling of atmospheric entry of micrometeorites, MAPS, p. A158.
Tuinstra, F. and Koenig, J.L. (1970) Raman spectrum of graphite. The Journal of chemical physics 53, 1126-1130.
van Boekel, R., Ratzka, T., Leinert, C., Henning, T., Min, M. and Waters, R. (2005) The spatially resolved mineralogy of proto-planetary disks, Protostars and Planets V, p. #8448.
Vinogradoff, V., Bernard, S., Le Guillou, C. and Remusat, L. (2018) Evolution of interstellar organic compounds under asteroidal hydrothermal conditions. Icarus 305, 358-370.
Vinogradoff, V., Le Guillou, C., Bernard, S., Binet, L., Cartigny, P., Brearley, A.J. and Remusat, L. (2017) Paris vs. Murchison: Impact of hydrothermal alteration on organic matter in CM chondrites. Geochimica et Cosmochimica Acta 212, 234-252.
Vollmer, C., Pelka, M., Leitner, J. and Janssen, A. (2020) Amorphous silicates as a record of solar nebular and parent body processes—A transmission electron microscope study of fine-grained rims and matrix in three Antarctic CR chondrites. Meteoritics & Planetary Science 55, 1491-1508.
Walsh, K.J., Morbidelli, A., Raymond, S.N., O'Brien, D.P. and Mandell, A.M. (2012) Populating the asteroid belt from two parent source regions due to the migration of giant planets—"The Grand Tack". Meteoritics & Planetary Science 47, 1941-1947.
Watanabe, H., Otsuka, T., Harada, M. and Okada, T. (2014) Imbalance between anion and cation distribution at ice interface with liquid phase in frozen electrolyte as evaluated by fluorometric measurements of pH. The Journal of Physical Chemistry C 118, 15723-15731.
Wooden, D.H., Butner, H.M., Harker, D.E. and Woodward, C.E. (2000) Mg-Rich Silicate Crystals in Comet Hale–Bopp: ISM Relics or Solar Nebula Condensates? Icarus 143, 126-137.
Wooden, D.H., Harker, D.E., Woodward, C.E., Butner, H.M., Koike, C., Witteborn, F.C. and McMurtry, C.W. (1999) Silicate Mineralogy of the Dust in the Inner Coma of Comet C/1995 01 (Hale-Bopp) Pre- and Postperihelion. Astrophysical Journal 517, 1034-1058.
Wooden, D.H., Woodward, C.E. and Harker, D.E. (2004) Discovery of Crystalline Silicates in Comet C/2001 Q4 (NEAT). The Astrophysical Journal Letters 612, L77-L80.
Wright, C.M., Do Duy, T. and Lawson, W. (2016) Absorption at 11 μm in the interstellar medium and embedded sources: evidence for crystalline silicates. Monthly Notices of the Royal Astronomical Society 457, 1593-1625.
Yabuta, H., Noguchi, T., Itoh, S., Nakamura, T., Miyake, A., Tsujimoto, S., Ohashi, N., Sakamoto, N., Hashiguchi, M., Abe, K.-i., Okubo, A., Kilcoyne, A.L.D., Tachibana, S., Okazaki, R., Terada, K., Ebihara, M. and Nagahara, H. (2017) Formation of an ultracarbonaceous Antarctic micrometeorite through minimal aqueous alteration in a small porous icy body. Geochimica et Cosmochimica Acta 214, 172-190.
Yada, T. and Kojima, H. (2000) The collection of micrometeorites in the Yamato meteorite ice field of Antarctica in 1998. AMR 13, 9-18.
Yesiltas, M. and Kebukawa, Y. (2016) Associations of organic matter with minerals in Tagish Lake meteorite via high spatial resolution synchrotron-based FTIR microspectroscopy. Meteoritics & Planetary Science 51, 584-595.
Zanetta, P.-M., Leroux, H., Le Guillou, C., Zanda, B. and Hewins, R. (2021) Nebular thermal processing of accretionary fine-grained rims in the Paris CM chondrite. Geochimica et Cosmochimica Acta 295, 135-154.

Zolensky, M., Nakamura-Messenger, K., Rietmeijer, F., Leroux, H., Mikouchi, T., Ohsumi, K., Simon, S., Grossman, L., Stephan, T., Weisberg, M., Velbel, M., Zega, T., Stroud, R., Tomeoka, K., Ohnishi, I., Tomioka, N., Nakamura, T., Matrajt, G., Joswiak, D., Brownlee, D., Langenhorst, F., Krot, A., Kearsley, A., Ishii, H., Graham, G., Da, Z.R., Ch, M., Bradley, J., Hagiya, K., Gounelle, M., Keller, L. and Bridges, J. (2008) Comparing Wild 2 particles to chondrites and IDPs. Meteoritics & Planetary Science 43, 261-272.

Zolensky, M.E., Zega, T.J., Yano, H., Wirick, S., Westphal, A.J., Weisberg, M.K., Weber, I., Warren, J.L., Velbel, M.A., Tsuchiyama, A., Tsou, P., Toppani, A., Tomioka, N., Tomeoka, K., Teslich, N., Taheri, M., Susini, J., Stroud, R., Stephan, T., Stadermann, F.J., Snead, C.J., Simon, S.B., Simionovici, A., See, T.H., Robert, F., Rietmeijer, F.J.M., Rao, W., Perronnet, M.C., Papanastassiou, D.A., Okudaira, K., Ohsumi, K., Ohnishi, I., Nakamura-Messenger, K., Nakamura, T., Mostefaoui, S., Mikouchi, T., Meibom, A., Matrajt, G., Marcus, M.A., Leroux, H., Lemelle, L., Le, L., Lanzirotti, A., Langenhorst, F., Krot, A.N., Keller, L.P., Kearsley, A.T., Joswiak, D., Jacob, D., Ishii, H., Harvey, R., Hagiya, K., Grossman, L., Grossman, J.N., Graham, G.A., Gounelle, M., Gillet, P., Genge, M.J., Flynn, G., Ferroir, T., Fallon, S., Ebel, D.S., Dai, Z.R., Cordier, P., Clark, B., Chi, M., Butterworth, A.L., Brownlee, D.E., Bridges, J.C., Brennan, S., Brearley, A., Bradley, J.P., Bleuet, P., Bland, P.A. and Bastien, R. (2006) Mineralogy and petrology of comet 81P/Wild 2 nucleus samples. Science 314, 1735-1739.